University of California
Santa Barbara

Integrated True Time Delays and Optical Beam Forming Networks for Wideband Wireless Communications

A dissertation submitted in partial satisfaction
of the requirements for the degree

Doctor of Philosophy
in
Electrical and Computer Engineering

by

Yuan Liu

Committee in charge:

Professor Jonathan Klamkin, Chair
Professor Larry A. Coldren
Professor John E. Bowers
Professor Clint Schow

September 2019

The Dissertation of Yuan Liu is approved.

Professor Larry A. Coldren

Professor John E. Bowers

Professor Clint Schow

Professor Jonathan Klamkin, Committee Chair

September 2019

Integrated True Time Delays and Optical Beam Forming Networks for Wideband Wireless Communications

by

Yuan Liu

Acknowledgements

This dissertation would not be possible without the help from a great number of people. The journey hasn't always been smooth, and I must acknowledge those that have been instrumental in guiding me to this end. It is not possible to thank everyone here and only a partial list is constituted in the following paragraphs.

First and foremost, I would like to thank my advisor Professor Jonathan Klamkin who gave me the opportunity to work in his research group and develop my engineering skills. He offered great support throughout this work and guided me to be in the right direction. Also, I greatly appreciate the research freedom he gave me that would let me pursue my own means to solve issues or make decisions, as well as his patience and enormous time spent in polishing my papers and this thesis. Over my three and a half years in Jonathan's group, I have been watching the group growing with a supportive atmosphere. It has been a great pleasure to be a member of his group and to work with him.

I would also like to thank the other faculty members that serve on my committee: Professor Larry A. Coldren, Professor John E. Bowers and Professor Clint Schow. Each of them has been willing to offer advice in improving this work. A special thank to Professor Coldren for providing the lab facilities that help me complete the experiments. Also I would like to thank him for sharing his valuable knowledge on semiconductor lasers both in class and conversions. Despite this dissertation hardly involves the laser work, I believe I would appreciate the knowledge gained from him in my future career.

The research experience in my early time in UCSB enhanced the chance of success of this dissertation. I would like to thank Professor Adel Saleh who taught me the way of thinking from the perspective of architecture. I would also like to thank Professor John E. Bowers and Professor Daniel J. Blumenthal for giving me the opportunity to get

trained in their labs, which was a great experience. A special thanks to Taran Huffman who firstly introduced the ultra-low loss silicon nitride waveguide technology to me and taught me the techniques for characterizing silicon nitride ring resonators.

This work would not be possible without the assistance of other graduate students and post-docs. I would like to give my thanks to all of them. To Sergio, who provided many valuable suggestions for the experiments in this work. To Brandon for the excellent collaboration in this project. To Fengqiao and Yu-Ning for the great assisting work in the lab. To Bowen, Hongwei, Fabrizio, Sarvagya and Victoria for their suggestions and experience in chip designs and fabrications. To Joseph, Thomas, Bei, Lei, Simone and other group members for sharing their varied technical knowledge. It has been my pleasure to work with all of you. Thanks also go out to Arda, Weiqiang, Songtao, Jinxi, Yujie and others outside the group who provided varied assistance towards the end of this journey. To all of you, thank you for making my time at UCSB an unforgettable experience.

I would also like to thank the help outside the university. Thanks to our project collaborators Jean Kalkavage and Eric Adles from the Johns Hopkins University Applied Physics Lab who provided valuable suggestions and initial funding for this project. To Adam Wichman, who initially worked on this project and answered all my questions. Also, I would like to thank NASA BROADCAST for the funding support.

Finally, I would like to thank my family for the continuous support and encouragement throughout my PhD, especially for the first few years. I could not have asked for anything more from you and thank you for making me the person I am today.

Curriculum Vitæ

Yuan Liu

Education

2019	Ph.D. in Electrical and Computer Engineering (expected), University of California, Santa Barbara.
2014	M.S. in Electrical and Computer Engineering, University of California, Santa Barbara.
2012	M.S. in Condensed Matter Physics, Technical Institute of Physics and Chemistry, Chinese Academy of Sciences.
2009	B.S. in Optical Information Science and Technology, Harbin Institute of Technology.

Journal Publications

1. A. S. Khope, M. Saeidi, R. Yu, X. Wu, A. M. Netherton, **Y. Liu**, Z. Zhang, Y. Xia, G. Fleeman, A. Spott, *et. al.*, *Multi-wavelength selective crossbar switch*, *Optics Express* **27** (2019), no. 4 5203–5216.
2. **Y. Liu**, A. R. Wichman, B. Isaac, J. Kalkavage, E. J. Adles, T. R. Clark, and J. Klamkin, *Ultra-low-loss Silicon Nitride Optical Beamforming Network for Wideband Wireless Applications*, *IEEE Journal of Selected Topics in Quantum Electronics* **24** (2018), no. 4 1–10.
3. S. Dwivedi, S. Pinna, R. Moreira, **Y. Liu**, B. Song, S. Estrella, L. Johansson, and J. Klamkin, *Multicore Fiber Link with SiN Integrated Fan-out and InP Photodiode Array*, *IEEE Photonics Technology Letters* **30** (2018), no. 22 1921–1924.
4. **Y. Liu**, A. Wichman, B. Isaac, J. Kalkavage, E. J. Adles, T. R. Clark, and J. Klamkin, *Tuning Optimization of Ring Resonator Delays for Integrated Optical Beam Forming Networks*, *Journal of Lightwave Technology* **35** (2017), no. 22 4954–4960.
5. **Y. Liu**, B. Wang, S. Xie, Y. Bo, P. Wang, J. Zuo, Y. Xu, J. Xu, Q. Peng, D. Cui, *et. al.*, *High-power Narrow-linewidth Quasi-cw Diode-pumped TEM_{00} 1064 nm Nd:YAG Ring Laser*, *Applied optics* **51** (2012), no. 10 C27–C31.
6. K. Liu, F. Li, **Y. Liu**, D. Cao, Y. Bo, Q. Peng, D. Cui, J. Zhang, and Z. Xu, *Compact Diode-directly-pumped Passively Mode-locked TEM_{00} Nd:$GdVO_4$ Laser at 1341 nm Using a Semiconductor Saturable Absorber Mirror*, *Laser Physics* **22** (2012), no. 1 95–99.
7. Z. Xu, S. Xie, Y. Bo, J. Zou, B. Wang, P. Wang, Z. Wang, **Y. Liu**, J. Xu, Q. Peng, *et. al.*, *Investigation of 30w-class Second-generation Sodium Beacon Laser*, *Acta Optica Sinaca* **31** (2011) 0900111–1.

Conference Publications

1. **Y. Liu**, B. Isaac, J. Kalkavage, E. Adles, T. Clark, and J. Klamkin, *Beamforming with Photonic Integrated Circuits for Millimeter WaveCommunications and Phased Arrays*, in *Photonics and Electromagnetics Research Symposium (PIERS)*, pp. 4–8, 2019.

2. **Y. Liu**, B. Isaac, J. Kalkavage, E. Adles, T. Clark, and J. Klamkin, *True Time Delay Millimeter Wave Beam Steering with Integrated Optical Beamforming Network*, in *CLEO: Science and Innovations*, pp. SF3N–6, 2019.

3. **Y. Liu**, B. Isaac, J. Kalkavage, E. Adles, T. Clark, and J. Klamkin, *93-GHz Signal Beam Steering with True Time Delayed Integrated Optical Beamforming Network*, in *2019 Optical Fiber Communications Conference and Exhibition (OFC)*, pp. 1–3, IEEE, 2019.

4. **Y. Liu**, B. Isaac, J. Kalkavage, E. Adles, T. Clark, and J. Klamkin, *Programmable Integrated Microwave Photonics Beamforming Networks for Millimeter Wave Communications and Phased Arrays*, in *2019 IEEE Avionics and Vehicle Fiber-Optics and Photonics Conference (AVFOP)*, pp. TuD5, 2019.

5. **Y. Liu**, B. Isaac, J. Kalkavage, E. Adles, T. Clark, and J. Klamkin, *Millimeter Wave Beamsteering with True Time Delayed Integrated Optical Beamforming Network*, in *2019 European Conference on Optical Communication (ECOC)*, 2019.

6. B. Isaac, S. Pinna, **Y. Liu**, and J. Klamkin, *Efficiency of Waveguide Uni-traveling-carrier Photodiodes for Microwave Signal Generation*, in *Optical Fiber Communication Conference*, pp. Th3B–6, Optical Society of America, 2019.

7. B. Isaac, **Y. Liu**, S. Pinna, L. Coldren, and J. Klamkin, *Waveguide Uni-Traveling-Carrier Photodiodes for mmW Signal Generation: Space-Charge Impedance and Efficiency Limitations*, in *Device Research Conference (DRC)*, 2019.

8. B. Isaac, **Y. Liu**, S. Pinna, and J. Klamkin, *Limitations to Power Conversion Efficiency of InP Based Uni-traveling-carrier Photodiodes Due to Space Charge Resistance*, in *Compound Semiconductor Week (CSW) Conference* , 2019.

9. B. Song, Y. Luo, S. Pinna, **Y. Liu**, and J. Klamkin, *Dilute Waveguide Reflective Semiconductor Optical Amplifier for 3D Hybrid Silicon Photonics Integration*, in *Compound Semiconductor Week (CSW) Conference* , 2019.

10. F. Gambini, **Y. Liu**, B. Song, H. Zhao, V. Rosborough, F. Sang, P. Velha, S. Faralli, and J. Klamkin, *Ultra-compact Bragg-assisted Silicon Photonics Orbital Angular Momentum Emitter*, in *Integrated Photonics Research, Silicon and Nanophotonics*, pp. ITh3C–4, 2019.

11. J. Klamkin, **Y. Liu**, B. Song, F. Sang, and B. Isaac, *Integrated Microwave Photonic Component Technologies*, in *CLEO: Science and Innovations*, pp. JTh3D–5, 2018.

12. **Y. Liu**, B. Isaac, J. Kalkavage, E. Adles, T. Clark, and J. Klamkin, *Low-loss Silicon Nitride Integrated Optical Beamforming Network for Wideband Communication*, in *Proc. SPIE, Terahertz, RF, Millimeter, and Submillimeter-Wave Technology and Applications XI*, vol. 10531, p. 1053118, 2018.

13. **Y. Liu**, F. Sang, B. Isaac, J. Kalkavage, E. Adles, T. Clark, and J. Klamkin, *Integrated Silicon Nitride Optical Beamforming Networks for Wideband Communications*, in *Integrated Photonics Research, Silicon and Nanophotonics*, pp. ITh3B–4, 2018.

14. J. Klamkin, H. Zhao, B. Song, **Y. Liu**, B. Isaac, S. Pinna, F. Sang, and L. Coldren, *Indium Phosphide Photonic Integrated Circuits: Technology and Applications*, in *2018 IEEE BiCMOS and Compound Semiconductor Integrated Circuits and Technology Symposium (BCICTS)*, pp. 8–13, 2018.

15. B. Song, S. Pinna, **Y. Liu**, L. Megalini, and J. Klamkin, *3D Hybrid Integrated Lasers for Silicon Photonics*, in *Proc. SPIE, Silicon Photonics XIII*, vol. 10537, p. 105370V, International Society for Optics and Photonics, 2018.

16. **Y. Liu**, F. Sang, S. Pinna, B. Isaac, J. Kalkavage, E. Adles, T. Clark, and J. Klamkin, *Integrated Optical Beamforming Network for Millimeter Wave Communications*, in *2017 International Topical Meeting on Microwave Photonics (MWP)*, pp. 1–4, 2017.

17. S. Pinna, **Y. Liu**, L. A. Coldren, and J. Klamkin, *Integrated Star Coupler-based Multi-beam Lidar*, in *2017 IEEE Avionics and Vehicle Fiber-Optics and Photonics Conference (AVFOP)*, pp. 41–42, 2017.

18. **Y. Liu**, A. Wichman, B. Isaac, J. Kalkavage, E. Adles, T. Clark, and J. Klamkin, *Ring Resonator Based Integrated Optical Beam Forming Network with True Time Delay for mmW Communications*, in *2017 IEEE MTT-S International Microwave Symposium (IMS)*, pp. 443–446,2017.

19. **Y. Liu**, F. Sang, A. Wichman, B. Isaac, J. Kalkavage, E. Adles, T. Clark, and J. Klamkin, *Ring Resonator True Time Delay Arrays with Sharing Optimization for Wideband Applications*, in *Integrated Photonics Research, Silicon and Nanophotonics*, pp. IW2A–2, 2017.

20. S. Dwivedi, B. Song, **Y. Liu**, R. Moreira, S. Estrella, L. Johansson, and J. Klamkin, *Integrated Silicon Nitride Fan-in/Fan-out for Multi-core Fiber Interconnects*, in *Integrated Photonics Research, Silicon and Nanophotonics*, pp. IW2A–3, 2017.

21. B. Song, **Y. Liu**, S. Ristic, and J. Klamkin, *Tunable 3D Hybrid Integrated Silicon Photonic External Cavity Laser*, in *2017 Conference on Lasers and Electro-Optics (CLEO)*, pp. 1–2, IEEE, 2017.

22. B. Isaac, **Y. Liu**, B. Song, X. Xie, A. Beling, and J. Klamkin, *Hybrid Integration of UTC-PDs on Silicon Photonics*, in *CLEO: Science and Innovations*, pp. SM4O–1, 2017.

23. S. Dwivedi, B. Song, **Y. Liu**, R. Moreira, L. Johanson, and J. Klamkin, *Demonstration of Compact Silicon Nitride Grating Coupler Arrays for Fan-out of Multicore Fibers*, in *2017 Conference on Lasers and Electro-Optics (CLEO)*, pp. 1–2, IEEE, 2017.

24. J. Klamkin, B. Song, **Y. Liu**, L. Megalini, S. Dwivedi, and S. Pinna, *3D Hybrid Integration for Active Silicon Photonics*, in *SPIE Photon. West*, vol. 10131, 2017.

25. **Y. Liu**, A. Wichman, B. Isaac, J. Kalkavage, E. Adles, and J. Klamkin, *Ring Resonator Delay Elements for Integrated Optical Beamforming Networks: Group Delay Ripple Analysis*, in *Integrated Photonics Research, Silicon and Nanophotonics*, pp. IW1B–3, 2016.

26. **Y. Liu**, A. Wichman, B. Isaac, J. Kalkavage, E. Adlest, T. Clark, and J. Klamkin, *Single Ring Resonator Delays for Integrated Optical Beam Forming Networks*, in *2016 IEEE International Topical Meeting on Microwave Photonics (MWP)*, pp. 321–324, 2016.

Abstract

Integrated True Time Delays and Optical Beam Forming Networks for Wideband Wireless Communications

by

Yuan Liu

Millimeter waves (mmW) ranging in frequency from 30 to 300 GHz provide a tremendous amount of spectrum to meet the rapid growth of wireless data traffic demand. The W-band (75 - 100 GHz) mmW frequencies are particularly attractive as they can support links faster than 100 *Gbps*. Microwave photonics (MWP) is promising for mmW signal generation due to the frequency-independent low optical loss. For mmW phased array antennas (PAAs), wide bandwidth and low loss optical true time delays (TTDs) mitigate the beam squint issue and reduce power consumption in comparison to RF phase shifters that require driver amplifiers. In combination with integrated photonics where large scale and compact TTDs can be realized, integrated MWP is particularly suitable for mmW PAA beamforming ultra-high-speed communications.

Among the various tunable integrated TTD implementations, switched delay lines (SDLs) and optical ring resonators (ORRs) are particularly promising for large scale optical beamforming networks (OBFNs) for PAAs. In this thesis, both SDL and ORR based TTD devices have been investigated, with emphasis on the reduction of ripple in the delay spectrum. A ripple-free SDL architecture was developed based on Mach-Zehnder interferometer (MZI) optical switches, and a 1×4 OBFN using 5-stage SDLs was realized for linear PAAs. Ultra-low loss silicon nitride was used as an integrated photonics technology platform. Six delay configurations with 0, 1.5, 3, 4.5, 6 and 7.5 *ps* path delay incremental steps were demonstrated for the SDL-OBFN. The ORR based delay

lines were optimized to minimize the ripple in the delay response by applying a genetic algorithm, which revealed a tradeoff between the ripple level, delay value, bandwidth and total number of rings used. A 1×4 3-ORR (three rings in each path) based OBFN was optimized. An ORR-OBFN architecture where one ORR is shared by two adjacent paths was determined to reasonably balance the ripple level and system complexity. Two 3-ORR based 1×4 OBFNs with the architecture of sharing one and two ORRs were realized on the silicon nitride platform as well. With optimized tuning, a single 3-ORR delay line generated continuous tuning ranges of 209 ps and 172 ps for bandwidths of 6.3 GHz and 8.6 GHz, respectively. Delay responses with delay increment of 4.6 ps for linear PAAs were generated by the two ORR-OBFNs, both of which demonstrated that the OBFN with one ORR shared exhibits much more flattened delay spectrum as expected. Based on the results, both the SDL-OBFN and ORR-OBFN are considered extremely promising for directional beamforming with PAAs.

Integrated OBFN chips were packaged and used in experiments for mmW signal generation and beamsteering. The ORR-OBFN was utilized for a 41 GHz mmW signal generation experiment. The SDL-OBFN was utilized for a W-band signal beamsteering experiment. Six beam angles from -51° to 31°, with at least 15 GHz TTD bandwidth from 85 to 100 GHz, and an SNR of 35 dB were demonstrated. Also, a 94 GHz W-band signal with 3 $Gbps$ amplitude shift keying (ASK) data was generated and the spectrum was measured. To the author's best knowledge, this is the first report of W-band beamsteering and data transmission using an integrated OBFN.

To further improve the scalability and reduce the power consumption and complexity of the current PAA system, the ongoing work on OBFN-photodiode-antenna integration has been considered. Also, a novel recirculating delay loop (RDL) based OBFN architecture was proposed. This re-uses a single TTD element for the signal delays in all channels. Some of the required components for this RDL-OBFN have been realized.

Contents

Chapter 1

Introduction

1.1 Motivation

Mobile data traffic is increasing dramatically in recent years. The global mobile data traffic has been projected to reach 77.49 exabytes per month by 2022 [1], as depicted in Fig. 1.1. Given that high spectral efficiency has already been achieved [2], to meet this incredible projected increase in traffic demand, the carrier has to be pushed to high frequency bands such as millimeter waves (mmWs), which have a tremendous amount of spectrum to achieve very high communication rates. Currently, mmW frequencies at Ka-band, V-band and even W-band for higher data rate [3] have been proposed for the 5th generation (5G) mobile cellular communication (expected in 2020). However, only 28 and 38 GHz are widely used in 5G solutions and deployments utilize all-electronic technology [4, 5] that is mature and economically efficient. A higher frequency (e.g. W-band) is needed for extremely high bit rate links. There remain many challenges for all-electronics systems at such high frequencies such as bandwidth constraints, passband non-uniformities, integration difficulties in electronic phased arrays and power consumption issues for amplifier-driven phase shifters [6]. Microwave photonics (MWP) technology presents an alternative that can ease or eliminate some issues associated with conventional all-electronic solutions due to properties of photonics such as large band-

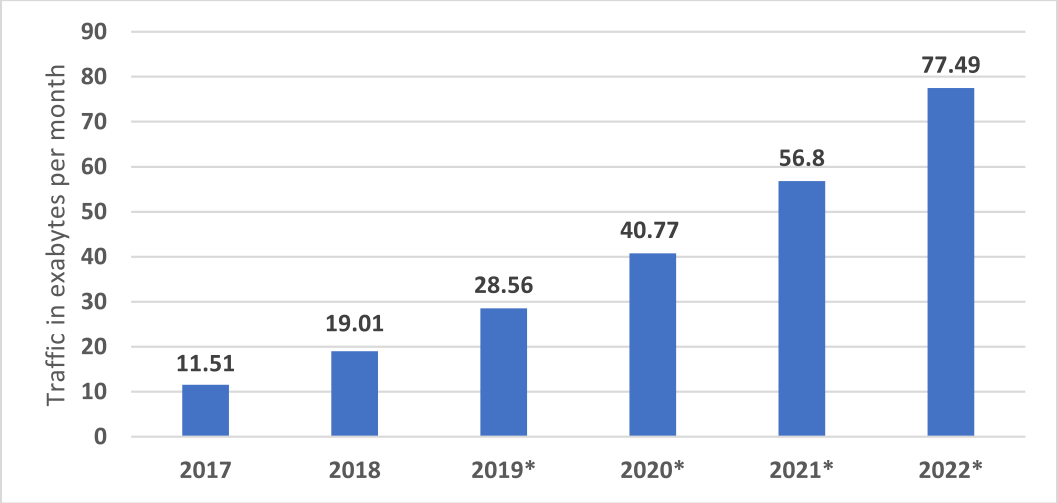

Figure 1.1: Global mobile data traffic from 2017 to 2022 (in exabytes per month) [1].

width, low propagation loss, immunity to electromagnetic interference and independence of radio-wave frequencies [7]. Moreover, MWP can be seamlessly integrated with fiber optic networks, which bridge optical and mmW communications.

Beamforming is inevitable in mmW communication systems to achieve a wideband communication, especially for densely deployed mmW networks such as 5G [8]. This capability will focus the beam in the desired direction, which increases the antenna gain to overcome the relatively high atmospheric loss of mmWs, as well as reduces the signal interference. In addition, the bandwidth limit of electronic components in conventional all-electronic beamforming systems where phase shifters are employed, the beam squint is a significant issue that limits the available bandwidth of the spectrum since the high frequency of the baseband signal will deviate the desired direction and result in a high attenuation. RF phase shifters which have high loss and require amplifiers are also power consuming. Using true time delays (TTDs) could solve the beam squint issue but it is very difficult to realize large bandwidth tunable TTDs using electronics. MWP is advantageous in terms of realizing broadband optical TTDs [9], which would transferred into the delay of the mmW signal through optical/electrical (O/E) conversion. Photonics en-

abled beamforming networks, so called optical beamforming networks (OBFNs), together with optical TTDs, we can bridge fiber optical networks and wireless communications [10] and achieve significant improvement in the data rate, and potentially the cost.

Integrated photonics technology is an effective approach to address concerns of MWP systems in terms of cost, size, weight and power consumption (CSWaP) [6, 11]. Particularly, for photonic-assisted beamforming, integrated MWP (IMWP) is advantageous for the realization of tunable optical TTDs for precise optical path length control and scalable OBFNs, making it possible to feed large-scale TTD phased array antennas (PAAs). Additionally, the emergence of high power lasers, ultra-low loss waveguides, ultra-high speed modulators, and ultra-fast high responsivity detectors[12] provide new possibilities for monolithically integrating mmW beamforming subsystems for wideband communications [13].

1.2 Millimeter Wave Frequencies

Millimeter waves refer to the band from 30 GHz to 300 GHz, which provides a huge amount of bandwidth to meet mobile communication demands. However, in the early days of satellite communications, high atmospheric and rain attenuation properties of mmWs led this band to have been largely dismissed for long range communications [2]. The physics of atmospheric propagation has been studied and reveals several frequency ranges with lower atmospheric attenuation [14, 15, 16], as shown in Fig. 1.2. The so-called atmospheric windows of mmWs occur naturally at 30, 90, 140, and 220 GHz. To be specific, atmospheric attenuation is approximately 0.06 dB/km and 0.08 dB/km at 28 GHz and 38 GHz, respectively, and is less than 0.5 dB/km at frequencies between 75 and 110 GHz (W-band). Within the atmospheric windows, the frequencies from 30 GHz to 40 GHz are widely used for commercial satellite and terrestrial communications,

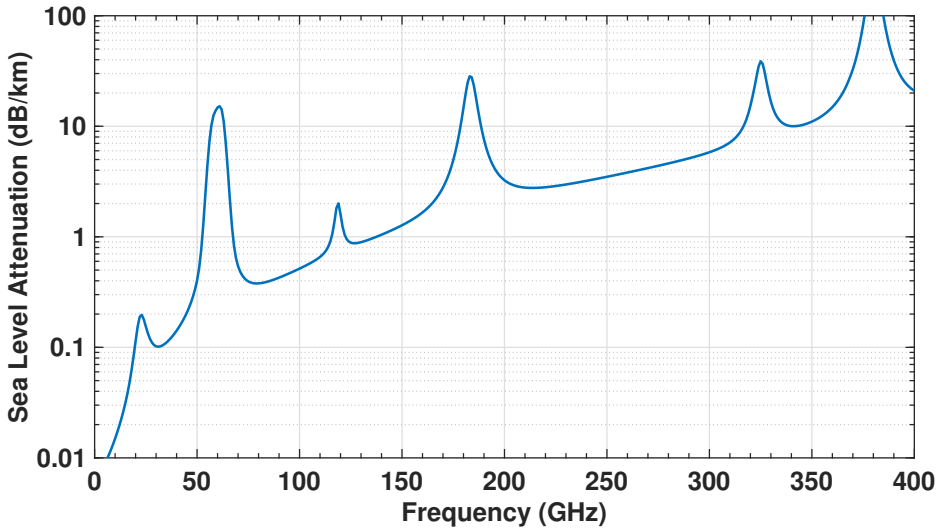

Figure 1.2: Average millimeter wave atmospheric absorption [14, 15, 16].

and will be used for 5G high speed channels; the frequency bands 75 GHz - 110GHz, 130 GHz - 150 GHz and 200GHz - 240 GHz (Terahertz) have not been allocated yet except for frequencies near 90 GHz which has been exploited primarily for military communications. These bands show a great potential for extremely high data rate long distance communications due to the wide bandwidths available, low atmospheric attenuation and lower interference.

Generally, the molecular absorption peaks of 60, 119, 183, and 325 GHz are to be avoided as they will limit transmission distances. One exception is 60 GHz, where there has been considerable work on mmW propagation in this band [17, 18, 19, 20, 21, 22, 23, 24, 25, 26, 27]. The 60 GHz mmWs reach a maximum of 15 dB/km absorption at sea level. This high level of attenuation severely limits link distances, making 60 GHz useful for only short-distance transmission. The high atmospheric attenuation adds advantages such as high-frequency reuse and secure communications because of the difficulty to eavesdrop. Also for out-of-atmosphere communications, between satellites for example, 60 GHz excels as the oxygen absorption limitations disappear and essentially free space

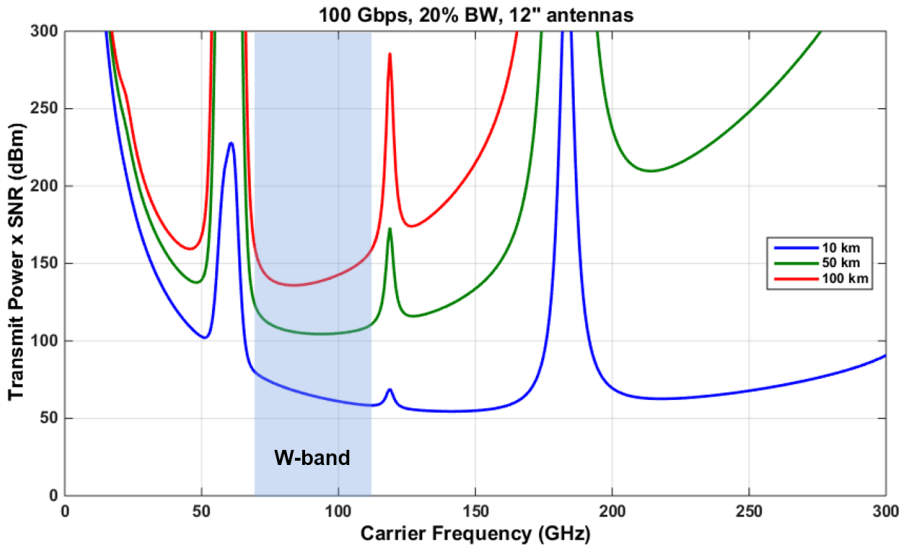

Figure 1.3: Link budget analysis of radio frequencies for high bit rate and long range at sea level [28].

communication conditions exist. Another benefit of 60 GHz wireless versus other mmW technologies is that, being at lower frequency, links can generally be realized at lower cost, since the building blocks such as transceivers, power amplifiers, low noise amplifiers, and mixers, are more readily available than at the higher mmW frequencies.

The W-band mmW is more popular recently and suitable for long haul high data rate communication. As shown in the figure of merit in Fig. 1.3, given the atmospheric attenuation, for 100 *Gbps*, 20% bandwidth usage and using 12" antennas, there is a window in the W-band with optimal link budget, especially for longer distances such as 100 *km*. In addition to the low atmospheric attenuation, despite the relatively smaller wavelength compared to other mmWs, the wavelength (~3 mm) is large compared to most small particle airborne effects such as fog, mist, sand, and dust. For example, thick fog has only 0.4 dB/km attenuation at 70/80 GHz [16, 29], yielding negligible impact on typical link distances. Similar to all high-frequency radio propagation, rain attenuation is a key factor that limits the practical link distance. Figure 1.4 shows the attenuation

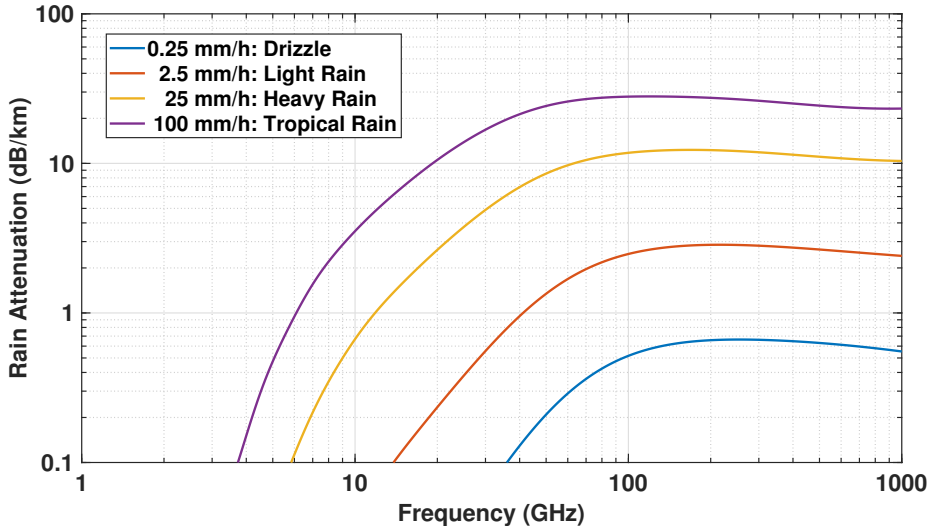

Figure 1.4: Rain attenuation at microwave and mmW frequencies [15, 30, 31].

at microwave and mmW frequencies in the presence of rain [15, 30, 31]. For most of the united states (US), the maximum rainfall experienced is less than 100 mm/h for 5 mins/yr, yielding up to 30 dB/km attenuation in the W-band. For 99.9% of the time, the rainfall is no more than 25 mm/h, yielding slightly greater than 10 dB/km attenuation. Currently, commercial 70/80 GHz equipment can provide a 2.5 Gbps link over 2 miles with 99.99% weather availability (50 mins of yearly outage) throughout most of the US [32, 33]. In some drier places such as Las Vegas, the distance could extend as far as 5 miles with the same weather availability.

1.3 Integrated Microwave Photonics

MWP is a multidisciplinary research discipline that unites the domains of RF engineering and optoelectronics. As depicted in Fig. 1.5, a basic MWP subsystem comprises of three parts: E/O conversion, photonic signal processing, and optical-to-electrical (O/E) signal conversion. The signal is imparted on an optical carrier through an E/O converter,

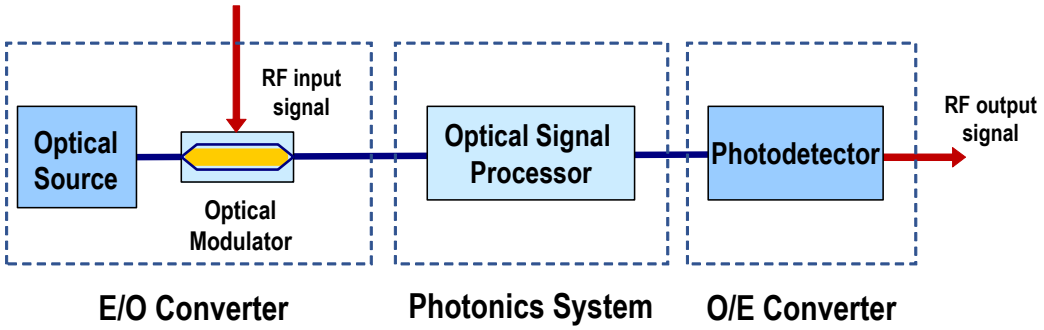

Figure 1.5: Schematic of a MWP subsystem.

typically a Mach-Zehnder modulator (MZM), which allows the signal to be processed in the optical domain using photonic signal processing components, such as optical filters. Then a RF carrier is regenerated and the processed signal is transferred to a RF carrier through an O/E converter (e.g. high speed photodiode (PD)), converting the signal from the optical domain back to the electrical domain.

MWP deals with the generation, processing, and distribution of microwave and mmW signals by optical means, leveraging the unique advantages of photonics including low loss, high bandwidth, frequency independence, and immunity to electromagnetic interference [7, 11, 12, 34, 35]. These advantages enable more RF application scenarios such as the remote location of antennas where conventional microwave cables would incur too much loss, and extremly high bit rate communication. This field has been gaining interest since the 1990s, when groundbreaking realizations demonstrated the potential of optical links for the transmission of microwave signals [36, 37, 38], followed by extensive research focused primarily on the generation of ultra-broadband signals [39, 40], frequency conversion [41, 42], RF remoting over fiber [43], MWP filters [44, 45], photonics-enhanced radar system [40, 46], and RF beam steering [40]. These processes reveal MWP as a promising solution for the impending challenges in telecommunications and provide new possibilities to approach the emerging information technology scenarios, such as 5G mobile commu-

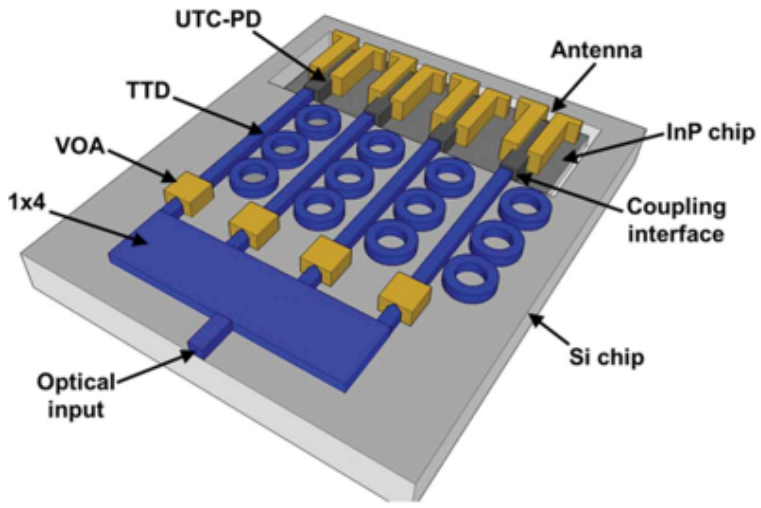

Figure 1.6: Integrated photonic-assisted beamforming subsystems.

nications, with capabilities beyond those of conventional electronic systems, in terms of enhanced flexibility, scalability, and capacity [12, 35]. In particular, a photonic based beamforming system could benefit from these advantages of MWP technology. Combining with optical TTDs, a photonics beamformer could provide beam squint free and frequency flexible beamforming performance.

Despite the tremendous potential of MWP, widespread use and application of this technology are currently limited by system high cost, bulkiness, complexity, and power consumption. The typical size, weight, and power consumption (SWaP) figures for commercial MWP systems are approximately 0.04 – 0.2 m^2 (size), 1.5 – 10 kg (weight), and 15 – 20 W (power consumption) [11], making them unsuitable for mass production and widespread use as required by next generation and emerging applications such as the Internet of Things (IoT) and mmW communications. Photonic integration has been leveraged to reduce the CSWap of photonic systems. Better reliability, stability, scalability and optical path length control could be achieved through photonic integration, which are all desirable for TTD and OBFN technology that would be used for data encoding and signal distribution for mmW communication systems. The potential of integration

of all key MWP components is attracting many research interests in applications such as photonic-assisted beamforming subsystems (depicted in Fig. 1.6). The loss of integrated waveguides is an important consideration as the optical loss in MWP systems is translated quadratically into electrical loss in an RF circuit, which is the so called the square law nature of photodetection. Many different low-loss waveguide technologies have been proposed and utilized for IMWP including silicon on Isolator (SOI), silicon nitride (Si_3N_4) and indium phosphide (InP), as shown in Table 1.1. The SOI platform can realize nano-scale waveguides that provide very compact footprint and large free spectral range [47] that is very attractive in many applications [48, 49, 50, 51]. However, the strong field confinement enhances loss induced by sidewall roughness [52], and leads to non-linear effects that limit the maximum power [53]. Although the propagation loss can be reduced by using micron-scale waveguides, this trades the compact footprint and requires careful design to minimize higher-order mode excitation [54]. The InP platform is highly advantageous for monolithic integration of active components such as lasers, detectors and modulators [55, 13]. Instead of only using heaters to tune the optical phase, plasmonic dispersion-based carrier injection mechanisms are available in InP, which allows for high-speed low-power tuning. However, the loss of InP waveguides is relatively high with 1 dB/cm in undoped regions and 2 dB/cm in active regions [56]. Si_3N_4 waveguides have demonstrated propagation loss below 0.1 dB/cm. This platform can reduce the overall optical loss significantly and attracts many research interests [57, 58, 59], but at the cost of consuming approximately an order of magnitude larger footprint than that required for comparable structures in submicron SOI. These waveguides also demonstrate very high optical power handling, up to 1 Watt in [60], which makes it possible to eliminate low noise amplifiers before antennas when performing microwave generation [61, 62, 63]. Besides optical loss, many efforts have been carried out for high performance active devices. On InP, active devices could be realized including lasers, semiconductor optical amplifiers

(SOAs), modulators and PDs. InP MZMs have demonstrated bandwidth larger than 67 GHz [64], and ultra-high speed InP uni-traveling carrier (UTC) PDs operating up to terahertz applications have been reported [65, 66, 67]. As for SOI, except for lasers and SOAs, modulators and PDs are available with bandwidth of $>$ 50 GHz and $>$40 GHz, respectively, as demonstrated in [68, 69]. Si_3N_4 is a pure dielectric material and does not inherently support for active devices. However, recent work has demonstrated high speed modulator with the integration of 2D materials such as graphene, or piezoelectric materials [12]. Beyond devices, many works have demonstrated the monolithic integration of multiple key components of a MWP system including lasers, modulators, photodiodes and patch antennas [70, 71]. The IMWP hybrid integration technology allows for integrating SOI and Si_3N_4 with InP, benefiting from both the low loss and CMOS compatibility of silicon photonics and highly efficient active devices of InP [72, 55]. In addition to the reduction of footprint and potential for monolithic integration, integrated photonics also provides a high optical confinement leading to new technological tools for IMWP, such as Kerr microresonator combs and on-chip stimulated Brillouin scattering [73, 74]. Therefore, both conventional and emerging components are available for various applications of IMWP technology.

1.4 Tunable Integrated Optical True Time Delays for Optical Beamforming Networks

An OBFN is the key component for MWP beamforming systems. An OBFN distributes the RF signal and provides appropriate delays or phase shifts in the optical domain for each antenna element (AE) in a PAA to generate the desired RF beam shape. Compared to TTD based OBFN, phase shifter (PS) based OBFN has an inherent

Table 1.1: Low Loss Waveguide Technologies for Integrated Microwave Photonics.

Platform	SOI		Si_3N_4	InP
loss (dB/cm)	3 (nanowire)	0.35 (multimode)	<0.1	1(undoped)/2(doped)
Tuning Mechanism	Thermo-Optic, Plasmonic Dispersion		Thermo-Optic	Thermo-Optic, Plasmonic Dispersion
Active Integration	Hybrid on lasers, monolithic on modulators and Ge detectors		Hybrid on all active components	Monolithic on all active components
References	[47, 54, 75]		[76, 77, 78, 79]	[80]

beam squint issue that could potentially limit the available communication bandwidth. For this reason, using TTDs for OBFNs is more desirable for the high communication bandwidth inherent to MWP technology. TTD-OBFN and PS-OBFN will be compared and discussed in detail in chapter 3.

Realizing TTD-OBFN using traditional MWP bulk TTD components is difficult as the optical path length for each AE is difficult to match. TTD based OBFNs are sensitive to path length difference, especially for high frequency mmW signals where the wavelength is only a few millimeters. Manufacturing optical connections with such a tight tolerance is impractical. Moreover, most of the commercial TTD components are mechanical based delay lines, which are bulky and unreliable for large scale PAAs. As discussed earlier, integrated photonics can eliminate these issues and is suitable for the application of OBFNs with integrated TTD lines.

Reconfigurability is desirable for OBFNs, which can be achieved using tunable integrated TTDs. Thus far, two primary approaches have been pursued to implement tunable TTDs – one makes used of dispersive structures such as optical ring resonators (ORRs),

gratings, Mach-Zehnder interferometers (MZIs) or photonic crystals. If the dispersion is sufficiently small and the delay within the signal bandwidth is approximately the same, the delay response can be considered as TTD, and the delay can be tuned by controlling the optical wavelength. The other approach switches between optical paths of various lengths using optical switches such as MZIs and arrayed waveguide gratings (AWGs). Brief introduction to TTD lines realized with these structures are provided next.

1.4.1 Dispersive Delay Lines

1.4.1.1 Optical Ring Resonators

An ORR can be described as an all-pass filter [81, 82]. If the loss of the waveguide is neglected, all optical power can be transferred through the ORR but the phase of the optical signal is altered, which will consequently change the group delay of the signal. An ORR displays a periodic delay response, where the maximum delay occurs at the resonance frequency, whereas the minimum delay occurs at the anti-resonance. The delay response can be continuously tuned by either changing the wavelength, ORR resonance frequency or coupling coefficient. Usually a single ORR can only provide limited delay or TTD bandwidth, whereas multiple ORRs can be combined to mitigate this limit using the so-called coupled resonator optical waveguide (CROW) structure [83, 79] or side-coupled integrated spaced sequence of resonators (SCISSOR) structure [84, 85, 76], as shown in Fig. 1.7(a). It has been shown that the SCISSOR can provide more stable and repeatable delay performance [86]. More details about ORRs and SCIRRORs will be discussed in Chapter 6.

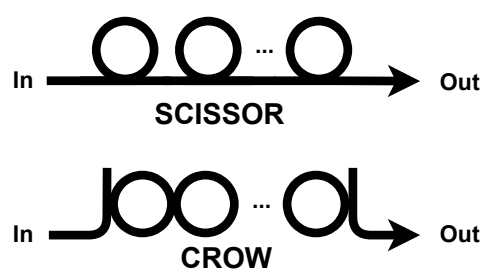

(a) ORRs

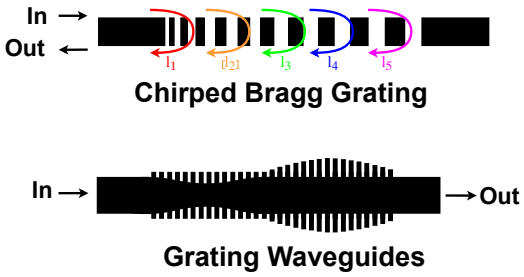

(b) Gratings

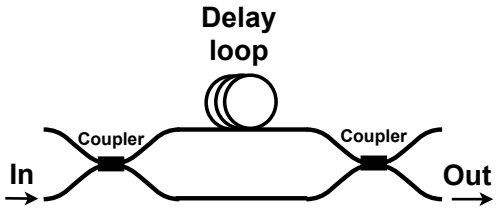

(c) Interferometers

(d) Photonic crystals

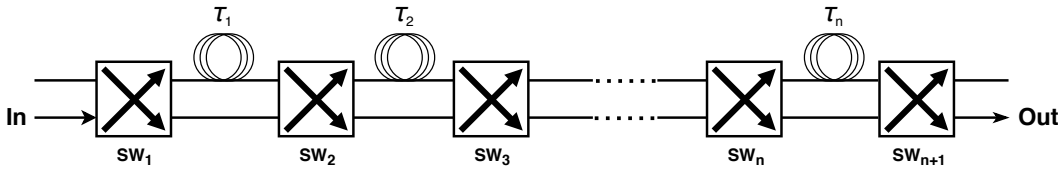

(e) Cascaded switched delay line

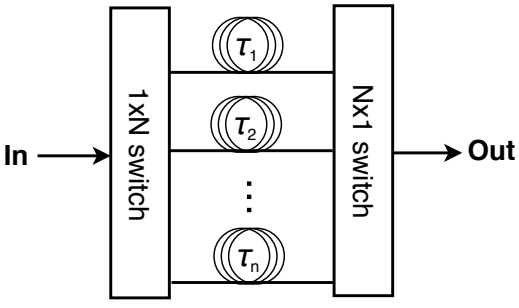

(f) Parallel switched delay line

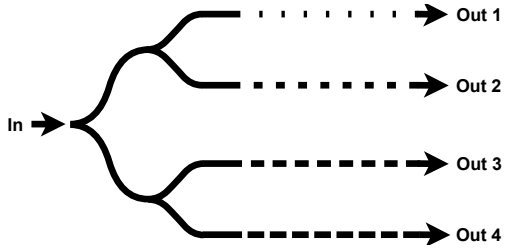

(g) Sub-wavelength grating waveguide

Figure 1.7: Tunable integrated TTD lines.

1.4.1.2 Gratings

Gratings are another compact structure that can provide continuous tuning of group delay. Two types of gratings are considered – reflective gratings and grating waveguides, as depicted in Fig. 1.7(b). Reflective gratings are based on Bragg gratings, where the grating period or grating effective index are chirped along the grating length so that the effective length is dependent on wavelength, and consequently a broadband totally reflective grating is achieved with a dispersive response. The chirp rate, chirp range, grating length, and grating index contrast determine the reflective bandwidth and dispersion. For wide band communications, where large TTD is required, the dispersion of the grating should be kept small. The chirped Bragg grating delay line was first used in fiber optics and combined with an optical circulator [87]. In integrated photonics where a circulator is not yet available, a structure with a 50/50 coupler and two chirped Bragg gratings could be employed to achieve in-line integration of the delay line [88, 89]. Recent research has shown a uniform Bragg with contra-directional coupler could also have a similar delay response but eliminates the circulator requirement [90]. Unlike reflective gratings, grating waveguide delay line structures use the transmission response of a grating. At the edge of a grating transmission stop band, a large dispersion regime exists, which can be utilized to provide tunable delay. For a uniform grating, the monotonic delay region is small and the dispersion is large. Fortunately this region can be extended and the dispersion can be reduced by applying grating apodization techniques [91, 92]. For grating delay lines, the slope of the monotonic delay can be positive or negative. Two gratings with opposite delay slope could be combined to generate a flat delay response (so-called TTD) with very large bandwidth [89]. The tunability of this structure could be achieved by blue/red-shift at the delay response of one or both of the oppositely chirped gratings using heaters or carrier injection.

1.4.1.3 Interferometers

Interferometers can generate a TTD response as well by splitting the optical signal into multiple delay paths, and then combining and interfering to alter the optical phase response. Figure 1.7(c) shows an asymmetric MZI based 2-tap interferometer delay structure that has been studied extensively [93, 94, 95]. This structure provides a periodic delay response, which is determined by the delay difference of the two arms. The delay can be tuned by changing the optical coupling ratio of the two arms. It should be noted that unlike all-pass filters such as ORRs, MZIs have a stop band for the transmission optical power. The delays near the stop band have a large loss and dispersion. Therefore, the working regime of MZI delay structures should be in the pass band, where almost all the optical power could pass through and provide a large TTD delay bandwidth. The tunable delays would range between the delays of the two arms.

1.4.1.4 Photonic Crystals

Photonic crystal slow light waveguides are another dispersive structure that can provide tunable delay. By making a sub-wavelength periodic defective structure near the waveguide core (shown in Fig. 1.7(d)), the group index could be engineered and the light could be slowed down by a factor of 20 or more [96, 97, 98]. The group index could also monotonously change with wavelength, which makes the delay line tunable. Unlike other dispersive delay lines, photonic crystal waveguides are distributed delay structure, which means the delay is proportional to the length of the waveguide. This feature will realize a linear OBFN where a linear delay distribution of the outputs could be achieved by simply designing the photonic crystal waveguide length in each path. However, photonic crystal waveguides usually have high propagation loss, which limits the widespread use of this structure.

1.4.2 Switchable Delay Lines

1.4.2.1 Mach-Zehnder based Delay Lines

The SDL changes the delay by switching the optical signal between various physical paths with different path length. Unlike dispersive delay lines, a SDL can provide a very large TTD bandwidth, which is only limited by the bandwidth of the optical switches. The total delay of the delay line is determined by the total path length, which simplifies the design. Also, the delay is tuned by operating the optical switches, which could ease delay tuning control and operation. On the other hand, the SDL could have a relatively large the footprint, and can only provide discrete delay tuning.

SDLs include two different types – cascaded SDLs and parallel SDLs, as depicted in Fig. 1.7(e) and (f), respectively. Cascaded SDLs have multiple stages of switchable delays in series. A MZI based SDL is a cascaded SDL where a MZI is used as the optical switch [99, 77, 100, 101]. At each stage, an optical delay can be tuned on or off, and the total delay is the combination of the delay line of each stage. However, in reality, an optical switch is imperfect and has a limited extinction ratio. This imperfection results in some light in both arms (with different delays), and hence will interfere and distort the delay response. Furthermore, this distortion will accumulate stage by stage, and transfer to the output with a severe TTD distortion, which could deteriorate the OBFN system performance. More details and a solution to eliminate the delay response distortion will be discussed in Chapter 5.

1.4.2.2 Arrayed Waveguide Grating based Delay Lines

The AWG based delay line is a parallel SDL, where the AWG is the optical switch that routes the light to different physical delay paths. Compared with the normal parallel SDL shown in Fig. 1.7(f), instead of using an input $1 \times N$ switch and an output $N \times 1$

switch, a $N \times N$ AWG can be re-used for both the input routing and output routing [102, 103], and hence simplified the parallel SDL structure. Similar to cascaded SDLs, the AWG based SDL also has the interference issue from channel crosstalk that could distort the TTD response. Fortunately, the distortion is not severe as an AWG usually has a small crosstalk ($<$ -20dB) and the crosstalk is not sensitive to the environment compared to a MZI switch. Moreover, since the switch is controlled by wavelength, the tuning of an AWG based SDL is simpler than the cascaded MZ-SDL, which requires control of the switches in each stage. However, because of the large footprint of AWGs, the delay line may not be made as compact as the MZ-SDL, which significantly limits the application of AWG-SDLs in large scale OBFNs.

1.4.3 Other True Time Delay Lines

In addition to the delay structures mentioned above, other structures were also explored by researchers, such as sub-wavelength waveguides [104] which modifies the filling factor of the subwavelength period; this can change the group index and consequently change the optical delay, as shown in Fig. 1.7(g). This approach is very compact and scalable, but is difficult to make tunable, and the connection to the sub-wavelength should be carefully designed to avoid mode matching loss. Moreover, the combination of multiple delay structures can also extend the delay performance. For example, SDLs and ORRs can be combined to achieve continuous group delay tuning from ORRs while maintaining the wide bandwidth feature of SDLs [54, 105, 106]; the combination of grating waveguides and ORRs enhances the delay tunability and delay per footprint of ORR only delay lines [107, 108].

1.5 Dissertation Overview

1.5.1 State-Of-Art and Impact

SDLs and ORR based delay lines are two primarily used TTDs for large scale integrated OBFNs due to the relative high fabrication reliability and tunability. Many works on these two structures have been reported. Among the reports for SDLs, the latest achievement is a seven-stage binary switched delay line with 0 to 191.37 ps tuning range and 1.42 ps tuning resolution [109]. However, to the author's best knowledge, no integrated OBFNs based on SDLs has ever been reported. Either, the work on the ripple of SDL TTD spectra, which could affect beam quality of the PAA with wideband communications, was keeping missing. As for ORR-OBFNs, researchers have successfully demonstrated ORR-based OBFNs with different platforms [47, 83, 84, 110, 78], and a delay of 0.63 ns with a bandwidth of 2 GHz targeting Ku-band PAA was reported [76, 111]. In order to achieve wide bandwidth TTDs for communications with higher frequencies (e.g. W-band) and mitigate fabrication variations, precise calibrations and tuning should be applied to all the rings in the OBFN. However, to our best knowledge, no such work has been reported. Regarding beamsteering experiments with TTD based integrated OBFNs, the 0^o beam pattern measurement of a Ka-band signal from a 8×8 PAA with ORR-OBFN was reported, but the beam steering experiment in other angles were not included. On the other hand, using discrete TTD elements, an 88 GHz photonic based mmW beamsteering PAA was implemented and a data rate of 10 Gb/s with $\pm 35^\circ$ beamsteering angle was demonstrated [40].

This thesis focuses on the study of integrated OBFNs based on SDLs and ORRs, as well as the mmW generation and beamsteering experiment using these OBFNs. A ripple-free SDL architecture is proposed and a 5-stage 1×4 SDL-OBFN for a linear W-band PAA is realized, which demonstrates 1.5 ps finest delay tuning resolution and 6 delay

distributions with tunable path delay increments ranging between 0 - 7.5 ps. 3-ORR SCISSOR structure are employed as the TTD element for a 1×4 ORR-OBFN. With many efforts put in calibration and tuning optimization of the ORRs, continuous tuning ranges of 209 ps and 172 ps with a bandwidth of 6.3 GHz and 8.6 GHz are achieved, respectively, for a single 3-ORR delay line. Delay responses with path delay increment of 4.6 ps for linear PAAs are demonstrated by the ORR-OBFN. The SDL-OBFN is employed for a W-band signal beamsteering experiment, which demonstrates beam-squint free beamsteering with six beam angles from -51° to 31° from 85 to 100 GHz and a SNR of 35 dB. Also, a 94 GHz W-band signal encoded with 3 $Gbps$ ASK data was generated. To the author's best knowledge, this is the first report of W-band beamsteering and data transmission using an integrated OBFN.

1.5.2 Thesis Organization

This thesis is divided into eleven chapters. The first chapter has provided the introduction to integrated microwave photonics, with a focus on OBFNs for mmW PAAs. Optical TTDs are preferred for PAAs for wideband communications as it mitigates the beam squint issue and reduces power consumption in comparison to RF phase shifters that require driver amplifiers. An introduction to integrated TTD implementations is also given in Chapter 1.

Chapter 2 discusses the system architecture of a photonic enabled mmW PAA beamsteering system, which is divided into three stages: generation, distribution and emission. The generation stage generate two optical tones, which are sent to the distribution stage for splitting and delay. The optical signal are up-converted to RF signals with UTC-PDs, and the outputs are emitted by an antenna array. The key components of each stage are described in detail.

Chapter 3 describes the beam forming theory of a PAA. The radiation pattern of a PAA is mainly determined by the geometry of PAA. The beam pattern equation and single main-lobe beam condition are derived. The beam squinting of a PAA is quantitatively studied, and the principle of beam-squint-free operation for a TTD based PAA is discussed.

Chapter 4 provides an introduction to the ultra-low loss silicon nitride (SiN) waveguide technology. Various waveguide structures are discussed for different requirements including ultra-low loss, tight bending, polarization dependence, and high confinement. The 400 nm Si_3N_4 technology is also being developed in-house and the waveguide loss and some realized devices are also presented in this chapter.

Chapter 5 covers the optimization and design of SDLs and the corresponding OBFN. A modified architecture of SDL is presented that eliminates ripple in the delay response due to the imperfection of the 3-dB couplers in MZI switches. A 1×4 SDL-OBFN for a linear PAA with the double stripe silicon nitride low-loss waveguide technology is demonstrated in this chapter.

Chapter 6 covers the optimization and design of ORR based TTDs and the corresponding OBFNs. The response of an general ORR are quantitatively studied and a SCIRROR structure is employed to increase the constant delay-bandwidth product of the ORR. A genetic algorithm is applied to optimize the parameters of ORRs in the OBFN and a look-up table is generated, which reveals inherent trade-offs between delay value, ripple level, bandwidth and number of rings for ORR-OBFNs. Two 1×4 ORR-OBFN with different topologies based on silicon nitride are demonstrated in this chapter.

Chapter 7 covers the highly scalable, high voltage and current output, multi-channel controllers for controlling the large number of tuning elements in the OBFNs. Two generations of controllers are demonstrated – a voltage source controller and a current source controller. The designs of both of the two controllers are detailed in this chapter.

Chapter 8 covers the experimental results of group delay response characterization of the ORR and SDL based delay lines and OBFNs. The tuning of both ORR delay lines and SDLs are optimized and the TTD responses of the 1×4 SDL-OBFN and ORR-OBFN are demonstrated as well.

Chapter 9 covers the experiments of mmW generation and beamsteering with data transmission using the silicon nitride OBFNs. With the ORR-OBFN, a 41 GHz mmW signal is generated, whereas with the SDL-OBFN, an experiment of W-band mmW signal generation and beamsteering is demonstrated.

Chapter 10 discusses the challenges of applying current OBFNs for large scale PAA applications. Some on-going and future work including the OBFN-PD-antenna integration and a novel recirculating delay loop (RDL) based OBFN architecture are presented regarding the overcome of these challenges.

Finally, Chapter 11 provides a conclusion, as well as a personal perspective for a realistic and compact optical TTD based PAA systems.

This page intentionally left blank

Chapter 2

System Architecture Overview

High carrier frequency, and subsequently narrow beams are desirable for future mobile communications in part to reduce signal interference and increase antenna gain. A PAA is a flexible all-solid state beam steering approach, which allows for steering by adjusting the relative phases or time delays of the elements instead of physically adjusting the orientation of the antenna. Furthermore, power addition due to multiple antenna elements can make phased array techniques scalable to high power. Figure 2.1 illustrates a schematic of a photonic-enabled PAA system, which comprises of three primary stages[1]. The generation stage generates an optical signal that contains the frequency component of the RF signal, where the transmitter data is encoded on that frequency component. The optical signal is then duplicated into multiple paths. These signals are delayed or phase shifted in the distribution stage to enable the desired beam steering angle. In the emission stage, all the optical signals are up converted into RF signals in electrical domain and feed an antenna array for RF signal emission. More details on this MWP system are discussed in this chapter.

[1]In general terms of a microwave photonics system, the generation stage refers to the "Back-end", and the distribution and emission stage refer to the "Front-end".

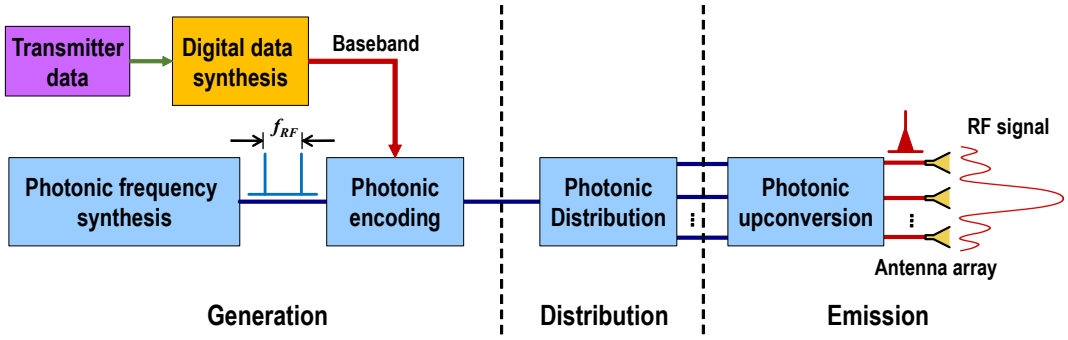

Figure 2.1: Schematic of a photonic-enabled RF PAA transmitter.

2.1 Optical Signal Generation

The RF carrier signal generation is based on low pass filtering of the RF frequency component encoded on the optical carrier. For efficiency considerations, the RF frequency component in the optical signal spectrum should be optimized. Many approaches can achieve this purpose such as using mode-locked laser pulse trains, quantum cascade lasers, or photo-mixing [6]. Photo-mixing is one of the most popular approaches as it provides a high power conversion efficiency and is easy to encode data; this approach will be discussed in this section.

2.1.1 Two-Photon Mixing

Two-photon mixing generates RF signals by mixing two optical signals with a frequency difference equal to the desired RF frequency. As will be discussed in Section 2.3, the RF power through the photonics up-conversion is proportional to the optical power. The interference of two optical signals can be mathematically described by (2.1).

$$\begin{aligned} P(t) &= \left[E_1\left(f_1,\phi_1\right)+E_2\left(f_2,\phi_2\right)\right]*conj. \\ &= \left[A_1 e^{j(2\pi f_1 t+\phi_1)}+A_2 e^{j(2\pi f_2 t+\phi_2)}\right]*conj. \\ &= A_1^2+A_2^2+2A_1A_2\cos\left(2\pi f_{RF}t+\Delta\phi\right) \end{aligned} \tag{2.1}$$

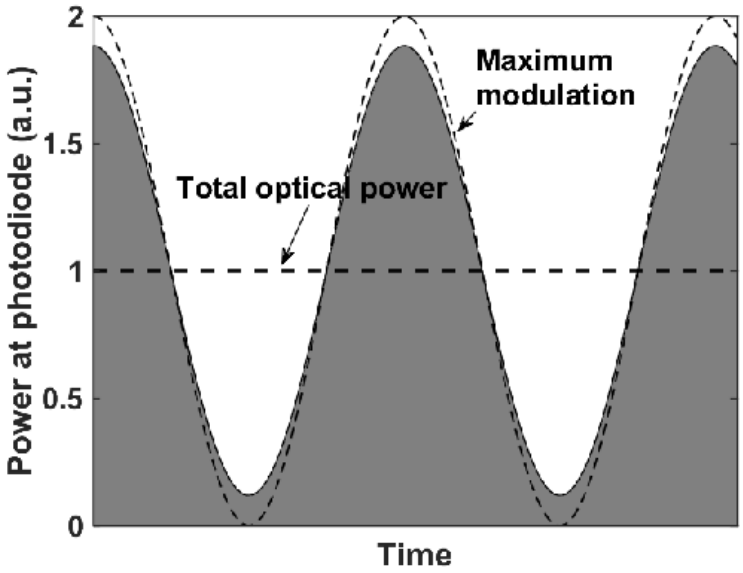

Figure 2.2: Normalized optical power beat note at the photodiode.

where $E_1(f_1, \phi_1)$ and $E_2(f_2, \phi_2)$ are the optical waves, A_1 and A_2 are the amplitude of the two optical signals and are assumed to be real numbers, f_1 and f_2 are the optical frequencies, ϕ_1 and ϕ_2 are the phases of the optical waves. $f_{RF} = f_2 - f_1$, $\Delta\phi = \phi_1 - \phi_2$ are the frequency and phase of the RF signal, respectively. As can be seen from (2.1), all of the optical power will be converted into the RF signal and a DC offset. The normalized optical power beat note at the photodiode is shown in Fig.2.2. The conversion gain G is described as

$$G = \frac{2A_1A_2}{A_1^2 + A_2^2} \leqslant 1 \tag{2.2}$$

where $G = 1$ when $A_1 = A_2$, which implies that the conversion gain is maximized when the amplitudes of the two optical tones are equal. It should be noted that, as the optical power cannot be a negative number, $G = 1$ is the maximum conversion gain for a photonic up-conversion process.

The data encoding of the RF signal for the photo-mixing approach can be achieved

by encoding the data on one of the optical signals and using the other optical signal as the local oscillator (LO). The up-converted RF signal can be described by (2.3).

$$\begin{aligned} P(t) &= \left[\tilde{s}(t) \cdot E_1\left(f_1, \phi_1\right) + E_2\left(f_2, \phi_2\right)\right] * conj. \\ &= \left[\tilde{s}(t) \mathrm{e}^{j2\pi f_1 t} + \mathrm{e}^{j2\pi f_2 t}\right] * conj. \\ &= |\tilde{s}(t)|^2 + 1 + 2 \cdot \mathrm{Re}\left\{\tilde{s}(t) \mathrm{e}^{j2\pi f_{RF} t}\right\} \\ &= |\tilde{s}(t)|^2 + 1 + 2 \cdot \mathrm{Re}\left\{\tilde{s}(t)\right\} \cos\left(2\pi f_{RF} t\right) - 2 \cdot \mathrm{Im}\left\{\tilde{s}(t)\right\} \sin\left(2\pi f_{RF} t\right) \end{aligned} \quad (2.3)$$

where $\tilde{s}(t)$ is the baseband signal, provided that $A_1 = A_2 = 1$ and $\phi_1 = \phi_2$ in (2.1). This equation implies that the baseband data signal modulated on the optical signal will be transferred to a electrical baseband signal as well as the modulation of the RF carrier. This feature could enable the RF front-end to be integrated directly into the optical network, which could simplify RF systems. Even for coherent optical networks, where complex optical modulation such as optical quadrature amplitude modulation (QAM) is utilized, the baseband signal on the optical carrier can be transferred into the RF carrier directly using this technique.

2.1.2 Harmonic Carrier Generation

The two-photo mixing generation process requires a photonic frequency synthesizer to generate two highly correlated optical tones in order to generate a RF signal with low phase noise. Many approaches can be employed for this purpose such as optical phase lock loops, mode lock lasers, and optical harmonic generation of MZMs. Optical harmonic generation of MZMs is attractive for its simple realization and excellent RF signal quality. Figure 2.3 shows the basic schematic of optical harmonic generation using a MZM. A RF synthesizer is used to modulate the optical signal by driving an external MZM, which

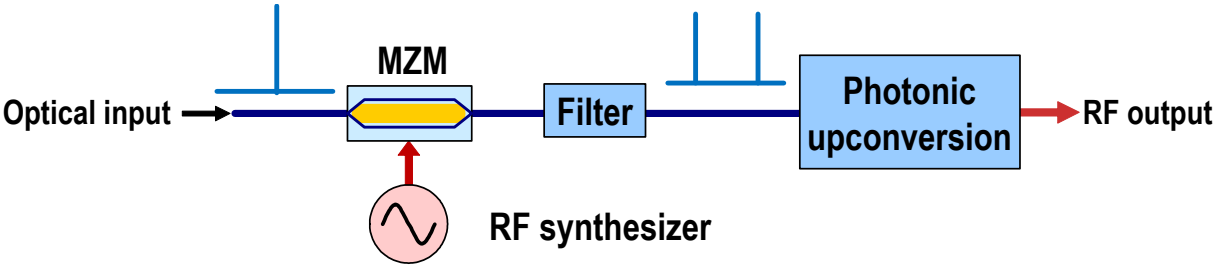

Figure 2.3: Basic schematic of optical harmonic generation using a MZM.

generates the desired optical sidebands for two-photo mixing. With this approach, the high signal quality of the RF synthesizer can be transferred to the optical signal, and the common-mode noise between the interfering signals can be canceled. Because of these reasons, a good RF signal quality can be maintained following the photonic up-conversion process.

Electrically overdriven MZMs can be exploited to efficiently generate optical LO signals for frequency conversion . The generation of LO signals directly at f_{LO} or harmonic signals at nf_{LO} can be obtained. By adjusting the bias point and RF drive power of the low frequency reference signal at f_{LO}, efficient frequency multiplication to generate mmW signals upon detection can be achieved. The time domain representation of the optical intensity can be expressed as

$$P(t) \quad = \quad t_m P_0 \left\{ 1 + \cos \left[\frac{V(t) + V_b}{V_\pi} \pi \right] \right\} \tag{2.4}$$

where $V(t)$ is the modulation driving amplitude of the reference RF signal, V_b is the modulator bias voltage, V_π is the modulator half-wavelength voltage, $2P_0$ is the incident laser power and t_m is the insertions loss of the modulator, provided that the MZM is in chirp-free operation (dual-drive or x-cut MZM). Using sinusoidal modulation applied to a MZM to introduce the LO signal and the Jacobi-Anger expression, (2.4) can be rewritten

as

$$
\begin{aligned}
P(t) &= t_m P_0 \left\{ 1 + \cos\left[\frac{V_{LO}\sin(\omega_{LO}t) + V_b}{V_\pi}\pi \right] \right\} \\
&= t_m P_0 \left\{ 1 + \cos\left(\frac{V_b}{V_\pi}\pi\right) \cos\left[\frac{V_{LO}}{V_\pi}\pi\sin(\omega_{LO}t)\right] - \sin\left(\frac{V_b}{V_\pi}\pi\right) \sin\left[\frac{V_{LO}}{V_\pi}\pi\sin(\omega_{LO}t)\right] \right\} \\
&= t_m P_0 \left\{ 1 + \cos\left(\frac{V_b}{V_\pi}\pi\right) J_0(m) \right. \\
&\qquad - \sum_{n=1}^{\infty} 2\left[J_{2n-1}(m)\sin\left(\frac{V_b}{V_\pi}\pi\right)\right] \sin\left[(2n-1)\,\omega_{LO}t\right] \\
&\qquad \left. + \sum_{n=1}^{\infty} 2\left[J_{2n}(m)\cos\left(\frac{V_b}{V_\pi}\pi\right)\right] \cos\left(2n\omega_{LO}t\right) \right\} \qquad (2.5)
\end{aligned}
$$

where ω_{LO} and V_{LO} are the angular frequency and driving amplitude of the reference RF signal, $m = \frac{V_{LO}}{V_\pi}\pi$ is the modulation index, and $J_n(x)$ is the first kind Bessel function of order n. It implies that the a MZM with optimum drive power and bias can produce either an efficient fundamental or a specified harmonic LO signal. Figure 2.4 shows the calculated relative output power at the detector versus signal amplitude of the MZM driving voltage for the 2nd to 10th harmonic with an optimum MZM bias. The reference power level (0 dB) corresponds to the electrical output obtainable from the heterodyne process described in (2.1) and (2.2) with the maximum modulation gain. A 4.5 dB optical insertion loss is assumed for the LO modulator, and the input optical power remains the same. For odd harmonics, the optimum modulator bias is the quadrature bias, where the even harmonic terms in (2.5) are eliminated, maximizing the odd harmonics terms. Then, a desired harmonic could be selected by setting the MZM modulation depth to maximize the corresponding Bessel function as the coefficient of the harmonic term. Similarly, for the even harmonics, the optimum bias point is the null or peak point, where the odd harmonic terms in the equation are eliminated, and the MZM modulation depth selects the desired harmonic. Table 2.1 summarizes the optimized signal amplitude of the MZM

Table 2.1: Calculated related electrical output power at nf_{LO} using a MZM and harmonic carrier generation with respective optimum modulator RF drive voltage and bias conditions. Same assumptions are made as Fig. 2.4.

MZM Bias	Quadrature					Null/Peak				
n=	1	3	5	7	9	2	4	6	8	10
V_{LO}/V_{π}	0.59	1.34	2.04	2.73	3.41	0.97	1.69	2.39	3.07	3.75
Rel. pwr. (dB)	-13.7	-16.2	-17.5	-18.4	-19.1	-15.3	-17.0	-18.0	-18.8	-19.4

drive voltage and the corresponding relative power with an optimum bias to the 10th harmonic order. The 2nd order harmonic has a relative electrical power loss of $-15.3\ dB$, in which the insertion loss of the MZM contributes 9 dB of electrical power loss as the optical loss of 4.5 dB is doubly transferred to the electrical power due to the square-law photo detection is used for photonic up-conversion. The optical loss of MZM is therefore very critical for the photon up-conversion efficiency and needs to be optimized. Moreover, from Table 2.1, the 10th order could be obtained at the cost of only 4.1 dB extra loss compared to the 2nd harmonic, which implies that harmonic carrier generation is a very efficient approach for generating high order frequencies such as extremely high frequency (EHF) that are far beyond the MZM bandwidth limit; this also relieves the requirement of the RF LO. In addition, it is evident in Fig.2.4 that for harmonics of order less than 5, there is >10 dB suppression ratio to other harmonics, whereas for 6th order or higher, the suppression ratio is significantly reduced and other harmonics must be filtered. As lower V_{π} optical modulators and higher power optical detectors become available at high frequencies, this frequency multiplication technique becomes more attractive due to the reduced RF drive power requirements, higher output power levels, and higher mmW frequencies attainable.

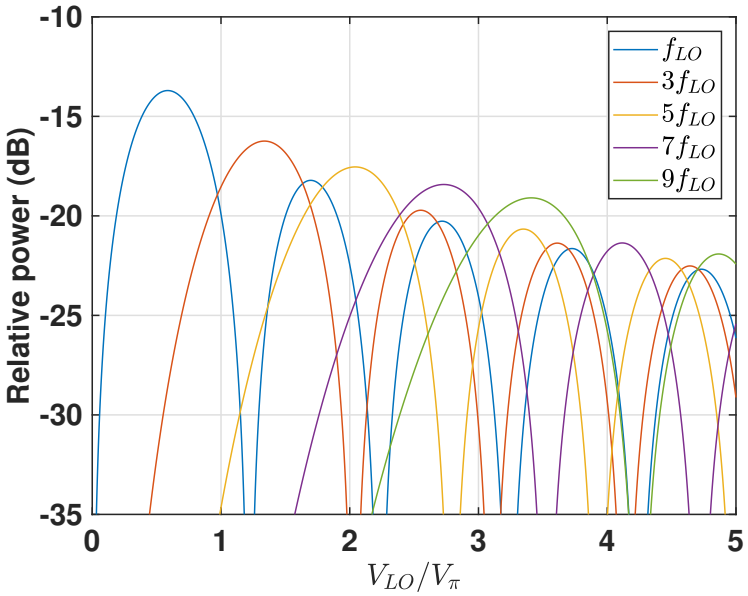

(a)

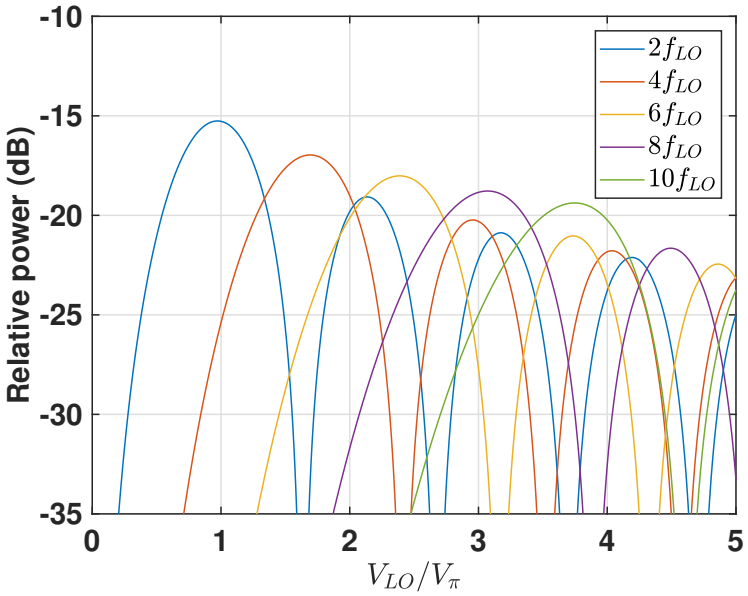

(b)

Figure 2.4: Calculated relative output power at detectors versus MZM driving voltage amplitude for 2nd to 10th harmonic with optimum MZM bias. The reference output level (0 dB) corresponds to the electrical output obtainable from the heterodyne process described in (2.1) and (2.2) with the maximum modulation gain. A 4.5 dB optical insertion loss is assumed for the LO modulator, and the input optical power remains the same. (a) shows odd harmonics with quadrature bias and (b) shows even harmonics with null or peak bias.

2.2 Optical Signal Distribution

For the beam steering system shown in Fig.2.1, the distribution stage includes theOBFN, which is one of the key components for a PAA system. As will be discussed in Chapter 3, the basic idea of a PAA for beam forming is the re-construction of multiple sub-sources to form the wave-front of the beam in the desired direction. A OBFN is the component that operates on each sub-source to generate the desired beam shape.

Figure 2.5 depicts the schematic diagram of the distribution stage with a OBFN. The source signal is firstly split into multiple sub-signals. Two parameters can be changed for each sub-signal — the phase and the amplitude. The relative phase difference of the sub-signals mainly determines the beam direction, beam collimation and beam focusing, and the amplitudes of the sub-signals will further control the beam shape including the beam width, and beam sidelobes. The phase and amplitude could be controlled by employing tunable phase shifters or TTD lines, and tunable attenuators, respectively. TTD lines are more preferable for phase tuning in order to eliminate the beam squint- issue [9] present in conventional electrical PAAs. More details on PAAs will be discussed in Chapter 3.

The distribution of the sub-signals could be realized in the optical domain with microwave photonics technology; this is the so called OBFN. The splitter can be realized with power splitters such as multi-mode interference (MMI) couplers, directional couplers (DCs), or star-couplers. The RF signal can be modulated on multiple wavelengths simultaneously and hence an AWG can be used as the power splitter. In each path, optical phase shifts and TTDs can be applied to the optical signal, and can be transferred to the phase shift of the RF signal. Also, variable optical attenuators can change the amplitude of the optical signal, which can be interpreted as RF signal attenuation through the square law described in Section 2.3.

Integrated photonics technology offers unique advantages for the realization of OBFNs

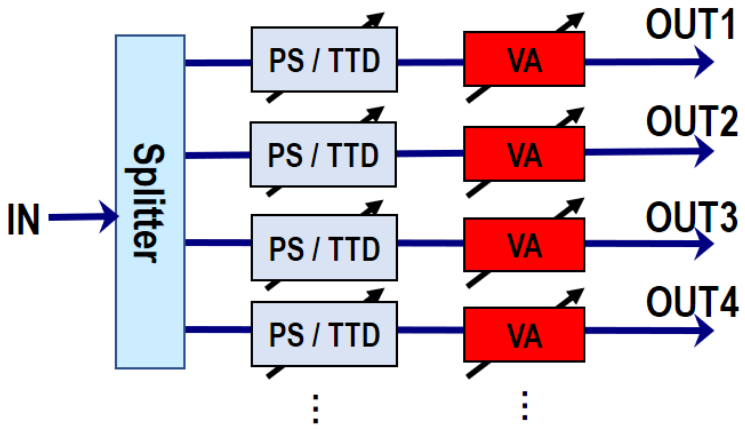

Figure 2.5: Diagram of the distribution stage. (PS: phase shifts; TTD: true time delays; VA: variable attenuator.)

in comparison to the electronics counterpart. Compared to electronic realizations with bulk components or monolithic microwave integrated circuits (MMICs), the footprint of the beamformer can be reduced to a very small size with integrated OBFNs due to the much shorter wavelength compared to the RF signal, and hence can be made more compact, lightweight, and also scalable for feeding large scale PAAs. Because of the large optical bandwidth and small footprint, the OBFN loss is low and the optical propagation loss doesn't change with the RF frequency, unlike the microstrip waveguides used in MMICs where the propagation loss increases dramatically with frequency. The phase shifters in integrated photonics, such as heaters and PN junctions, are almost frequency independent. Particularly for heaters and PN junction phase shifters, very little optical loss would be introduced in addition to the waveguide loss. Furthermore, as mentioned in Section 1.4, integrated photonics offers tunable TTDs. In this way, the PAA bandwidth can be extremely wide and the beam squint issue can be eliminated. There is no doubt that integrated OBFNs offer unique advantages for PAAs.

2.3 Optical-Electrical Conversion

Photonic signals are up-converted to RF for emission through photodetectors that drive an antenna in the emission stage of Fig. 2.1. With a photodetector, the RF signal is generated through the beating of the two optical tones from the generation stage. Figure 2.6 shows a circuit schematic of a photodetector, which includes a reverse biased photodiode and a high-pass filter that couples out the generated RF signal. Since the photodiode has an output of current, a 50 Ω resistor is employed to convert the signal to voltage and to match impedance. The output of a photodetector is given as

$$v(t) = Z_L \cdot R_p \cdot P(t) \tag{2.6}$$

where $P(t)$ is the incident optical power, R_p is the responsivity of the photodiode and Z_L is the load impedance. (2.6) shows that the output signal is proportional to the optical power incident on the photodiode. Substituting the optical power with (2.3) illustrates the two photo-mixing with signal modulation, that also filters the low frequency terms. The output signal is expressed as

$$v(t) = 2 \cdot Z_L \cdot R_p \cdot \{\mathrm{Re}\{\tilde{s}(t)\}\cos(2\pi f_{RF}t) - \mathrm{Im}\{\tilde{s}(t)\}\sin(2\pi f_{RF}t)\} \tag{2.7}$$

where $\tilde{s}(t)$ is the baseband signal and f_{RF} is the frequency of the RF signal, which implies that the signal modulated on the optical carrier in the optical domain will be converted to the electrical domain with a RF carrier through the photonic generation process.

The carrier frequency of the RF signal through the photonic up-conversion process is limited only by the bandwidth of the photodiode. Moreover, for simplified schemes where the photodiode drives the antenna directly and eliminates the electrical RF amplifier, the radiative intensity of the RF signal is proportional to the output power of the

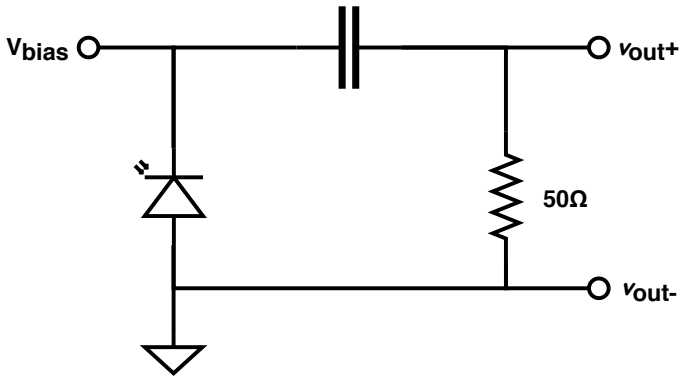

Figure 2.6: Circuit schematic for a typical photodetector.

photodiode. Therefore, high-speed and high-saturation output power photodiodes are desired for photonic generation. A UTC-PD and its derivatives have been shown to have high bandwidth while delivering large output power. Therefore, among the various types of long-wavelength photodiodes, these are strong candidates for both photonic-enabled mmW and terahertz applications [112, 113, 114, 115, 116]. Figure 2.7 shows the band diagram of a UTC-PD, which comprises of a thin p-type InGaAs light absorption layer and an InP carrier collection layer. The light is absorbed in the absorption layer, generating electron-hole pairs. The generated minority carrier electrons in the quasi neutral absorption layer diffuse into the depletion layer and drift to the n-contact layer; the photo generated holes, the majority carriers in the absorption layer, respond according to the relaxation time of the the dielectric with their collective motion. Therefore, unlike conventional PIN photodiodes, where both electrons and holes are transported, only the transportation of electrons will contribute to the response time for a UTC-PD. Due to the relatively small electron effective mass, the electron velocity is typically an order of magnitude higher than the hole velocity in the depletion layer [117, 118]. Therefore, the elimination of drifting holes is an essential difference of a UTC-PD from the conventional PIN PD, which makes a UTC-PD respond much faster. Moreover, a thin absorption layer is desired for photodiodes to reduce the carrier transit time and hence improve operation

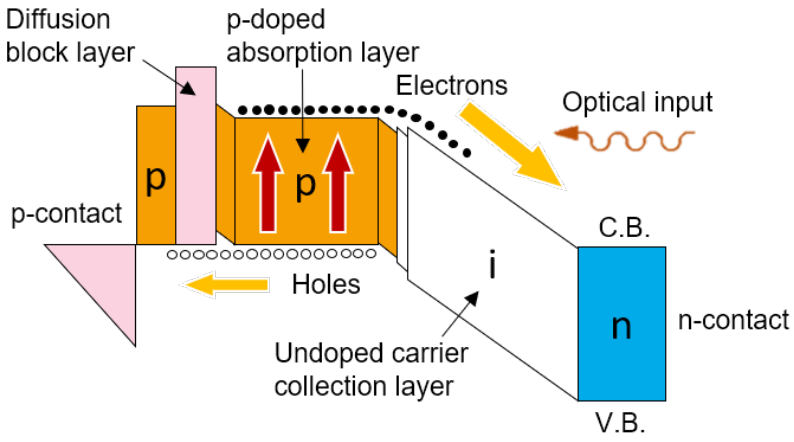

Figure 2.7: Band diagram of a UTC-PD.

speed. The UTC-PD structure decouples the design of the absorption layer and depletion layer, allowing for a very thin absorption layer without increasing the capacitance. By comparison for a PIN PD,the capacitance increases significantly when the thickness of the absorption layer is excessively reduced. In addition, the UTC-PD structure could also benefits from velocity overshoot of electrons [117] in the depletion layer.

A UTC-PD could also support a high saturation current. For a high photo-carrier excitation condition in a PD, where the carrier generation speed is larger than the speed of the carriers being swept, the carriers will accumulate in the depletion layer. This forms space charges that weaken the intensity of the electric field in the depletion region, reducing the drift velocity of carriers, and finally leading to the output saturation of the output current. As the electron velocity is an order of magnitude higher than that for holes, UTC-PDs, in which space charges are due primarily to electron accumulation, do not saturate until the current density reaches an order of magnitude higher than that for PIN PDs. Moreover, the intensity of the electric field required for maintaining high velocity is much smaller for electrons than that for holes. Thus, the bias voltage of UTC-PDs could be much lower than conventional PIN PDs, thereby lowering power

consumption, simplifying the peripheral components design, and improving the reliability. Therefore, UTC-PDs are particularly suitable for high frequency mmW photonic-enabled PAA systems.

2.4 Summary

This chapter discussed the system architecture of a photonics enabled PAA system. The system comprises of three stages including the generation stage, distribution stage and emission stage. The two-photo mixing method is preferred for the generation stage for its high power conversion efficiency and ease of data encoding. And the two highly correlated optical tones for up-conversion can be generated simply through high order harmonics by modulating a single frequency laser signal with a MZM. The distribution stage distributes and phase-shifts or delays optical signals instead of electrical signals using OBFNs, which benefits from the low loss, wide bandwidth, TTDs, small footprint and immunity to electromagnetic interference of optics, compared to the electrical counterparts. The emission stage generates and emits the RF signal through up-conversion process and an antenna array. UTC-PDs are preferred in this process due to the high bandwidth and output power and planar antenna array can be used for integration. A photonic-enabled PAA system is a lightweight, power efficient approach for EHF beam-steering, and the entire system is potential for full integration.

Chapter 3

Phased Arrays and True Time Delays

A PAA system is an attractive approach for realizing reconfigurable all-solid state RF beam steering. Compared to other RF directional emission solutions such as Cassegrain antennas, PAAs do not require any mechanical parts to achieve beam steering, and hence, PAAs could be made very agile, compact and reliable, and the entire PAA system could be fully integrated. The antenna aperture can be made very large resulting in a highly directional beam and high antenna gain. Moreover, because of it comprises of many antenna elements, a PAA system is also highly scalable and the transmit power is no longer limited by a single antenna, but rather quadratically increases with the number of antenna elements in the constructively interfered direction. Also, the antenna elements can be grouped to emit beams in multiple directions simultaneously. These features make PAAs superior to conventional mechanically scanning Cassegrain antennas and are widely used in many applications such as radar detection and remote sensing.

PAAs also have been attracting interest in the communication field, especially for scenarios of communication between moving objects such as satellites, airplanes, trains, or next generation cellular communications. Use of conventional PAAs that utilize phase shifters do, however, pose challenges. Unlike signal frequency applications like radar

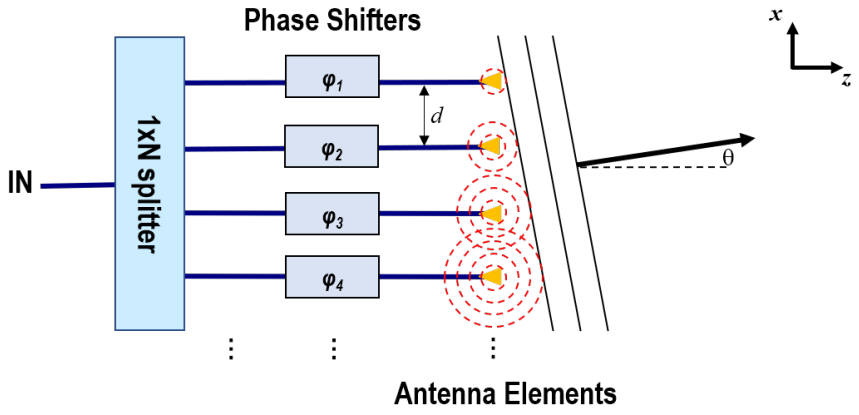

Figure 3.1: Schematic diagram of a 1-D PAA with phase shifters.

detection, communications require a certain amount of bandwidth. PAAs with phase shifters exhibit beam squint for the communication signal, which limits the bandwidth usage of the RF carrier. Using TTDs instead of phase shifters in a PAA provides a solution for this issue for wideband communications. In this chapter, the operation principle of PAAs and the superiority of applying TTDs in PAAs will be discussed.

3.1 Operation Principle of Phased Arrays

A PAA is based on the Huygens–Fresnel principle, in which the signal is split into multiple sub-sources and the wavefront is reconstructed in the desired transmit direction. The schematic diagram of a conventional PAA is shown in Fig. 3.1. The input signal is split into N paths through a 1xN splitter. Each path employs a phase shifter that can change the phase of the signal individually. Then the sub-signal is emitted again through an antenna and forms the beam for the desired direction. The relation of the beam emission angle and the phase of each sub-signal is given as follows

$$x_i \sin(\theta) - \frac{c}{2\pi f}(\varphi_i + m_i \cdot 2\pi) = 0 \tag{3.1}$$

where θ is the beam angle, x_i and φ_i are the spatial position and signal phase of antenna element i, c is the speed of light, f is the signal frequency, and m_i is an independent integer for each antenna element. (3.1) ensures that all the sub-sources are constructively interfered in the desired beam direction.

For 2-D beam steering PAA applications, planar antennas can be employed to make a 2-D array [119, 120], as shown in Fig. 3.2, and (3.1) could be expanded as

$$x_i \sin(\theta) + y_i \sin(\eta) - \frac{c}{2\pi f}(\varphi_i + m_i \cdot 2\pi) = 0 \tag{3.2}$$

where x_i and y_i are the two dimensional spatial position of antenna element i, θ and η are the angles with the x-axis for the beam angle projection in the xy-plane and xz-plane, receptively. The following discussions will focus on 1-D PAAs. 2-D beam steering shares

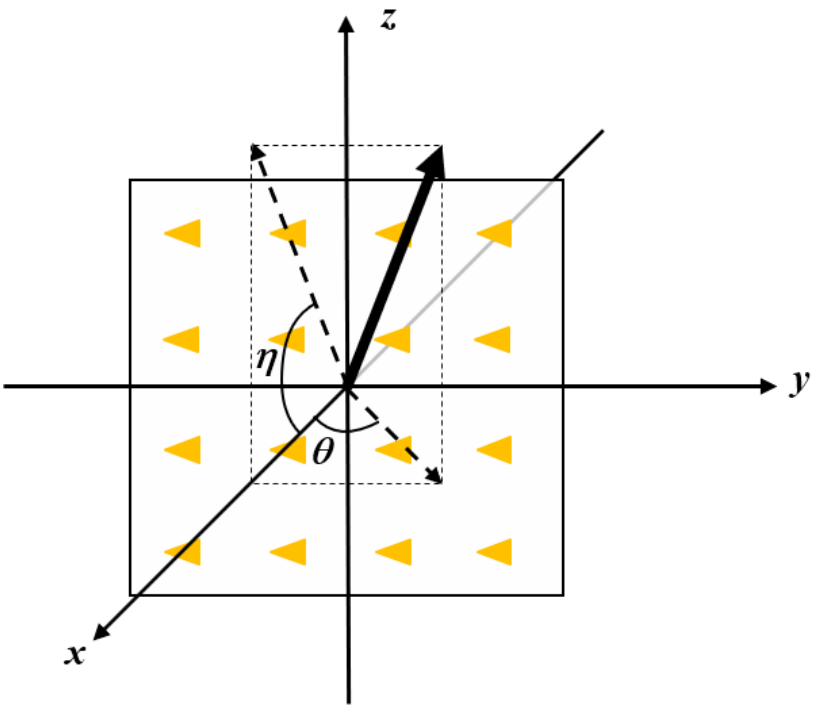

Figure 3.2: Schematic diagram of a 2-D PAA.

the same principle.

The simplest PAA is a linear PAA where the separation of the antenna elements is constant. In this case, for a specific beam angle, the phase increment is constant and the beam angle equation (3.1) can be rewritten as

$$\sin(\theta) = \frac{(\Delta\varphi + m \cdot 2\pi) \cdot c}{2\pi f d} \tag{3.3}$$

where $\Delta\varphi$ is the wrapped phase increment between adjacent antenna elements, and m is the desired beam order, which will be discussed in Section 3.2. Note that usually the antenna elements of a conventional PAA have different signal path lengths, therefore the absolute phase may vary over several periods. A phase shifter typically has a limited phase tuning range, but as long as the wrapped phase agrees with (3.3), the PAA will generate the same beam angle. This feature can simplify the PAA design and is very useful in large scale PAAs where the accumulated phase could be significant.

3.2 Beam Pattern of Linear Phased Arrays

3.2.1 Beam Pattern Equations

The beam pattern of a linear phased array comprises of two factors – the array factor and the radiation pattern of a single antenna element. Figure 3.3 shows a schematic diagram of a linear PAA where the antenna elements are separated by d. For a desired angle, the optical amplitude is the superposition of the electromagnetic waves from all of the elements, which has the same radiation pattern but a phase shift in the far field because of the spatial offset. The optical far field pattern can be analytically expressed

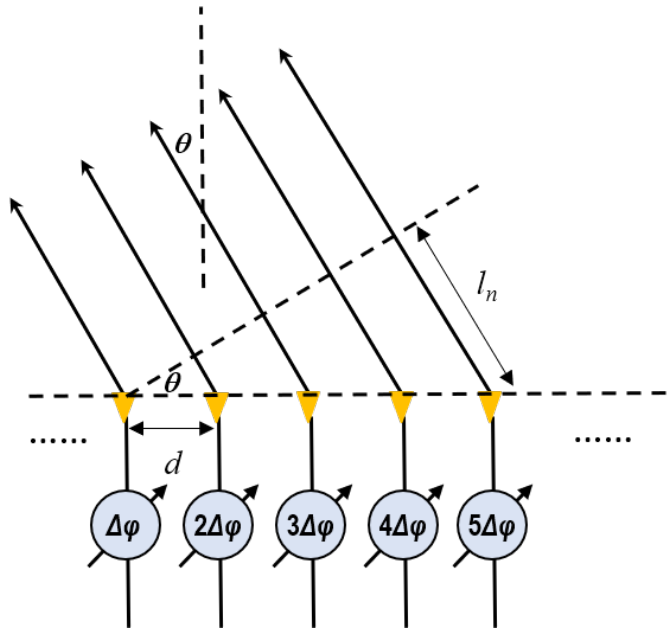

Figure 3.3: Schematic diagram of a linear PAA.

as

$$\begin{aligned} U(\theta) &= \sum_{n=1}^{N} U_{AE}(\theta) \exp\left\{-j \cdot \left[2\pi \frac{l_n}{\lambda} - n \cdot \Delta\varphi\right]\right\} \\ &= U_{AE}(\theta) \cdot \sum_{n=1}^{N} \exp\left\{-j \cdot n \cdot \left[2\pi \frac{d \sin(\theta)}{\lambda} - \Delta\varphi\right]\right\} \\ &= A(\theta).U_{AE}(\theta) \cdot AF(\theta) \end{aligned} \tag{3.4}$$

and

$$AF(\beta) = \frac{\sin \frac{N}{2}\beta}{\sin \frac{1}{2}\beta} \tag{3.5}$$

where

$$\beta = 2\pi \frac{d}{\lambda} \sin\theta - \Delta\varphi \tag{3.6}$$

where θ is the angle from the normal, d is the spacing of the antenna elements, λ is the wavelength of the electromagnetic wave, $\Delta\varphi$ is the phase increment, $U(\theta)$ is the far-field amplitude of the electromagnetic waves, $U_{AE}(\theta)$ is the far-field amplitude pattern of a single antenna element, $A(\theta)$ is an additional phase shift, and $AF(\theta)$ is the array factor provided that all the antenna elements are identical and have the same radiation power. The power radiation pattern of the PAA is then given by

$$\begin{aligned} P(\theta) &= U(\theta) \cdot U(\theta)^* \\ &= |U_{AE}(\theta)|^2 |AF(\theta)|^2 \end{aligned} \tag{3.7}$$

(3.4)-(3.7) imply that the radiation pattern of a linear PAA is determined by the single antenna element radiation and the phased array design. Figure 3.4 shows a graphic example for the pattern formation of a PAA where Fig. 3.4 (a)-(c) depicts the the radiation pattern of a single antenna element, the array factor, and the final pattern from the PAA, respectively. Actually, as shown in Fig. 3.4, the radiation pattern of a single antenna element varies very slow with the angle as the element aperture is usually smaller or comparable with the wavelength. The beam shape of the PAA is mostly determined by the array factor $AF(\theta)$, or the PAA design.

3.2.2 Array Factor

The beam characteristics of a PAA are mainly determined by the array factor, which includes the beam power, beam width and beam side lobes. Figure 3.5 depicts the array factor versus β for a PAA with 4 elements. Multiple lobes are observed and the peaks occur at the maxima of (3.5) when $\beta = m \cdot 2\pi,\ m = 0, \pm 1, \pm 2, \cdots$, where m is the order

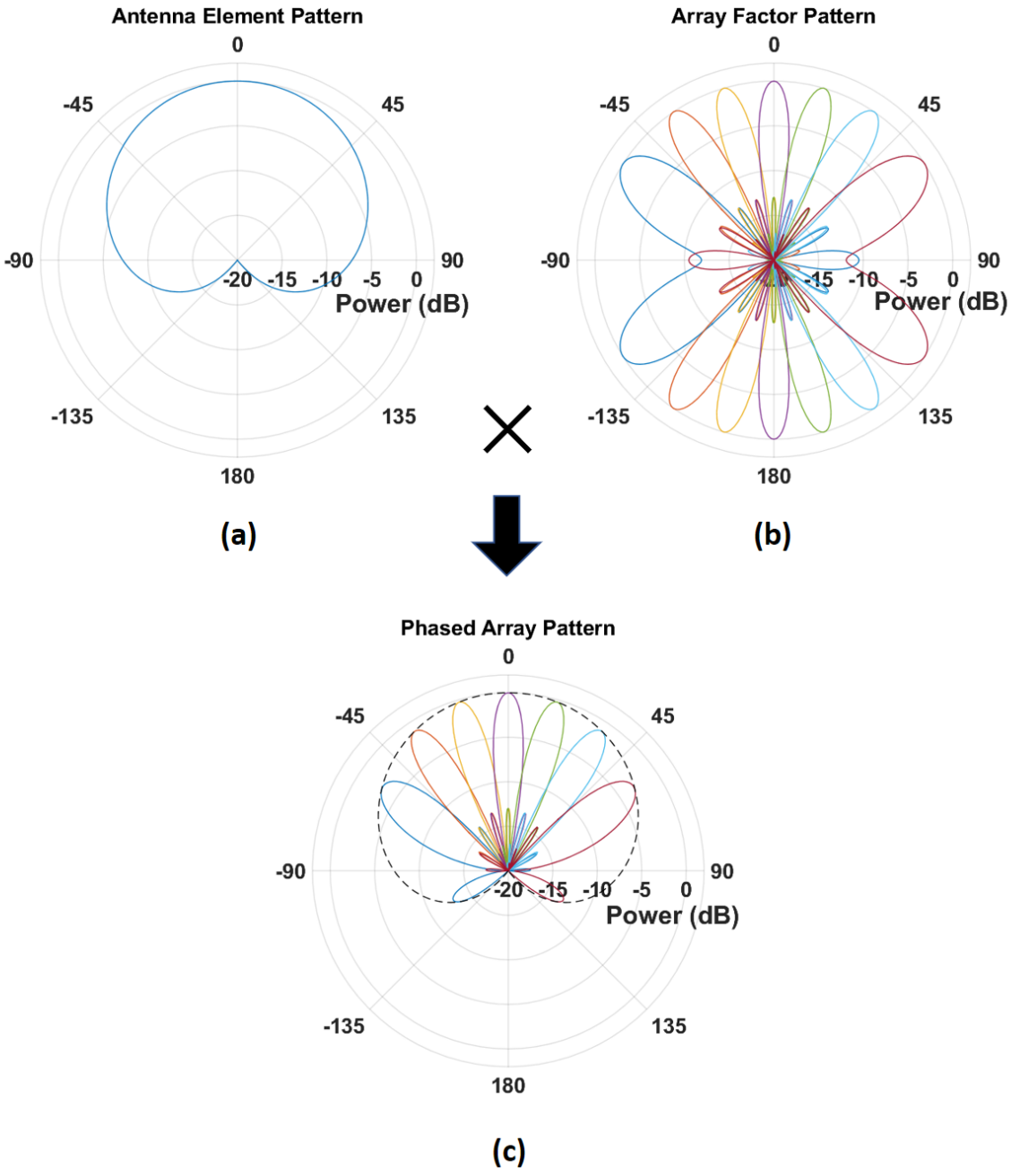

Figure 3.4: Pattern formation of a linear PAA with 10 antenna elements, half wavelength pitch and antenna aperture of one third of a wavelength. (a) The radiation pattern of a single antenna element, (b) the pattern of the array factor for various beam directions, and (c) the synthesized radiation pattern of the PAA.

of the beam, and the peak power is given by

$$P_{max} = \lim_{\beta \to m \cdot 2\pi} |AF(\beta)|^2 = N^2 \tag{3.8}$$

This implies that the peak power is quadratically proportional to the array size. Therefore, if the output power of a signal antenna element is limited, a PAA could quadratically increase the power in the desired direction by increasing the size of the PAA.

Among the multiple lobes shown in Fig. 3.5, only the mainlobe is useful; the sidelobes are undesired as they will reduce the power in the main lobe and waste power in undesired directions. In applications such as cellular communications, the side lobes could also cause more signal interference; or applications where PAAs are receiving signals, the side lobes will collect the signal from undesired directions, which will reduce the signal to noise ratio.

The side lobes could be eliminated by controlling the pitch of the antenna elements. (3.6) implies that given that $\sin(\theta) \in [-1, 1]$, the value range of β is limited to

$$\Delta\beta = \beta_{max} - \beta_{min} = 4\pi \frac{d}{\lambda} \tag{3.9}$$

which means not all the maxima in Fig. 3.5 could exist. To ensure only one maxima (main lobe) exists, $\Delta\beta$ must be less than or equal to 2π, which will lead to the single lobe condition

$$d \leq \frac{\lambda}{2}, \tag{3.10}$$

i.e. the pitch of antenna elements should be no greater than half of the signal wavelength to have a main-lobe-only beam pattern from a PAA.

The beam width of the PAA emission is also determined by the PAA geometry. As illustrated in Fig. 3.5 and (3.4)-(3.7), there are several null points between the lobes.

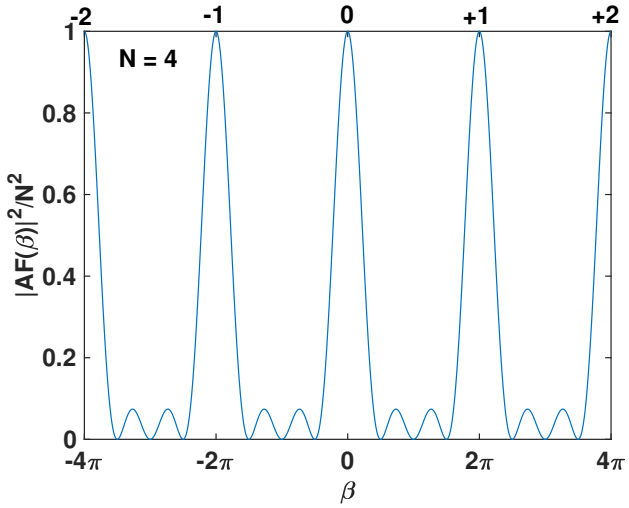

Figure 3.5: Array factor versus β for array size of 4.

The beam width of the lobe is defined as the angular distance between the two closest null points of a lobe, which can be given as (for the m-th order)

$$\beta_{m+\frac{1}{N}} - \beta_{m-\frac{1}{N}} = 2\pi\frac{d}{\lambda}\sin\theta_{m+\frac{1}{N}} - 2\pi\frac{d}{\lambda}\sin\theta_{m-\frac{1}{N}} = 2\pi\cdot\frac{2}{N}$$

which can be re-written as

$$\Delta\theta_m = \frac{\lambda}{Nd\cos\theta_m} \tag{3.11}$$

where $\beta_{m\pm\frac{1}{N}}$ are the β values of the two null points around the m-th lobe, $\Delta\theta_m$ is the beam width, and θ_m is the beam angle. Equation 3.11 implies that the beam width is only inversely proportional to Nd, i.e., the aperture of the PAA, but has no relation to the number or properties of the antenna elements. The beam width also increases along with the increase of beam angle. The 3-dB beam width can be calculated from a more general equation, which can be expressed as follows:

$$\Delta\theta = \frac{\lambda}{2\pi d\cos\theta}\Delta\beta \tag{3.12}$$

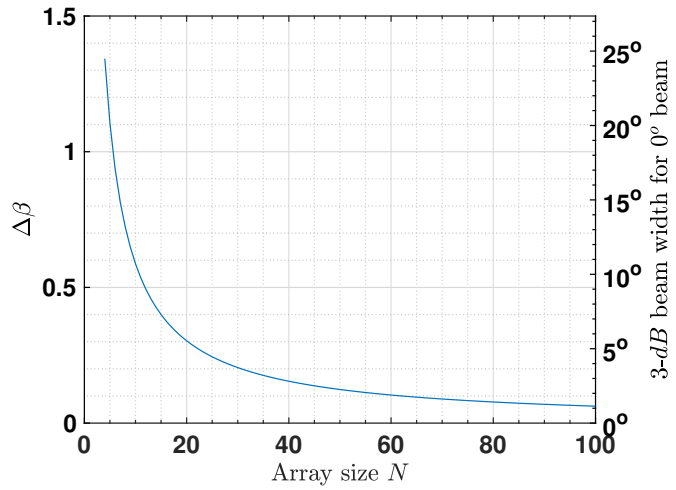

Figure 3.6: $\Delta\beta$ and equivalent 3-dB beam width for 0° beam with half wavelength antenna pitch.

where $\Delta\beta$ is numerically calculated for different array size and is shown in Fig. 3.6, which also exhibits inversely proportional relations to the PAA aperture. The 3-dB beam width for the 0° beam with half wavelength antenna element pitch are also shown in Fig. 3.6. Note that (3.11)-(3.12) are valid only when the beam angle is not close to 90°.

The PAA geometry also determines the required phase increment of each antenna element for beam steering. As mentioned above, the required phase increment $\Delta\varphi$ for m-th order lobe in a given angle can be derived from $\beta = m \cdot 2\pi$, which leads to the beam angle equation being consistent with (3.3). Practically, we usually design the PAA to have only one lobe in the beam pattern with the single lobe condition (3.10). In this case, we only have the 0-th order beam, i.e., $\beta = 0$, which leads to the main lobe angle equation as follows

$$\sin(\theta) = \frac{\Delta\varphi}{2\pi f} \cdot \frac{c}{d} \tag{3.13}$$

3.2.3 Antenna Element Patterns

The radiation pattern of an antenna element is another parameter that determines the radiation pattern of a PAA, as described in (3.7) and Fig. 3.4. In theory, the array factor of a PAA forms a uniform radiative intensity in all direction. The actual relative radiative intensity of a PAA in a certain beam angle depends on the radiative ability of a single antenna element in that direction. To achieve a large beamsteering range, a uniform (or in-directional) beam pattern of a single antenna element is desired. Figure 3.7-3.9 depict three antenna element examples and the simulated radiation patterns for 1-D PAAs – dipole antenna, patch antenna and sectoral antenna. Both these three antenna elements have large beam width that can support large beamsteering range for the corresponding PAAs. The dipole antenna is suitable for balanced photodetections with push-pull configurations, whereas the patch antenna can be used with single drive of photodetector. Both the dipole antenna and the patch antenna can be realized as planar antennas that are easy for integration. The sectoral horn antenna flares in H-plane and has directional radiation in E-plane. Therefore, it is very suitable for 1-D PAA with a

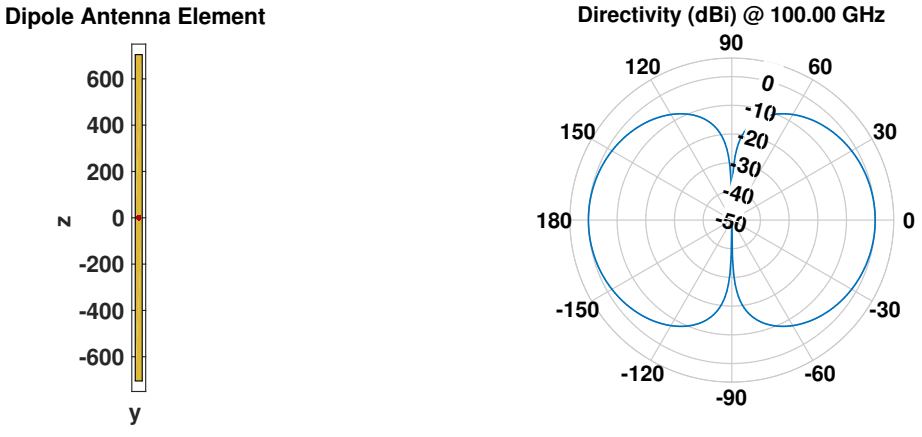

(a) (b)

Figure 3.7: Schematic of a 100 GHz dipole antenna and the simulated relation pattern in the x-z plane.

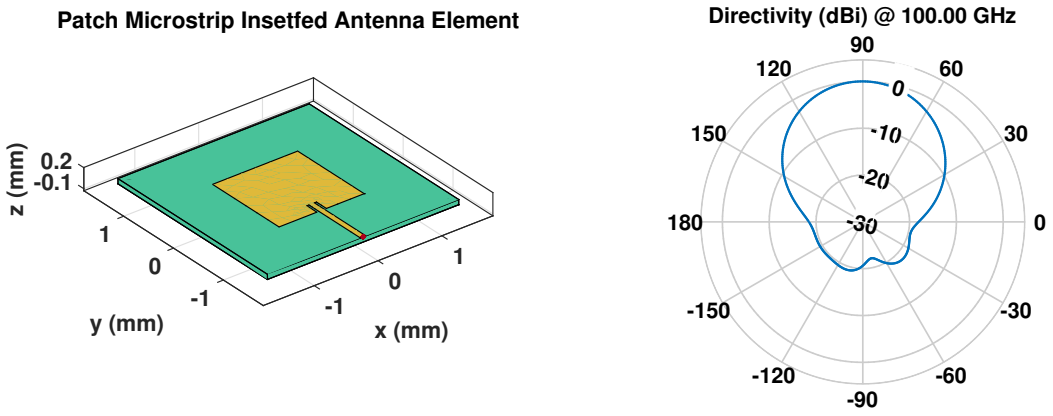

(a) (b)

Figure 3.8: Schematic of a 100 GHz patch antenna and the simulated relation pattern in the x-z plane.

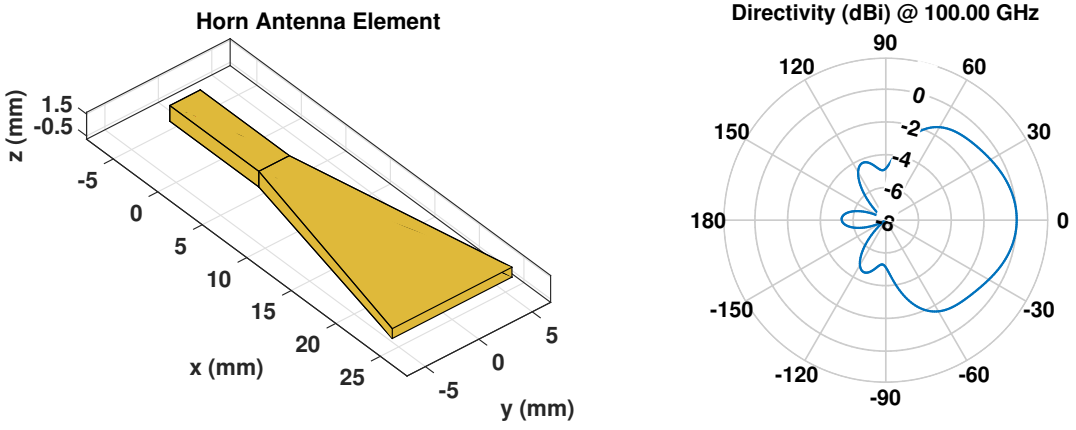

(a) (b)

Figure 3.9: Schematic of a 100 GHz sectoral antenna and the simulated relation pattern in the x-z plane.

discrete antenna array. All the three antennas have the strongest radiation in the normal direction of the antenna aperture.

3.3 Beam Squint

Conventional PAAs, where electrical phase shifters are employed to realize phase shift of the signal, work well for radar or sensing applications as only single frequency is required in these scenarios. As for wideband communications where a large bandwidth is desirable, phase shifters are not ideal for PAAs because they limit the carrier bandwidth utilization. The beam angle equation (3.13) shows that the angle of the beam is not only determined by the phase shift $\Delta\varphi$, but is also related to the signal frequency. By taking the first derivative of (3.13), one can obtain

$$\begin{aligned} \mathrm{d}\theta &= -\frac{\Delta\varphi}{2\pi f\cos\theta}\cdot\frac{c}{d}\cdot\frac{\mathrm{d}f}{f}+\frac{1}{2\pi f\cos\theta}\cdot\frac{c}{d}\cdot\mathrm{d}\Delta\varphi \\ &= -\frac{\mathrm{d}f}{f}\tan\theta+\frac{1}{f\cos\theta}\cdot\frac{c}{d}\cdot\frac{\mathrm{d}\Delta\varphi}{2\pi\mathrm{d}f}\mathrm{d}f \\ &= -\left(\tan\theta+\frac{\Delta\tau\cdot c}{d\cos\theta}\right)\frac{\mathrm{d}f}{f} \end{aligned} \tag{3.14}$$

where θ is the angle of the beam and

$$\Delta\tau = -\frac{\mathrm{d}\Delta\varphi}{2\pi\mathrm{d}f} \tag{3.15}$$

is the group delay of the signal due to path length difference. The first term of (3.14) refers to the beam angle change due to the frequency offset, which is the so-called beam squint. It implies that the beam squint becomes severe as the beam angle increases. The array factor beam pattern plot that shows the beam squint for different frequency offset is depicted in Fig. 3.11(a). The beam squint could lead to power attenuation of the high

frequency components of the data signal and thereby limit the usable data bandwidth. Based on (3.6), the 3-dB bandwidth due to the beam squint can be calculated by solving the following equations

$$\begin{aligned}\beta_{3dB} &= 2\pi\frac{d}{c}(f_c + \frac{\Delta f_{3dB}}{2})\sin\theta_c - \Delta\varphi \\ &= 2\pi\frac{d}{c}f_c\sin\theta_c - \Delta\varphi + 2\pi\frac{d}{c}\frac{\Delta f_{3dB}}{2}\sin\theta_c \\ &= \beta_c + 2\pi\frac{d}{c}\frac{\Delta f_{3dB}}{2}\sin\theta_c \\ &= \frac{\pi}{2}\frac{\Delta f_{3dB}}{f_c}\sin\theta_c \end{aligned} \tag{3.16}$$

$$|AF(\beta)|^2 = \frac{\sin^2\frac{N}{2}\beta_{3dB}}{\sin^2\frac{1}{2}\beta_{3dB}} = \frac{1}{2} \tag{3.17}$$

where f_c is the carrier frequency, θ_c is the beam angle of the carrier, $\beta_c = 0$ is required for the angle beam, Δf_{3dB} is the 3-dB bandwidth, provided the pitch of the antenna element is half of the wavelength $d = \lambda/2$. Figure 3.10 shows the 3-dB bandwidth due to the beam squint for different array size and beam angles. The bandwidth shrinks as the beam angle increases. The beam squintimpacts the bandwidth of large scale PAAs more, which is expected as a large scale PAA yields a narrow beam, which is more sensitive to beam angle changes.

Further, in conventional PAAs, especially for bulk implementations, only the optical phase is tuned and the path length of each antenna element may not be equalized. The second term of (3.14) refers to the beam angle change due to group delay difference of the signal due to unequalized path length between two adjacent antenna elements. This implies that a linear path length difference can introduce additional beam squint for all beam angles even for a 0^o beam. This can also distort the beam at the offset frequency if there are random variations in the unequalized path length of each antenna element. The additional beam squint also increases as the beam angle increases.

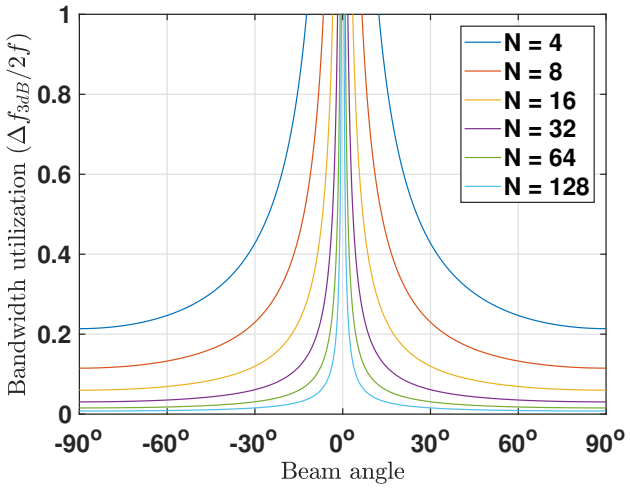

Figure 3.10: The 3-dB bandwidth due to beam squint versus beam angles for different array size with half wavelength antenna element pitch.

The beam squint and path length imbalance limits the signal bandwidth. For example, for beam at 45° with beam squinting, 10% of frequency offset will lead to a 6° beam directional deviation; for a 0° beam, a 0.1 ns linear delay difference could also result in a 6° beam squint even for 1 GHz frequency offset. Therefore, to achieve wideband communications, beam squint and path length matching should be considered when designing PAAs.

3.4 Optical True Time Delay based Phased Arrays

Two additional requirements – signal path length matching and beam squint avoidance – are included in PAA designs for wideband communications. Signal path length matching is difficult and costly for PAA bulk implementations. However, for high frequency carriers such as W-band mmW signals where the wavelength is small, signal path length matching could be easily achieved with integration technology such as MMIC [121]. As for beam squint avoidance, TTD technology should be employed for PAAs. Upon further investigating (3.13), we find that the term $\frac{\Delta\varphi}{2\pi f}$ is actually the time delay of

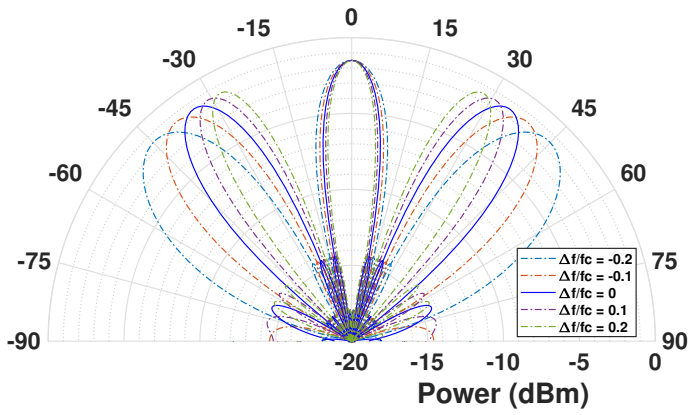

(a)

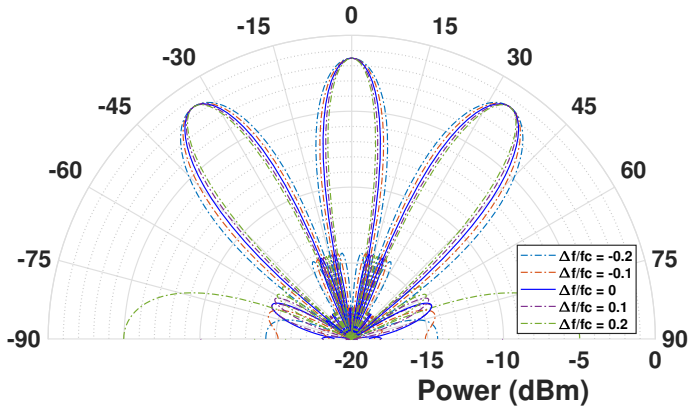

(b)

Figure 3.11: Beam pattern of an 1×8 half-wavelength pitch array factor for different frequency offset with path lengths matched. (a) Beam squint with phase shifters, and (b) Beam-squint-free operation with TTDs.

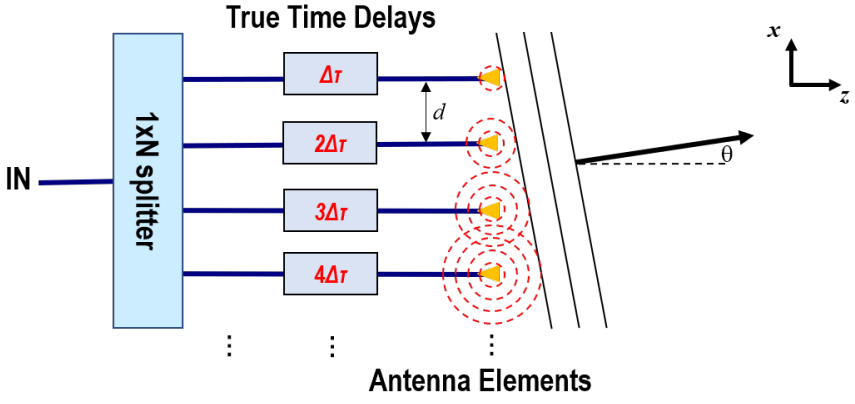

Figure 3.12: Schematic diagram of a TTD based 1-D PAA .

the signal with respect to the adjacent signal channel. Since the signal phase velocity is the same in vacuum for all frequencies, it is the delay increment of the signal that determines the beam angle. Therefore, (3.6), (3.13) and (3.14) can be re-written in terms of delays as

$$\beta = 2\pi\frac{d}{\lambda}\sin\theta - 2\pi\frac{c}{\lambda}\Delta\tau = \frac{2\pi}{\lambda}(d\sin\theta - c\Delta\tau) \tag{3.18}$$

$$\sin\theta = \Delta\tau \cdot \frac{c}{d} \tag{3.19}$$

$$\mathrm{d}\theta = \frac{1}{\cos\theta} \cdot \frac{c}{d} \cdot \frac{\mathrm{d}\Delta\tau}{\mathrm{d}f}\mathrm{d}f = 0 \tag{3.20}$$

where $\Delta\tau$ is the signal delay increment with respect to the adjacent antenna element provided the path lengths are matched. (3.19)-(3.20) implies that if we control the group delay of the signal for each antenna element instead of only controlling the phase, as depicted in Fig. 3.12, the beam for all frequencies will point in the same direction, thereby eliminating the beam squint issue. Figure 3.11(b) plots the beam pattern of an 1×8 half wavelength pitch array factor for different frequency offset with TTDs, which illustrates that compared to Fig. 3.11(a), all frequencies have the same beam orientation and beam squint is eliminated.

Electrical delay lines are characteristic of very large propagation loss in CMOS processes, especially for high frequency carriers [34, 11]. Electromagnetic interference also should be considered in the beamforming network design. Thus, it is impractical to realize large scale PAAs with electrical TTDs for mmW signals. Integrated optical delay lines, which leverage the low propagation loss waveguides and very large bandwidth compared to the RF signal frequency, are very suitable for TTD based beam forming networks in PAAs.

The up-conversion process is required for a photonic-assisted PAAs, as discussed in Section 2.1. The RF signal is generated through the beating of two optical signals with

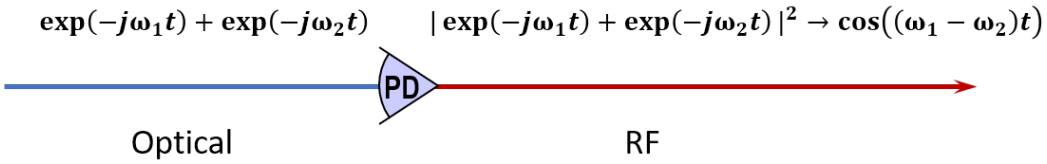

Figure 3.13: Up-conversion process for photonics assisted mmW signal generation. (PD: photodiode.)

angular frequencies ω_1 and ω_2 separated by the RF frequency ω_{RF}. Figure 3.13 illustrates a photonic-assisted mmW signal generation the up-conversion process. With optical delay lines, when two optical tones are both delayed by the same amount, τ, then

$$\begin{aligned} P(t) &= \left[e^{-j\omega_1(t+\tau)} + e^{-j\omega_2(t+\tau)}\right] * conj. \\ &= 2 + 2\cos\left[(\omega_1 - \omega_2)\cdot(t+\tau)\right] \\ &= 2 + 2\cos\left[\omega_{RF}\cdot(t+\tau)\right] \end{aligned} \tag{3.21}$$

The term $\cos\left[\omega_{RF}\cdot(t+\tau)\right]$ implies the resulting RF signal is true time delayed by τ. However, if only one optical tone is delayed by τ, the other optical tone is not delayed, and then we have

$$\begin{aligned} P(t) &= \left[e^{-j\omega_1(t+\tau)} + e^{-j\omega_2 t)}\right] * conj. \\ &= 2 + 2\cos\left[(\omega_1 - \omega_2)\cdot(t+\tau) - \omega_2\tau\right] \\ &= 2 + 2\cos\left[\omega_{RF}\cdot(t+\tau) - \omega_2\tau\right] \end{aligned} \tag{3.22}$$

which implies that the resulting RF signal is not only delayed by τ, but also is shifted in phase by $\omega_2\tau$. This phase is very sensitive to τ since the optical frequency is so high. For example, for an optical frequency of 193 THz, a τ of only $1.44e^{-17}$ seconds results in a 1^o phase shift of the RF carrier. Therefore, for optical TTD based PAAs, the two optical tones must be true time delayed by the same amount so that the optical delay

line generates the equivalent RF signal delays.

3.5 Summary

This chapter discussed the operation principle of PAAs, which reveals that the radiation pattern of a PAA is dominated by the array factor, whereas the radiation pattern of a single antenna element determines the maximum radiative intensity in different angles. For PAAs used in communication links, the traditional PAAs based on phase shifters may limit the available bandwidth for the data signal due to beam squint. On the contrast, TTD based PAA exhibits beam-squint-free beamsteering capability that is desired for wideband communications. However, this requires very precise control of signal delays. Therefore, integrated photonics technology is more suitable for realizing TTD based OBFNs for PAAs.

This page intentionally left blank

Chapter 4

Ultra-low Loss Silicon Nitride Waveguide Technology

The loss of integrated waveguides is an important consideration for IMWP systems as the optical loss is quadratically transferred to electrical loss in the RF circuit described as the square-law nature of photodetection. As mentioned in chapter 1, among the three widely used material systems for IMWP, the stoichiometric Si_3N_4 waveguides have the lowest propagation loss compared to SOI material platform due to the relatively low optical confinement. The lack of two-photon absorption in SiN waveguides make it capable of handling much higher optical power that is desired in IMWP compared to SOI waveguides. However, SiN waveguides can still maintain reasonable bending radius for large integration density since the refractive index contrast is relatively high between SiN core and the SiO_2 cladding. One main drawback of SiN integration platform is the lack of active components such as optical gains, modulators and photodetectors. This drawback can be overcomed by hybrid integrating active material platforms. To date, several reports have demonstrated hybrid integration of SiN and InP and a coupling loss of 2 dB is reported [122, 123, 124]. SiN is a promising platform and compatible to CMOS fabrication process. Many foundries, such as IME, Gent and LioniX have put much effort in developing different waveguide technologies for applications including RF signal

processing, data communications, biosensing, spectroscopy, quantum communication. In this chapter, different SiN waveguide structures will be discussed. We are also developing the low loss SiN waveguide technology in house, and the fabricated waveguides and devices will be demonstrated in this chapter as well.

4.1 Silicon Nitride Waveguides Overview

The SiN layer is usually formed by using low-pressure chemical vapor deposition (LPCVD). LPCVD is capable of batch processes and can result in very good uniformity of layer thickness and refractive index, and the SiN layer can be deposited on both sides of the substrate at the same time [125, 126]. However, due to the difference in the thermal expansion coefficient between the deposited Si_3N_4 film and the Si substrate, internal stress will accumulate along with the thickness of the deposited film and cracks will occur if the thickness of the film beyond a critical value. The critical layer thickness for Si_3N_4 layer is in the order of 300-400 nm [127].

Within the thickness limitation, several waveguide geometries are developed, as described in Fig. 4.1. The single stripe geometry consists of a very thin SiN core (several tens of nm), as shown in Fig. 4.1(a) , and is usually used to ultra-low loss waveguides[128, 129]. As low as 0.045 dB/m of loss was reported at 1580 nm in 20-m long waveguide spiral delay lines with the bending radius in the order of 10 mm [130]. This low propagation loss is achieved due to the low optical confinement in the thin Si_3N_4 waveguide (40 nm), which minimizes sidewall scattering. Most of the mode is guided in SiO_2 and therefore, the layers of the buried oxide (BOX) and cladding are very thick. The top cladding is formed by a flip-chip bonding a thermally grown SiO_2 film.

Despite the restriction of Si_3N_4 thickness, a thicker waveguide with higher optical confinement could be achieved by alternating oxide and nitride layers. The stress of Si_3N_4

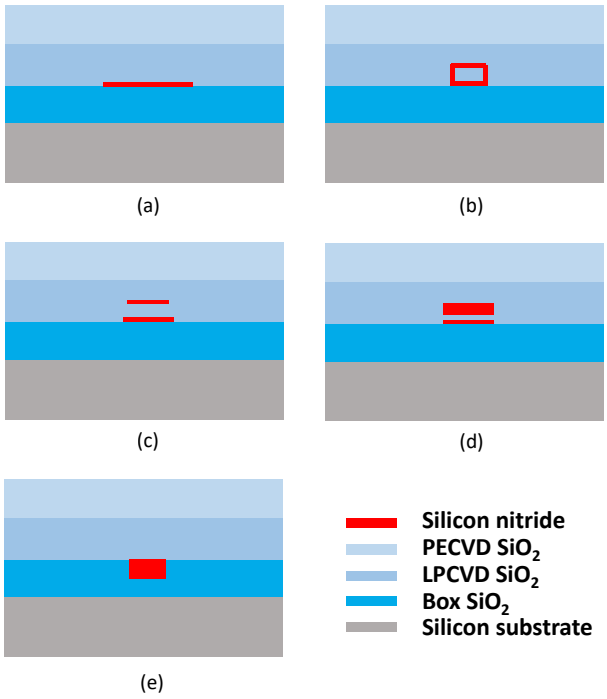

Figure 4.1: SiN waveguide structure for (a) single stripe, (b) box-shell, (c) symmetric double stripe, (d) asymmetric double stripe, and (e) buried waveguide.

on Si is tensile, while that of SiO_2 films are compressive. Alternating stacks of oxide and nitride could thereby exhibit reduced macroscopic stress, and consequently allows for more Si_3N_4 incorporated in the waveguide. This technique leads to the waveguide structures of box-shell, symmetric double stripe, and asymmetric double stripe, as depicted in Fig. 4.1(b)-(d), which is known as the TriPleX technology [129]. The box-shell structure usually have a square SiO_2 surrounded by a thin Si_3N_4 layer. The symmetric shape significantly reduces the polarization dependence in the waveguide [79]. The box shell is available in a low [79] and high [131] index contrast variant based on the thicknesses ratio of the Si_3N_4 shell to the SiO_2 core, which have a propagation loss of 0.2 dB/cm and 0.06 dB/cm [132], and bending radius of 500 μm and 150 μm, respectively. Double stripe waveguide structures are useful when large polarization birefringence is required. The symmetric double stripe structure is typically applied in the scenario where tight bending radius is required, and the attenuation and bending radius were reported less

than 0.1 dB/cm and down to 70 μm [133], respectively. The asymmetric double stripe structure is highly suitable for combining both low and high contrast regions of the mode on a single chip. The transition between the two contrast regions can be made adiabatic by tapering the SiN layers, and the loss of the low and high modal confinement waveguides on the same chip were demonstrated as 0.015 dB/cm and 0.15 dB/cm [129], respectively.

The buried waveguide geometry in Fig. 4.1(e) was developed for applications requiring ultra-high confinement of the modal field in the core layer such as nonlinear optics [134]. Due to the thickness restrictions in stoichiometric LPCVD Si_3N_4 growth, a photonic damascene process is applied for the fabrication of crack-free waveguides. Damascene waveguides can as thick as 6.5 μm and thereby can provide strong optical confinement [127], which is suitable for highly compact and nonlinear optical applications such as compact Kerr comb generation resonators [135]. A realized buried waveguide demonstrated the optical propagation loss of 0.4 dB/cm at 1.55 μm with a calculated minimum bending radius of 12.5 μm [136].

4.2 Silicon Nitride Waveguide for This Work

The OBFNs in this work requires only the fundamental transverse electric (TE) mode, and the coupling from TE to transverse magnetic (TM) mode should be as low as possible. Thus, a waveguide structure with high large polarization birefringence is required. Also, the bending radius should be in a reasonable range. Therefore, the high contrast symmetric Si_3N_4 waveguide is a good option among the waveguide structures discussed above.

The SiN OBFN chip is fabricated in foundry and the fabrication process is depicted in Fig. 4.2. The process starts with the single crystal silicon wafer. The BOX is thermal

grown on the silicon. The BOX layer thickness must be sufficient to minimize absorption in the silicon substrate, which is dependent on the optical waveguide confinement. Thermally oxidized silica remains one of the lowest loss oxide-based cladding materials due to a low surface roughness from the original high-quality silicon substrate, and the absence of hydrogen in the material and during the growth process. The Si_3N_4 waveguide core is formed using LPCVD with a thickness of 170 nm, followed by SiO_2 waveguide core deposition of 0.5 μm using tetraethoxysilane (TEOS) precursor LPCVD. Another 170 nm top Si_3N_4 waveguide core is formed using the same LPCVD process to complete the high contrast symmetric waveguide core structure. Then the core layer is patterned and etched to form the waveguides. The next step is the top cladding SiO_2 deposition. The top cladding thickness should be sufficient to reduce the waveguide loss. However, similar to SiN layers where the thickness is restricted due to the internal stress, the LPCVD TEOS SiO_2 also has a thickness restriction around 1500 nm. To reach a sufficiently thick cladding layer, a part of the SiO_2 is deposited using plasma-enhanced chemical vapor deposition (PECVD) beyond the critical thickness.

For efficient thermal tuning, the heater is placed on top of the waveguides. To form the heaters, a chromium/gold layer stack is first deposited to form the metal traces and the resistant region through metal lift-off process. Then use another photo lithography to exposure the heater resistant region and wet etch the gold, leaving only the thin chromium film as the heater resistor.

4.3 In-House Silicon Nitride Technology Development

SiN fabrication process are also developed in house. In this platform, the thick single stripe Si_3N_4 waveguide structure are employed. The Si_3N_4 layer is deposited by a single LPCVD growth, and the thickness is close to the critical values. This thickness of the

Figure 4.2: Process flow of the TriPlex^{TM} waveguides with chromium heaters and gold/chromium leads [137].

Si_3N_4 waveguide are suitable for general applications since it provides moderate optical confinements with acceptable waveguide propagation loss, but the fabrication process is much simpler than other waveguide structures, which could lower the cost per chip and have higher yield. Many works have been reported for the 150 - 400 nm thick single stripe waveguide platform demonstrating the waveguide loss ranging from 0.11 - 1.45 dB/cm [138].

Figure 4.3 presents the process flow of the in-house Si_3N_4 stripe waveguides. The fabrication starts from the 380 nm thick LPCVD Si_3N_4 layer wafer grown on a 3 μm thick oxide wafer. To realize devices with small feature size, the PICs are patterned with the 248 nm deep ultraviolet (DUV) ASML stepper which can provide resolution below 200 nm. Then the waveguide is formed with dry etching. The top cladding is deposited for 2 μm by PECVD and the chip is annealed at the temperature of 1050°. Since most of the attenuation of the waveguide mainly origins from the sidewall roughness of the waveguide and the density non-uniformity of the PECVD top cladding, the high resolution DUV stepper and annealing could further alleviate the waveguide loss. The simulation results of the single mode waveguide widths, effective indices n_{eff}, group indices n_g and minimum bending radii R_{min} (0.01 dB/cm criterion) for 1310 nm and

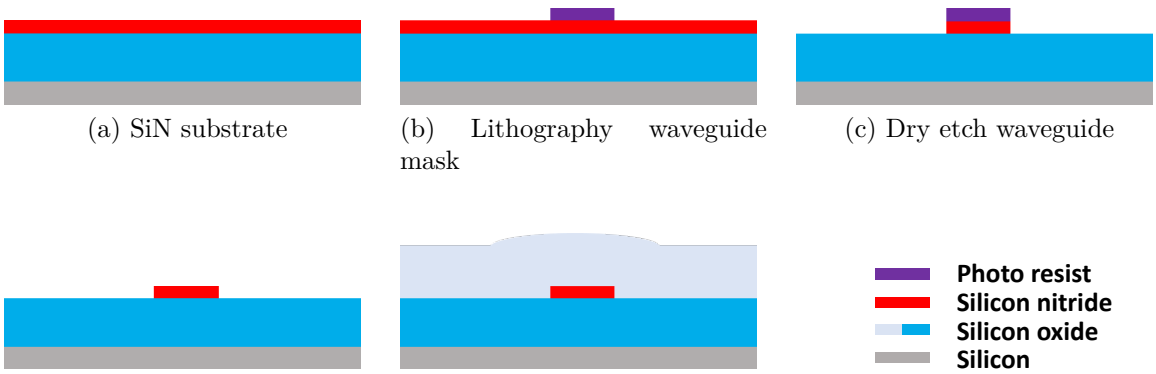

(a) SiN substrate (b) Lithography waveguide mask (c) Dry etch waveguide

(d) Removal of photo resist (e) PECVD SiO_2 deposition

Figure 4.3: Process flow of the in-house SiN stripe waveguides.

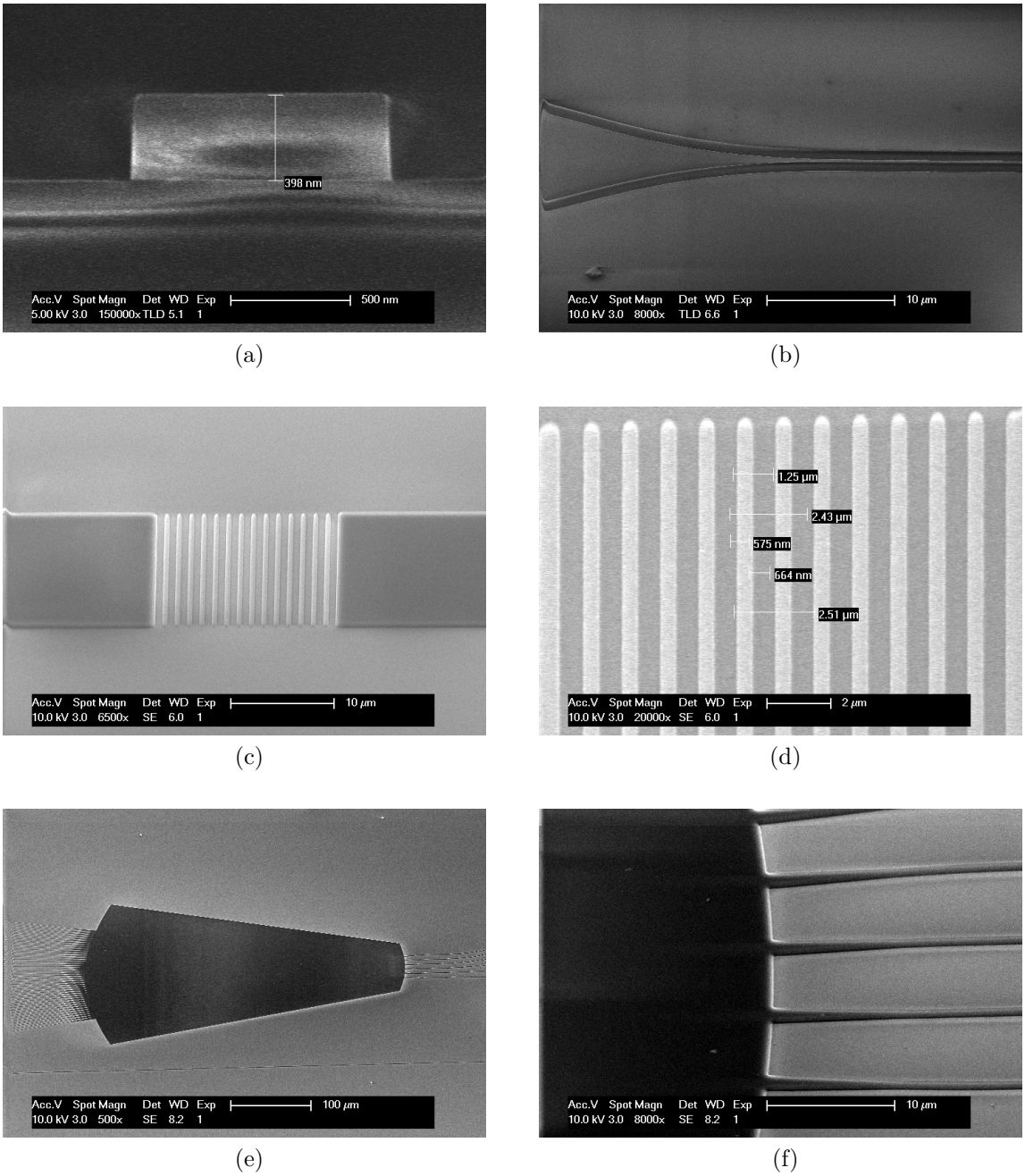

(a) (b)

(c) (d)

(e) (f)

Figure 4.4: SEM picture of (a) the waveguide cross section, (b) directional coupler, (c-d) grating coupler, and (e-f) star coupler of the AWG.

Wavelength	Width	TE			TM		
		n_{eff}	n_g	R_{min}	n_{eff}	n_g	R_{min}
1310 nm	0.8 μm	1.65	2.04	23 μm	1.59	1.98	36 μm
1550 nm	1.0 μm	1.62	1.99	32 μm	1.55	1.89	64 μm

Table 4.1: The single mode waveguide width, effective index n_{eff}, group index n_g and minimum bending radius R_{min} (0.01 dB/cm criterion) for 1310 nm and 1550 nm, and TE and TM mode, respectively.

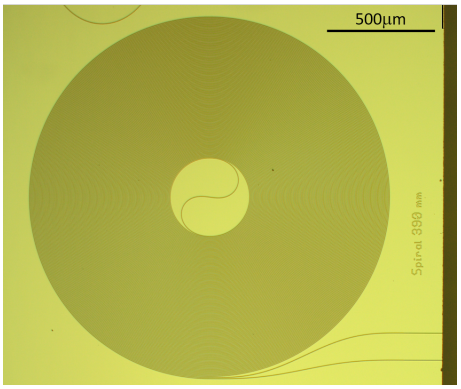

Figure 4.5: Microscope picture of the Archimedean spiral waveguide with 390 mm length.

1550 nm, and TE and TM mode are listed in Tab. 4.1. Figure 4.4 depicts the scanning electron microscope (SEM) pictures of the waveguides and some devices on the chip. The SEM of the waveguide cross section is shown in Fig. 4.4 (a). This picture a very smooth etching of the Si_3N_4 waveguide with 1 μm width. Fig. 4.4 (b) presents the close-up of a DC. Fig. 4.4 (c) and (d) illustrate the picture of 1550 nm grating coupler with 1.25 μm period and 0.46 filling factor; Fig. 4.4 (e) and (f) shows the star coupler and the tapered input waveguide of an AWG.

The waveguide loss is characterized by sending optical signals into a very long waveguide and measuring the back scattering using an optical backscatter reflectometry (OBR). The long waveguide was spiraled in a 3 $mm \times 3$ mm area with the total length of 0.39 m, as illustrated in Fig. 4.5. The clock-wise spiral and counter-clock-wise spiral was connected with a specifically designed adiabatic s-bend to reduce the loss in the joints due to

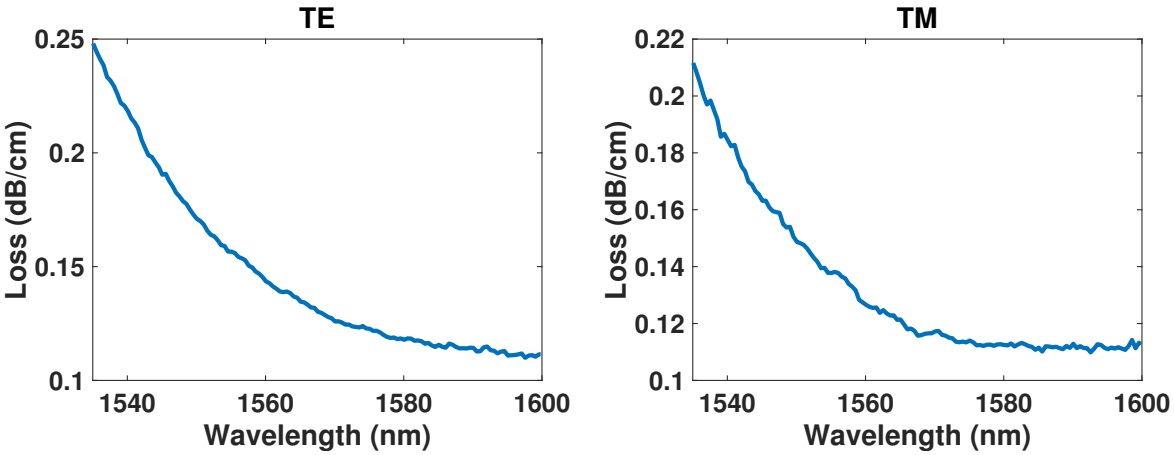

Figure 4.6: Measured waveguide loss for (a) TE mode and (b) TM mode, respectively.

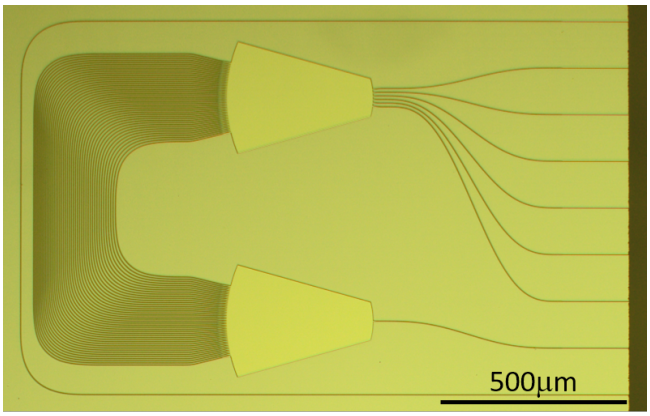

Figure 4.7: Microscope picture of the AWG.

the radius discontinuity. The measured waveguide loss is demonstrated in Fig. 4.6. For both TE mode and TM mode, as the wavelength increases, the waveguide loss decreases to the lowest measured value 0.11 dB/cm, and for 1550 nm optical signals, the waveguide losses can still remain less than 0.2 dB/cm.

More complex devices such as arrayed waveguide gratings (AWG) are also realized with the SiN platform, as depicted in Fig. 4.7. The AWG is designed to have 6 output channels and 6 nm channel spacing. Figure 4.8 presents the measured output transmission spectra from all of the 6 channels. The channel spacing is measured as 6.3 nm,

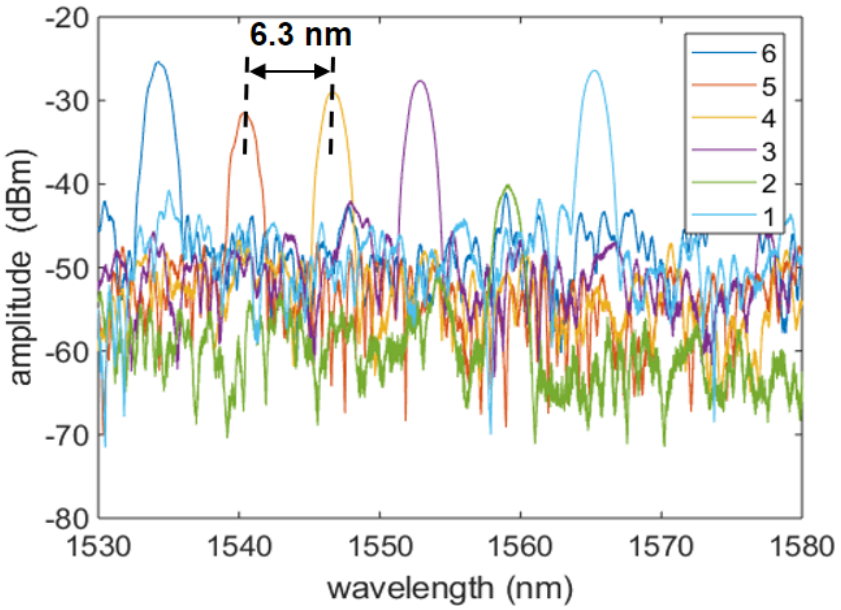

Figure 4.8: Measured transmission spectrum of the 6-channel AWG.

which has a little offset from the designed value. This probably because there is a small difference between the simulated group index and the actual waveguide group index. The non-uniformity of the output intensities is probably due to the non-uniform coupling between the waveguide facet and the fiber as the chip facets are formed by dicing and are not polished. The extinction ratio is measured as 17 dB and can be improved due to the low loss of the waveguide.

4.4 Summary

In this chapter, various SiN waveguide structures including the single stripe, box-shell, symmetric and asymmetric double stripe and buried waveguide were briefly reviewed. The in-house low loss 380 -nm thick single stripe Si_3N_4 waveguide technology were also demonstrated with the measured waveguide loss as low as 0.11 dB/cm, and < 0.2 dB/cm at 1550 nm. A 1×6 AWG was realized demonstrating 6.3 nm channel

spacing and 17 dB extinction ratio. SiN waveguides is suitable for IMWP due to low loss and large integration density. Despite the lack of optical active components, this can be complemented by hybrid integrating with high performance active InP devices.

Chapter 5

Switched Delay Line based Optical Beamforming Network

TTD is desirable for PAAs for wideband communications, especially for large beam steering angles and high bandwidth utilization. As mentioned in Section 3.4, integration technology is favorable for communication-oriented PAAs as the effective signal path of each antenna element could be more precisely equalized. However, electrical delay lines with CMOS processes have a very large propagation loss, which also increases exponentially with RF frequency [34, 11]. In contrast, integrated photonics technology is free from the electromagnetic-interference, and provides frequency independent low propagation loss waveguides. Therefore, integrated optical TTD lines have great potential for realizing TTD-based integrated OBFNs for PAAs.

TTD lines are the fundamental components for a OBFN. Section 1.4 summarized the widely used schemes for implementing integrated tunable TTDs, which include ORRs, chirped gratings, interferometers, photonic crystals, and cascaded/paralleled SDLs. Among these structures, ORRs and SDLs are two popular implementations for OBFNs given the considerations on complexity, unpredictable fabrication variations, and OBFN footprint. ORRs are dispersive devices and can realize very compact OBFNs and continuous tuning of delays. However, an ORR has a limited bandwidth and requires complex control.

SDLs tune the delays by turning on/off optical paths with different path lengths using optical switches. This mechanism naturally supports very wide bandwidth, but only supports discrete delays. Also, the tuning resolution depends on the shortest delay path. In practice, optical switches are non-ideal switches, which will intermix optical signals with different delays and cause ripple in the delay response. In this chapter, a modified SDL architecture eliminating the influence of the non-ideal switch imperfection will be discussed. An OBFN realized with this SDL configuration was also demonstrated. The OBFN was realized using the SiN technology. Chip design will also be discussed.

5.1 Switched Delay Line

SDLs can be realized in parallel mode and cascade mode. Parallel SDLs use an individual delay path for each delay, which minimizes the switches involved in a signal path, and hence minimizes the influence from non-ideal optical switches. However, this redundancy of optical paths will result in a large footprint. Cascaded SDLs tune the delay by changing the combination of the physical delay paths, and each delay path can be re-used for different delays. Thus, cascaded SDLs can be made very compact. However, since the optical signal passes through multiple switches, the influence of the switch imperfection needs to be considered. Given the large scale of delay lines required for an OBFN, a large footprint for the delay line will increase the OBFN chip cost and potentially reduce reliability and yield. Therefore, cascaded SDLs are employed for the OBFN pursued here.

5.1.1 Mach-Zehnder Switches

SDLs tune delays by switching “on” / “off” multiple delays with integrated optical switches. A MZI is a simple structure that can be used as an integrated optical switch.

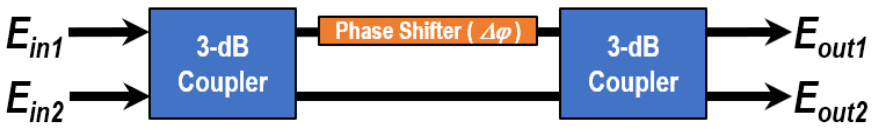

Figure 5.1: Schematic diagram of a 2×2 balanced MZI switch.

Figure 5.1 depicts the schematic diagram of a 2×2 MZI switch, which comprises of two 3-dB couplers and one phase shifter. The incident optical signal is split into two paths, a phase difference between the paths is induced by the phase shifter, and the signals are combined. The phase difference affects the interference result after the signal re-combination and determines the state of the MZI switch. A balanced MZI scheme is employed, which provides a large bandwidth and compact footprint.

The response of the MZI switch could be represented by transfer matrices given

$$\begin{bmatrix} E_{out1} \\ E_{out2} \end{bmatrix} = T_{MZ} \begin{bmatrix} E_{in1} \\ E_{in2} \end{bmatrix} = T_c \cdot T_\varphi \cdot T_c \begin{bmatrix} E_{in1} \\ E_{in2} \end{bmatrix} \tag{5.1}$$

where T_{MZ} is the transfer matrix of the MZI switch, T_c is the transfer matrix of the 2×2 coupler, which can be realized using 2×2 DCs and 2×2 MMI couplers, for both of which the transfer matrix is given by [139]

$$T_c = \begin{bmatrix} \sqrt{1-\kappa} & -j\sqrt{\kappa} \\ -j\sqrt{\kappa} & \sqrt{1-\kappa} \end{bmatrix} \tag{5.2}$$

where κ is the power coupling coefficient of the coupler, which implies that the two output of the coupler has 90^o phase difference. $T_{\Delta\varphi}$ in (5.2) is the transfer matrix of the two

arms of the MZI switch with the phase shifter, which can be given as

$$T_{\Delta\varphi} = \begin{bmatrix} \mathrm{e}^{j\Delta\varphi} & 0 \\ 0 & 1 \end{bmatrix} \tag{5.3}$$

where $\Delta\varphi$ is the optical phase shift due to the tuning of phase shifter. Plugging (5.2)-(5.3) into (5.1), the transfer matrix of a MZI switch can be rewritten as

$$\begin{aligned} T_{MZ} &= T_c \cdot T_\varphi \cdot T_c \\ &= \begin{bmatrix} \sqrt{1-\kappa} & -j\sqrt{\kappa} \\ -j\sqrt{\kappa} & \sqrt{1-\kappa} \end{bmatrix} \cdot \begin{bmatrix} \mathrm{e}^{j\Delta\varphi} & 0 \\ 0 & 1 \end{bmatrix} \cdot \begin{bmatrix} \sqrt{1-\kappa} & -j\sqrt{\kappa} \\ -j\sqrt{\kappa} & \sqrt{1-\kappa} \end{bmatrix} \\ &= \begin{bmatrix} (1-\kappa)\mathrm{e}^{j\Delta\varphi} - \kappa & -j2\sqrt{\kappa(1-\kappa)}\cos\frac{\Delta\varphi}{2}\mathrm{e}^{j\frac{\Delta\varphi}{2}} \\ -j2\sqrt{\kappa(1-\kappa)}\cos\frac{\Delta\varphi}{2}\mathrm{e}^{j\frac{\Delta\varphi}{2}} & (1-\kappa) - \kappa\mathrm{e}^{j\Delta\varphi} \end{bmatrix} \end{aligned} \tag{5.4}$$

For MZI as switches, there are two operation states – the cross-state and the bar-state. For the bar-state, where the phase shift $\Delta\varphi = 0$, the transfer matrix

$$T_{MZ,cross} = \begin{bmatrix} 1-2\kappa & -j2\sqrt{\kappa(1-\kappa)} \\ -j2\sqrt{\kappa(1-\kappa)} & 1-2\kappa \end{bmatrix} \tag{5.5}$$

whereas for the cross-state where $\Delta\varphi = \pi$, the transfer matrix of a MZI switch is expressed as

$$T_{MZ,bar} = \begin{bmatrix} -1 & 0 \\ 0 & 1 \end{bmatrix} \tag{5.6}$$

(5.5) and (5.6) imply that in bar-state, the MZI switch can perfectly pass the optical signal if the phase shifter is accurately tuned, whereas in the cross-state, the response of the MZI switch depends on κ, as shown in Fig. 5.2(a). The perfect switch condition

occurs exactly at $\kappa = 0.5$ where the cross-state transfer matrix $T_{MZ,cross}$ can be simplified as

$$T_{MZ,cross} = -j \begin{bmatrix} 0 & 1 \\ 1 & 0 \end{bmatrix} \tag{5.7}$$

and the cross-state extinction ratio decreases with the coupling coefficient deviation from this condition. This could be explained as, for the cross port of the MZI switch, the two interfered optical signals from two arms of the switch both go through a bar coupling and a cross coupling of the coupler once, and hence, has the same amplitude and can be completely canceled through deconstructive interference, which means the all the optical power will be transferred to the bar-port due to the energy conservation. However, for the bar port of the MZI switch, optical signals of the two arms experience unbalanced couplings (twice of the bar coupling for one signal, and twice of the cross coupling for the other), which cannot completely deconstructed if the bar coupling and cross coupling are not equal, and thereby results in the reduction of the extinction ratio.

The phase response of a MZI is not important in switching application, but it need to be considered in other applications where MZI is used as a tunable coupler. As indicated in (5.4), the cross port responses of a MZI, given by $T_{MZ,12}$ and $T_{MZ,21}$, have a linear phase repose versus the phase shift tuning $\Delta\varphi$, whereas the bar port phase response, given by $T_{MZ,11}$ and $T_{MZ,22}$, depends on κ. Figure 5.2(b) gives the bar-port phase responses of a MZI. It shows that for a MZI depicted as Fig. 5.1 where the phase shifter is placed the on the upper arm, although the upper bar port ($T_{MZ,11}$) and lower bar port ($T_{MZ,22}$) have the same power transmit response, the phase responses is different. For example, when the coupler is a perfect 3-dB coupler ($\kappa = 0.5$), the phase response is linear with $\Delta\varphi$ and have a phase jumping of π at cross switching state. However, when the 3-dB couplers are not perfect, presuming under coupled ($\kappa < 0.5$), the phase response of the upper bar-port ($E_{in1} \rightarrow E_{out1}$) will keep increasing with $\Delta\varphi$, whereas the phase response

of the lower bar-port ($E_{in2} \rightarrow E_{out2}$) will be confined and oscillate within a finite range.

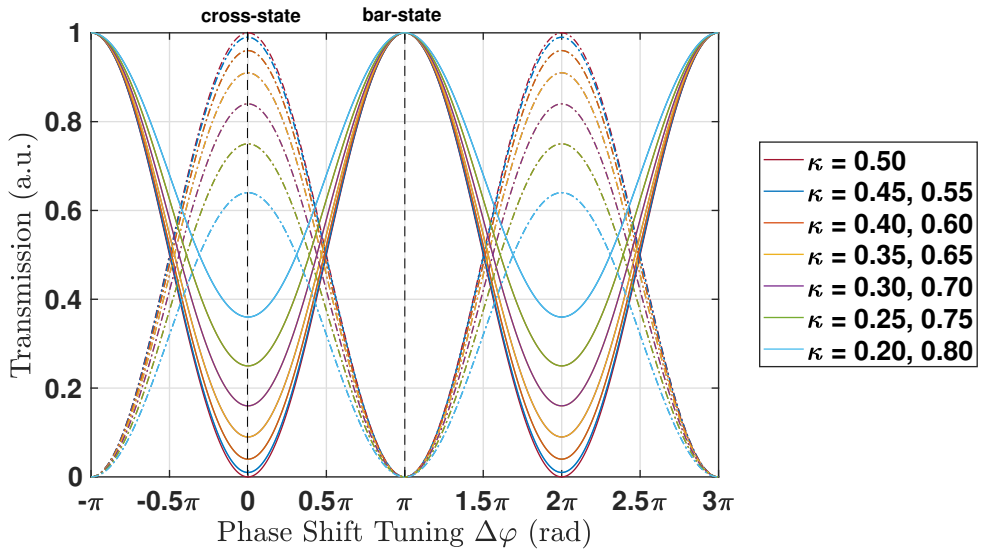

(a)

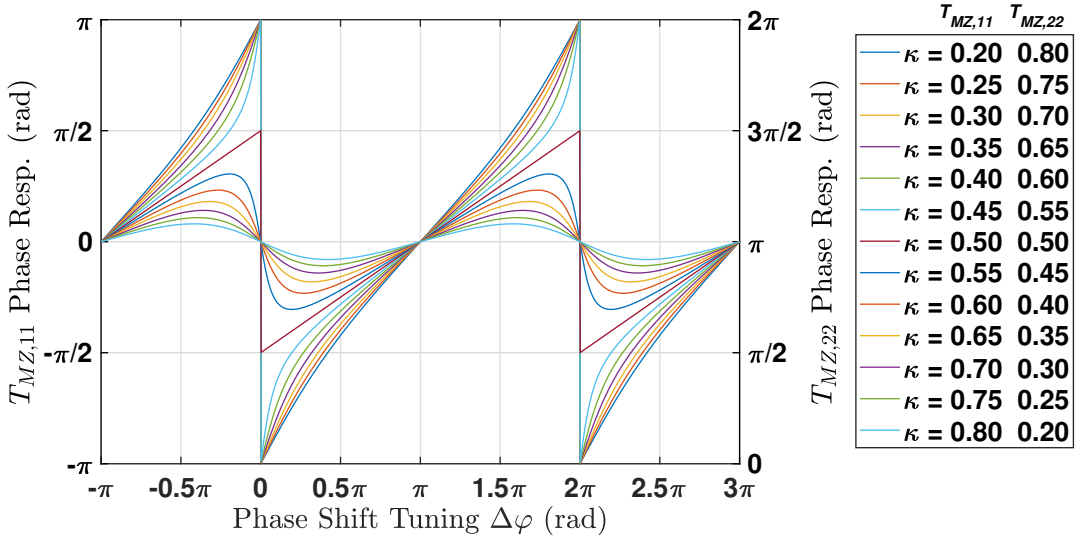

(b)

Figure 5.2: (a) Transmission response and (b) bar port phase response of an imperfect MZI switch for various coupling ratio of the power splitters. (The solid curves refer to the bar port, whereas the dash curves refer to the cross port.)

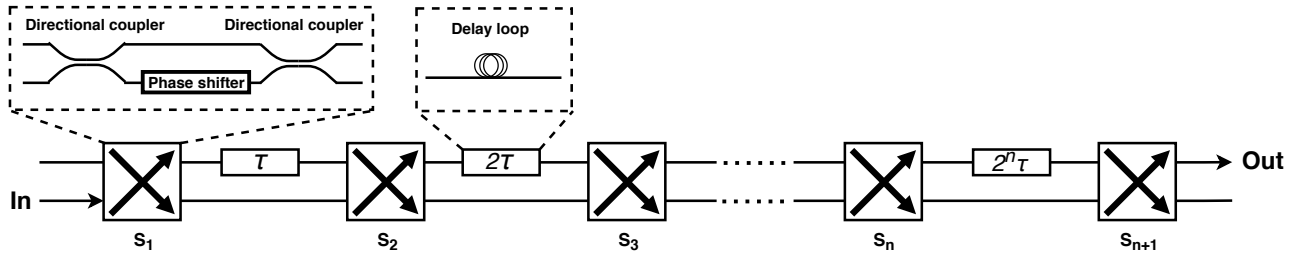

Figure 5.3: Schematic diagram of a conventional n-stage SDL.

5.1.2 Conventional Switched Delay Line

SDL is a straight-forward scheme for integrated tunable delay lines. Figure 5.3 shows the schematic diagram of a conventional n-stage SDL where $n+1$ switches are used to switch on or switch off n stages of delays individually. MZI are used as the optical switches and physical waveguides with different lengths are used as the delay component. Usually, the path length of each stage is doubled for every next stage, which forms a binary-coded delay configuration and the delays of the SDL can be mathematically expressed with a binary number representation given by

$$\tau_{tot} = (b_n b_{n-1} ... b_1)_2 \cdot \tau \tag{5.8}$$

where τ_{tot} is the total delay of the SDL, τ is the delay of the shortest path, and b_n is the state of the n-th delay component where "1" refers to delay "on" and "0" refers to delay "off". (5.8) implies that the SDL can support 2^n discrete delays ranging from τ to $2^n\tau$, where the delay tuning resolution is determined by the delay of the shortest path. This architecture of SDL maximizes the delay tuning efficiency, which, however, requires ideal switches. Actually, as discussed in Section 5.1.1, a real MZI switch device has limited extinction ratio in cross-state, and hence a SDL will have optical signals intermixing with different delays, which will cause distorted non-ideal TTD response. Figure 5.4

illustrates the power transmission and delay responses versus normalized phase shift of the delay loop (linearly related to optical wavelength) for 1-stage and 3-stage SDLs for the worst case with different coupling coefficients of the coupler. Ideally with perfect 3-dB couplers, the response should be flat for both power transmissions and delays. However, ripple, notches and spikes begin to appear due to the imperfection of the 3-dB coupler, and the more deviation the coupler from 3-dB, the more severe the distortion is. These distortions are undesirable since for communication applications, a flat response is desired over the whole bandwidth. The distortions will cause large attenuations and additional beam squint to some frequency components of the signal and thus deteriorate the signal quality. Therefore, these distortions should be eliminated. As mentioned above, the origin of the response distortion is from the limited extinction ratio of the MZI switches. Some work was reported to put additional absorbers at the output of the switch to help kill the undesired optical signal [106, 54]. However, this approach requires additional controls and power consumption, and is only valid in active material systems such as SOI and InP. However, for pure dielectric material such as SiN, other approaches should be explored to eliminate the distortions.

The ripple of the delay response could be studied quantitatively using transfer matrices. Figure 5.5 depicted the schematic diagram of a 1-stage SDL, which comprises of two MZI switches and a delay loop for a delay of $\Delta\tau$. Using (5.4), the transfer matrix of the SDL can be given by

$$T_{DL} = T_{MZ}(\Delta\varphi_1) \cdot T_{delay} \cdot T_{MZ}(\Delta\varphi_2) \tag{5.9}$$

There are two operation modes for this SDL – cross-bar mode and cross-cross mode. The first operation mode has the first MZI switch in cross-state, and the second MZI switch in bar-state, in which $\Delta\varphi_1 = 0$ and $\Delta\varphi_2 = \pi$, and the optical signal outputs from the

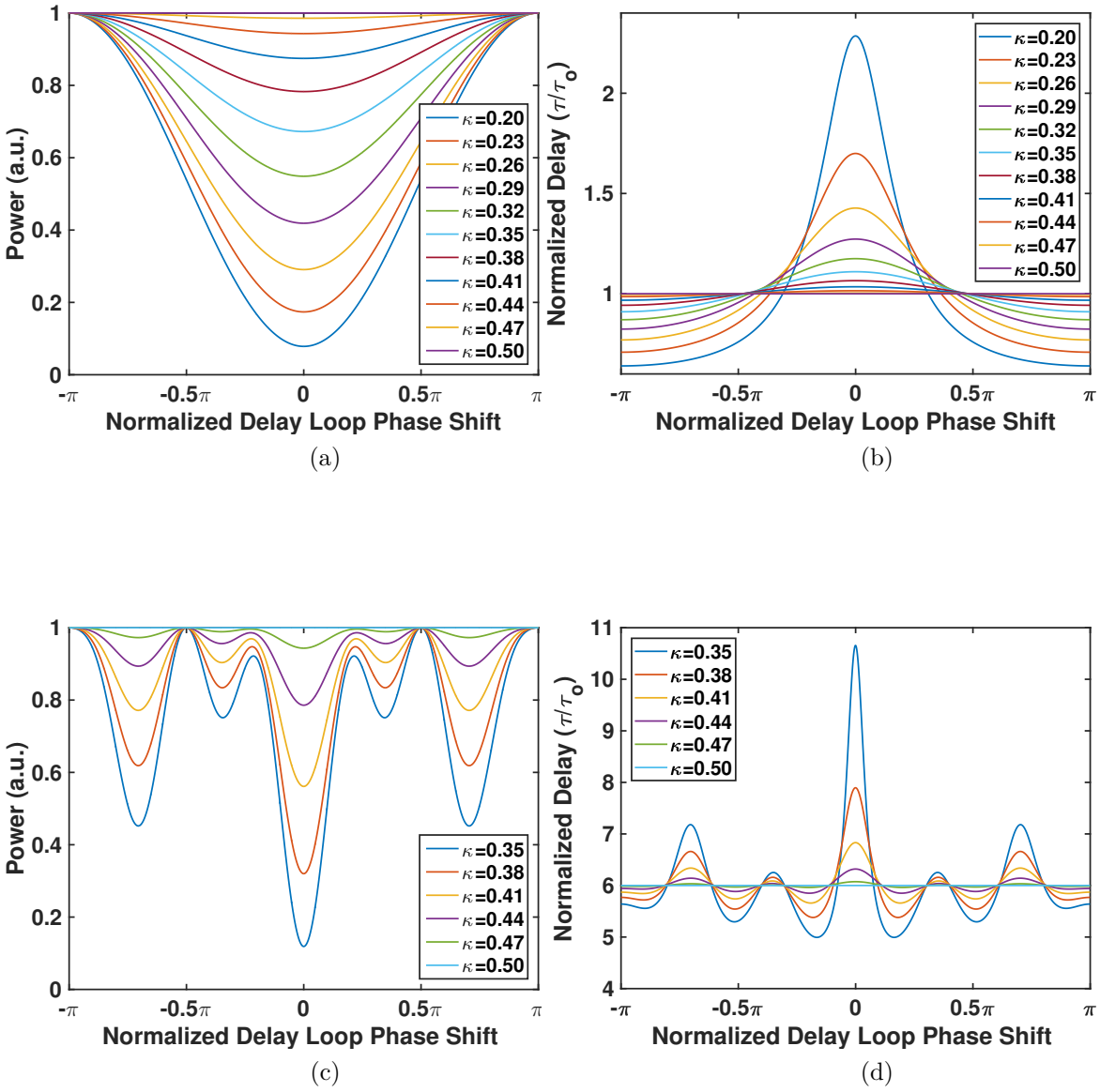

Figure 5.4: The worst case of (a) and (c) power transmission responses for 1-stage and 3-stage SDLs, and (b) and (d) the delay responses for 1-stage and 3-stage SDLs, for various coupling coefficient of the coupler.

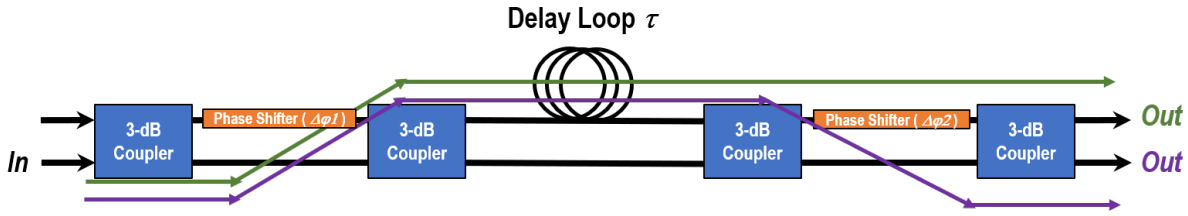

Figure 5.5: Schematic diagram of a 1-stage SDL. The green path refers to the cross-bar operation, whereas the purple path refers to the cross-cross operation.

upper path, as depicted by the green path in Fig. 5.5. Plugging (5.5) and (5.6) into (5.9) and transfer matrix the SDL in the corss-bar mode is given by

$$\begin{aligned} T_{DL,c-b} &= T_{MZ,cross} \cdot T_{delay} \cdot T_{MZ,bar} \\ &= \begin{bmatrix} 1-2\kappa & -j2\sqrt{\kappa(1-\kappa)} \\ -j2\sqrt{\kappa(1-\kappa)} & 1-2\kappa \end{bmatrix} \cdot \begin{bmatrix} \mathrm{e}^{-j\omega\cdot\tau} & 0 \\ 0 & 1 \end{bmatrix} \cdot \begin{bmatrix} -1 & 0 \\ 0 & 1 \end{bmatrix} \\ &= \begin{bmatrix} -(1-2\kappa)\cdot\mathrm{e}^{-j\omega\cdot\tau} & -j2\sqrt{\kappa(1-\kappa)}\mathrm{e}^{-j\omega\cdot\tau} \\ j2\sqrt{\kappa(1-\kappa)} & 1-2\kappa \end{bmatrix} \end{aligned} \tag{5.10}$$

where ω is the angular frequency of the optical signal, and τ is the delay of the delay loop in Fig. 5.5. Because the input is from the lower port, only $T_{DL,c-b,12}$ need to be considered for the upper output. Therefore, the delay response of the SDL can be given as

$$\tau_{tot} = -\frac{\mathrm{d}\angle T_{DL,c-b,12}}{\mathrm{d}\omega} = -\frac{\mathrm{d}(-\omega\cdot\tau)}{\mathrm{d}\omega} = \tau \tag{5.11}$$

which implies that the delay of the SDL is independent of κ and ω, which means it will yield a flat delay response. Moreover, (5.11) also implies that this SDL operation mode can generate a flat transmission and delay response as long as only one of the input ports has optical signal injection.

The cross-cross operation mode has the both of the MZI switches in cross-state where $\Delta\varphi_1 = \Delta\varphi_2 = 0$, and the optical signal outputs from the lower path, as depicted by the purple path in Fig. 5.5. Similarly, the transfer matrix of the SDL in the corss-cross mode can be given by plugging (5.5) into (5.9)

$$\begin{aligned} T_{DL,c-c} &= T_{MZ,cross} \cdot T_{delay} \cdot T_{MZ,cross} \\ &= \begin{bmatrix} 1-2\kappa & -j2\sqrt{\kappa(1-\kappa)} \\ -j2\sqrt{\kappa(1-\kappa)} & 1-2\kappa \end{bmatrix} \cdot \begin{bmatrix} \mathrm{e}^{-j\omega\cdot\tau} & 0 \\ 0 & 1 \end{bmatrix} \cdot \begin{bmatrix} 1-2\kappa & -j2\sqrt{\kappa(1-\kappa)} \\ -j2\sqrt{\kappa(1-\kappa)} & 1-2\kappa \end{bmatrix} \\ &= \begin{bmatrix} -(1-2\kappa)^2 \cdot \mathrm{e}^{-j\omega\cdot\tau} - 4\kappa(1-\kappa) & -j4\sqrt{\kappa(1-\kappa)}(1-2\kappa)\cos\frac{\omega\cdot\tau}{2}\mathrm{e}^{-j\frac{\omega\cdot\tau}{2}} \\ -j4\sqrt{\kappa(1-\kappa)}(1-2\kappa)\cos\frac{\omega\cdot\tau}{2}\mathrm{e}^{-j\frac{\omega\cdot\tau}{2}} & -(1-2\kappa)^2 - 4\kappa(1-\kappa)\cdot\mathrm{e}^{-j\omega\cdot\tau} \end{bmatrix} \end{aligned} \tag{5.12}$$

Because the input is from the lower port, the delay of the the SDL in cross-cross mode is determined by $T_{DL,c-b,22}$ and is given by

$$\begin{aligned} \tau_{tot} &= -\frac{\mathrm{d}\angle T_{DL,c-b,22}}{\mathrm{d}\omega} \\ &= -\frac{\mathrm{d}}{\mathrm{d}\omega}\left[\arctan\frac{\sin(\omega\cdot\tau)}{a-\cos(\omega\cdot\tau)}\right] \\ &= \tau\cdot\left(1-\frac{1}{2-\frac{1-a^2}{a\cos(\omega\cdot\tau)-a^2}}\right) \end{aligned} \tag{5.13}$$

where

$$a = \frac{1}{4\kappa(1-\kappa)} - 1 \tag{5.14}$$

Figure 5.6(a) plots a as a function of κ,where a is zero for ideal 3-dB coupler and increases to infinity as κ goes to 0 or 1. The ripple in the delay response of the delay line depends on the value of a, where the maximum delay is $\frac{1}{1-a}$ and the minimum delay is $\frac{1}{1+a}$. Figure 5.6(b) shows the normalized delay response of the SDL versus wrapped optical phase shift

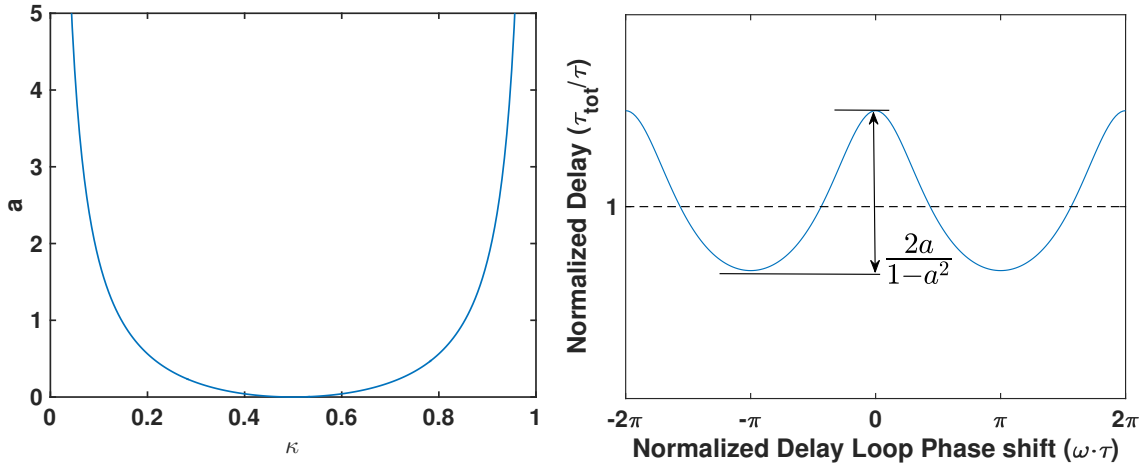

(a) (b)

Figure 5.6: (a) Plot of a in (5.14). (b) The normalized delay response of the SDL versus wrapped phase shift of the optical signal due to the delay loop with $a = 0.2$, which shows the delay ripple in the delay response.

of the delay line, which depicts that the delay response oscillates with the amplitude of $\frac{2a}{1-a^2}$. Based on the analysis above, it can be concluded that only the cross-cross mode of a 1-stage SDL will distort the delay response from a ideally flatted delay spectrum, but the cross-bar mode gives a distortion free response.

5.1.3 Modified Ripple-Free Switched Delay Line

As explained above, from system point of view, the delay ripple appears when more than 2 MZI switches are in cross-state in a SDL with non-ideal switches. Therefore, in order to achieve a SDL with flat delay and power response, the number of MZI switches in cross-state should be limited to 1. To meet this requirement, a modified ripple-free SDL architecture is proposed and the schematic diagram is depicted in the bottom of Fig. 5.7. Instead of using doubled delay paths in every next stage and having the optical signal bounced up and down in each stage, the same delays are employed in all the stages and having only one MZI switch in cross-state and all the other switches are in bar-state.

In this case, the optical signal is injected from lower of the first switch and output from upper port of the last switch, as illustrated in Fig. 5.7. The position of the switch in cross-state determines the delay of the SDL, which can be intuitively given by

$$\tau_{tot} = (s-1)\cdot\tau \tag{5.15}$$

where s is the position number of the switch that in cross-state. Similar transfer matrix analysis is carried out to verify the ripple-free delay response, which can be given as

$$\begin{aligned}
T_{SDL} &= (T_{MZ,bar}\cdot T_{delay})^{s-1}\cdot T_{MZ,cross}\cdot T_{delay}\cdot(T_{MZ,bar}\cdot T_{delay})^{n-s}\cdot T_{MZ,bar} \\
&= \left(\begin{bmatrix} -1 & 0 \\ 0 & 1 \end{bmatrix}\cdot\begin{bmatrix} \mathrm{e}^{-j\omega\cdot\tau} & 0 \\ 0 & 1 \end{bmatrix}\right)^{s-1}\begin{bmatrix} 1-2\kappa & -j2\sqrt{\kappa(1-\kappa)} \\ -j2\sqrt{\kappa(1-\kappa)} & 1-2\kappa \end{bmatrix} \\
&\quad\cdot\begin{bmatrix} \mathrm{e}^{-j\omega\cdot\tau} & 0 \\ 0 & 1 \end{bmatrix}\cdot\left(\begin{bmatrix} -1 & 0 \\ 0 & 1 \end{bmatrix}\cdot\begin{bmatrix} \mathrm{e}^{-j\omega\cdot\tau} & 0 \\ 0 & 1 \end{bmatrix}\right)^{n-s}\cdot\begin{bmatrix} -1 & 0 \\ 0 & 1 \end{bmatrix} \\
&= \begin{bmatrix} (-1)^{s-1}\mathrm{e}^{-j\omega\cdot[(s-1)\tau]} & 0 \\ 0 & 1 \end{bmatrix}\cdot\begin{bmatrix} (1-2\kappa)\mathrm{e}^{-j\omega\cdot\tau} & -j2\sqrt{\kappa(1-\kappa)} \\ -j2\sqrt{\kappa(1-\kappa)}\mathrm{e}^{-j\omega\cdot\tau} & 1-2\kappa \end{bmatrix} \\
&\quad\cdot\begin{bmatrix} (-1)^{n-s+1}\mathrm{e}^{-j\omega\cdot[(n-s)\tau]} & 0 \\ 0 & 1 \end{bmatrix} \\
&= \begin{bmatrix} (-1)^{n}(1-2\kappa)\mathrm{e}^{-j\omega\cdot n\tau} & (-1)^{s}j2\sqrt{\kappa(1-\kappa)}\mathrm{e}^{-j\omega\cdot(s-1)\tau} \\ (-1)^{n-s}j2\sqrt{\kappa(1-\kappa)}\mathrm{e}^{-j\omega\cdot(n-s+1)\tau} & 1-2\kappa \end{bmatrix}
\end{aligned} \tag{5.16}$$

where n is the number of stages and s is the position number of the MZI switch in cross-state provided the delay in the lower paths in Fig. 5.7 is "0". $T_{SDL,12}$ of (5.16) represents the optical signal input from the lower port and output from the upper port, which has

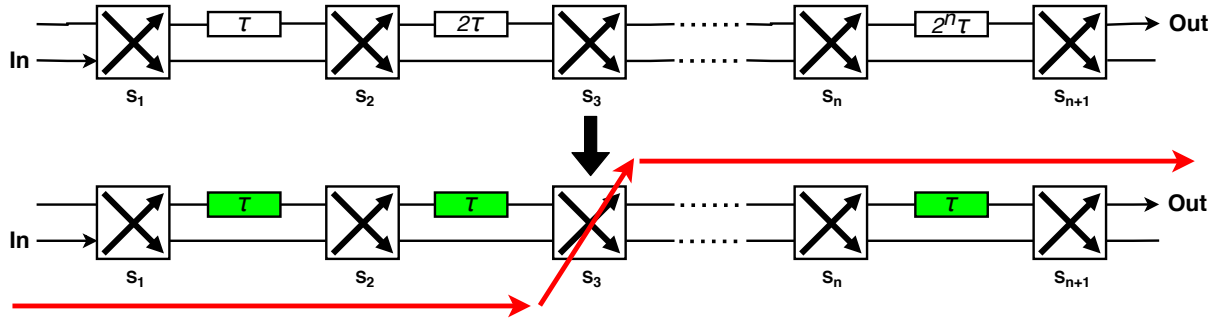

Figure 5.7: Schematic diagram of the ripple-free modified SDL architecture (bottom).

a delay written as

$$\tau_{tot,lower} = (s-1)\tau \tag{5.17}$$

$(s-1)\tau$, which is consistent to the intuitive expression (5.15). $T_{SDL,12}$ represents the optical signal input from the lower port and output from the upper port, which has a delay written as

$$\tau_{tot,upper} = (n-s+1)\tau \tag{5.18}$$

(5.17) and (5.18) shows that the upper input and lower input have complementary delays and ripple free delays that controlled by the position number of the MZI switch in cross-state. Equation (5.16) also shows that both the transmission power and delay response is independent of optical frequency, and the transmission power is independent of the SDL configuration, which can provide a stable output power for all delays (if the loss of the delay loop is neglected). Therefore, as long as no coherent optical signals injected into both inputs at the same time, the SDL could generate a flat and ripple-free response for both power transmission and delay response. Note that (5.16) is derived with the condition $s < n+1$, but it is valid for $s = n+1$ as well.

Comparing to the conventional SDL, as mentioned above, the modified SDL architecture sacrifices the tunable flexibility and reduces the tuning range from $2^n\tau$ to $n\tau$. However, this architecture can provide a much more ideal power transmission and TTD

response given the imperfection of the 3-dB couplers in the MZI switches. For real devices, the actual working environments may vary a lot, which thereby changes the actually coupling coefficient of the 3-dB couplers. The modified SDL architecture is independent of the coupling coefficient deviation of the couplers, and thus has more tolerance to the working environment fluctuations.

5.2 Switched Delay Line based Optical Beamforming Network

A OBFN for TTD mmW beamforming is used to distribute the signals including evenly splitting the signals into multiple paths and provide appropriate delays to each signal path. Based on the ripple-free modified SDL architecture mentioned above, a $1 \times N$ SDL based OBFN could be designed as the schematic diagram depicted in Fig. 5.8 for a linear PAA. First, the optical signal is split into N sub-signals through a $1 \times N$ splitter, and each sub-signal is delayed individually by a SDL. For a linear PAA, the delay increment between the adjacent paths are constant and determines the beam angle of the PAA, as implied by (3.19). Therefore, the delay loop (delay tuning resolution) in each SDL is linear increased, as shown in Fig. 5.8, and the delay of n-th signal path is given by

$$\tau_{n,s} = s(n-1)\tau \tag{5.19}$$

where s is the position of the switch in cross-state. With this architecture, the switches are grouped in columns and each column of the switches need the same control and are switched in cross-state or bar-state simultaneously, and the delay increment of the two adjacent optical signals is given by

$$\tau_s = s\tau \tag{5.20}$$

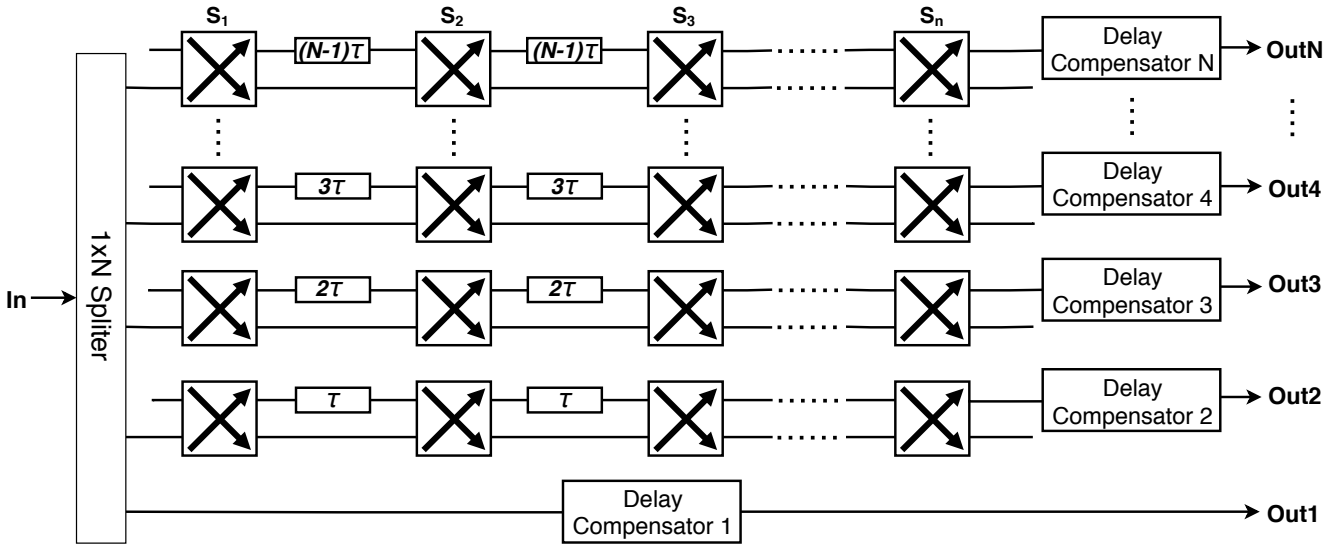

Figure 5.8: Schematic diagram of OBFN architecture with the ripple-free modified SDLs for a linear PAA.

where s is also the position of switch-column in cross-stateand determines the beam angle of the PAA. Benefiting from this arrangement of switches, it can simplify the metal connections in the photonics chip and control circuit design, minimize the footprint, and scale up very easily. Moreover, because of the linear delay configurations of the SDLs in the OBFN architecture, the delay of signal path 1 does not need to be tuned and a fixed delay path can be used as the reference path of a SDL, which further reduces the control complexity of the OBFN. For each SDL, there is an inherent optical path delay in addition to the designed delays due to physical geometry of the MZI switches. Therefore, the "delay compensator 1", which is a fix delay loop, is added in path 1 to compensate the inherent delays of the MZIs. In addition, because the delay increment $\Delta\tau$ of the SDLs can only increase positively, in order to perform both negative and positive angles of beam steering, a delay compensator is added to each optical path to bias the "0" delay increment OBFN configuration to a negative beam angle, and thus, a full-plane beam steering is achieved.

5.3 Chip Design

Based on the analysis above, a 1×4 modified ripple-free SDL based OBFN was designed using ultra-low loss silicon nitride waveguide technology [100]. Figure 5.9 illustrates the layouts of a MZI switch. Two directional couplers are employed as the 2×2 3-dB couplers of the MZI. A 1-mm long chromium heater is put on top of the waveguide to form a thermo-optical phase shifter, which is used to thermally control the MZI switch to cross-state or bar-state.

The layout of the SDL is illustrated in Fig. 5.10(a). The delay loop is sandwiched between the MZI switches, and is designed to have extra delays of τ with respect to the bottom path. Figure 5.10(b) depicts a image of one delay loop of a working SDL captured by an IR camera from the top of the chip. The highlighted curves indicate the scattering of the optical signals propagating in the waveguides. The MZI switches was tuned in an intermediate state between the bar and cross so that the optical signal can be routed into both the upper and lower path. Since the silicon nitride waveguide has very low loss and the scattering is very weak. Therefore, an ultra-sensitive InGaAs IR camera was used to capture this image.

The 1×4 SDL based OBFN is realized on a chip with a footprint of 8 $mm \times 32$ mm, as shown in Fig. 5.11, and the OBFN is placed at the bottom of the chip, as indicated in the blue box in Fig. 5.12(b). Figure 5.12(a) describes the schematic of the 1×4 5-stage SDL-OBFN, which includes 6 switch groups. Only one group of switch are in cross-state

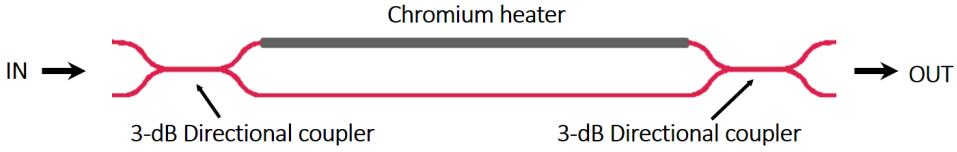

Figure 5.9: Layout of the MZI Switch.

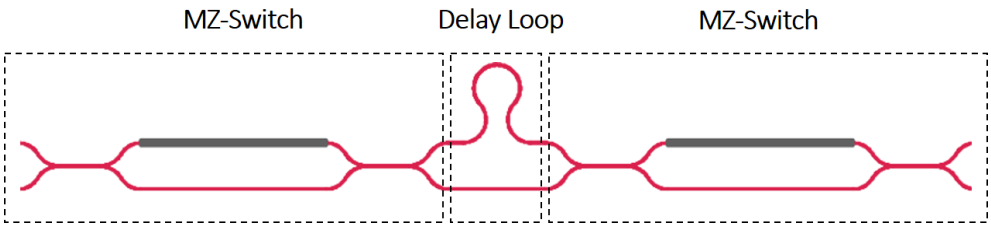

(a)

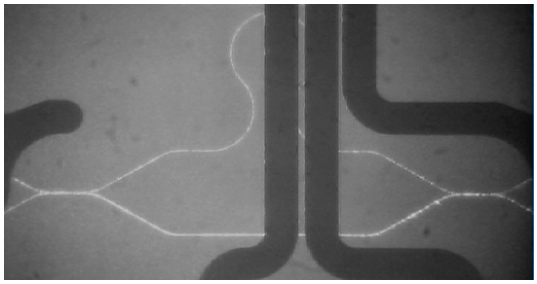

(b)

Figure 5.10: (a) Layout of a 1-stage SDL. (b) IR image of the delay loop in a working SDL. The highlighted curves indicate the optical signals propagating in the waveguides and the dark bold lines are the metal traces.

whereas all other switch groups are in bar-state. The group number of switch group in cross-state determines the OBFN delay configuration. The delay compensator is not realized due to the chip footprint limit. Figure 5.12(b) shows the complete layout of the chip, in which the 1×4 SDL-OBFN is located in the bottom of the chip indicated by the blue box. The optical signal is input from the right of the chip and split into 4 paths using 2 stages of cascaded 3-dB directional couplers. The first path is a fixed delay path and all the four paths are designed to have the same path delays for "0"-delay configuration. The delay loop of each SDL stage is designed to have the integral number of 1.5 ps of delay given the group index of the waveguide $n_g = 1.71$ at 1550 nm. With this design, 0, 1.5, 3, 4.5, 6 and 7.5 ps delay increments can be achieved at the output of the OBFN, which is able to steer beams to -57^o, -34^o, -16^o,0^o, $16^o$and 34^o for a 94-GHz signal with half wavelength pitch antenna arrays, respectively. The delay compensators after the SDLs (shown in Fig. 5.8) are not included in the layout. Instead,

Figure 5.11: The picture of the fabricated silicon nitride chip with metal connections.

external delay compensators will be used after the OBFN chip, which will be explained in detail in Chapter 9. Note that since this OBFN is designed for TTD beamsteering, all the path lengths of the sub-signals are precisely matched on the chip. This is one of biggest benefits of using integrated photonics for TTD based OBFNs. The chip also includes a 1×4 optical ring resonator based OBFN, which will be discussed in Chapter 6.

5.4 Summary

A modified ripple-free SDL based OBFN are discussed in this chapter. A SDL can naturally provide extremely large TTD bandwidth, but only support discrete delays. The MZI switches and the corresponding SDLs were theoretically analyzed using transfer matrices. The analysis reveals that due to the imperfection of the 3-dB couplers in the MZI. it can perfectly pass the optical signal in bar-state whereas in cross-state, the optical signal cannot be completely routed to cross-port, which could lead to ripples in the delay response of a SDL. The transfer matrix analysis also exhibits that to achieve a ripple-free delay response, only one MZI is allowed in a SDL. Based on these conclusions, a ripple-free SDL OBFN architecture is proposed, and a 5-stage 1×4 SDL-OBFN is designed and realized using the ultra-low loss SiN waveguide technology.

Figure 5.12: (a) Schematic of the 1×4 5-stage SDL based OBFN, and (b) the layout of the chip. The 1×4 SDL-OBFN is enclosed in the blue box.

Chapter 6

Optical Ring Resonator based Optical Beamforming Network

ORRs are promising as optical TTD devices for OBFNs in addition to SDLs discussed in Chapter 5. Instead of switching optical signal between physical paths, an ORR delays signal by generating a dispersive phase response. The equivalent path of the ORR delay can be much larger than the physical loop lengths of the ORR. Therefore, an ORR based delay line, and the realized OBFN, can be made very compact. Moreover, the delay response of an ORR is determined by the resonance frequency and coupling coefficient. Since the two parameters can be continuously tuned by optical phase shifters, continuous tuning of delays could be achieved for ORR based delay lines. However, due to the periodic response of resonators, a ORR has a limited delay-bandwidth product. The product can be extended by cascading multiple ORRs, which is the so-called SCISSOR (Side-coupled Integrated Spaced Sequence of Resonators) structure, but the resonance frequencies and coupling coefficients of all ORRs need to be optimized. In this chapter, the responses of a single ORR and multiple cascaded ORRs will be mathematically explained, and the ORR based OBFN architecture will be discussed. The optimization of the ORR parameters for ORR delays and OBFN using genetic algorithm will be presented. Last, the chip design and layout of an integrated 1×4 OBFN using silicon

nitride photonic technology will be illustrated.

6.1 Single Optical Ring Resonator Response

6.1.1 Transfer Function

An optical ring resonator (ORR) comprises of a optical feedback loop and a waveguide coupled to the loop as the optical input and output. Figure 6.1 depicts the schematic of a single waveguide coupled ORR where κ is the power coupling coefficient between the single waveguide and loop, and L_r is round-trip length of the loop. To study the characterization, the ring structure can be modeled as described in Fig. 6.2, where the coupler waveguide-loop coupler is modeled as a 2×2 DC and the feedback loop is modeled as an attenuator and a phase shifter of the optical signal [140]. Assuming that the coupling of the DC is lossless, single unidirectional mode with single polarization is excited, and no mode and polarization conversion existed in the waveguide. Given the transfer matrix of the coupler shown in (5.2), the relation between optical signal amplitudes can be described as

$$\begin{bmatrix} E_{o1} \\ E_{o2} \end{bmatrix} = \begin{bmatrix} \sqrt{1-\kappa} & -j\sqrt{\kappa} \\ -j\sqrt{\kappa} & \sqrt{1-\kappa} \end{bmatrix} \cdot \begin{bmatrix} E_{i1} \\ E_{i2} \end{bmatrix} \tag{6.1}$$

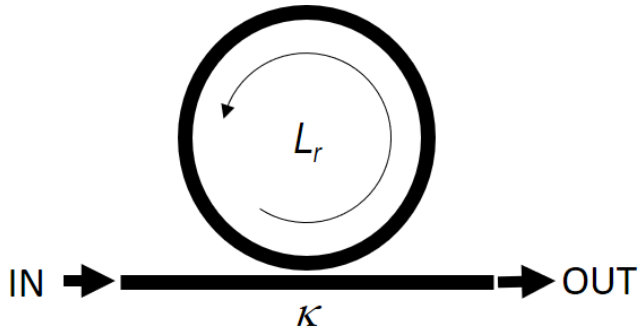

Figure 6.1: Schematic diagram of a ring structure.

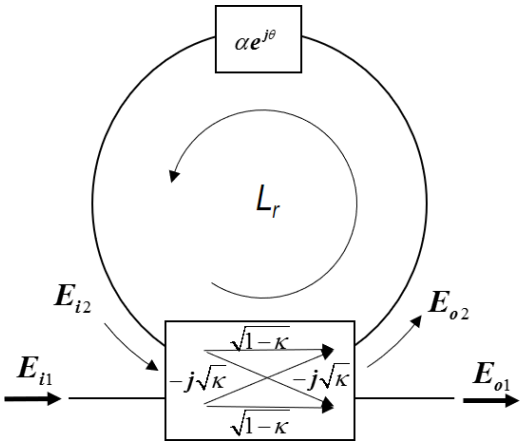

Figure 6.2: Model of a single waveguide coupled ORR.

$$E_{i2} = \alpha \cdot \mathrm{e}^{j\theta} E_{o2} \tag{6.2}$$

where α is the round trip amplitude gain ($\alpha > 1$) or loss ($\alpha < 1$) of the feedback loop, $\theta = \beta \cdot L_r + \phi$ is the round trip optical phase shift, $\beta = 2\pi/\lambda \cdot n_{eff} = \omega/c$ is the propagation constant of the optical signal in the loop waveguide, λ is the wavelength, n_{eff} is the effective index of the loop waveguide, ω is the angular frequency of the optical signal, c is the speed of light in the loop waveguide, L_r and ϕ is the circumference and additional phase shift of the loop. Plugging (6.2) into (6.1) and normalizing to E_{i1}, the amplitude of outputs can be solved as

$$E_{o1} = \frac{-\alpha + \sqrt{1-\kappa} \cdot \mathrm{e}^{-j\theta}}{-\alpha\sqrt{1-\kappa} + \mathrm{e}^{-j\theta}} \tag{6.3}$$

$$E_{o2} = \frac{-j\sqrt{\kappa}}{1 - \alpha\sqrt{1-\kappa} \cdot \mathrm{e}^{j\theta}} \tag{6.4}$$

$$E_{i2} = \frac{-j\sqrt{\kappa} \cdot \alpha}{-\alpha\sqrt{1-\kappa} + \mathrm{e}^{-j\theta}} \tag{6.5}$$

where (6.3) is the transfer function for single waveguides coupled rings.

6.1.2 Free Spectrum Range

(6.3) implies that an ORR has an periodic response due to the periodic factor $e^{\pm j\theta}$, in which the response is repeated for every increment of 2π in θ. Hence, θ can be rewritten as

$$\theta_m = 2m \cdot \pi + \varphi$$

where m is an non-negative integer and is the order of the resonance, φ is the wrapped phase of θ. Then we have

$$\theta_{m+1} - \theta_m = 2\pi = \frac{2\pi}{\lambda_{m+1}} \cdot n_{eff}(\lambda_{m+1}) \cdot L_r - \frac{2\pi}{\lambda_m} \cdot n_{eff}(\lambda_m) \cdot L_r \tag{6.6}$$

In optical domain, since the round trip length L_r is usually much larger than wavelength λ, thereby m is very large and λ_{m+1} is very close to λ_m. Therefore, (6.6) can be rewritten as

$$\begin{aligned} 2\pi &= 2\pi \cdot L_r \cdot \frac{\partial}{\partial\lambda}\left(\frac{n_{eff}}{\lambda}\right) \cdot \Delta\lambda_{FSR} \\ &= 2\pi \cdot L_r \cdot \left[n_{eff}\frac{\partial}{\partial\lambda}\left(\frac{1}{\lambda}\right) + \frac{1}{\lambda}\frac{\partial n_{eff}}{\partial\lambda}\right] \cdot \Delta\lambda_{FSR} \\ &= -\frac{2\pi \cdot L_r}{\lambda^2} \cdot \left[n_{eff} - \lambda\frac{\partial n_{eff}}{\partial\lambda}\right] \cdot \Delta\lambda_{FSR} \end{aligned}$$

i.e.

$$\Delta\lambda_{FSR} = -\frac{\lambda^2}{n_g \cdot L_r} \tag{6.7}$$

where

$$n_g = n_{eff} - \lambda\frac{\partial n_{eff}}{\partial\lambda} = n_{eff} + \omega\frac{\partial n_{eff}}{\partial\omega} \tag{6.8}$$

where $\Delta\lambda_{FSR}$ is the period of the ORR response in frequency domain, which is termed as the Free Spectrum Range (FSR), and n_g is the group index of the loop waveguide.

Based on (6.7), the FSR in terms of frequency is given by

$$\Delta f_{FSR} = \frac{c}{n_g \cdot L_r} \tag{6.9}$$

6.1.3 Power Transmission and Critical Coupling

(6.3) can lead to the transmission power P_{o1} in the output waveguide given by

$$P_{o1} = |E_{o1}|^2 = \frac{\alpha^2 + 1 - \kappa - 2\alpha\sqrt{1-\kappa}\cos(\theta)}{1 + \alpha^2(1-\kappa) - 2\alpha\sqrt{1-\kappa}\cos(\theta)} \tag{6.10}$$

which implies that the transmission power also responds periodically. Note that for loss-less waveguide where $\alpha = 1$, the transmission power is constantly equal to 1. The ORR has a response of an all-pass filter where all the optical power will pass the ORR regardless the frequency of the optical signal, only inducing non-uniform phase response.

At resonance conditions where the optical path length of the feedback loop is integral number of wavelength, i.e. $\theta = m \cdot 2\pi$, and optical signal is constructively interfered, the transmission power at resonance is obtained

$$P_{o1,res} = \frac{\left(\alpha - \sqrt{1-\kappa}\right)^2}{\left(1 - \alpha\sqrt{1-\kappa}\right)^2} \tag{6.11}$$

The output power is less that one due to the loss of the loop waveguide. It can be noticed that at the condition $\alpha = \sqrt{1-\kappa}$, the output power of the ORR reaches zero, which is the so called critical coupling. This is because the optical signal in the output waveguide comprises light coupled from the ring loop and that from the input waveguide. At resonance condition, the two parts of light has opposite phase. With critical coupling, the two parts of light has the same amplitude, thereby the output light is eliminated due to destructively interference. Figure 6.3 shows the transmission power at resonance as

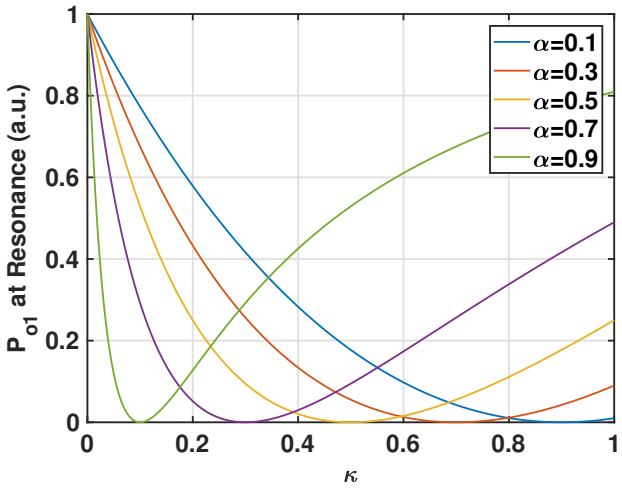

Figure 6.3: Transmission power of a single waveguide coupled ORR at resonance for different round trip loop loss α.

a function of κ for varied round trip loop loss. For under coupled condition ($\kappa < \kappa_c$) where the optical signal from the input is larger than the coupled optical signal, the light from input dominates the output and the transmission power decrease from 1 to 0 as κ increase from 0 to critical coupling. Whereas for over coupled condition ($\kappa > \kappa_c$) where the coupled optical signal is larger than the optical signal from the input, the coupled light dominates the output and the transmission power increase from 0 to α^2 as κ increase from critical coupling to 1. At $\kappa = 0$, all the light will pass the ring loop and be transferred to the output directly, and the transmission power is 1, whereas at $\kappa = 1$, all the light will be coupled to the ring and coupled back to output waveguide after one round trip, and the loss is the round trip loss, i.e., α^2.

6.1.4 Group Delay

6.1.4.1 Group Delay Response

The group delay of a signal is defined as the negative first derivative of phase response with respect to the signal angular frequency ω, which, taking an ORR for an example,

can be given by

$$\tau = -\frac{\mathrm{d}\angle E_{o1}}{\mathrm{d}\omega} = -\frac{\mathrm{d}\angle E_{o1}}{\mathrm{d}\theta} \cdot \frac{\mathrm{d}\theta}{\mathrm{d}\omega} \tag{6.12}$$

where $\theta = \beta L_r + \phi = L_r \cdot n_{eff} \cdot \omega / c_0 + \phi$. To simplify the equation, we have

$$\begin{aligned} \frac{\mathrm{d}\theta}{\mathrm{d}\omega} &= \frac{\mathrm{d}}{\mathrm{d}\omega}\left(L_r \cdot n_{eff} \cdot \frac{\omega}{c_0} + \phi\right) \\ &= \frac{L_r}{c_0}\left(n_{eff} + \omega \frac{\partial n_{eff}}{\partial \omega}\right) \\ &= \frac{n_g L_r}{c_0} = \tau_r \end{aligned} \tag{6.13}$$

where $\tau_r = 1/\Delta f_{FSR}$ is the round trip delay of the feedback loop. Plugging into 6.12, the normalized group delay can be obtained by

$$\tau_0 = \frac{\tau}{\tau_r} = -\frac{\mathrm{d}\angle E_{o1}}{\mathrm{d}\theta} \tag{6.14}$$

Since the group index changes very slow compared to the FSR of the ORR, we can rewrite θ as

$$\begin{aligned} \theta &= \frac{\mathrm{d}\theta}{\mathrm{d}\omega} \cdot 2\pi \cdot \Delta f + \beta L_r + \phi \\ &= 2\pi \cdot \left.\frac{\Delta f}{\Delta f_{FSR}}\right|_{\omega=\omega_0} + \beta L_r|_{\omega=\omega_0} + \phi \\ &= 2\pi \cdot \left.\frac{\Delta f}{\Delta f_{FSR}}\right|_{\omega=\omega_0} + m \cdot 2\pi + \phi \end{aligned} \tag{6.15}$$

where ω_0 is the closest resonant angular frequency near ω when $\phi = 0$, and $\Delta f = (\omega - \omega_0)/2\pi$ is the frequency offset from the resonance frequency $\omega_0/2\pi$. Substituting with (6.15), the phase response of the ORR output E_{o1} can be given by

$$\angle E_{o1} = \arctan\left[\frac{\sin(\Omega)}{\alpha\sqrt{1-\kappa} - \cos(\Omega)}\right] - \arctan\left[\frac{\sqrt{1-\kappa} \cdot \sin(\Omega)}{\alpha - \sqrt{1-\kappa} \cdot \cos(\Omega)}\right] \tag{6.16}$$

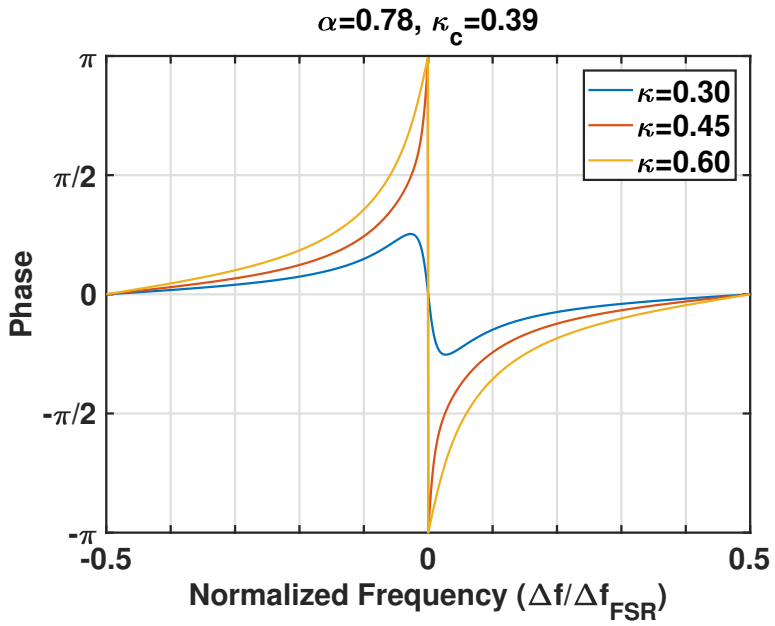

(a)

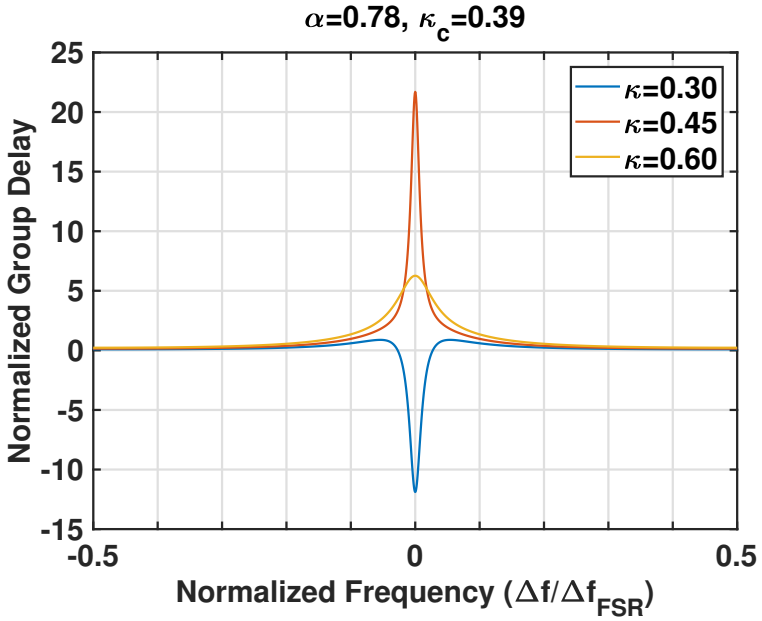

(b)

Figure 6.4: (a) The phase response and (b) corresponding delay of an ORR for various coupling with $\alpha = 0.78$.

and then the corresponding normalized group delay of the ORR can be obtained by plugging (6.16) into (6.12), i.e.

$$\tau_0 = \frac{\alpha\sqrt{1-\kappa}\cos(\Omega) - (1-\kappa)}{1-\kappa+\alpha^2-2\alpha\sqrt{1-\kappa}\cos(\Omega)} - \frac{\alpha\sqrt{1-\kappa}\cos(\Omega) - 1}{1+\alpha^2(1-\kappa)-2\alpha\sqrt{1-\kappa}\cos(\Omega)} \tag{6.17}$$

$$\Omega(\Delta f, \phi) = 2\pi \cdot \frac{\Delta f}{\Delta f_{FSR}} + \phi \tag{6.18}$$

where ϕ describes additional phase shifts that affects the ORR resonance such as the waveguide phase error and the thermal-induced phase shift.

Figure 6.4 describes the phase and delay responses of a single waveguide coupled ORR for varied coupling coefficient with loop attenuation coefficient $\alpha = 0.78$. As mentioned above, under the under-coupled condition, the input signal dominates the output response and the light coupled from the ring loop only slightly disturbs the phase of the input light, and thus, the phase response is confined around zero. Therefore, the group delay of the ORR, where the integral over one FSR is the phase transition of the input, which is zero, will have negative group delay response at the resonance, as described by the blue curves in Fig. 6.4(a) and (b). Oppositely, under the over-coupled condition, the output response is dominated by the light coupled from the loop waveguide, which has a phase response linearly increases with the optical frequency due to the loop delay. Therefore, the phase response of the output is unconfined and only have positive group delays, as depicted by the orange and yellow curves in Fig. 6.4. Figure 6.5 shows the normalized group delays at resonance against κ for various loop round trip attenuation coefficients, in which the solid curves refer to the delays whereas the dash lines refer to the critical coupling. It can be noticed that as the coupling increases, the resonant delays decreases from 0 to negative infinity in under-coupled region, and from positive infinity to 1 in over-coupled region. To achieve the same delay, a higher κ is required for a higher waveguide

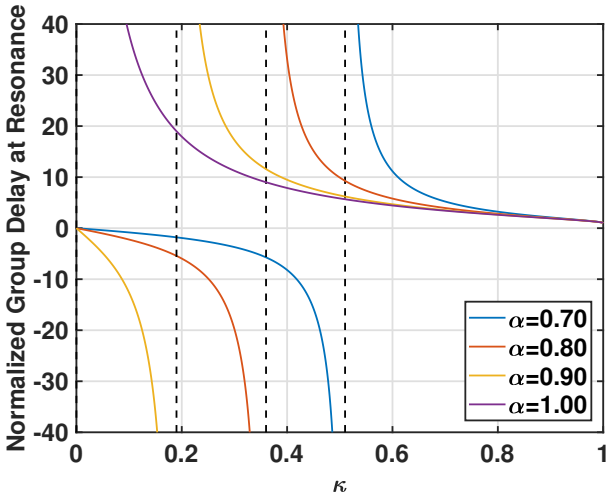

Figure 6.5: Normalized group delays at resonance against κ for various loop round trip attenuation coefficients. The solid curves refer to the delays whereas the dash lines refer to the critical coupling.

loss. As for loss-less waveguides, the critical coupling is zero and the ORR only works in over-coupled condition.

For a mmW beamforming system, the RF signal power is proportional to the square of the input light intensity and is more sensitive to the optical loss. Currently, very low loss waveguides in integrated photonics can be achieved, which will lead to a low critical coupling. For example, the loss of the silicon nitride waveguide can be achieved as low as 0.2 dB/cm and the corresponding critical coupling is 0.05. Therefore, the over-coupled ORR delay response is mostly used [133, 85, 100]. In this case, a simplified loss-less model of an ORR delay response can obtained by assuming $\alpha = 1$ in (6.17) as

$$\tau_0(\Delta f, \phi) = \frac{\kappa}{2 - \kappa - 2\sqrt{1-\kappa}\cos(\Omega)} \tag{6.19}$$

This thesis will focus on the study of TTD delays based on integrated ultra-low loss waveguide technology. Therefore, delay responses of over-coupled ORRs will be explored using the loss-less ORR delay response model described in (6.19).

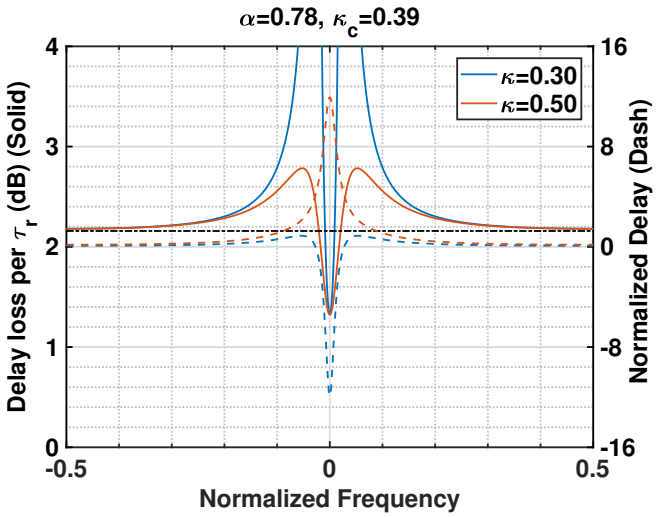

Figure 6.6: The delay loss per round trip delay τ_r of under-coupled and over-coupled single-ORRs over one FSR. (The solid curves refer to the relative loss, the blue and orange dash curves refer to the normalized delays. The black dash line refers to round trip loss, which is also the equivalent physical straight waveguide delay line.)

6.1.4.2 Delay Loss

The loss of a delay device is characterized by the loss per unit delay. The loss of an ORR is studied by comparing the loss of the ORR and the loss of a physical straight waveguide path with the same delay and waveguide loss coefficient, based on the result of single ORR power transmission response and delay response in (6.10) and (6.17), respectively. Figure 6.6 shows the delay loss per round trip delay τ_r of an single-ORR (solid curves) comparing to round trip loss α (black dash lines), which is also the equivalent physical straight waveguide delay line for under-coupled and over-coupled conditions over one FSR. Unlike physical path delays, the relation of loss and delay of an ORR is not linear. Under both under-coupled and over-coupled conditions, the delay around the resonance frequency has lower loss than physical delay paths, whereas around anti-resonance frequencies, the delay-loss ratio is almost the same as physical delay paths. Beyond this region, the delays have larger loss than physical delay paths .

Figure 6.7 illustrates the delay loss per round trip delay τ_r at resonance frequency for

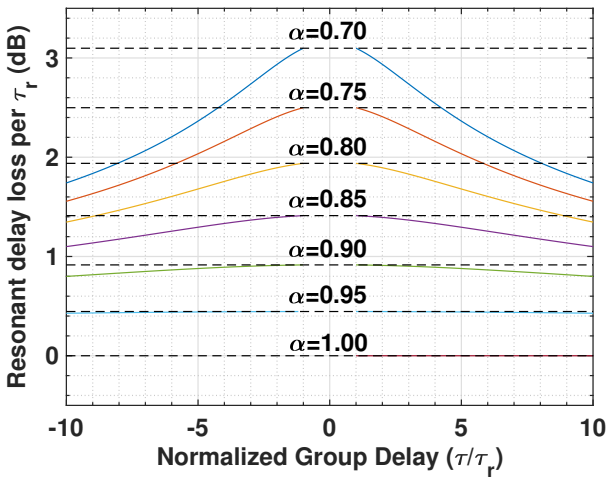

Figure 6.7: The delay loss per round trip delay τ_r at resonance frequency for various round-trip attenuations. (The black dash lines refer to to round trip loss, which is also the equivalent physical straight waveguide delay line.)

various round-trip attenuations. All the resonant delay loss is less than the equivalent physical waveguide delay lines. Either the larger loss of the waveguide or the higher delays would lead to a more efficient delay-loss ratio. Moreover, as noticed, for round-trip attenuation $\alpha < 0.9$ ($\alpha < 1\ dB$) within 5 times the round-trip delay, or $\alpha < 0.95$ ($\alpha < 0.5\ dB$) within 10 times the round-trip delay, the loss per unit delay is very close to flat, which means in these regions, the delay-loss relation can be treated as physical waveguide delay lines.

6.1.4.3 Delay-Bandwidth Tradeoff

The loss-less ORR delay response model described in (6.19) will be used to illustrate the delay-bandwidth trade-off. A loss-less single ORR only works in over-coupled mode, which exhibits a bell-shaped group delay spectrum, with the peak centered at the resonance frequency and minima at the anti-resonant frequencies, as depicted in Fig. 6.4(b) and inset of Fig. 6.8. Figure 6.8 also describes the group delay and bandwidth as a function of coupling coefficient for over-coupled single ORR. Here, the bandwidth is defined

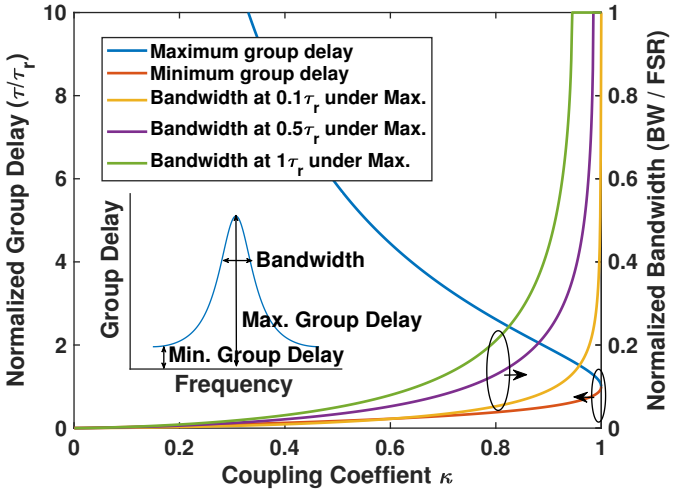

Figure 6.8: Group delay and bandwidth as a function of coupling coefficient for over--coupled single ORR with typical delay spectrum inset. The bandwidth is defined at the frequency where delays fall down by 0.1, 0.5 and 1 times of τ_r (one round-trip ORR delay).

as the frequency range where delays fall down by 0.1, 0.5 and 1 times of τ_r , respectively. As shown by the blue and orange curves in Fig. 6.8, with increasing κ, the maximum group delay at resonance frequency decreases rapidly whereas the minimum group delay at anti-resonance frequency increases gradually. The group delay spectrum therefore flattens with increasing κ and the bandwidth increases, depicted by the green, purple and yellow curves, respectively. When κ becomes equal to 1, all the light will be coupled to the ring and coupled back to output waveguide after one round trip, thereby the bandwidth becomes infinity and the delay response becomes a flat line that equals to the round trip delay of the ring. Therefore, a trade-off between resonant delays and bandwidth is exhibited, as depicted in Fig. 6.8. This can be explained as that the integral group delay of the ORR over a FSR is the phase transition, which is a constant, i.e., 2π. This is an inherent delay-bandwidth trade-off for ORR delays. Since this thesis focus on communication applications, which requires a large bandwidth, the delay should be low for a single ORR due to this delay-bandwidth trade-off, which leads to a high κ. Multiple

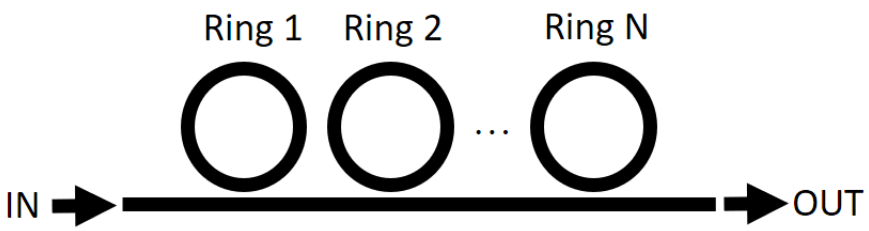

Figure 6.9: Schematic diagram of a SCISSOR based delay line.

ORRs can be used to break the single ORR delay-bandwidth limit to achieve both large delays and wide bandwidth, which will be discussed in Section 6.2.

6.2 Side-coupled Integrated Spaced Sequence of Resonators based Delay Line

6.2.1 SCISSOR Structure

Sufficient bandwidth and delays are both desired for wide bandwidth communications for large-scale PAAs. However, as mentioned above, a higher peak delay at resonance will have a sharper delay response. The bandwidth and delays are constrained by the constant bandwidth-delay product of a single ORR. One approach that can break this constrain is using SCISSOR structure [141, 84], as illustrated in Fig. 6.9. A SCISSOR based delay line comprises of multiple identical rings cascaded in series in a straight waveguide. Each ring can change the coupling coefficient κ and phase shift ϕ individually. Based on the transfer function of a single ORR (6.3), the transfer function of a N-stage SCIRROR delay line can be described by

$$H(\Omega) = \prod_{i=1}^{N} E_{o1,i} = \prod_{i=1}^{N} |E_{o1,i}| \, \mathrm{e}^{j\Psi_i} \tag{6.20}$$

which leads to the amplitude, power transmission, phase and group delay of the N-stage SCISSOR delay line given by

$$|H(\Omega)| = \prod_{i=1}^{N} |E_{o1,i}(\Omega)| \tag{6.21}$$

$$|H(\Omega)|^2 = \prod_{i=1}^{N} P_{o1,i}(\Omega) \tag{6.22}$$

$$\Psi(\Omega) = \sum_{i=1}^{N} \Psi_i(\Omega) \tag{6.23}$$

$$\tau(\Omega) = \sum_{i=1}^{N} \tau_i(\Omega) \tag{6.24}$$

where Ω is defined in (6.18). (6.23) implies that the total phase transition of a SCISSOR delay line over one FSR is linearly increasing with the number of ORRs cascaded in the delay line. The increased phase transition breaks the inherent delay-bandwidth trade-off in a single-waveguide coupled ORR, which makes it possible to achieve large bandwidth and delay simultaneously.

6.2.2 Delay Optimization and Bandwidth Trade-off

The group delay response of a SCISSOR delay line is the sum of each ring's delay response, as described by (6.24). Despite that a SCISSOR delay line extends the inherent delay-bandwidth trade-off of a single ORR, the coupling coefficient (κ) and resonance frequency (tuned by ϕ) of each ORR should be properly tuned to achieve a flattened TTD response with wide bandwidth and larger dynamic tuning range. Figure 6.10 illustrates an optimized 3-stage SCISSOR delay line response where the 3-ORR yields a larger delay and a much wider TTD bandwidth than a single ORR. As it can be noticed, the flattened group delay response, however, may still yield delay ripple, or deviation from the desired delay across frequency. This ripple may lead to a beam squint for different signal

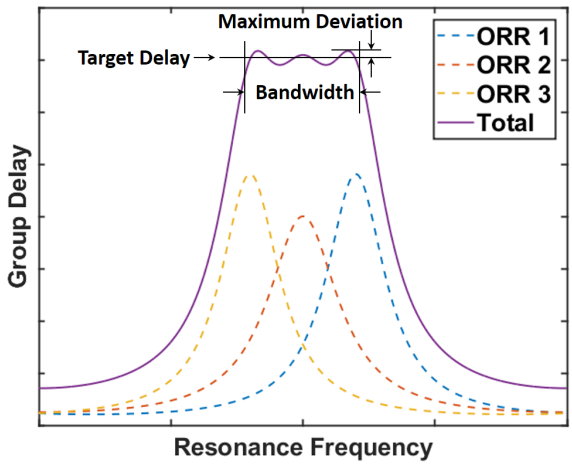

Figure 6.10: Optimized group delay response for a 3-ORR delay line. The dashed curves denote the group delay responses of each individual ring, whereas the solid curve denotes the total group delay response.

frequency components and distort the output microwave signal, which possibly results in a system operation failure. The ripple can be improved by cascading more rings, but this would increase the complexity of both the photonic subsystem and the controls. Ultimately, for ORR-based time delays, inherent tradeoffs exist between bandwidth, ripple, delay, and complexity (number of rings) [142, 143]. A detailed quantitative understanding of these tradeoffs is extremely valuable for designing wide bandwidth ORR-based OBFNs.

The lossless ORR delay model in (6.19) is utilized to evaluate the inherent tradeoffs of multi-ORR based delays. In this study, we normalized the group delay, delay ripple and bandwidth to round trip delay τ_r and the FSR to make the analysis applicable to generic ORRs. For a N-ORR delay line, N pairs of (κ, ϕ) or $2N$ parameters in total need to be optimized. However, as noticed in Fig. 6.10, the delay responses of the delay line are symmetric with respect to the resonance frequency, which implies the ORRs in the one side shares the same κ and complementary ϕ. Therefore, the degree of freedom of a N-ORR delay line can actually be reduced from $2N$ to N parameters, which simplifies

the optimization.

A standard genetic algorithm can be applied to minimize the delay ripple. The genetic algorithm is a global optimization algorithm for nonlinear problems. It is based on natural selection, which is the driving force of biological evolution. The genetic algorithm repeatedly modifies a population of individual solutions. At each step, the genetic algorithm selects individuals based on selection rules from the current population to be parents, which will be used to produce the children for the next generation. Over successive generations, the population will evolve toward an optimal solution.

The cost function is the selection rule that determines the evolution direction of the population. In our case for the optimization, the cost function, which also defines the normalized ripple, was chosen as the maximum delay deviation from the target value within the desired bandwidth, which is described in Fig. 6.10 and by

$$\mathbf{R}(f) = \max\{\frac{|\tau(\Delta f) - \tau_t|}{\tau_r},\ \Delta f \in desired\ bandwidth\} \tag{6.25}$$

Since a genetic algorithm has the probability of being trapped in a local optimal solution, the algorithm should repeat multiple times to ensure a global optima.

3-Stage SCIRROR Delay Response

Fig. 6.11(a) shows the group delay spectra for varied target group delays for a 3-ORR structure. Three parameters in total are optimized, which includesκ_0 for the coupling of the central ORR, $\kappa_{-1,1}$ and ϕ_{-1} or $-\phi_1$ for the coupling coefficient and resonance frequency of the two side ORRs. The optimization was repeated more than 50 times to get a global optima.

Table 6.1 lists the optimized parameters and the corresponding ripple for various target delays of a 3-ORR delay line. The group delay is reported as the ratio τ/τ_r and

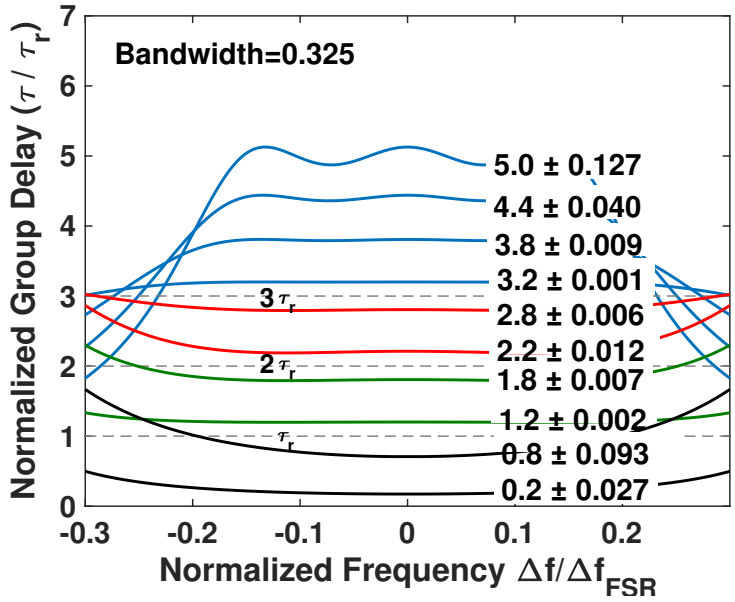

(a)

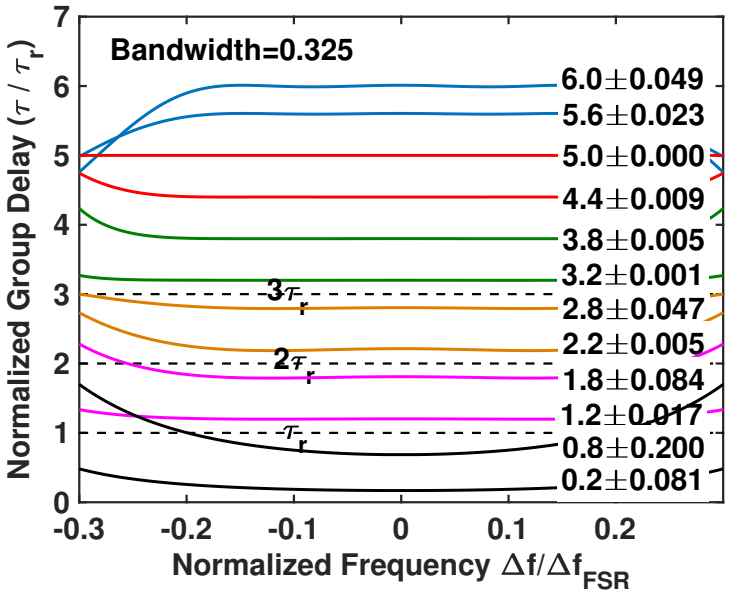

(b)

Figure 6.11: Ripple optimized group delay spectrum of a (a) 3-ORR and (b) 5-ORR delay line and for various target group delays with bandwidth of 0.325.

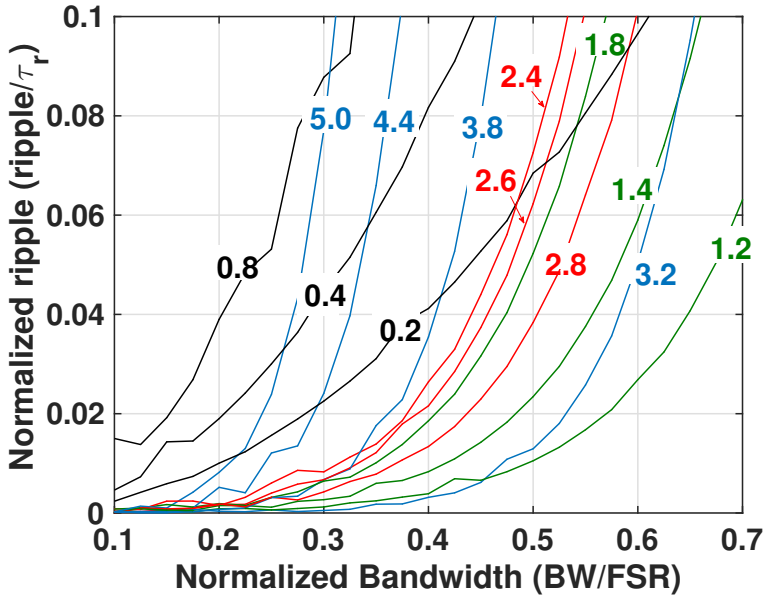

(a)

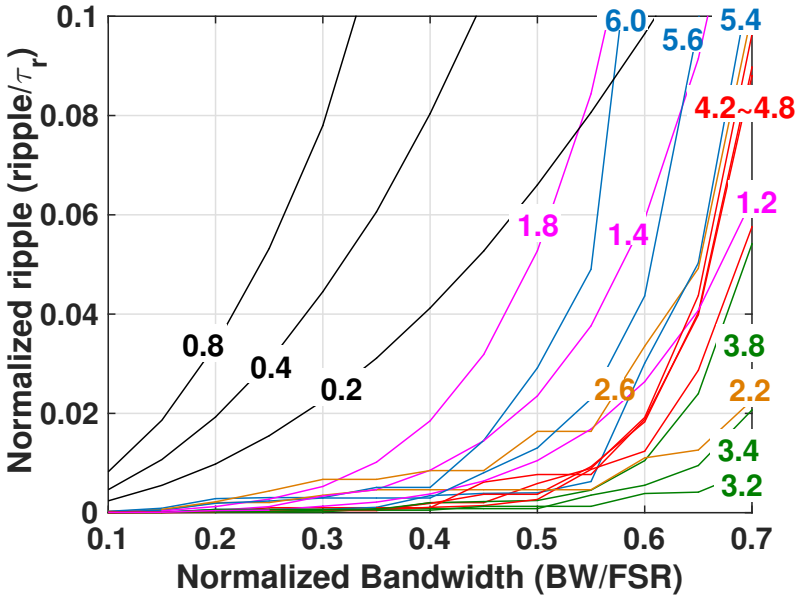

(b)

Figure 6.12: Optimized ripple and bandwidth relation for a (a) 3-ORR delay line and (b) 5-ORR delay line for various target delays.

Table 6.1: Optimized ripple and parameters of a 3-stage SCIRROR delay line with bandwidth of 0.325 for various target delays. The bandwidth and ripple are normalized to the round-trip delay τ_r, and $\phi_0 = 0$.

Target	Ripple	$\kappa_{-1},\ \kappa_1$	$\phi_{-1},\ -\phi_1$	κ_0
5.0	0.12744	0.75457	0.85371	0.82005
4.8	0.088694	0.77732	0.88645	0.8412
4.6	0.060199	0.80219	0.91718	0.86586
4.4	0.039724	0.82088	0.97232	0.8791
4.2	0.025271	0.84369	1.0244	0.89794
4.0	0.015356	0.86487	1.0906	0.91435
3.8	0.0088787	0.88932	1.1627	0.93276
3.6	0.0048053	0.90913	1.2681	0.946
3.4	0.0024043	0.94284	1.3514	0.96978
3.2	0	0.96203	1.5622	0.97883
3.0	0	0.98025	1.9557	0.987
2.8	0.0063329	0.97914	2.6563	0.98613
2.6	0.009075	0.9564	3.1104	0.98372
2.4	0.011253	0.88246	2.5343	0.9776
2.2	0.012029	0.83906	2.7132	0.98153
2.0	0	1	1.8116	0
1.8	0.0072138	0.68992	3.0181	0.98934
1.6	0.0055448	0.571	3.019	0.99305
1.4	0.0033722	0.32397	2.3424	0.99373
1.2	0.002028	0.19251	2.485	0.99851
1.0	0	0	0.92647	1
0.8	0.092554	0.77728	2.6869	0
0.6	0.073853	0.62547	2.3993	0
0.4	0.051499	0.53246	3.0966	0
0.2	0.026563	0.31339	3.1268	0

the ripple for each curve is reported as the maximum deviation from the target delay within a normalized bandwidth ($\Delta f/FSR$) of 0.325. Figure 6.11(a) plots some of the optimized 3-ORR delay responses with target delays ranging from 0 - $5\tau_r$. As shown, for the delay range of $\tau > 3\tau_r$ (blue curves), the group delay response is flattened with the resonant delay response of the three bell-shaped group delay spectrum of the single-ORR delay elements, where the ripple is smaller for smaller target delay (larger κ). In the range $\tau_r < \tau_g < 3\tau_r$ (red and green curves), the group delay response is flattened by the delay curves of two rings at the anti-resonance and the delay at the resonance of the other ring with large κ. The last region, $\tau < \tau_r$ (black curves) utilizes only two rings for flattening the group delay response, hence the normalized ripple value is relatively large for large bandwidths. Figure 6.12(a) shows the corresponding relation between ripple and bandwidth for various target group delays for the 3-ORR structure. The target delays, ripple and bandwidth are normalized to apply to general ORRs. These numbers can be adapted to a specific ring geometry with its round-trip delay.

5-Stage SCIRROR Delay Response

The same technique was applied to 5-ORR delay lines. Similar as the the 3-ORR delay line, Table 6.2 lists the optimized parameters and the corresponding normalized ripple for various target delays of a 5-ORR delay line over the same bandwidth. The optimized delay responses for target delays ranging from 0 - $6\tau_r$ is depicted in Fig. 6.11(b), and the ripple-bandwidth-delay trade-off relations of a 5-ORR delay line are shown in Fig.6.12(b). As expected, adding two more rings improves the ripple, bandwidth or delay tuning range significantly. For example, for a dynamic tuning range of $2\tau_r$ and ripple smaller than 0.01, a 5-ORR delay can achieve a normalized bandwidth up to 0.5, while for 3-ORR delay, the bandwidth is 0.25, which corresponds to bandwidths of 11.5 GHz and 5.75 GHz for ORRs with $FSR = 23$ GHz, respectively. Although increasing the number of rings improves

Table 6.2: Optimized ripple and parameters of a 5-stage SCIRROR delay line with bandwidth of 0.325 for various target delays. The bandwidth and ripple are normalized to the round-trip delay τ_r, and $\phi_0 = 0$.

Target	Ripple	κ_{-2},κ_2	ϕ_{-2},$-\phi_2$	κ_{-1},κ_1	ϕ_{-1},$-\phi_1$	κ_0
6.0	0.049034	0.96024	0.87723	0.85558	1.3474	0.91675
5.8	0.027397	0.8709	1.4078	0.97808	0.41145	0.96255
5.6	0.022935	0.92155	1.5867	0.94461	1.1549	0.92896
5.4	0.0062729	0.96644	0.83976	0.91329	1.7438	0.97081
5.2	0.0094414	0.96897	1.6135	0.98303	1.6019	0.96862
5.0	0	1	0.44688	1	0.061105	1
4.8	0.0087177	0.83149	2.3884	0.93729	1.065	0.95036
4.6	0.0076879	0.93652	1.1829	0.84738	2.9755	0.95065
4.4	0.0089257	0.76099	2.6545	0.95076	1.1341	0.96395
4.2	0.0092833	0.95378	1.229	0.72272	2.9575	0.96491
4.0	0	1	1.0414	1	0.045085	0
3.8	0.00454	0.95791	1.2797	0.44339	2.5592	0.97087
3.6	0.0045933	0.37212	2.8262	0.95632	1.4522	0.96723
3.4	0.0035329	0.3384	3.0454	0.98826	1.4818	0.99146
3.2	0.0012786	0.97848	1.6458	0.098845	2.5584	0.98598
3.0	0	1	2.8366	0	3.0131	1
2.8	0.046503	0.98117	3.1291	0	2.3122	0.98419
2.6	0.016379	0.97471	0.9727	0.43657	2.8888	0
2.4	0.009672	0.967	1.0396	0.18755	2.6696	0
2.2	0.00462	0.0048377	3.1248	0.84154	3.0841	0.97785
2.0	0	1	0.90427	0	0.25562	0
1.8	0.084379	0.0018846	2.5143	0.66834	3.1362	0.98579
1.6	0.061271	0.017377	3.1021	0.53104	2.9286	0.99012
1.4	0.037636	0.3654	3.1048	0.052284	2.9984	0.99506
1.2	0.016842	0.18827	3.0177	0.035232	2.9842	0.99854
1.0	0	0	1.0155	0	1.0239	1
0.8	0.2	0.7526	2.8962	0.0096188	2.9717	0
0.6	0.23225	0.0040416	3.0577	0.64767	3.1306	0
0.4	0.15815	0	2.2463	0.49548	3.1414	0
0.2	0.080629	0	2.8629	0.28642	3.1407	0

the SCIRROR TTD performance, this also increases the system complexity considerably. For a 5-ORR delays, 10 individual parameters need to be precisely controlled, whereas only 6 individual parameter controls are required for a 3-ORR delay. This saves 40% of controls comparing to a 5-ORR delay line, which could be a large difference for OBFNs where multiple delay lines are employed.

6.3 Optical Ring Resonator based Optical Beamforming Network

Although increasing the number of rings improves performance, this also increases the system complexity considerably. Three stage SCIRROR delay lines can provide large bandwidth and high TTDs for mmW communications while maintaining low control complexity. However, as mentioned above, a single 3-ORR delay line requires 6 individual parameter controls, and 24 individual controls are required for a 1×4 OBFN if the 3-ORR delay lines are simply repeated for each OBFN path, as depicted in Fig. 6.13(a). This is still requires complex control circuits, control algorithms and high power consumption. Efforts can be put on OBFN topologies to maintain the TTD performance while simplifying the system complexity by reducing the number of rings.

To limit the total number of rings, binary-tree topologies are employed, which makes one or more rings shared by adjacent paths. Assuming a linear PAA is fed by the OBFN, a N-stage binary tree topology would have 2^N antenna elements. This topology divides the signal distribution process into N stages and each stage splits the signal into two paths and provides the relative delays of $\tau/2^n$ provided n is the stage index number and τ is the relative delays required between the first antenna element and last antenna element of the PAA. τ can be either a positive number or negative number, which indicates

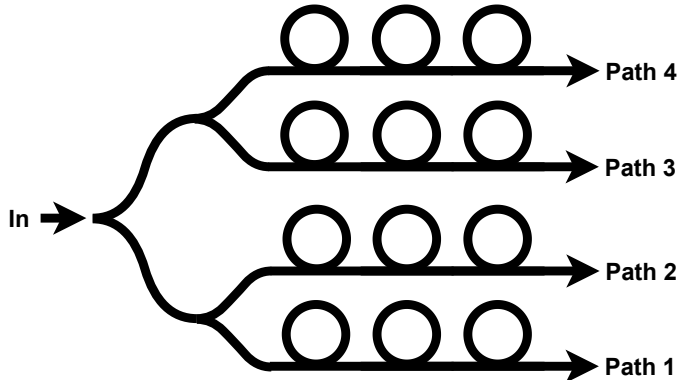

(a)

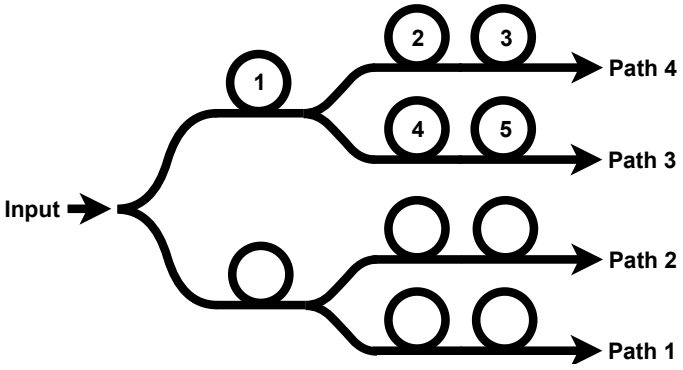

(b)

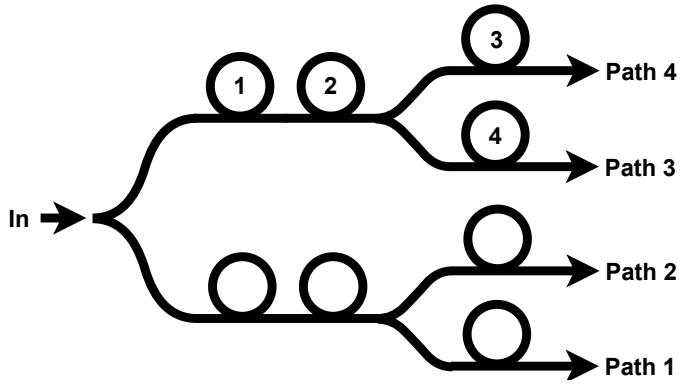

(c)

Figure 6.13: Different topologies for 1 × 4 3-ORR-based OBFNs with (a) no ring shared, (b) 1 ring shared and (c) 2 rings shared.

to positive beam angle and negative beam angle. After each stage, the number of the outputs is doubled, each output of the stage will feed into the next stage and repeat the delay procedure until the number of outputs meet the size of PAA. Figure 6.13 (b) and (c) shows the schematic diagrams for two stage binary tree topologies for a two stage binary tree 1×4 3-ORR based OBFN with one ring and two rings shared in the first stage, respectively.

Using binary tree topology can reduce the number of ORRs in a OBFN. However, sharing of rings impacts the ability to minimize ripple since the delay response of each path has to compromise with its neighbor path to achieve a joint ripple minimization. Intuitively, the more ring shared, the weaker ability of the ORRs in flattening the delay response. Thus, the topology shown in Fig. 6.13(c) has two rings shared in the common stage, which has the minimum number of rings and delay response controls, whereas in the Fig. 6.13(b), the topology increases the number of rings and controls, and can has a more flattened delay response.

The relation between bandwidth, ripple and delay are further studied for the two OBFN topologies using the same TTD optimization techniques mentioned in Section 6.2.2. Two path are simulated in the same time due to the coupling of two adjacent paths. For the topology shown in Fig. 6.13(b), one ring is shared by two adjacent paths in the first stage with 5 parameters that need to be optimized, whereas for the topology shown in Fig. 6.13(c), two rings are shared by two adjacent paths in the first stage and 4 parameters are needed to be optimized. The relations between ripple, bandwidth, and target group delays for a 2-stage binary-tree topology based 3-ORR OBFN with one shared ring and with two shared rings are shown in Fig. 6.14 (a) and (b), respectively. Compared to the topology with no shared rings shown in Fig. 6.13(a), where the ripple, bandwidth and delay relation is the same as that of a 3-ORR delay line shown in Fig. 6.12(a), we can conclude that sharing two rings has the least complexity but likely limits the

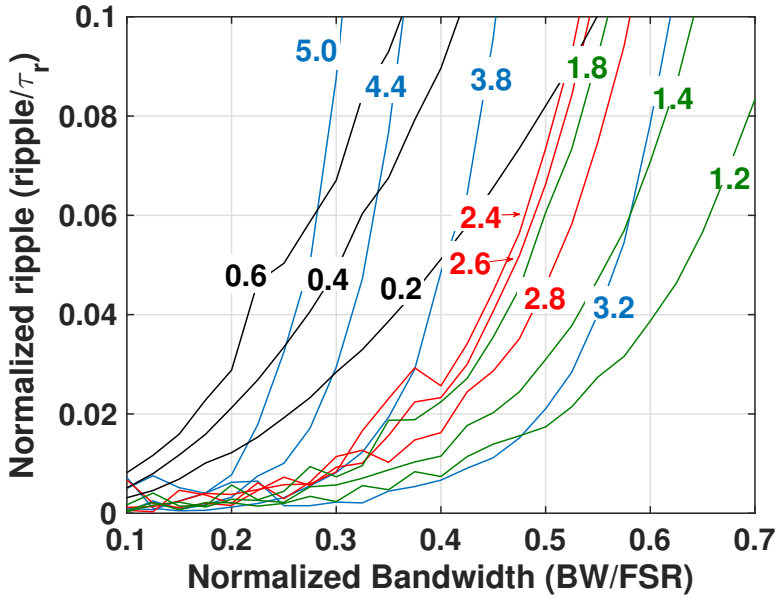

(a)

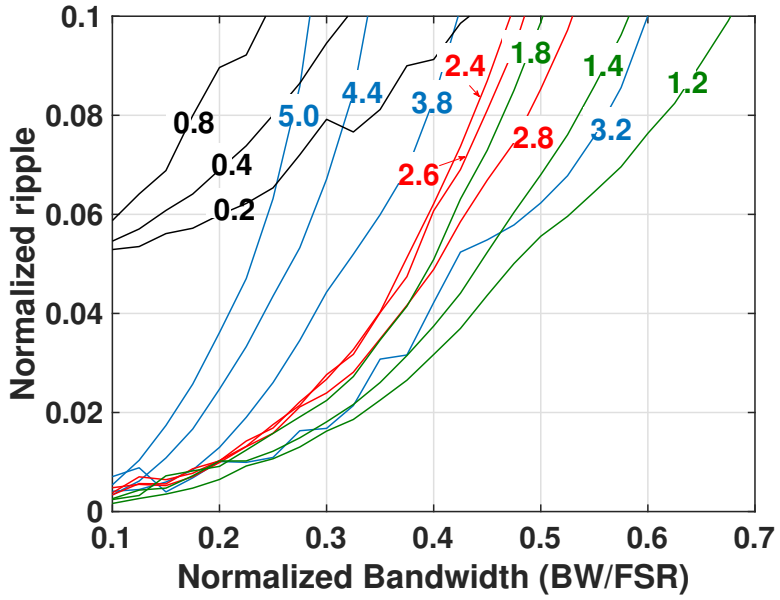

(b)

Figure 6.14: Optimized ripple and bandwidth relation for a (a) 3-ORR with one shared ring topology and (b) 3-ORR with two shared rings topology for various target delays.

Table 6.3: Optimized ripple and parameters of a 1-ring shared 1×4 3-ORR based OBFN with bandwidth of 0.275 for various target delays, provided $\phi_1 = 0$. Two paths are optimized simultaneously with 0.1 relative delay difference. The bandwidth, ripple and delays are normalized to the round-trip delay τ_r.

Target	Ripple	κ_2, κ_3	ϕ_2, $-\phi_3$	κ_4, κ_5	ϕ_4, $-\phi_5$	κ_1
5.05/4.95	0.14693	0.75469	0.83177	0.75918	0.86287	0.82559
4.85/4.75	0.10227	0.77639	0.86425	0.78254	0.89779	0.84554
4.65/4.55	0.073904	0.80097	0.89324	0.80813	0.92816	0.86897
4.45/4.35	0.047242	0.81573	0.96094	0.81748	1.0028	0.87469
4.25/4.15	0.031619	0.84136	1.0004	0.84464	1.0495	0.89791
4.05/3.95	0.020523	0.86603	1.0522	0.86954	1.1098	0.91821
3.85/3.75	0.013543	0.88985	1.1194	0.89449	1.1889	0.93576
3.65/3.55	0.0074592	0.9257	1.1228	0.93281	1.2083	0.96788
3.45/3.35	0.0046032	0.92723	1.3594	0.93084	1.4641	0.95797
3.25/3.15	0.0060561	0.87248	1.5647	0.85829	1.6227	0.93176
3.05/2.95	0.0025052	0.99613	2.0114	0.99574	2.6188	0.99358
2.85/2.75	0.012689	0.8835	1.9222	0.84925	1.9184	0.95322
2.65/2.55	0.010098	0.9615	3.041	0.9354	2.644	0.98213
2.45/2.35	0.01935	0.80226	2.1524	0.70823	1.9616	0.95837
2.25/2.15	0.012518	0.83921	2.5364	0.82396	2.8409	0.98066
2.05/1.95	0.014509	0.68157	2.2407	0.6239	2.2478	0.97514
1.85/1.75	0.0095958	0.63323	2.4796	0.50744	2.1935	0.98194
1.65/1.55	0.011221	0.48392	2.2678	0.41486	2.3686	0.98789
1.45/1.35	0.0073419	0.42796	3.0198	0.19766	1.9066	0.99325
1.25/1.15	0.0057057	0.23287	2.8239	0.073122	2.4256	0.99687
1.05/0.95	0.05	0	0.16665	0	0.88075	1
0.85/0.75	0.095703	0.74293	2.2704	0.76889	2.9269	0
0.65/0.55	0.084912	0.7204	3.0683	0.59049	2.3951	0
0.45/0.35	0.064499	0.57518	3.0384	0.46494	2.6923	0
0.25/0.15	0.032967	0.37558	3.1123	0.22737	2.5748	0

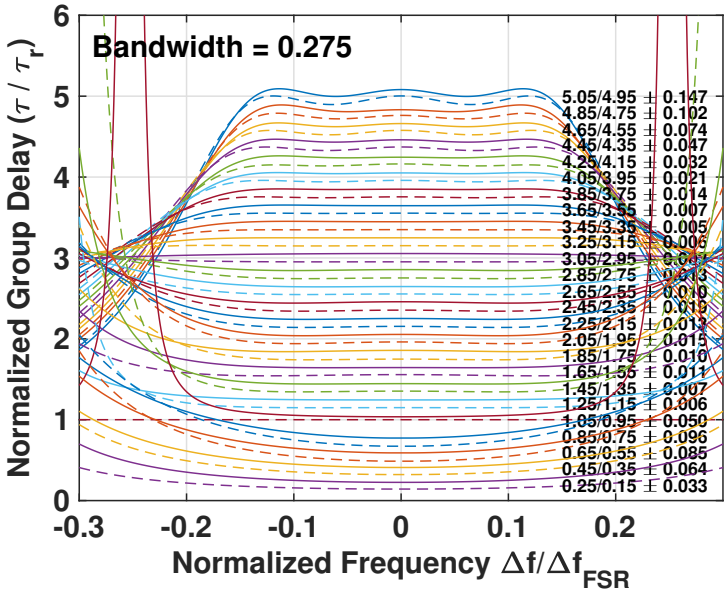

(a)

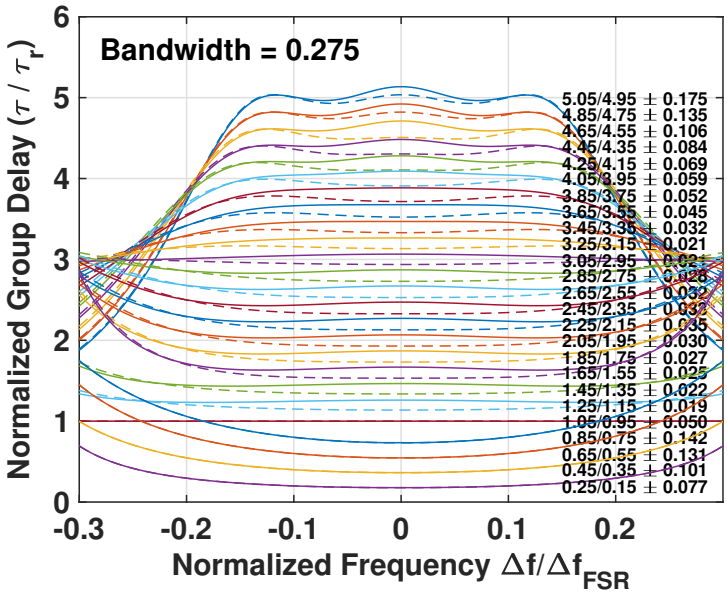

(b)

Figure 6.15: Ripple optimized group delay spectrum of a (a) 3-ORR with one shared ring topology and (b) 3-ORR with two shared rings topology and for various target group delays with bandwidth of 0.275. The solid curves refer to the delay response from path 1, whereas the dash curves refer to the delay response from path 2.

Table 6.4: Optimized ripple and parameters of a 1-ring shared 1×4 3-ORR based OBFN with bandwidth of 0.275 for various target delays, provided $\phi_3 = \phi_4 = 0$. Two paths are optimized simultaneously with 0.1 relative delay difference. The bandwidth, ripple and delays are normalized to the round-trip delay τ_r.

Target	Ripple	κ_1, κ_2	ϕ_1, $-\phi_2$	κ_3	κ_4
5.05/4.95	0.17527	0.74598	0.87259	0.79768	0.82287
4.85/4.75	0.13535	0.77266	0.89486	0.8245	0.85088
4.65/4.55	0.10583	0.79777	0.92604	0.84825	0.87396
4.45/4.35	0.084454	0.82611	0.95274	0.87543	0.90007
4.25/4.15	0.069419	0.85577	0.97634	0.90405	0.927
4.05/3.95	0.059408	0.88638	0.9867	0.93511	0.95522
3.85/3.75	0.051957	0.91004	1.0416	0.9526	0.97004
3.65/3.55	0.044929	0.93652	1.0333	0.97921	0.9909
3.45/3.35	0.032125	0.95634	1.1932	0.9818	0.99261
3.25/3.15	0.021393	0.97782	1.3501	0.99048	0.99788
3.05/2.95	0.021205	0.99922	2.0687	0.99716	1
2.85/2.75	0.028138	0.97045	2.4337	0.97679	0.98909
2.65/2.55	0.031743	0.95311	2.8651	0.97669	0.989
2.45/2.35	0.032713	0.88711	2.5752	0.9713	0.98495
2.25/2.15	0.035074	0.85592	2.9366	0.97718	0.98937
2.05/1.95	0.030215	0.71386	2.455	0.9736	0.98671
1.85/1.75	0.027256	0.63046	2.5364	0.97992	0.99132
1.65/1.55	0.024637	0.44993	2.2995	0.9823	0.99294
1.45/1.35	0.02162	0.32291	2.3283	0.98935	0.99729
1.25/1.15	0.018593	0.10394	1.8959	0.99348	0.99921
1.05/0.95	0.05	0	0.47521	1	1
0.85/0.75	0.14161	0.79673	3.1246	0	0
0.65/0.55	0.13136	0.68681	3.0865	0	0
0.45/0.35	0.10142	0.5323	3.1079	0	0
0.25/0.15	0.076633	0.31306	3.0896	0	0

bandwidth, whereas sharing one ring for two adjacent paths could reduce the number of rings without significantly limiting the performance.

To be specific, Table 6.3 and 6.4 lists the optimized parameters and the corresponding ripple for varied target delays of 1-ring shared topology and 2-ring shared topology, respectively. Since two paths are jointly simulated, the optimization targets 0.1 delay difference between the two paths for various delays for the normalized bandwidth of 0.275. Figure 6.15 (a) and (b) plots the delay spectra based on the parameters listed in Table 6.3 and 6.4. Comparing the two figures, the delay response of 1-ring shared OBFN topology (Fig. 6.15(a)) has more evenly distributed and ideal TTD delay responses. Especially for delays less than τ_r where the delay response is formed by delays at the anti-resonance of two rings and the third ring is turned off ($\kappa = 0$), the 2-ring shared OBFN topology loses the capability in making delay difference between two adjacent paths as the ring in the second stage must be set as "off". Therefore, 1-ring shared topology is reasonable for a 3-ORR OBFN in terms of balancing the system complexity and OBFN TTD performance.

6.4 Chip Design

6.4.1 Optical Ring Resonator Implementation

The ORR is the key component for a ORR based OBFN. Figure 6.16(a) shows the design of the of an ORR. Based on the analysis in the above sections, the coupling and resonance frequency both need to be controlled. For this reason, a 2×2 balanced MZI is employed as a tunable ring coupler, and the upper two ports are connected as the feedback loop of a ring resonator. A heater is placed on the feedback loop as a thermo-optical phase shifter to tune the resonance of the ORR. Another heater is placed on one arm of the MZI coupler to achieve tunable coupling ranging $0 \sim 1$. Figure 6.16(b) shows

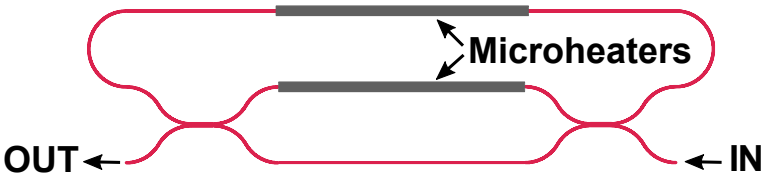

(a)

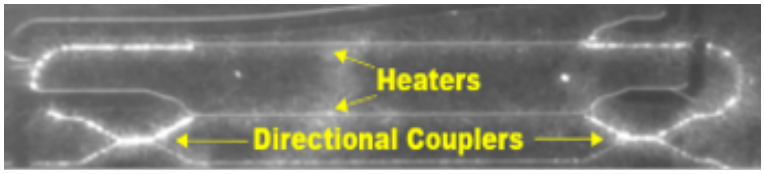

(b)

Figure 6.16: (a) Layout of a single ORR. (b) IR image of a working ORR on a real chip. The highlighted curves indicate the optical signals propagating in the waveguides and the dark bold lines are the metal traces.

the IR image of a working ORR on a real chip captured by an IR camera from the top, in which the highlighted curves indicate the optical signals propagating in the waveguides and the dark bold lines refer to the metal traces.

The ORR in the IR image shows strong scattering since the coupling of the ORR is small and very high optical power is trapped in the ring. Based on the analysis of MZIs in Chapter 5, tuning one arm of a MZI does not only change the coupling, but also introduces additional phase shifts, which will shift the resonance frequency of the ORR. Figure 6.17 shows the simulated normalized delay of a same structure as depicted in Fig. 6.16(a) by only tuning of MZI coupler. As shown, the coupling and resonance are related due to the MZI coupler. Therefore, in order to precisely control the ORR resonance and coupling to optimized the delay response of a multi-ORR-OBFN, this coupler induced resonance shift need to be compensated by tuning the heater on the feedback loop.

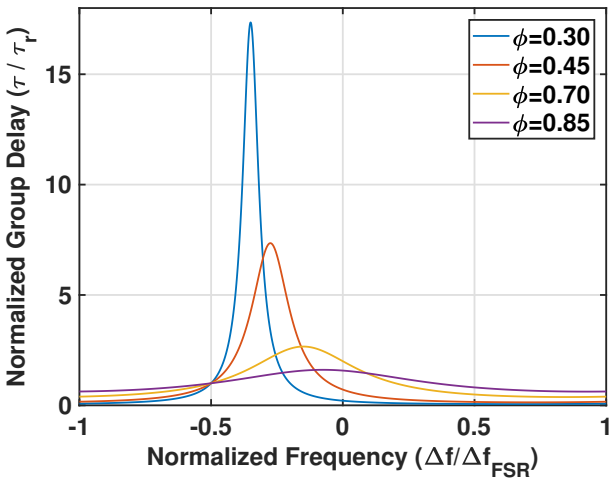

Figure 6.17: Delay response of an ORR with a MZI coupler for different coupling, where ϕ refers to phase shift of one arm of the MZI coupler.

6.4.2 True Time Delay Bandwidth Extension

The OBFN chips were realized for C-band operation and fabricated with an ultra low-loss silicon nitride waveguide technology. Given the the group index of the waveguide $n_g = 1.71$ at 1550 nm and the optical path length of the MZI coupler, the FSR of the ORR was designed to be 22 GHz. As discussed in Chapter 3, for TTD based beam steering with photonic up-conversion process, the two optical tones must be delayed by the same amount of time, which requires a very wide TTD bandwidth for mmW signals. This may be acceptable by SDLs, which naturally provide very wide bandwidth. As for ORRs, the required bandwidth may leads to a very small ring radius that may not be fabricable for low confinement waveguides like silicon nitride. However, although the continuous TTD bandwidth of a ORR based delay line is limited, it provides periodic delay response over a very large wavelength range. If the two optical tones are precisely aligned to different orders of the resonance of the ORR with the same delay, the equivalent TTD bandwidth can be extended. And then, the bandwidth requirement of TTD is reduced to the data signal bandwidth instead of the carrier frequency, as described in Fig. 6.18. In our case,

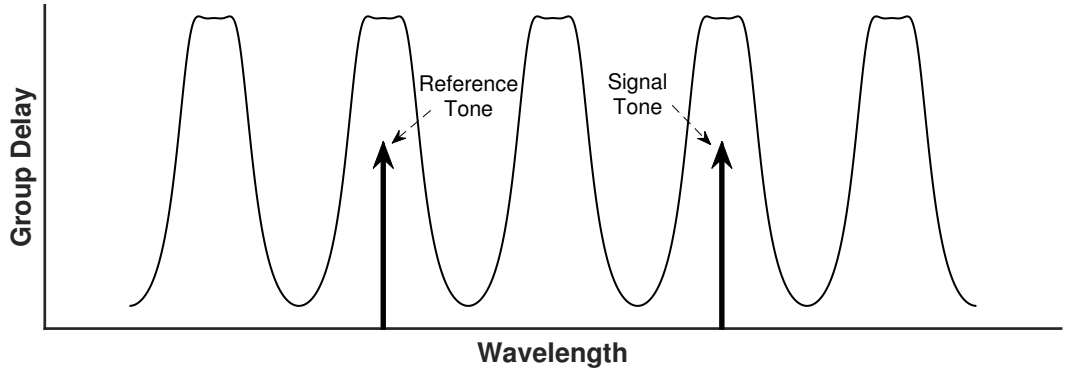

Figure 6.18: Schematic diagram of the TTD bandwidth extension with the periodic delay response of ORRs.

the FSR of the ORRs is 22 GHz, which can be used for mmW frequencies that is integral number of FSR such as 44 GHz, 66 GHz, 88 GHz and 110 GHz.

6.4.3 Chip Layout

Two versions of integrated ultra low-loss silicon nitride chips were designed for ORR based OBFNs, which include the 1×4 ORR-OBFN with 1-ring shared and 2-ring shared 2-stage binary-tree topologies, as depicted in Fig. 6.19 (a) and (b), respectively. Both of the chips have a footprint of 8×32 mm^2 and the waveguide is demonstrated with low optical loss less than 0.5 dB/cm. The yellow lines in Fig. 6.19 indicate the metal traces and pads for electrical connections of heaters. Figure 6.19 (a) and (b) shows the mask layout of the two chips, respectively, and the ORR-OBFNs are enclosed in the blue boxes. The optical signal inputs from the right of the chip and coupled out at the left side. At both edges of the chips, taper arrays are included with a pitch of 127 μm so that the chip can be pigtailed to a standard commercial fiber array for optical input and output. These waveguides are tapered to match the mode size of the fiber array in order to improve the coupling efficiency. For a TTD based beamsteering, the path length from the outputs of each OBFN to the chip edge couplers are equalized. In addition to the

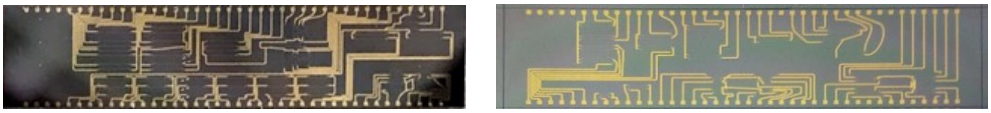

(a) (b)

Figure 6.19: The picture of the fabricated silicon nitride chip with metal connections for (a) layout 1 and (b) layout 2 with a footprint of 8 $mm \times 32$ mm.

OBFNs, layout 1 also includes the 1×4 SDL-OBFN mentioned in Chapter 5 and layout 2 also includes flattened bandpass filters for signal processing taking advantage of the ultra-low loss of the SiN waveguide in optical domain. MZI and ORR test structures are also included in both of the chips.

6.5 Summary

ORR based delay lines and OBFNs were discussed in this chapter. The response of an ORR is theoretically analyzed, which exhibits that an ORR can generate continuously tunable group delay responses beyond the physical dimension of the ORR. Despite that bandwidth-delay product of a single ORR is constant, this limit can be overcomed by employing a SCISSOR structure, but the resonant frequency and coupling coefficient of each ORR should be optimized to achieve a TTD delay response with large bandwidth. A genetic algorithm was applied to optimize these parameters, which exhibits trade-offs between the delay value, bandwidth, delay ripple and the total number of ORRs. For OBFNs, ORRs can be shared by neighbor paths to reduce the system complexity. The optimization also shows that for 3-ORR based 1×4 OBFNs, sharing one ORR by two adjacent paths has acceptable ripple in the delay responses and maintains moderate system complexity, whereas sharing two ORRs by two adjacent paths yields the largest ripple in the delay responses but has the most simplified system complexity. Based on the analysis, two 1×4 OBFNs were designed and realized with the two ORR-OBFN

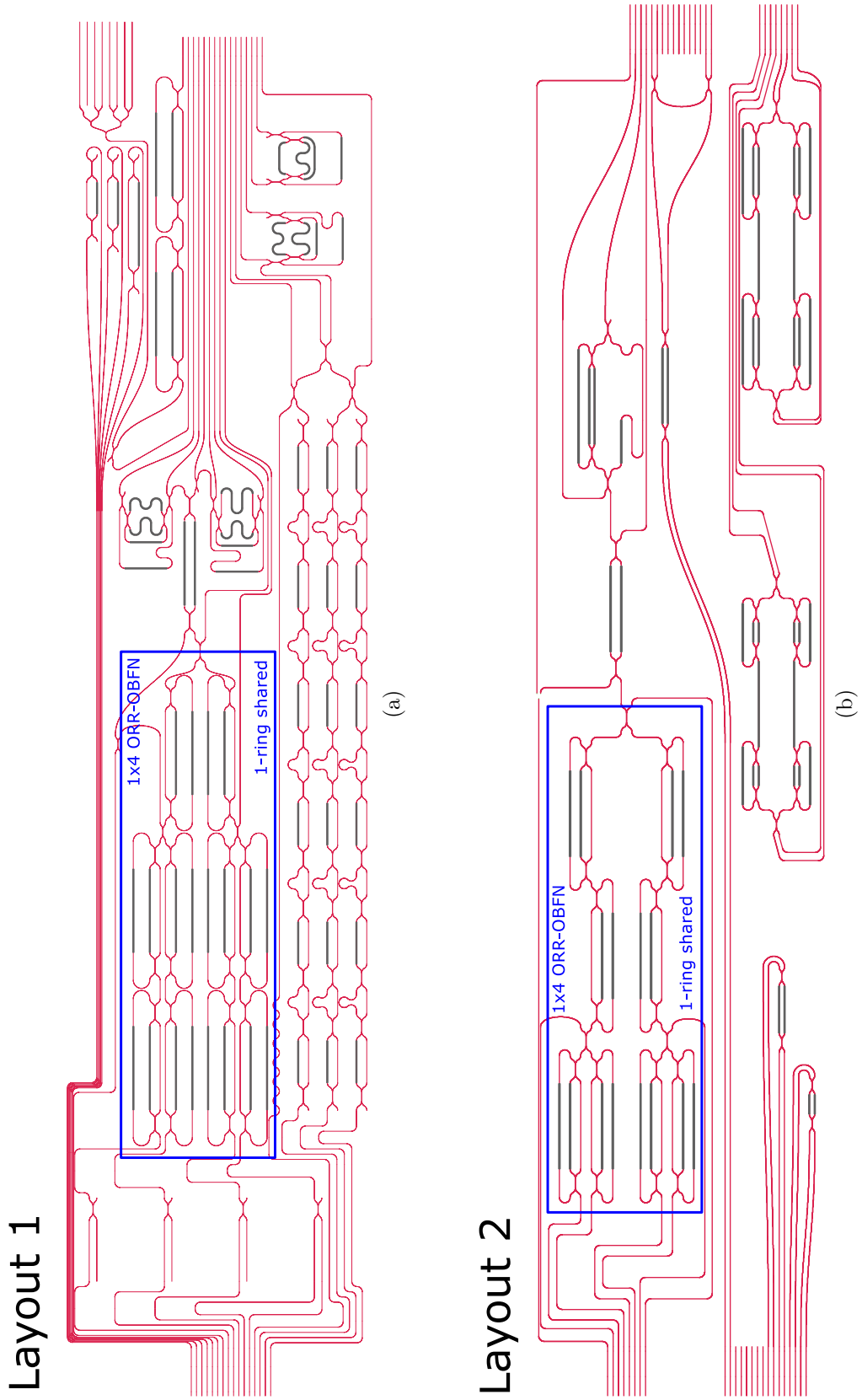

Figure 6.20: Layout of the silicon nitride chips for 1×4 ORR-OBFNs based on 2-stage binary-tree topologies with (a) one ring shared and (b) two ring shared. The OBFNs are enclosed in the blue boxes.

architectures using the low loss SiN platform. Look-up tables were generated in the optimization as the tuning reference of the chip, and this table can be applied to general ORRs as well.

Chapter 7

Scalable Multi-channel Controller

Previous chapters have demonstrated 1×4 OBFNs based on SDLs and ORRs. To achieve programmable delay distributions for these OBFNs for beamsteering, a large number of phase shifters in the OBFNs need to be precisely controlled. To be specific, the 1×4 3-ORR based OBFN has up to 20 phase shifters need to controlled, and number of phase shifters for the 5-stage 1×4 SDL based OBFN is 18. For a larger scale OBFN or better tuning resolution, the number of phase shifters will be even larger. Moreover, the OBFN is implemented using SiN technology and thermo-optical effect for phase shifting. The thermo-optical coefficient of SiN is low, which requires up to 500 mW of heat dissipation for a 2π phase shift. The heater for thermo-optical tuning is made of chromium thin film, which has a resistance of $\sim 700\ \Omega$. Thus, a voltage of 19 *volts* is required for the heater to achieve the 2π phase shift. Considered the specifications above, it is difficult to find a compact commercial solution to meet the power and voltage requirement with such large number of channels. Therefore, we decided to make a controller specifically for the OBFNs. In this chapter, two generations of the OBFN controller will be discussed. The first generation is a multi-channel programmable high power voltage controller, and the second generation is a multi-channel programmable high power current controller. Both of the two controller designs are modularized and are highly scalable. The number of channel can be changed simply by adding or removing driving modules connecting to the

central controller. A control software will also be developed and demonstrated in this chapter.

7.1 First Generation Multi-channel Voltage Controller

The first generation controller is a multi-channel programmable voltage controller. Since chromium thin film resistors are used as heaters, applying a voltage controller is equivalent to a current controller according to Ohm's law. As mentioned above, to achieve a complete OBFN tuning, the required heat dissipation power for the phase shifter should be greater than 500 mW. Given load of the controller is around 700 Ω, the output voltage and current should be greater than 19 V and 27 mA, respectively. Therefore, with some redundancy, the specifications of the voltage controller are chosen with maximum 30 V of voltage output and 30 mA of current output.

Figure 7.1 shows the schematic circuit for the voltage driver unit (DU). As a programmable voltage controller, the output of a digital-to-analog converter (DAC) serves as the input of DU. Actually, most of the multi-channel commercial DACs have a voltage output up to 5 V. Given this reason, an non-inverting operational amplifier (op-amp) topology is employed with gain of 6, which requires the ratio of resistance $R2$ to $R1$ to be 5. To achieve a precise voltage output, resistors of 25 $k\Omega$ and 5 $k\Omega$ with high precision were chosen for $R1$ and $R2$. Since the op-amp used in the circuit has limited output current, the output of the op-amp is followed by a high-power NPN bipolar-junction-transistor (BJT) to boost the output power of the DU. The circuit for the DU in Fig. 7.1 is a power linear regulator circuit. Comparing to other kinds of power regulators, this circuit has very high precision, but also associates with a high power consumption. Most of the power is consumed by the BJT as heat and the power consumption can be given

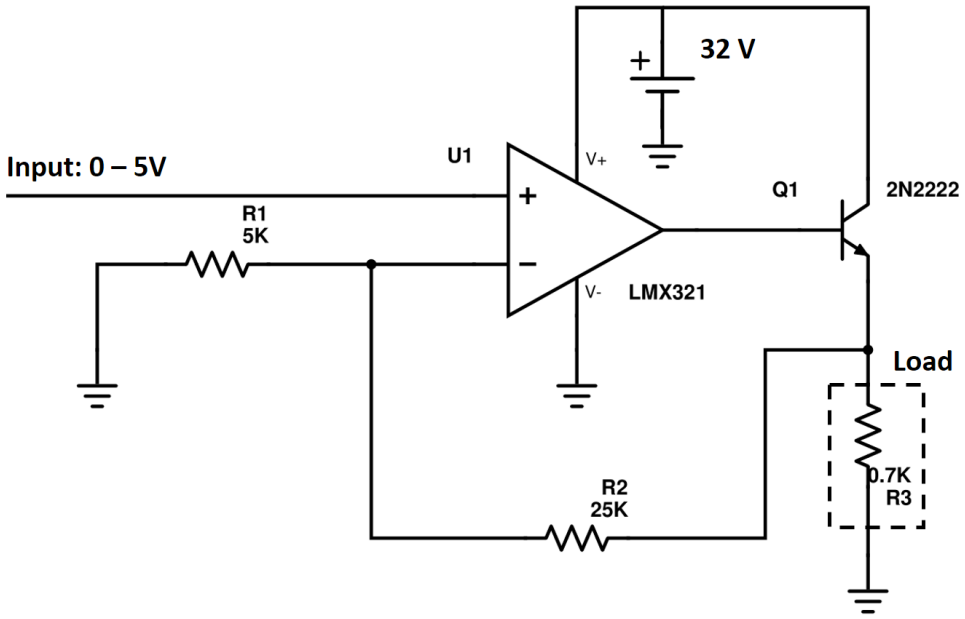

Figure 7.1: Schematic diagram of the voltage driver unit.

by

$$P_{BJT} = (V_+ - V_L) \cdot \frac{V_L}{R_L} \leq \frac{V_+^2}{4R_L} \tag{7.1}$$

where V_+ is the voltage of the supply power, V_L is the DU output voltage, and R_L is the load resistance. The maximum power consumption is achieved when $V_L = V_+/2$. Using the typical numbers for $R_L = 700\ \Omega$ and $V_+ = 32\ V$, the maximum heat dissipated power in the BJT is 366 mW. Therefore, given the large number of channels, the cooling of the boards should be considered for reliable operation of the controller.

Figure 7.2 depicts the system architecture of the voltage controller. The voltage controller has a modularized design. Each driver module communicates to a central micro-control unit (MCU) using the Inter-integrated Circuit (I^2C) serial protocol. The central MCU is the bridge between the computer and the driver modules, which accepts the commands from a computer through a USB protocol and interprets and forwards it to the driver modules to output the right voltage from the desired channel. Each driver

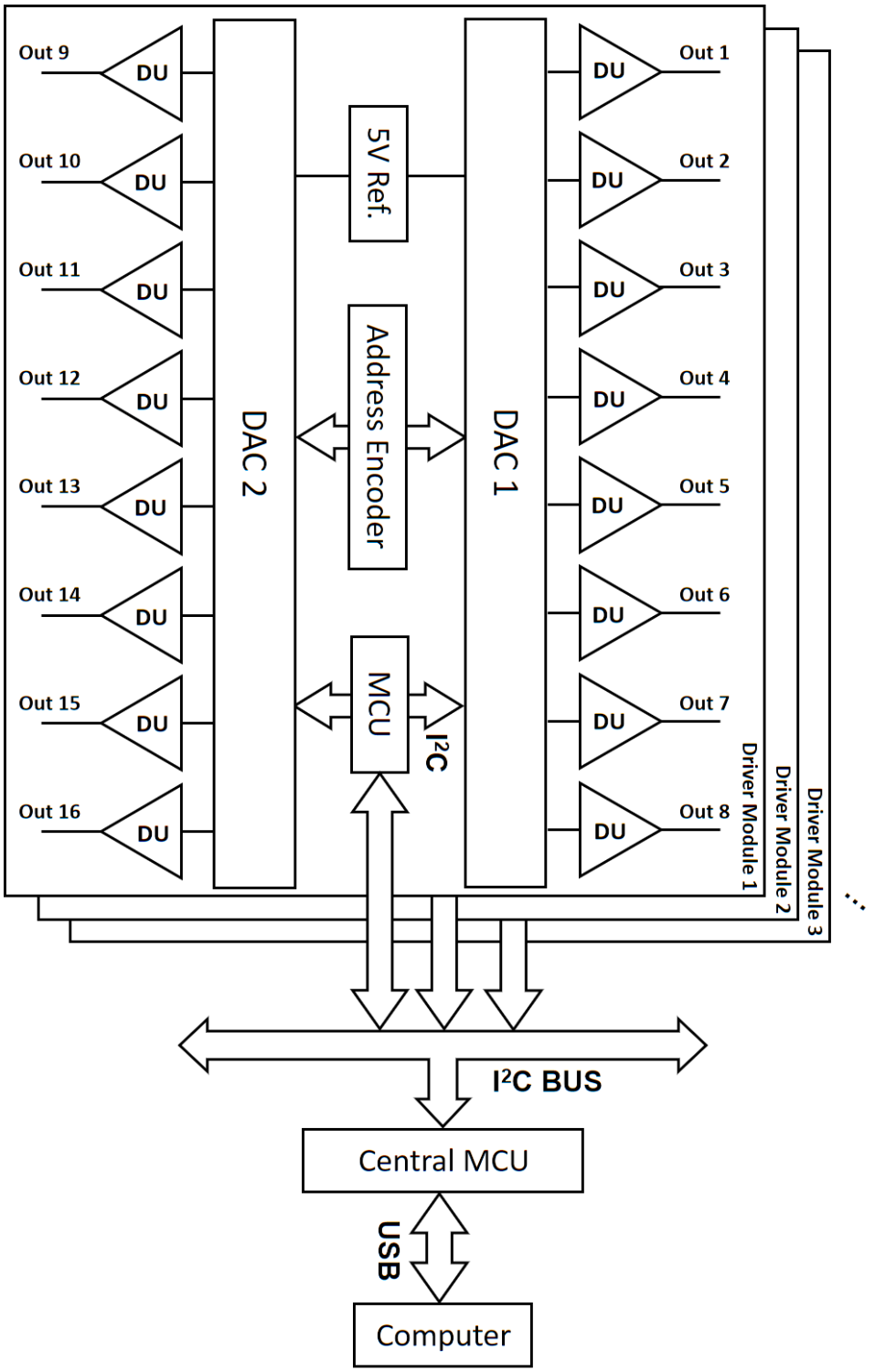

Figure 7.2: System architecture of the voltage controller. (DU: Driver Unit; MCU: Micro-controller Unit.)

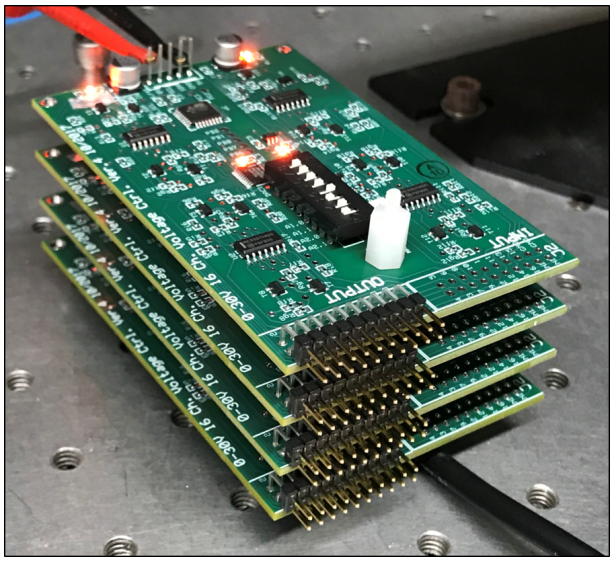

Figure 7.3: Picture of the voltage controller with 4 driver modules (64 channels).

module includes 16 DUs driven by two Octal-Channel DACs (MAX5824). The DAC has a 10-bit resolution, which corresponds to 7 mV tuning resolution of the controller. A ultra-precise 5 V voltage reference is employed as the external reference for the DACs to precisely output 0 - 5 V signals for the DUs. There are two pins in the DAC for encoding address. Each pin can accept three states (V_{DD}, GND and $FLOAT$), which is programmed using a tri-state switch, and thereby up to 9 DACs can be connected to the same data bus. In our case, only 4 boards and 64 channels can be supported if the DACs are directly connected to the central MCU. For further scalability, another MCU can be employed in the driver module as the communication interface to the central MCU, as shown in Fig. 7.2. In this case, up to 127 driver modules can be supported, in which the number of channels could be limited by other issues such as limited power supply and system heat dissipation. Figure 7.3 illustrates a picture of the voltage controller with 4 driver modules (64 channels). The driver module boards were designed to be stacked and connected with a rectangular connector, and no wire connections are needed to assemble the modules. With this design, it would be easy to scale the voltage controller by simply

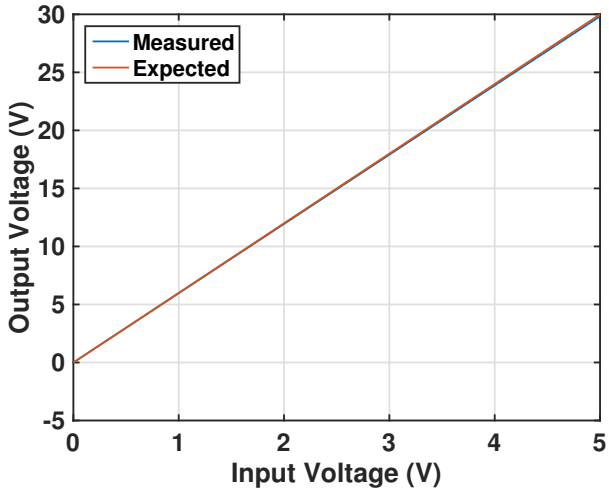

Figure 7.4: Comparison of measured output from a channel of the voltage controller with expected output value.

stacking or removing boards from the controller. Figure 7.4 demonstrates the output characterization of the controller and compared with the expected values. As shown, the controller output the expected voltage from 0 - 30 V except for hardly notable lower slope. This may be due to the slightly lower $R2$ to $R1$ resistance ratio. However, since silicon nitride has a low thermo-optical coefficient, this difference would not impact on the actual OBFN tuning.

7.2 Second Generation Multi-channel Current Controller

In theory, a voltage source and a current source based controller are equivalent for a metal thin film heater in the OBFN chip. However, parasitic resistance is inevitable in the electrical connections between the controller and the heaters. With a voltage controller, this parasitic resistance may reduce the actual voltage on the heaters and hence make the calibrated parameters dependent on the entire electrical path and the

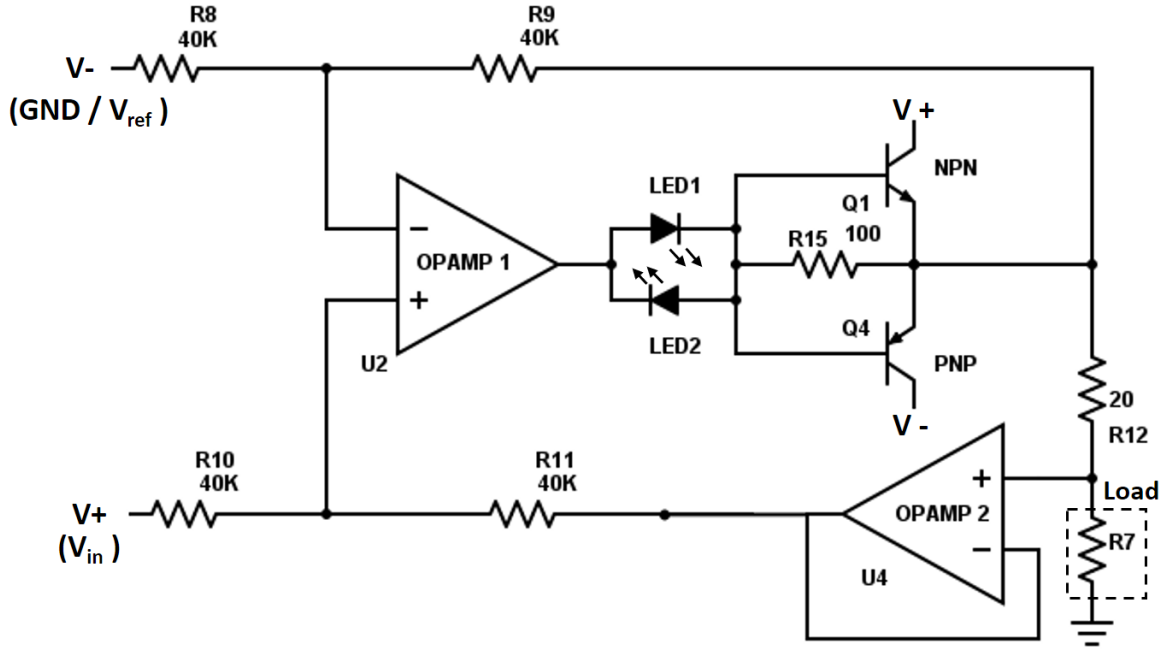

Figure 7.5: Schematic diagram of the current driver unit.

specific controller that used. Using a current source based controller can eliminate this issue as the current going through a heater does not related to the serial resistance in the circuit loop. Based on this consideration, a second generation multi-channel current controller was developed.

The schematic circuit of the current DU is depicted in Fig. 7.5. The circuit is based on a Howland current pump topology [144]. Two balanced arms ($R9/R8 = R11/R10$) are employed as the negative feedback and positive feedback of an op-amp, which sample the signal from each node of a shunt resistor $R12$, respectively. This configuration can linearly relate the voltage potential difference over $R12$ with the input voltage difference, which thereby determines the output current going through the load regardless the load

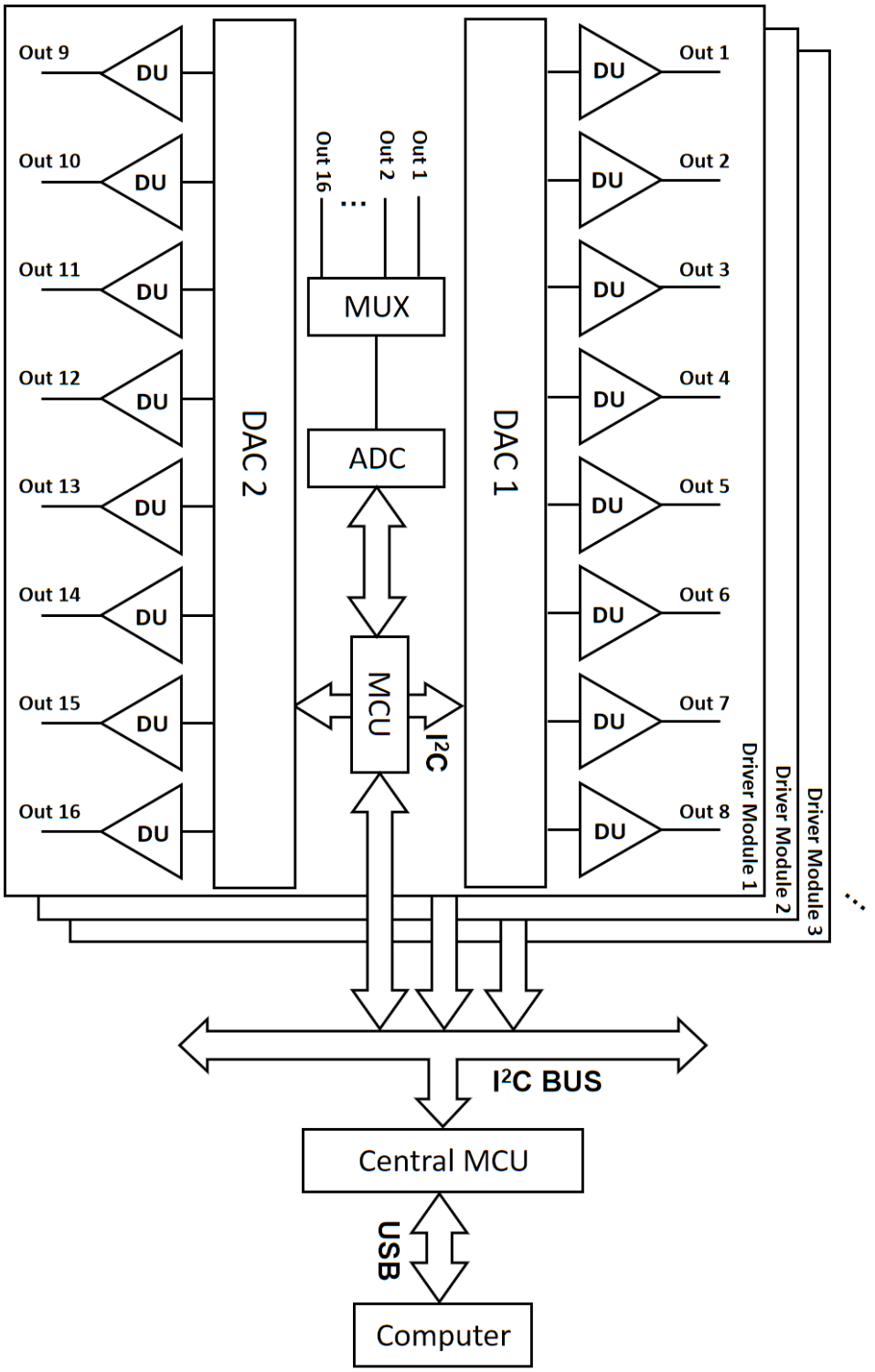

Figure 7.6: System architecture of the current controller. (DU: Driver Unit; MCU: Micro-controller Unit.)

impedance. The output current can be given as follows

$$I = \frac{R11}{R10} \cdot \frac{V+ - V\text{-}}{R12} \tag{7.2}$$

where ratio of $R11/R10$ is the circuit gain. The positive feedback is connected to the output through a voltage follower, which takes advantage of the high input impedance of the op-amp so that the current drawn from the output for the feedback is minimized, thereby increasing the output accuracy. BJTs are used to boost the output current as the output current of the op-amp is limited. Since the DU was designed with a bipolar operation, which can both output and sink currents, a complementary BJT structure is employed as the current booster. In output mode, the current will go through LED1 and the amplified by the NPN transistor, while in sink mode, the current go through LED2 and is sunk by PNP transistor. The lightened LED indicates the operation mode of the DU. Most of the current of the DU is provided/suck by the transistor, and only a little portion go through the LEDs and op-amp. Therefore, no protection circuit is required for the LEDs.

The system architecture of the current controller is similar to the voltage controller architecture, as illustrated in Fig. 7.6. The DACs are replaced by a AD5675R, which also has 8 channels and I^2C interface but 16-bit resolution. AD5675R also includes a high precision 2.5 V internal reference that allows the external reference to be eliminated. The address of the DACs is hard encoded so that we can get rid of the "Address Encoder" in Fig. 7.2. Instead of direct communications, the DAC communicates with central control module through an on-board MCU. The outputs of the driver module are routed to a 16×1 multiplexer, and connected to a analog-to-digital converter (ADC), which measures the voltage and current of the channel outputs by switching multiplexer periodically. In addition to the specifications of the voltage controller, the maximum output for 2nd

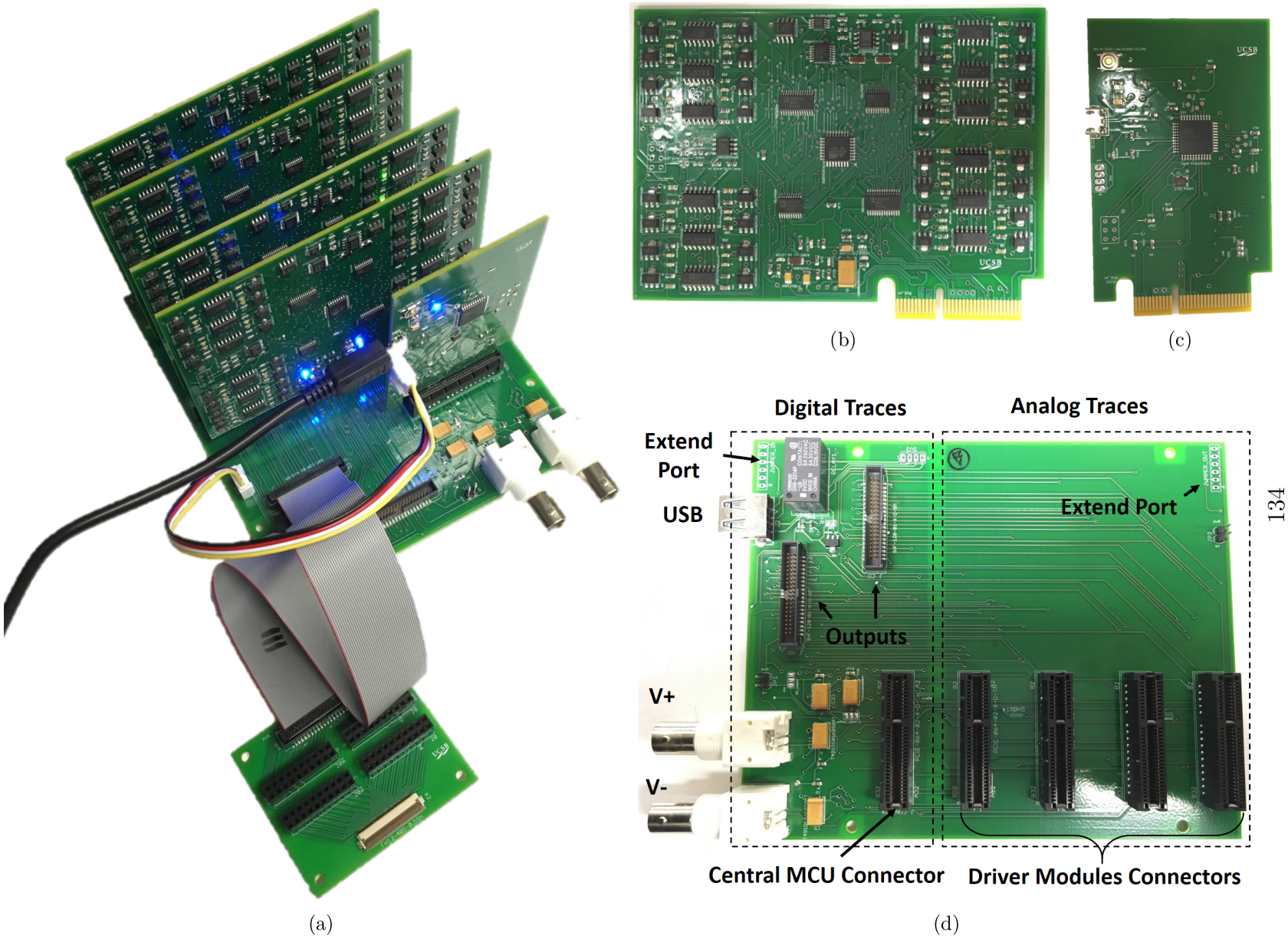

Figure 7.7: Pictures of (a) assembled current controller, (b) current driver module, (c) central controller module, and (d) base board.

generation current controller is extended to 250 mA and 30 V for unipolar operation, or $\pm$125 mA and $\pm$15 V for bipolar operation. The DAC has an output of $0 \sim 5$ V. Therefore, the circuit gain of the driver module is chosen to be 1, and the shunt resistor $R12$ of the driver module is chosen to be 20 Ω. The $V+$ port of the driver module is connected to the output of a DAC, and the V- port is connected to GND or the 2.5 V internal reference of the DAC for unipolar or bipolar operations, respectively. Moreover, filters were also designed to eliminate the noise from the power supply.

Figure 7.7 shows the pictures of the fabricated circuit boards. The modules are connected to a base board using PCI-E connectors and a base board can support 4 driver modules or 64 channel outputs. As shown in Fig. 7.7(d), the board are deliberately designed to isolate the power supply for digital circuits and analog circuits to avoid the noise caused by the digital circuits transferred to the outputs of the controller. The analog circuits such as op-amps, DACs and BJTs are powered through two BNC connectors, and the digital circuits is powered by the computer through the USB port. The extend ports on the base board are designed to cascade more boards to scale the number of channels. Up to 127 driver modules can be cascades in theory, which is able to provide sufficient number of channels on demand.

7.3 Control Software

The control software is one of the indispensable parts of the OBFN control system. A well designed, fully functional and easy to use control software will make the tuning of the OBFNs more efficient and can achieve complex tunings. Here, control softwares are specifically designed for each version of the OBFN chips.

Figure 7.8 presents the snapshot of the graphic user interface (GUI) of the control software. It is developed in C++ and with Qt [145] framework. A schematic diagram

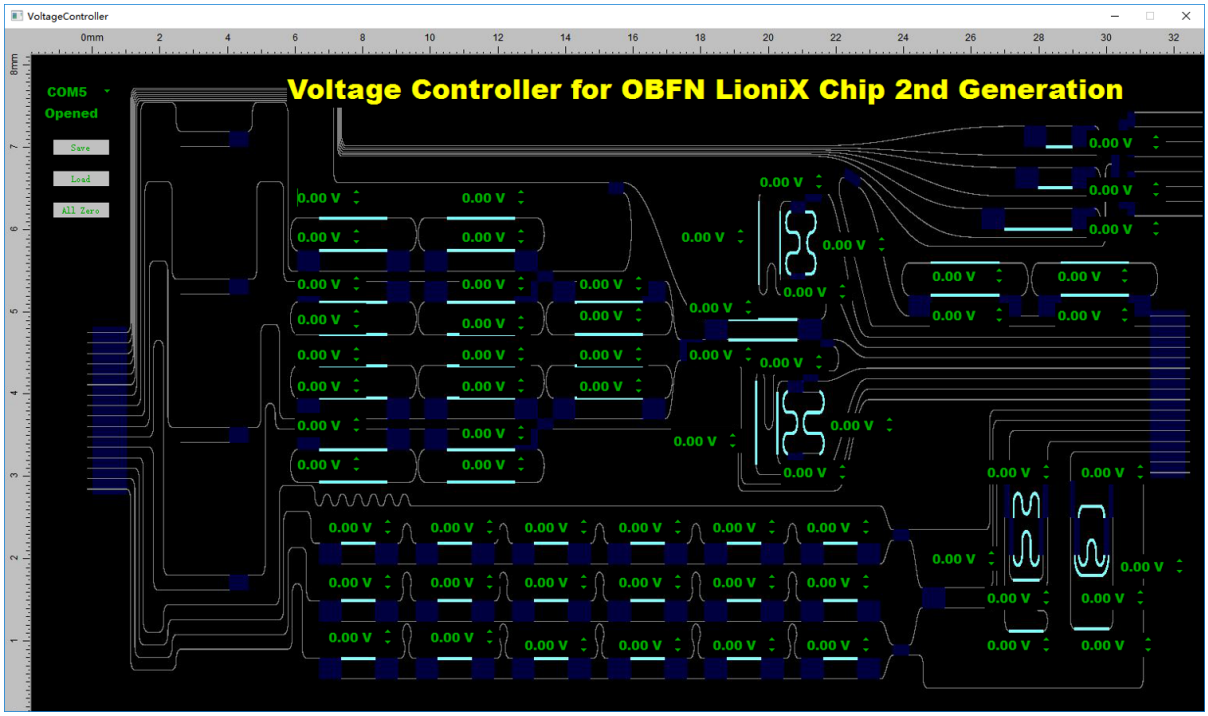

Figure 7.8: The graphic user interface of the control software.

of the chip layout is drawn in the GUI showing the locations of the heaters. Spin boxes are placed by the heaters to control the voltage or current going through the heater by rolling the mouse wheel. The control software are specifically designed for the OBFN and the spin boxes are mapped to the channels of the controller accordingly depending on the electrical connections. The communication between the controller and the software is through USB. However, since the controller has a simple communication protocol, the controller is simulated as a USB based virtual serial port to simplify the software development work and the communication is implemented with standard serial libraries. As it can be noticed at the top-left of Fig. 7.8, the software provides a "save" and "load" feature, which can save the tuned parameters into a file, and load it in the next time. These feature is very usefully as the tuning of a OBFN need several days of time. Also, the calibrated parameters of the OBFN can be saved and the states can be restored later for further system experiments. Despites that the software is customized for a specific

chip design and controller, it is very easy to adapt to another chip designs by simply redrawing the chip layout schematic and relocating the positions of the spin boxes.

7.4 Summary

In this chapter, two generations of compact controllers are demonstrated for the SiN OBFNs chips. The controller are specifically designed to meet the requirement of high power and large number of channels as the SiN has a low thermo-optical coefficient and a large number of TTD elements that needs to be tuned in the OBFN. A control software was designed for communicating with the controllers. The calibrated OBFN states can be saved and restored, which makes the use of OBFNs easy, efficient and repeatable.

This page intentionally left blank

Chapter 8

Delay Response Characterization

In previous chapters, the designs of tunable integrated TTD structures and the corresponding OBFNs have been discussed and analyzed. Two versions of chips were designed and taped out with LioniX using the ultra-low loss silicon nitride TripleX technology [122], which include two 1×4 3-ORR based OBFNs with different topology and one 1×4 5-stage SDL based OBFN. The chip pictures and layouts are shown in Fig. 5.12, Fig. 6.19 and Fig. 6.20. This chapter will demonstrate the delay characterizations of the OBFNs. The characterization experimental setup will be discussed including the chip testbed and group delay measurement system. Both the ORR delay lines, SDLs and the corresponding OBFNs were optimized, and the resulting TTD responses will be presented in this chapter.

8.1 Experimental Setup

8.1.1 Chip Testbed

The testbed for the OBFN chip characterization is shown in Fig. 8.1. The chip was mounted on a copper stage with silver epoxy (H20E) to ensure good thermal conductive for the chip. The whole piece is put on top of a thermoelectric cooler (TEC) to stabilize

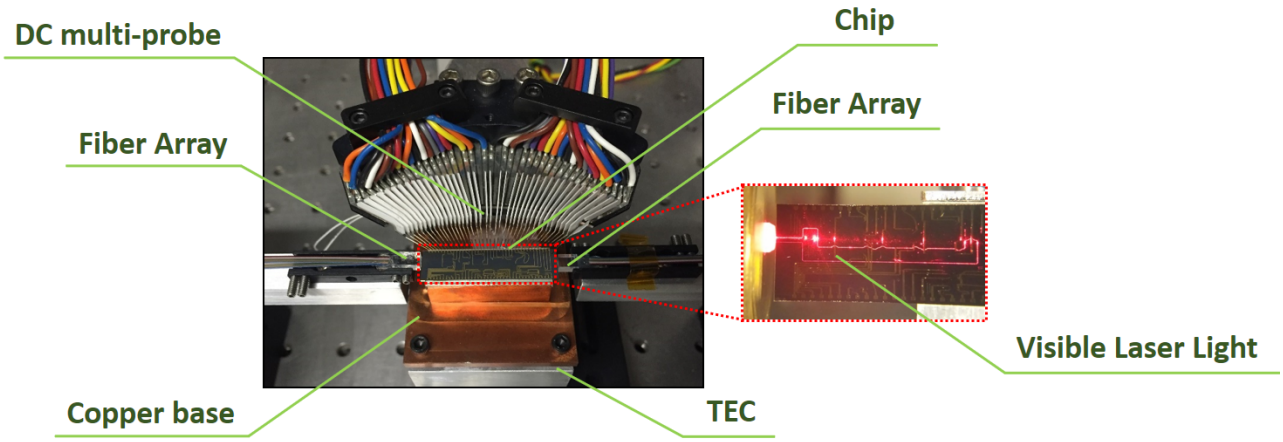

Figure 8.1: Testbed for the OBFN chip with fiber-array I/O and a customized 40-pin probe. On the right depicts a close-up picture of the chip injecting a red visible laser light.

the chip temperature. Light is coupled in and out from the edges of the chip with two pigtailed standard commercial fiber arrays with a pitch of 127 μm, as depicted in Fig. 8.1. A 40-pin probe was used to contact the pads on the the chips and connect to the multi-channel controller demonstrated in Chapter 7.

8.1.2 Group Delay Measurement System

A modulation phase shift method was used to measure the group delay response as shown in Fig. 8.2. A tunable laser (Yenista, TUNICS T100S-HP) emitting in the C-band was coupled to a Lightwave Component Analyzer (LCA) (Hewlett-Packard, HP8703A). The LCA modulates the intensity with a constant 200 MHz sinusoidal signal. The light was then amplified by an erbium-doped fiber amplifier (EDFA) (IPG Photonics, EAR-2K-C) and coupled to the device and then split with a 50/50 fiber coupler. One output of the coupler was input to a power meter for monitoring, and the other output was coupled back to the LCA for measurement of the group delay. The the output power level of the EDFA was adjusted in order to maximize the accuracy of the measurement of the LCA.

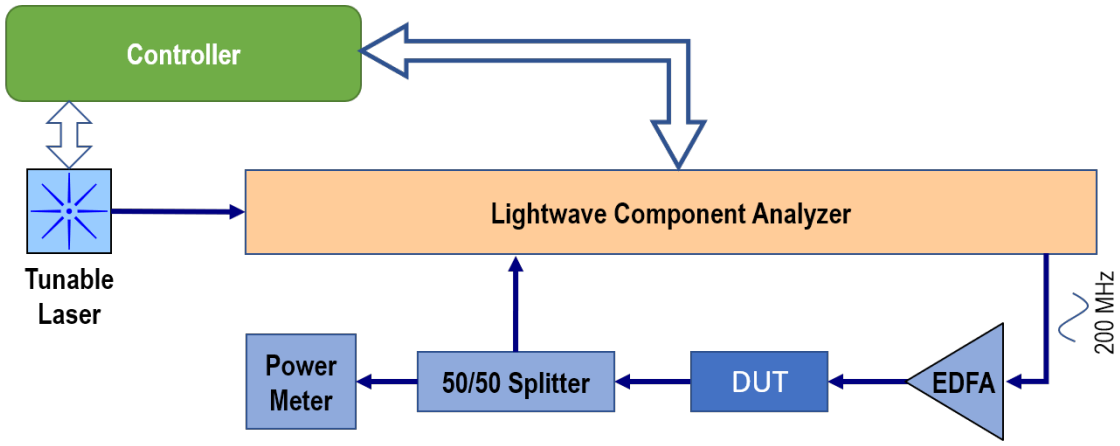

Figure 8.2: Group delay measurement setup. (LCA: lightwave component analyzer; DUT: device under test; EDFA: erbium-doped fiber amplifier.)

The LCA measures the phase shift of the modulated RF signal, which can be converted to the group delay by

$$\tau(\lambda) = \frac{\Delta\phi_{RF}(\lambda)}{2\pi f_{RF}} \tag{8.1}$$

where λ is the wavelength, $\Delta\phi_{RF}$ is the measured phase shift of the RF signal and f_{RF} is the RF modulation frequency. Absolute measurement of the ORR group delay is not possible using this method due to the additional delay from external fibers and waveguides on the chip. However, these extra delays can be accounted for by fitting the measured delay spectrum using the model in (6.19) plus a extra constant delay term, which represents the additional path delays of the optical connections.

Tuning TTD devices requires a fast measurement of the group delay spectrum. This can be achieved by synchronizing the light source and the LCA by a controller. The controller is realized on PC and coded with Python, which starts the laser wavelength sweeping and then trigger the LCA for signal amplitude and phase measurement acquisition. A speed of 1.6 s per sweep over 0.5 nm is finally achieved, enabling real-time tuning of TTD devices in the OBFN. The controller also retrieves the measured data from the LCA after every sweep, and calculates the power transmission and group delay,

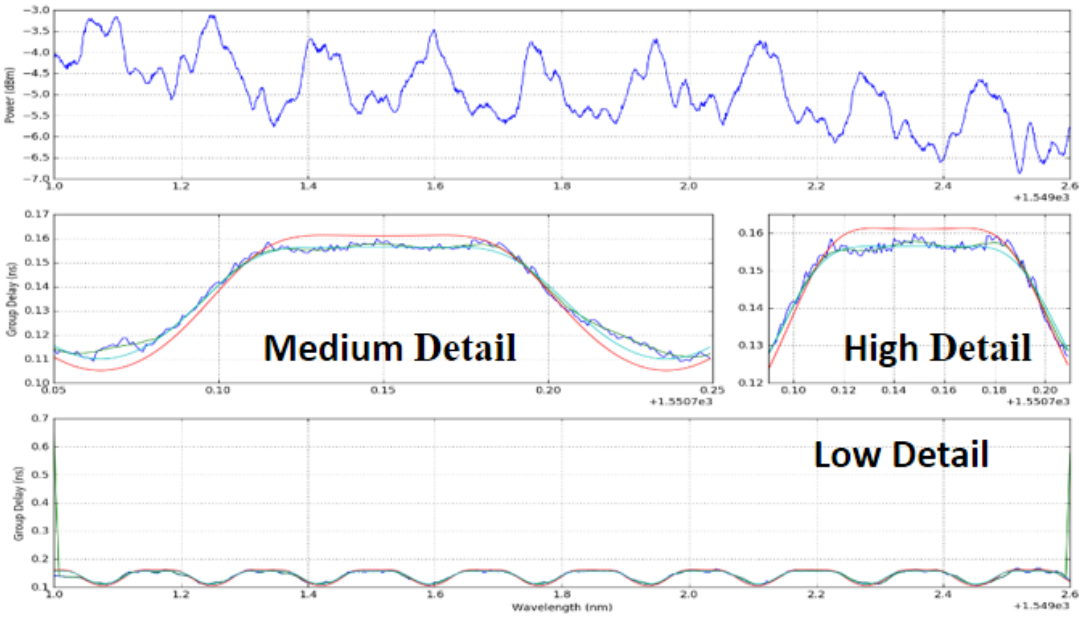

Figure 8.3: Software interface for group delay response real-time monitoring. The blue lines refer to the measured raw data, the green lines refer to the smoothed curve of the raw data and the red curves refer to the optimized theoretical delay response.

and plots the results in real-time. Figure 8.3 shows the software GUI displaying the power transmit spectrum and group delays spectrum. The first figure on the top shows the power transmission, and middle and bottom three figures show the group delays with different scales. The blue lines refer to the measured raw data and the green lines refer to the smoothed curve. The red curves refer to the optimized theoretical delay response of ORRs discussed in chapter 6, which makes it easier to realtimely tune the to align the actual delays with the optimized response.

8.2 Heater Characterization

Since heaters are employed as the phase shifters in the SiN chip, the behavior of the heater need to be characterized. The heater was characterized by measuring a balanced MZI with 2-mm heaters on the each of the two arms, as described in Fig. 8.4(a). The

output power of the MZI was recorded as the current of the lower heater sweeps from $0 \sim 50\ mA$. Given that the chromium heater can be treated as a thin metal film resistor, and the change of refractive index is proportional to the power dissipation of the heater, the phase shift of the heater is proportional to the current square. As discussed in Chapter 5, the output power of a MZI has a sine square relation with phase shifts. Therefore, we can model the relation between the MZI output power and current as

$$P = a \cdot \sin^2(b \cdot L \cdot I^2 + c) + d \tag{8.2}$$

where P is the output power of the MZI, I is the current of the heater, L is the length of the heater, a, b, c and d are parameters that need to fitted using the measured data. Figure 8.4(b) shows the behavior of a MZI where the dots refers to the measured data whereas the blue line refers to the fitted curve. The fitting gives value of the parameters listed as

$$\begin{aligned} a &= 1.69 \times 10^{-5}\ W \\ b &= 0.58 \times 10^{-3}\pi\ mm^{-1} \cdot mA^2 \\ c &= -0.185\pi \\ d &= 9.08 \times 10^{-8}\ W \end{aligned}$$

The tuning efficiency of the heater can be given by $2b/R$, which is $5.3\pi\ rad/W$. The extinction ratio of the MZI can be calculated as $-10log_{10}(d/a) = 22.7\ dB$, and the coupling coefficient of the 3-dB coupler of the MZI can be extracted as $\kappa = 0.46$ using (5.4).

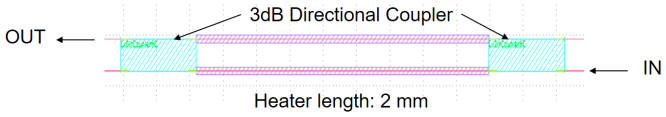

(a)

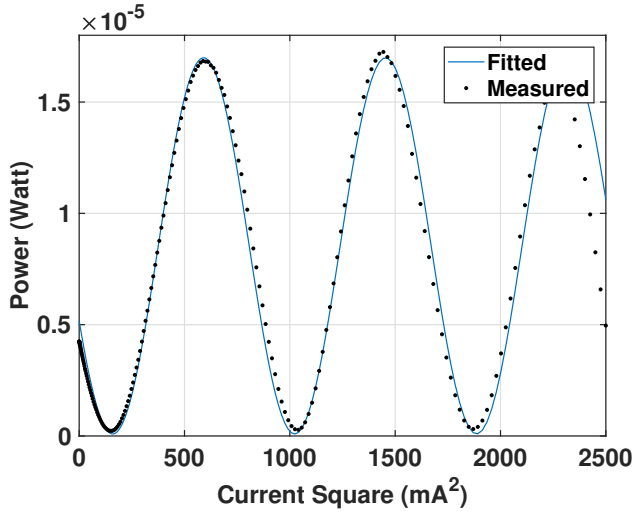

(b)

Figure 8.4: (a) Characterized MZI with 2-mm heaters. (b) The output power from the MZI versus the current square of the heater.

8.3 ORR-OBFN Delay Response and Tuning Optimization

8.3.1 Single-ORR Delay Calibration

The delay response of the an single ORR is characterized using the group delay measurement system described in Fig. 8.2 [78]. As discussed in Chapter 6, a single ORR exhibits a bell-shape delay response. Based on the experimental setup, the group delay response of a single ORR for different MZI coupler current levels over two FSRs were measured and shown in Fig. 8.5. The measured data (denoted by the crosses) is fit using the model in (6.19) (denoted by the solid curves) to extract the tuning parameters (κ and ϕ) and the FSR of the ring, as well as to eliminate external optical path delays. The

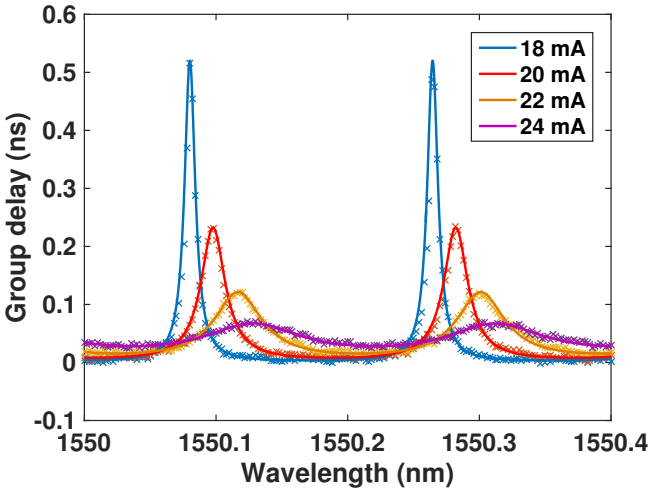

Figure 8.5: Measured delay spectra and the corresponding fits for single ORR at various current levels. The crosses denote the measured delays, whereas the solid curves denote the fits that use the model in (6.19).

excellent fit indicates the accuracy of the lossless model for the ORRs. Increasing the current increases the coupling coefficient while flattening the bell-shape delay spectrum, as expected, which demonstrates the inherent trade-off between the delay bandwidth and peak delay value. The FSR of the ORR was extracted to be 23.1 GHz, which is close to the designed FSR.

A notable shift of delay spectrum is observed in Fig. 8.5 while tuning the coupler in addition to the change of the delay curve shape. This is because, as discussed in Section 5.1.1 and Section 6.4.1, tuning the MZI coupler will not only change the coupling coefficient of the ORR, but also induce a phase chirp, which can be interpreted as a shift in the delay spectrum. This shift of the delay response and the change of coupling are consistent with the simulations in Fig. 6.17.

The group delay response of multi-ORRs can be optimized to have very wide bandwidth to overcome the beam squint in PAAs for wideband communications. In Section 6.2.2, the inherent trade-offs between bandwidth, ripple, and delay for ORR-based TTDs was studied using a genetic algorithm, and look-up tables of coupling coefficient

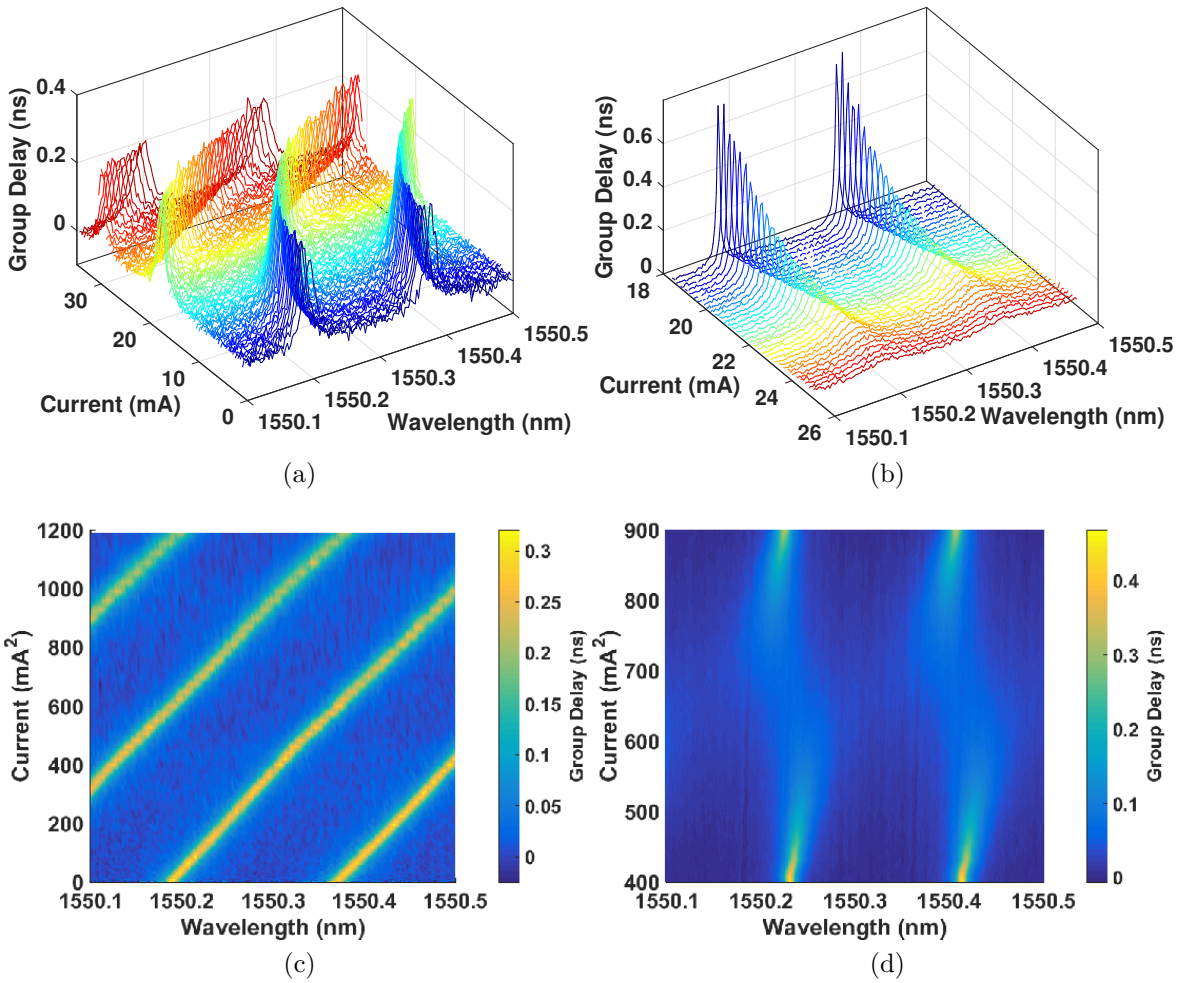

Figure 8.6: Measured delay responses of a single ORR for various tuning currents for (a) and (c) phase shifter, and (b) and (d) MZI coupler. (a) and (b) shows the delay spectra versus current, and (c) and (d) shows delay response versus current square.

and phase offset for the minimized ripple were built. Careful calibrations of a single ORR should be performed in order to precisely control the rings, to use the look-up table and to compensate MZI induced delay spectrum shift mentioned above.

Figure 8.6 shows the measured group delay spectra for a single ORR for varied phase tuning currents and coupling tuning currents. The parameters (κ and ϕ) are extracted by fitting the datum utilizing the lossless model described in (6.19) and the results are plotted in Fig. 8.7. Figure 8.6 (a) and (c) depicts the measured delay responses of a single

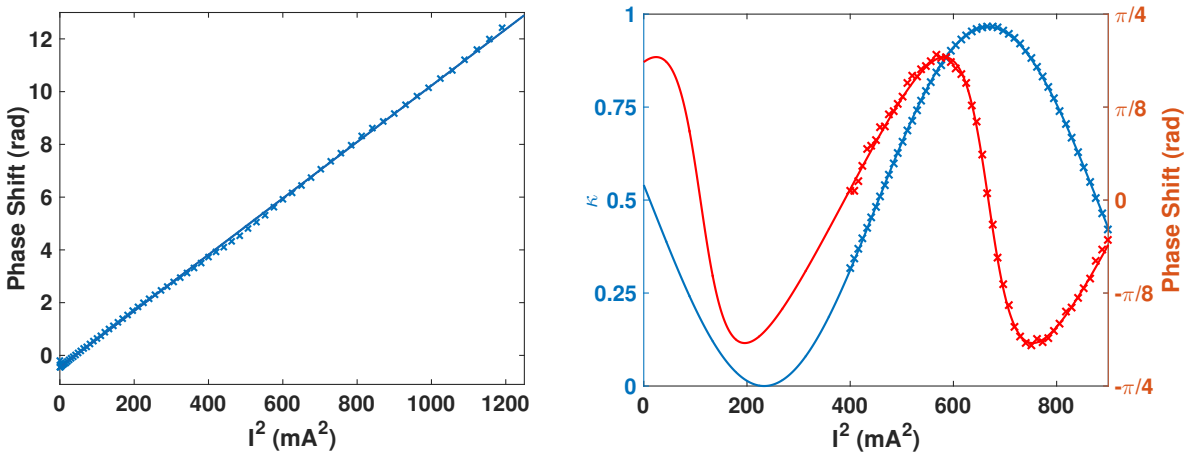

(a) (b)

Figure 8.7: Parameters (crosses) extracted from measured delay spectra, and their corresponding curve fits (solid lines) as a function of current squared. (a) Phase shift of the ORR phase shifter. (b) Coupling coefficient (blue) and phase shift (red) of the ORR MZI coupler.

ORR for various tuning current of the phase shifters, whereas Fig. 8.6 (b) and (d) shows the delay responses for various tuning current of the MZI coupler. Figure 8.6 (a) and (b) describe the change of the delay spectra versus tuning current, whereas Fig. 8.6 (c) and (d) focus on the change of the delay peaks versus the tuning current square. As depicted in Fig. 8.6(c), since the change of refractive index is proportional to the power dissipated in the heaters, the phase shift induced by the ORR phase shifter is proportional to the square of the current. Figure 8.7(a) shows the extracted phase shift versus the current square of the ORR phase shifter.

Ideally, the ring coupling coefficient is determined by the cross power transmission of the MZI coupler and has a cosinusoidal squared relation with respect to the square of current, and the MZI induced phase shift should have a linear relation, as described in (5.4) provided $\kappa = 0.5$. However, as indicated in Fig. 8.7(b), the coupling coefficient does not reach 1, neither the phase shift is perfectly linear with the current squared, which is due to the imperfections of the 3-dB couplers of the MZI. Taking the coupling coefficient

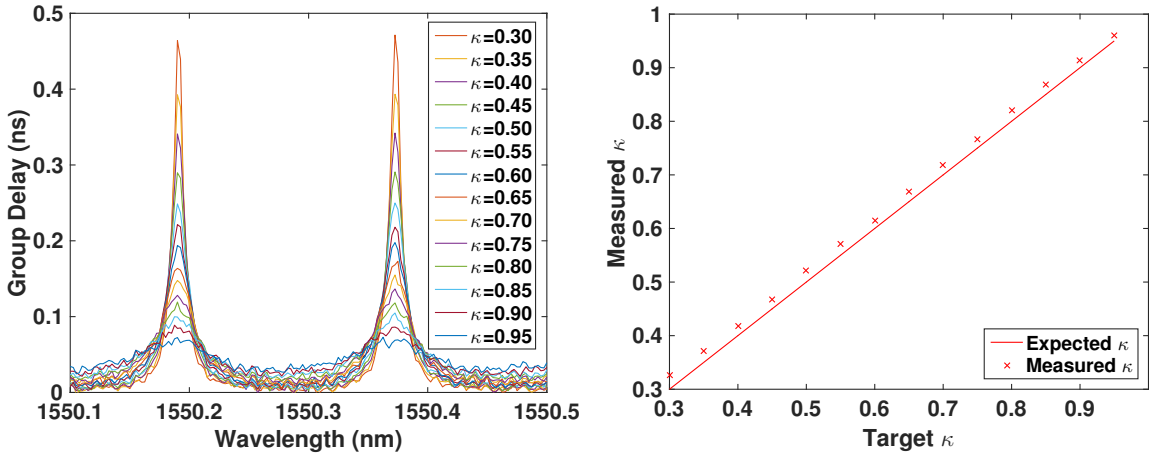

(a) (b)

Figure 8.8: Verification of calibration. (a) Measured delay spectra for a given central wavelength and various coupling coefficients using the calibration table. (b) Comparison between expected and measured coupling coefficients.

of couplers as a fitting parameter, the model was able to fit the data well as shown in Fig. 8.7(b) and the coupling coefficient κ was extracted as 0.6. A look-up table between the tuning currents and ring parameters was then built for tuning the ORR after the calibrations.

Verification was performed to test the accuracy of the ORR tuning look-up table. The group delay spectra for various coupling coefficients with a given resonant frequency were measured, as indicated in Fig. 8.8(a). Comparing to Fig. 8.5 where the ORR is not calibrated, the measurement indicates that the phase shift induced by the MZI coupler is fully compensated and the resonant frequencies of all the delay spectra are aligned as desired. Fig. 8.8(b) compares the target coupling coefficient with the measured coupling coefficient extracted utilizing the fitting method. In spite of a small offset, this figure shows a strong consistency between the measured and expected coupling coefficient. Therefore, it can be concluded that the verification demonstrates an accurate calibration and controllability for tuning the group delay of the ORR.

Table 8.1: A typical look-up Table for a 23 GHz FSR 3-ORR delay line.

Delay (ps)	Ripple (ps)	κ_1	κ_2 and κ_3	ϕ_2 or $-\phi_3$ (rad)
208.7	1.30	0.8154	0.7539	0.9249
182.6	0.48	0.8803	0.8261	1.0618
165.2	0.15	0.9269	0.8821	1.1806
147.8	0.05	0.9642	0.9359	1.3808
139.1	0.01	0.9792	0.9624	1.5590
113.0	0.25	0.9815	0.9490	2.8025
95.7	0.33	0.9752	0.8001	2.5066
78.3	0.19	0.9867	0.6588	2.7576
69.6	0.20	0.9891	0.4912	2.5032
26.1	2.32	0	0.6705	2.9489
8.7	0.82	0	0.3035	3.0273

κ_x and ϕ_x refer to the coupling coefficient and phase offset from the resonance of ring$_x$, as described in (6.19); ϕ_1 is set to zero in the simulation.

Ripple defines as the maximum deviation from the desired delay across the bandwidth.

8.3.2 Multi-ORR Delay Optimization

8.3.2.1 3-ORR Delays

Due to the fabrication variation, the initial statuses of the rings on the chip are not exactly the same. Fig. 8.9 shows the initial group delay response of a 3-ORR delay line with identical rings, which exhibits the delay spectrum of each ring with random phase-shifts and coupling-coefficients. After applying the calibration method to every ORR in the OBFN, the resonance frequency and coupling coefficient of each ORR could be individually and precisely controlled [85]. Table 8.1 is the optimized loop-up table of a 3-ORR delay line adapted to ORRs with 23 GHz FSR, based on Chapter 6. Each ORR in the delay line needs to be tuned to the corresponding state in the loop-up table to achieve the target TTD response. However, the OBFN exhibited a thermal crosstalk among different ORRs that reduces the tuning accuracy when attempting to simultaneously tune all the ORRs in a delay path. Therefore, in addition to using the

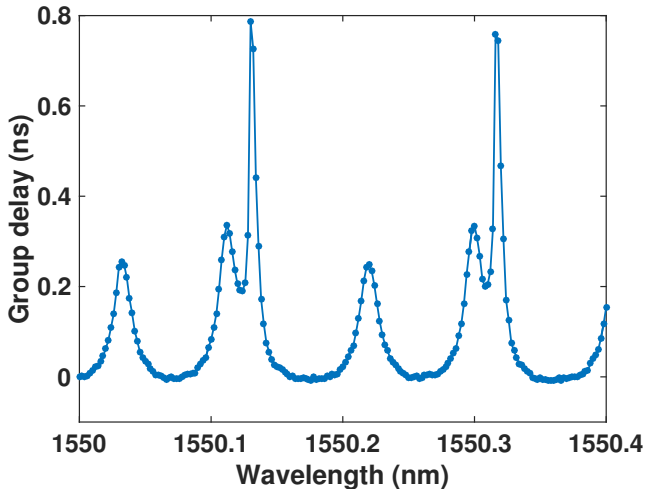

Figure 8.9: The initial group delay spectrum for a 3-ORR delay line without tuning.

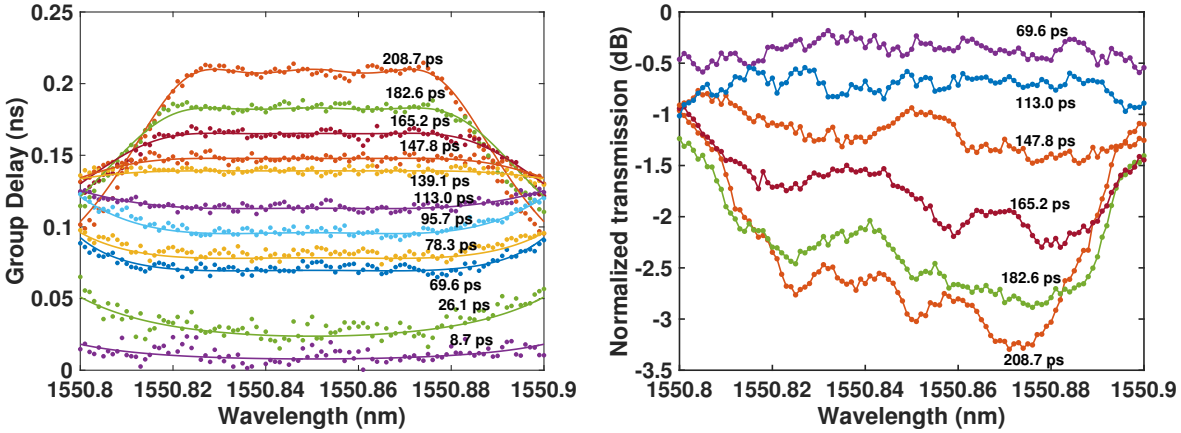

(a) (b)

Figure 8.10: (a) Measured group delay spectra with $6.3\ GHz$ TTD bandwidth (the points denote raw measured delays, whereas the solid curves denote theory) and (b) the corresponding normalized power transmission spectra for 3-ORR delay line with optimized tuning.

simulation data set from Table 8.1 to directly set the ORR state for flattened delay responses, the ORRs are manually and precisely tuned to compensate the offset induced by the thermal cross talk using the simulated delay response as a reference. Fig. 8.10(a) shows the simulated delay responses (solid curves) and measured delay responses (points) for a 3-ORR delay line. Comparing with Fig. 8.9, it shows that the delay spectra can be precisely controlled, and the measured results agree well with simulation results. A flattened group delay response of a 3-ORR delay line with a bandwidth of 6.3 GHz and a dynamic tuning range of 209 ps was achieved with the delay response ripple less than 1.3 ps, which corresponds to a phase shift of 37.5π for an 90-GHz signal. For half wavelength pitch antenna arrays at this frequency, this delay tuning range could feed a large scale PAA up to 1×38 1-D or 19×19 2-D array for a half-plane beamsteering. A larger scale of the PAA is available if a smaller beamsteering angle is desired. The normalized power transmission spectra of the 3-ORR delay line is shown in Fig. 8.10(b), which indicates that the delay line loss is less than 3.5 dB and the loss variation within

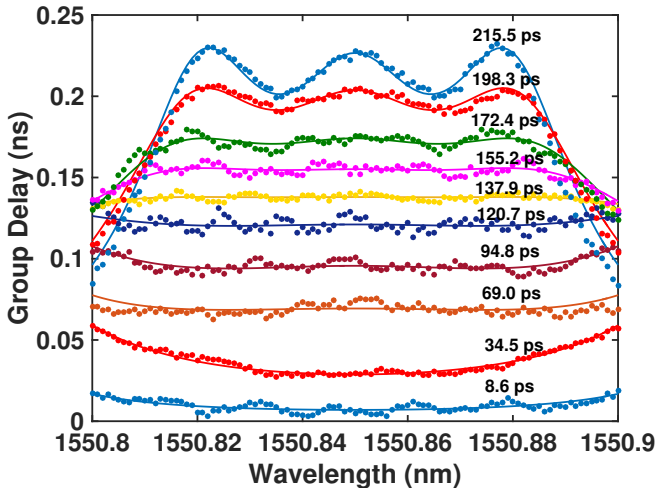

Figure 8.11: Ripple optimized group delay spectra for 3-ORR delay line with TTD bandwidth of 8.6 GHz. The dots refer to the measured delays, whereas the solid curves refer to the simulation result.

the TTD bandwidth of each delay configuration is less than 1 dB. The total power consumption of heaters for the 3-ORR line with this tuning range varies from 1.25 W to 2.57 W.

A larger bandwidth can be achieved by reducing the dynamic tuning range. A delay response for a bandwidth of 8.6 GHz, shown in Fig. 8.11(b), was also achieved using the same ORR tuning technique. As expected, the ripple at high delay is more noticeable, and the dynamic tuning range falls to 172.4 ps and phase shift of 31π with inperceptible ripple, which conforms the analysis of tradeoffs between the bandwidth, delay and ripple in the multi-ORR delay line in Section 6.2.2.

8.3.2.2 OBFN Delays

In addition to a single delay line, the delay response of complete OBFNs are tuned and characterized. As mentioned in Chapter 6, two 1×4 OBFNs with different ring sharing topologies are realized. Using the same optimization technique for single delay lines, Fig. 8.12 (a) and (b) show the optimized delay response of all the four paths of the

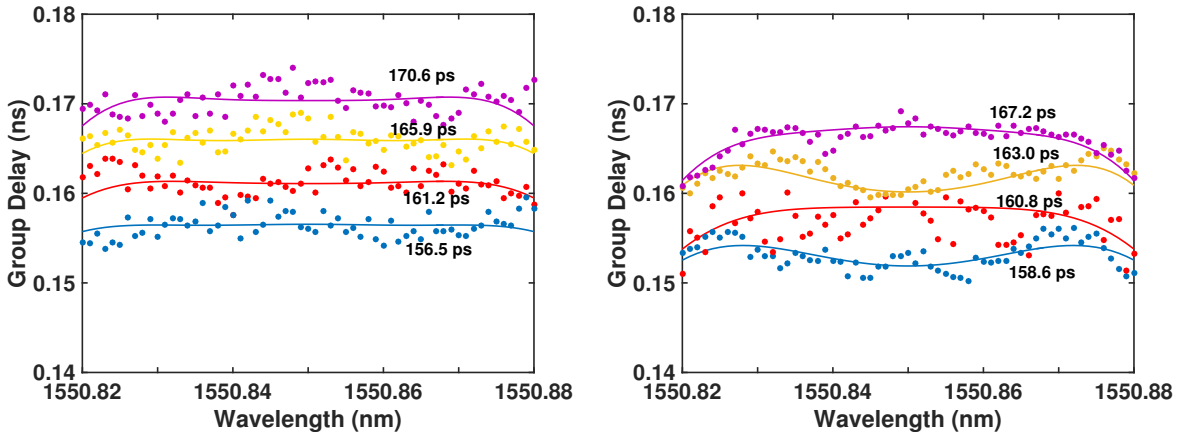

Figure 8.12: Ripple optimized group delay spectra for 3-ORR delay line with (a) one shared ring and (b) two shared rings at the TTD bandwidth of 6.3 GHz. The dots denote the measured delays, whereas the solid curves denote the simulation result.

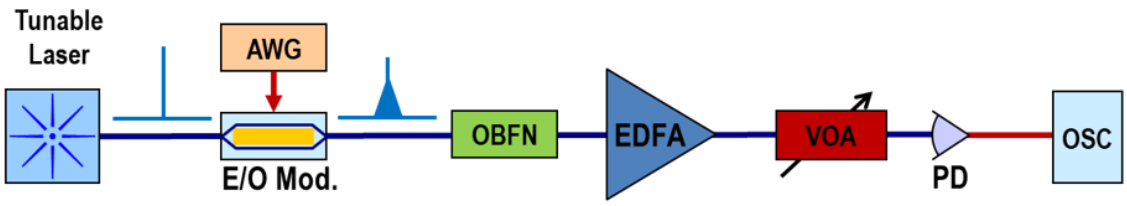

Figure 8.13: Data transmission test setup for single 3-ORR true time delay lines. (OSC: oscilloscope; Mod.: modulator; AWG: arbitrary waveform generator; VOA: variable optical attenuator; PD: photodiode.)

OBFN for the topologies of with one shared ring (Fig. 6.13 (b)) and two shared rings (Fig. 6.13 (b)) with a TTD bandwidth of 6.3 GHz, respectively. Each path was tuned to have a linear delay distribution with delay increments $\sim 4.5\,ps$, which is equivalent to a 51^o of beamsteering angle for a $90\,GHz$ half-wavelength pitch antenna array. As shown, the measured data, denoted by the dots, has relatively large variation around the simulation delay response. This is because the the measurement system has a resolution of ~ 10 ps, which beyonds the delay difference. Actually, the OBFN tuning resolution is better than resolution of the delay measurement technique. Comparing with Fig. 8.12 (a) and (b), we can see that the topology sharing two rings ((Fig. 6.13 (c)) yields a ripple around 1.5 ps, whereas the topology sharing one ring ((Fig. 6.13 (b)) provides a inperceptible ripple. Therefore, for a 3-ORR based OBFN, the topology sharing one ring in the common path can provide high quality TTD response while maintaining a moderate system complexity, which is promising for wideband applications.

8.3.2.3 Data Transmission Delay Experiment

Systematic tests of the 3-ORR delay line using the setup in Fig. 8.13 was performed to evaluate the 3-ORR delay overall performance [146, 147]. An external cavity laser (ECL) is modulated with a $3\,Gbps$ OOK NRZ data signal by a Mach-Zehnder modulator (MZM) driven by an arbitrary waveform generator (AWG), and then sent into a OBFN

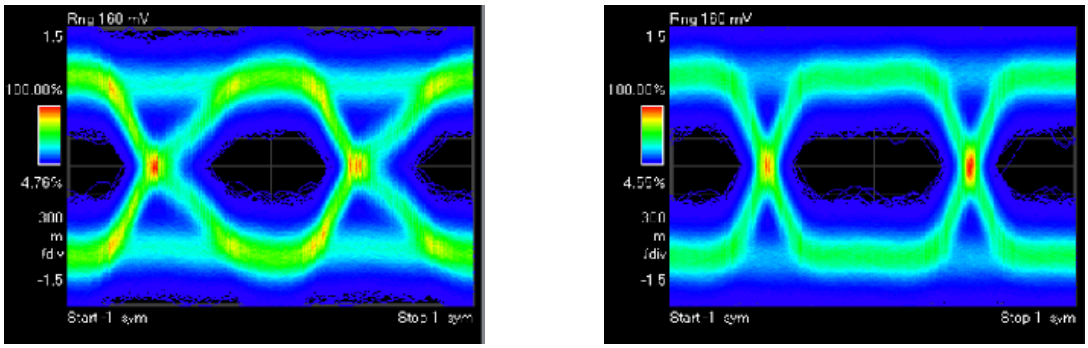

(a) (b)

Figure 8.14: Comparison of eye diagrams for 3 *Gbps* OOK data transmitted through 3-ORR delay line with (a) no tuning and (b) optimized to 155.2 *ps*.

chip, which is optimized to various TTDs with the bandwidth of 8.6 GHz. The output of the chip was amplified by an EDFA and then attenuated by a variable optical attenuator. The signal then is detected by a photodiode and monitored by an oscilloscope to acquire the eye-diagrams. Figure 8.14 compares the eye diagrams for the 3 *Gbps* data transmitted through 3-ORR delay line for no tuning and tuned to 155.2 *ps*. As depicted in Fig. 8.9, the delay line does not initially form a TTD delay response without tuning of the ORRs due to the fabrication variation. The signal is distorted and may become an issue when the bit rate is increased, as illustrated in Fig. 8.14(a). As a comparison, when optimized to a TTD of 155 *ps* , no noticeable distortion to the signal was observed and the signal quality is preserved, as depicted in Fig. 8.14(b). Both eyes were measured at the optical power of $-15\,dBm$. Figure 8.15 shows the eye diagram after the 3-ORR tunable TTD line over the delay range of $0-209\,ps$, in which open and clear eyes are preserved. The optical power at the photodiode was measured to be 3.5 dBm, and the delay of the transmitted signal can be continuously tuned up to 209 *ps*, as shown in Fig. 8.11. In the desired working range $(0-172.4\,ps)$, no signal deterioration was observed, whereas for higher delays, small signal distortion was observed due to the increasing ripple (dispersion) in the delay response. This test confirms the accurate control and continuous tunability for

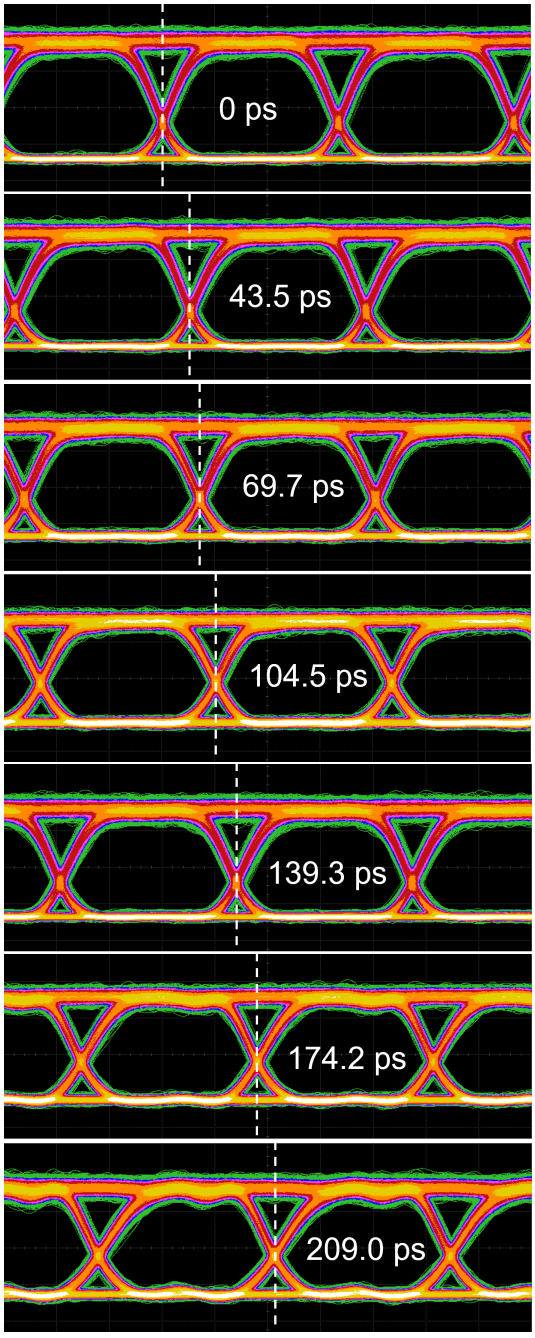

Figure 8.15: Tunable 3-ORR true time delay line test with 3 *Gbps* OOK NRZ modulation for tuning range of 0 to 209 *ps*.

the optimized 3-ORR delay line.

8.4 SDL-OBFN Delay Response

The experimental setup for SDL delay response calibration is described in Fig. 8.16. Similar to the the characterization of ORR based delay lines and the corresponding OBFNs, a group delay measurement system is also employed to calibrate and tune the MZI switches in the SDL-OBFN. However, as indicated by the OBFN schematic in Fig. 5.12(a), since up to 5 delay stages are cascaded in the each SDL, 6 analogical MZI switches need to be tuned simultaneously to the "on" or "off" state precisely. Otherwise, based on the analysis in Chapter 5, the optical signal with different delays will intermix with each other, which will cause delay ripple in the delay response. And the delay ripple is severe as the number of stages increase. It is different to tune the 6 MZI switches at the same time to achieve designed delay response by just monitoring the delay spectrum from the group delay measurement system. Additionally, the longest loop delay is 4.5 ps in the SDLs. The path delay of the delay loop is smaller than the delay measurement resolution ($\sim$ 10 ps), which makes the tuning the SDL even more difficult. Tuning the MZI switches individually is the best tuning strategy for the SDLs. However, no tap signal is reserved in each delay stage due to the limited chip footprint, as indicated by the OBFN layout in Fig. 5.12(b). Alternatively, an IR camera is placed on top of the chip to monitor the optical intensity in the waveguide by observing the photon scattering. As the chip is fabricated using ultra-low loss silicon nitride technology, the scattering is very weak. Therefore, a very sensitive HAMAMATSU InGaAs infrared (IR) camera is employed with a IR $50\times/0.42$ lens (Mitutoyo, NIR). Figure 8.18(a) and (b) illustrate the IR images of the same delay stage of the SDL-OBFN captured by the IR camera for the "on" and "off" state of the delay loop, respectively. The high-lighted lines refer to the

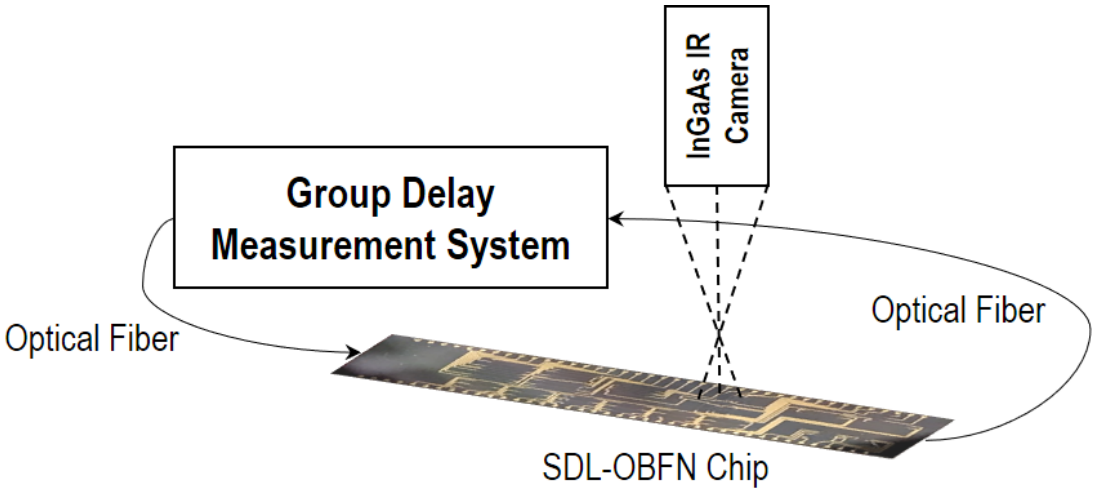

Figure 8.16: SDL-OBFN chip calibration setup.

waveguide with light propagating, and the dark and bold areas refer to the metal traces on top of the chip. As shown, the scattering of the light can be observed very clearly, which could reduce the tuning complexity of the SDLs and OBFN.

The tuning of the SDL is described by the flowchart enclosed in the dash box in Fig. 8.17, which comprises two tuning steps – the coarse tuning and the fine tuning. The coarse tuning is achieved with the assistant of the IR camera. Firstly, the field view of the IR camera was positioned to the delay loop right after the first MZI switch that to be tuned. Then the MZI was slowly tuned until the scattering strength in the designed waveguide is visually maximized. It may not reliable for human eyes staring at the IR image to recognize the maxima intensity, especially when the MZI is tuned close to the "cross" or "bar" state where the changes is very small with the tuning that can hardly be observed. Instead, we can focus on the scattering of the two output waveguides of the coupler after the delay path, and then sweep the laser waveguide very fast. Since the two unequalized delay waveguides and the coupler form a unbalance MZI, if the switch is not 100% routing the optical signal, the optical power transmission spectrum

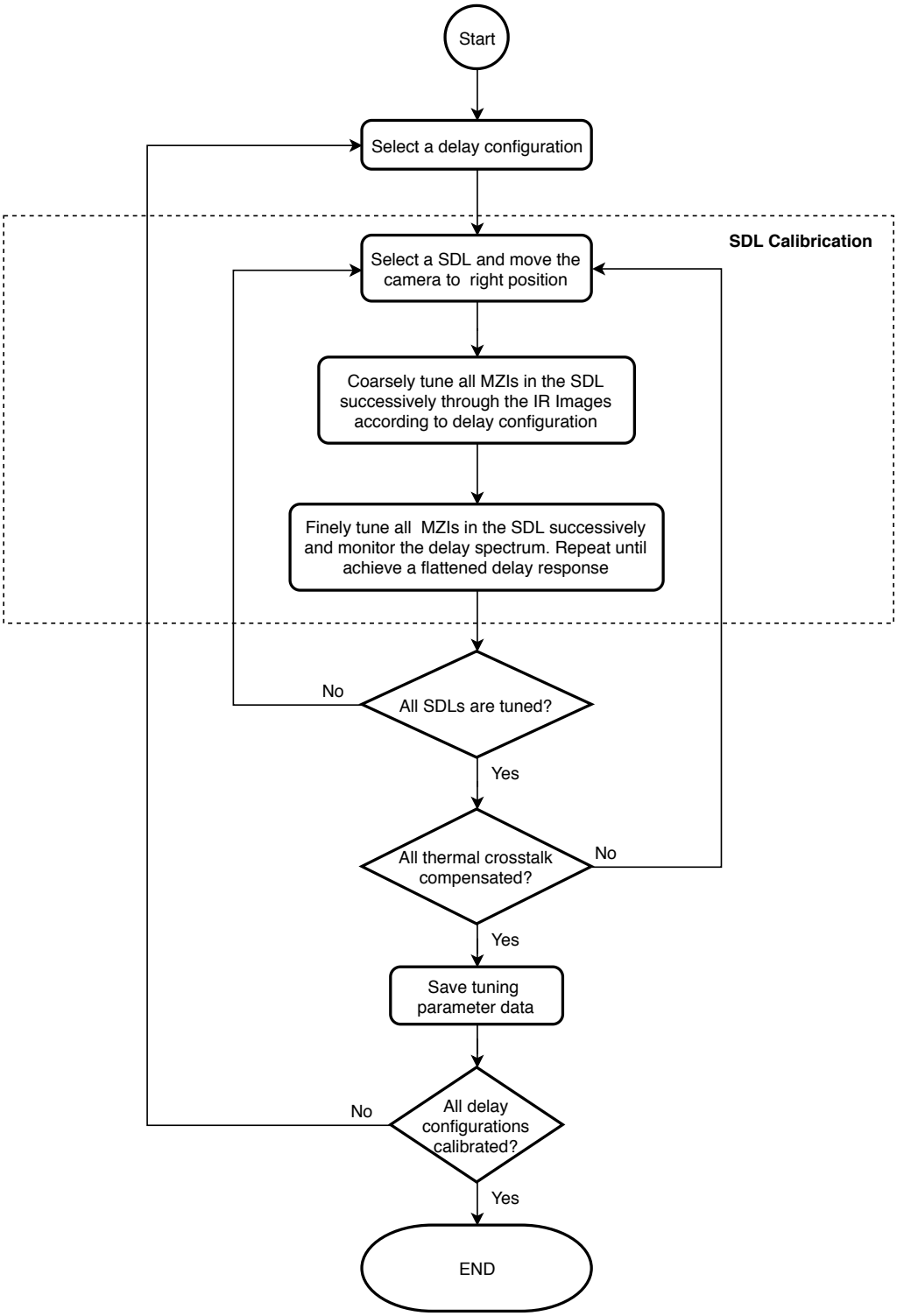

Figure 8.17: The tuning flowchart for SDL-OBFN calibration. The steps enclosed in the dash box are for single SDL calibration.

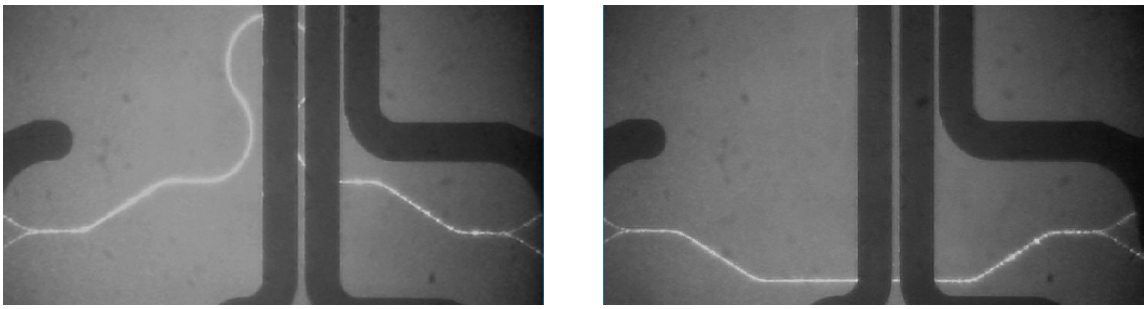

(a) (b)

Figure 8.18: IR images of the same delay stage of the SDL-OBFN captured by the IR camera demonstrating (a) the "on" state and (b) the "off" state of the delay loop. (The high-lighted lines refer to the waveguide with light propagating, and the dark and bold areas refer to the metal traces on top of the chip).

in the output of the coupler is not constant, which can be interpreted as blinks in the IR image in time-domain when sweeping the laser wavelength. A blink is much easier to be observed by human eyes and can help to achieve more accurate tuning of the MZI switches of the SDL using IR camera. Note that, this technique works only for bar-state MZI switches in which optical signals can be ensured totally routed, based on the analysis in Chapter 5. As for cross-state MZI switches, the tuning has less requirement since this SDL architecture allows imperfect switching of optical signal in cross-state without deteriorating the TTD quality.

The MZIs in the SDL were finely tuned after the coarse tuning with IR cameras. The delay spectrum is monitored in real-time over a large range of wavelength using the group delay measurement system. The MZIs were slowly and successively tuned one after another starting for the first stage to flatten the delay spectrum as much as possible. This fine tuning may be repeated several times until the most flattened delay spectrum is achieved. Figure 8.19 depicts the measured TTD response of the four 5-stage SDLs in the 1×4 SDL-OBFN with a TTD bandwidth of around 8 nm. For each SDL, the delay for all the delay units are bypassed (conf. 1) is considered as the reference (zero delay).

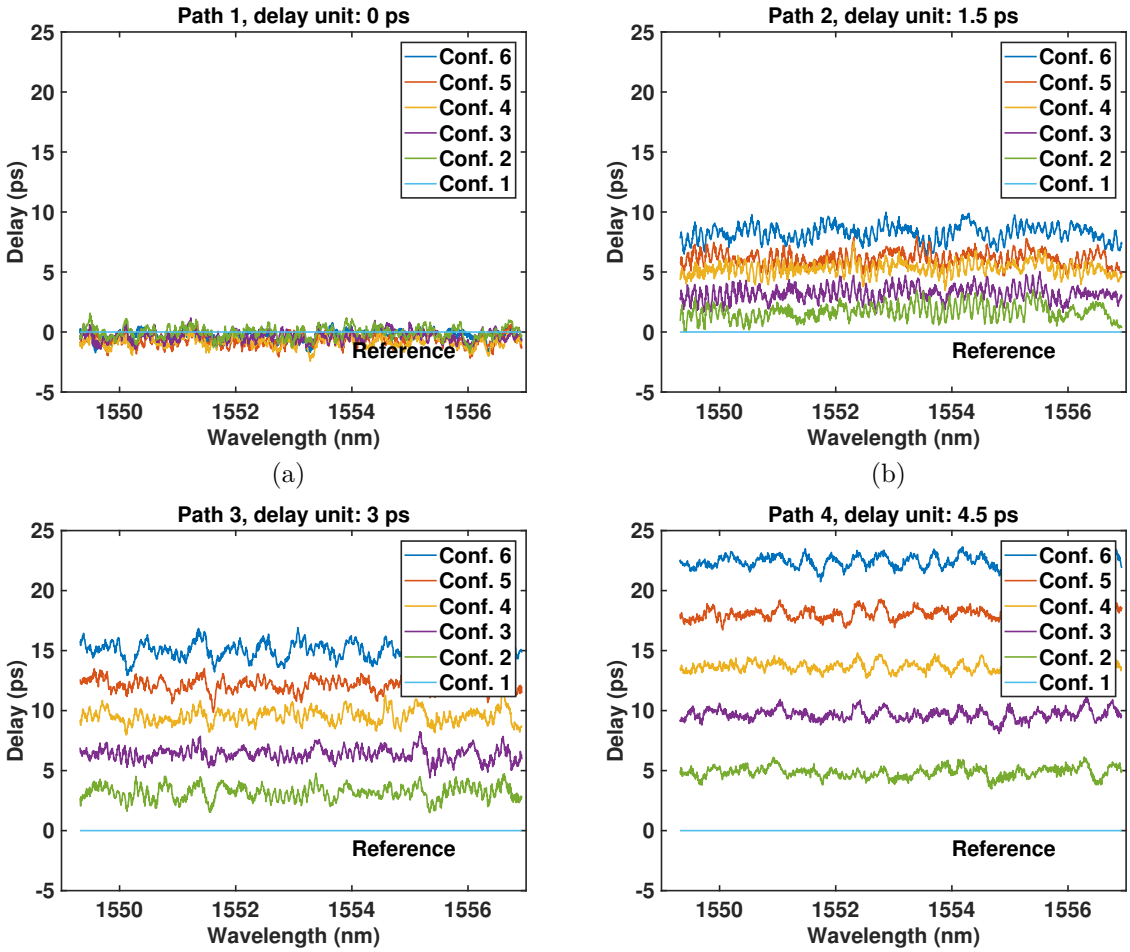

Figure 8.19: The measured TTD responses supported by the four 5-stage SDLs in the SDL-OBFN with the loop delay of (a) 0 *ps*, (b)1.5 *ps*, (c) 3 *ps* and (d) 4.5 *ps*, respectively. Each SDL can support 6 delays.

As described by the schematic in Fig. 5.12(a), Path 1 in the OBFN is a pure waveguide that generates the reference delay. The delay of this path is not changed for different configurations, and thus, the measured delay response of path 1 in Fig. 8.19(a) is always zero. As for path 2 to path 4, the delay unit for each SDL is designed to delay by 1.5 *ps*, 3 *ps* and 4.5 *ps*, respectively. Therefore, in Fig. 8.19 (b) - (d), each SDL increases by corresponding amount of delay from conf. 1 to 6, and this delay increments are consistent

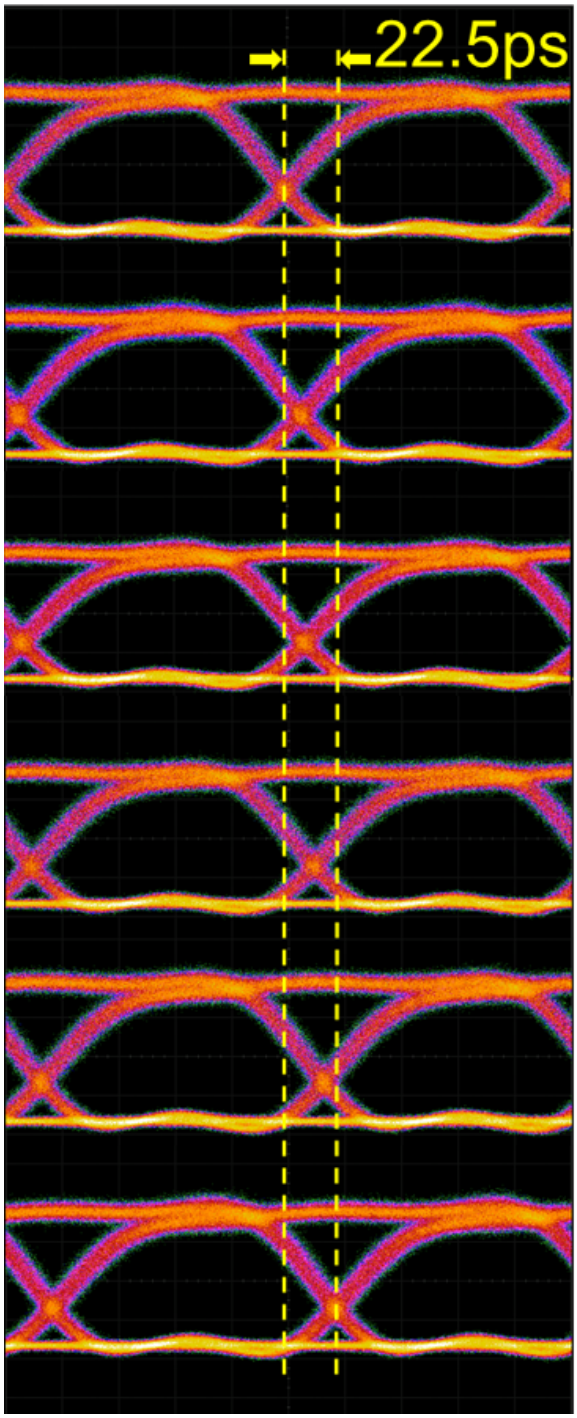

Figure 8.20: Test of tunable SDL with 10 *Gbps* OOK NRZ modulation for 6 delays ranging from 0 to 22.5 *ps*.

with the design. Note that due to the the resolution of the delay measurement system, the measured delay spectrum was smoothed with a 0.15 nm average window. Moreover, similar as the 3-ORR delay lines, the overall delay performance of a SDL is systemically tested by sending through a data signal using the same experimental setup described in Fig. 8.13. Since a SDL can support a very large TTD bandwidth, and has a relatively small overall delay range, a 10 *Gbps* NRZ OOK data signal, instead of 3 *Gbps* for 3-ORR delays, are sent to the SDL (path 4). The optical at the photodiode was measured as -6.5 dBm. Figure 8.20 shows the eye-diagrams of the data signals after passing through the SDL. The eyes illustrate that the signal is delayed by the SDL as expected from 0 to 22.5 ps, and no impact to the signal quality is observed for different delays.

The tuning of the entire OBFN is more complex that a single SDL calibration, and the tuning flowchart is illustrated in Fig. 8.17. Firstly, a delay configuration is picked to determine, which group of switches ($S_1..S_6$) need to be tuned to cross-state. Then use the same tuning steps of a single SDL calibration to coarsely and finely tune each of the SDLs in the OBFN successively one after another. Since a large volume of heaters are involved in the OBFN (18 heaters in total), a large amount of heat transfers through the chip. These heat flow will affect the thermal tuning of other phase shifters nearby, i.e., the thermal crosstalk. The thermal crosstalk is usually small since the MZI switches are designed with large separation, but can still affect the tuning accuracy. To compensate this thermal crosstalk, the steps of tuning all the SDLs in the OBFN are repeated for several iterations until all the paths output delays with flatten delay spectrum, as described in Fig. 8.17. Figure 8.21 shows the calibrated delay response of the OBFN for 6 delay configurations, respectively. The delay for each SDL is referenced to the SDL delay for all the delay units are bypassed (conf. 1). As shown, the delays are distributed evenly with the delay increment between two adjacent path of 0, 1.5, 3, 4.5, 6, and 7.5 ps, respectively, which is consistent with the design of the SDL-OBFN for feeding a linear

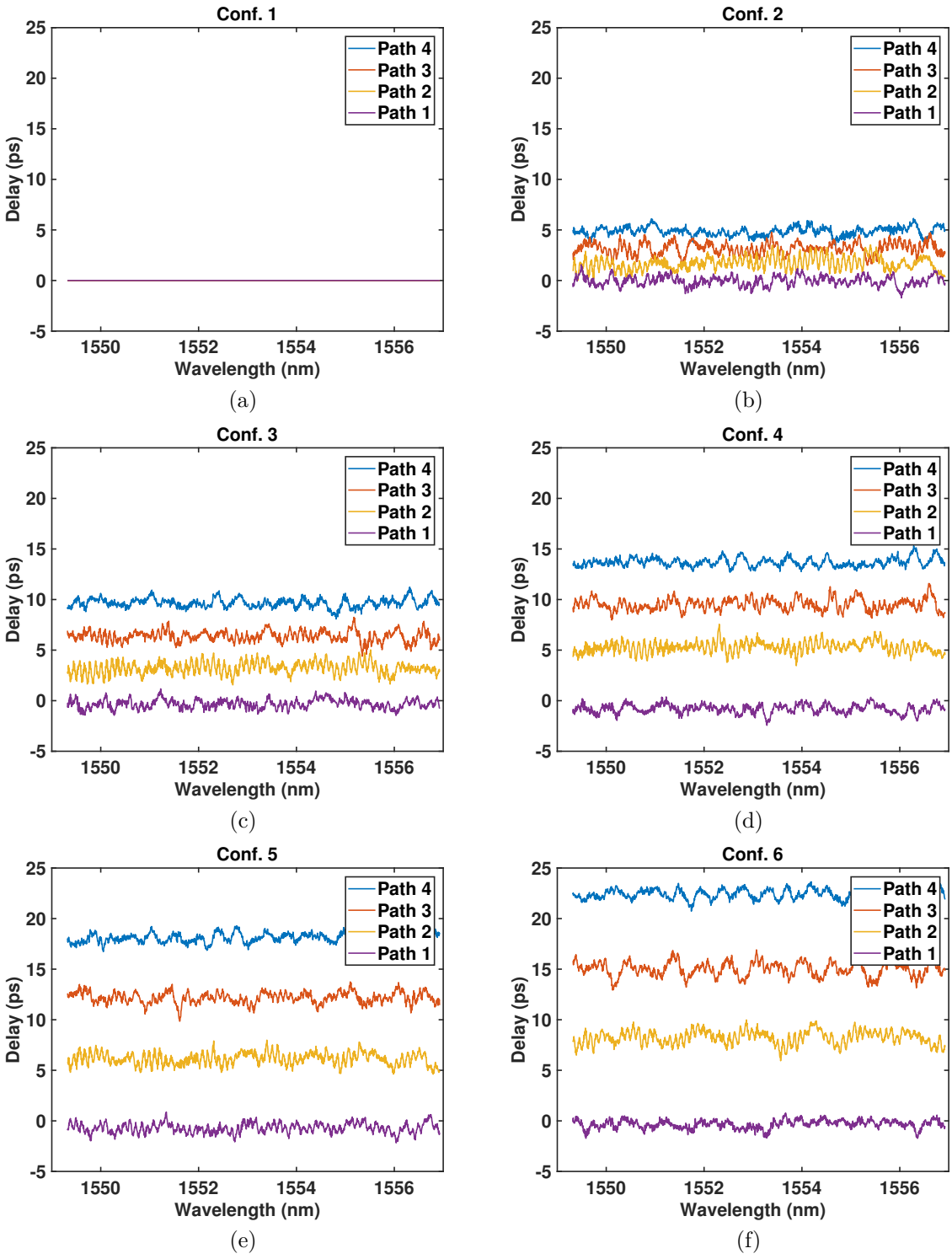

Figure 8.21: The delay responses of the 1×4 SDL-OBFN with 6 configurations for linear PAAs.

PAA. Similarly, the measured delay spectrum data was averaged over 0.15 nm to smooth the delay response to reduce the impact of the limit of the delay measurement resolution.

8.5 Summary

The delay responses of the SDLs, ORR delay lines and their corresponding OBFNs realized on SiN were characterized in this chapter. A phase shift method was applied to measure the delay spectra of the delay lines in real-time, and the in-house made multi-channel controller and control software were used to drive the heaters on the chips. For single delay lines, the 3-ORR delay line demonstrated a TTD delay response with a continuously tunable range pf 209 ps and 172 ps over a bandwidth of 6.3 GHz and 8.6 GHz, respectively, which also conforms the tradeoffs between delay value, ripple level and bandwidth for multi-ORR delay lines discussed in Chapter 6. Whereas the three 5-stage SDLs demonstrated 6 discrete delays equally distributed in the range of 7.5, 15 and 22.5 ps, respectively, with a TTD bandwidth over 8 nm. NRZ OOK modulated optical signals were sent through both the ORR delay lines and SDLs, and the shift of eyes in the eye diagrams verifies that all the delay lines delay the signal as expected. As for OBFNs, the ORR-OBFNs were optimized to generate a linear delay response with an delay increment of 4.6 ps, whereas the SDL-OBFN was tuned to generated 6 linear delay responses with delay increments of 0, 1.5, 3, 4.5, 6, 7.5 ps, respectively. Both the ORR-OBFNs and SDL-OBFNs shows great potential for feeding linear PAAs. However, the ORR based OBFNs exhibit the capability of continuous beam angle support but limited bandwidth and complex controls, whereas the SDL based OBFNs can support extremely large bandwidth and simplified controls but can only support discrete beam angles.

Chapter 9

Millimeter Wave Signal Generation and Beam Steering

In previous chapters, two generations of integrated 1×4 OBFNs chips for mmW beam steering based on ORRs and SDLs were demonstrated. Tuning optimizations were applied to both of two OBFNs for TTD response, and the delay responses were characterized with sophisticated measurement and control systems. Beyond that, in this chapter, mmW signal generation experiments will be presented demonstrating 41 GHz with ORR-OBFNs and W-band signal with SDL-OBFNs, respectively. With the SDL-OBFN, TTD based beam steering experiments will be demonstrated, which, to the author's best knowledge, is the first TTD based W-band mmW signal beam steering experiment with integrated OBFNs.

9.1 Chip Packaging

Since the system for mmW generation and beam steering is complex, the OBFN chips were packaged to increase the OBFN chip reliability and reduce the environmental impacts such as vibration and air turbulence. The picture of the packaged chip is depicted in Fig. 9.1(a). As shown, several components were packaged including a thermoelectric cooler (TEC), a thermistor, fiber arrays and high density electrical connection cables.

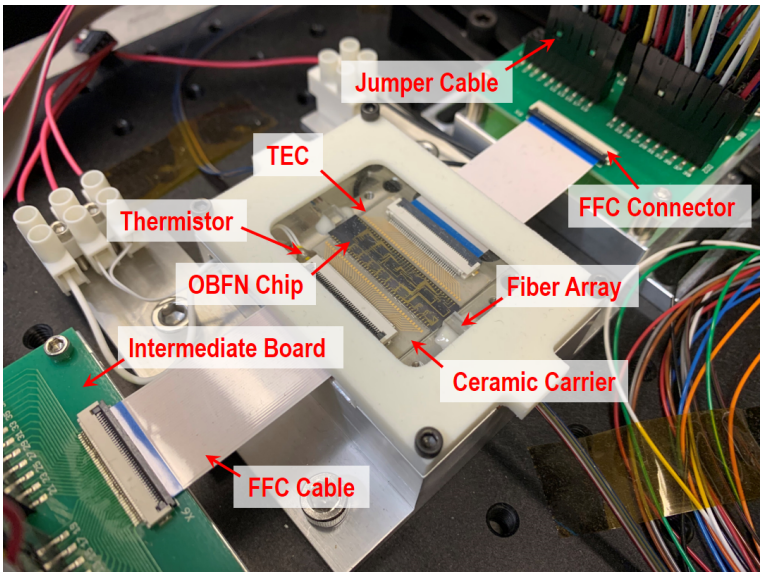

(a)

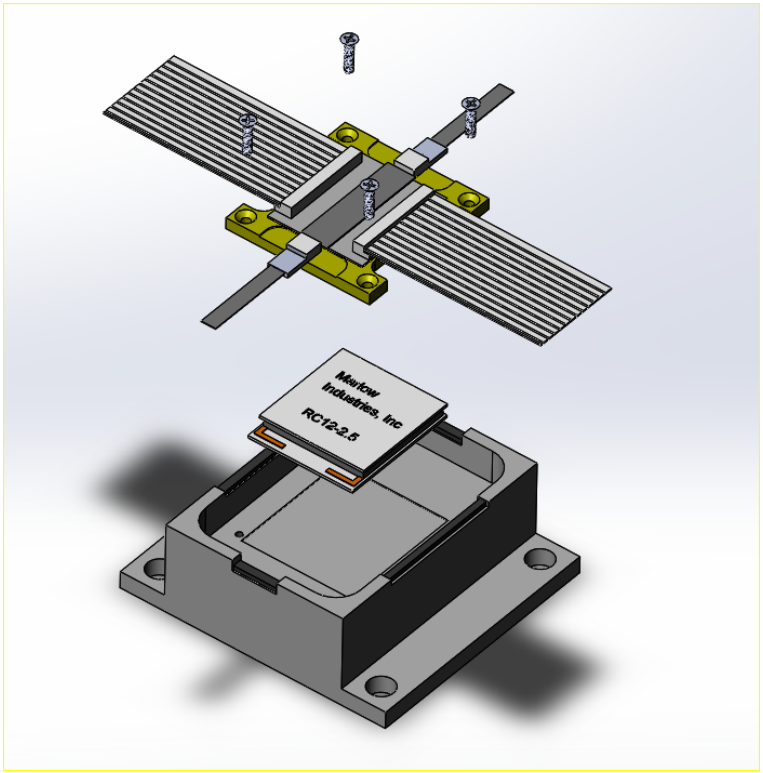

(b)

Figure 9.1: (a) Actual picture and (b) assembling diagram of the packaged chip.

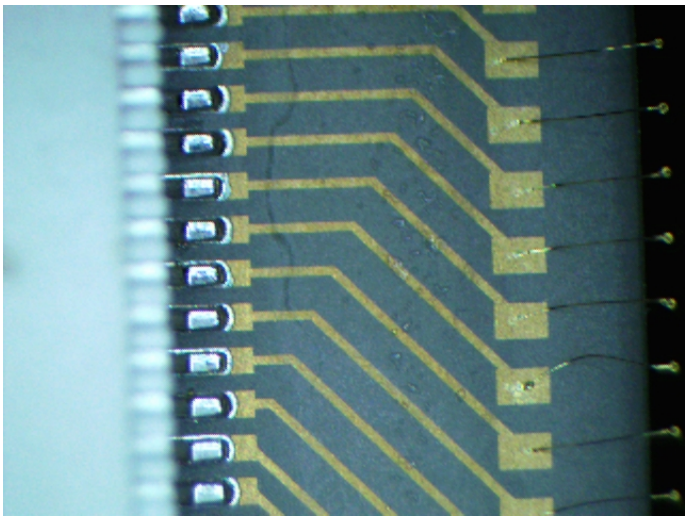

Figure 9.2: Close-up picture of the metal traces, connector-to-carrier soldering and chip-to-carrier wirebonding.

An aluminum nitride (AlN) ceramic board was designed and fabricated in house as a intermediate carrier. AlN ceramic is a very good thermal conductive dielectric material, which is very suitable as a carrier for a chip with thermal tuning. Metal layer with compositions of Ti(80 nm)/Pt(80 nm)/Au(800 nm) is deposited on the carrier, and patterned with pads and traces to route the metal connections on the chip to two 40 pin high density flexible flat cable (FFC) connectors. The chip is bonded to the carrier using a Norland one part adhesive. Norland, although not thermally conductive, gives a very thin bond line that is flat and is very stable. Then the 80 pads on the chip were wirebonded to the carrier. Two 40-pin surface mount FFC connectors with 0.5 mm pitch are soldered directly on the carrier using reflow soldering technique and connect to a second stage intermediate board. Figure 9.2 shows the close-up picture of the metal pattern, wirebonding, and soldered connection on the AlN carrier. A thermistor is also mounted on the AlN carrier for sensing the temperature of the chip.

Figure 9.2 describes the detailed assembling diagram for the chip packaging. After the procedures mentioned above, the AlN carrier is then attached to a precisely machined

shim. Two fiber arrays are automatically aligned to the edges of the chip using a closed loop 6-axis piezoelectric station, and then the fiber arrays are bonded to the shim with 3408UV epoxy. The 3408UC epoxy gives very good mechanical stability. It is a thick adhesive and the component to be bonded is slightly pressed into the epoxy to assure it attaches the carrier and compensates the gaps. The shim is made of Kovar. Kovar is not a very good thermal conductor, but has a much better coefficient of thermal expansion, so you will not lose fiber alignment when the temperature changed by the TEC and the chip. The shim was then mounted into a aluminum base with a TEC in between, and then secured by a glass lid. Finally, the I/Os of the packaged chip end up with multiple single mode fiber FC connectors for optical connections, two 40-pin FFC cables for electrical currents. The two FFC cables are connected to intermediate PCBs, which can configurate the connections between the OBFN controller and the chip with jumper cables.

9.2 41 GHz mmW signal Generation

A system test was performed for mmW generation through frequency up-conversion heterodyne process with one path of the OBFN[40, 148, 149]. The schematic of the experimental setup is depicted in Fig. 9.3. A coherent laser light is modulated by driving a null biased MZM modulator (EO Space 50 GHz 3-dB bandwidth) using a local oscillator

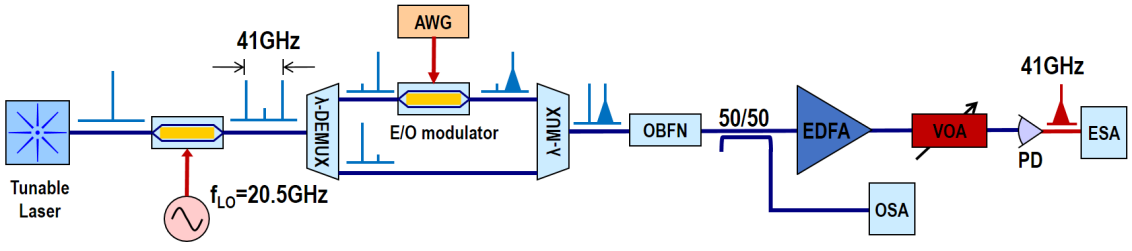

Figure 9.3: mmW generation and delay experiment test setup. (ESA: electrical spectrum analyzer; OSA: optical spectrum analyzer; DE/MUX: de/multiplexer.)

(LO) with half the mmW carrier frequency, which suppresses the central optical carrier but generates two dominant optical sidebands spaced by the mmW carrier frequency. A standard wavelength division multiplexing (WDM) with 50 GHz channel grids separates the two sidebands. One sideband is modulated by a quadrature biased MZM driven by an arbitrary waveform generator (AWG) and serves as the data tone, and the other sideband serves as the reference tone for the heterodyne process. The two optical tones are combined by another identical WDM and both tones are coupled to the integrated OBFN chip. The signal is split into four paths and appropriately delayed by the OBFN depending on the desired beamsteering angle. The output signal of one path is then amplified by an erbium doped fiber amplifier (EDFA). After properly attenuation by the variable optical analyzer (VOA), the two optical sidebands heterodyne at a high speed photodiode to generate the mmW signal with data encoded. Since the polarization of the two optical tones must be aligned to maximize the efficiency in the heterodyne process, polarization maintaining fibers are employed for all the optical connections, which makes the system simple and robust.

The laser wavelength, center wavelength of the delay line and the channel wavelengths of the WDMs need to be matched in the system. The wavelength of the laser is set to the middle between two WDM channels at 1551.10 nm. One path of the OBFN chip is used and optimized to have a delay of 157 ps and bandwidth of 8.6 GHz centered at the central wavelength of the data sideband. The preliminary test was done at mmW frequency of 41 GHz, where the LO is set to 20.5 GHz. The output signal from the OBFN chip is tapped and monitored by an optical spectrum analyzer, which shows the two dominated sidebands centered at 1550.94 nm and 1551.27 nm, respectively. Figure 9.4 shows optical spectrum for one path of the chip outputs after amplified by EDFA and the transmission responses of the WDM. The laser wavelength is suppressed with the null-bias modulation and two dominate ± 1 st order sidebands are separated by 41 GHz.

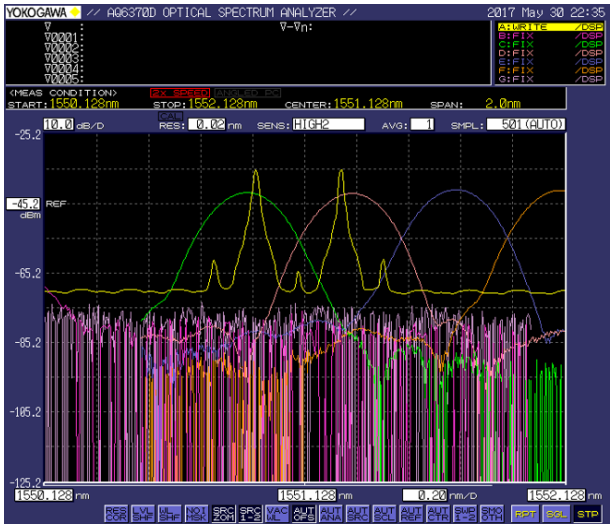

Figure 9.4: Optical spectrum for one path of the chip outputs after amplified by EDFA and the transmission responses of the WDM. The yellow line denotes the optical spectrum, whereas the green, pink, blue and orange line denote the transmission spectrum of different channels of the WDM .

The AWG generates a 3 *Gbps* OOK NRZ signal, and optical power before the photodiode is attenuated to 5 dBm. Figure 9.5 provides the generated 41 GHz mmW signal spectrum with the data band, which is measured by an high speed electrical spectrum analyzer. The available data rate of the system is determined by the TTD bandwidth of the delay line. In our case, the bandwidth of the delay line is 8.6 GHz, which can support a much higher data rate by employing more advanced data modulation formats. In addition, the mmW frequency generated by the up-conversion process is widely tunable and can go up to double of the LO and the modulator bandwidth. In this experiment, the 41 GHz was chosen because the ESA can only measure signal up to 46 GHz without using any mixer. Given the data bandwidth, 41 GHz is the highest carrier frequency can be used with the experiment. Also, since 50 GHz WDMs are employed, the 41 GHz can be fitted into the WDM channel grids. Moreover, as discussed in Chapter 6, the ORR-OBFN has a periodic response with $FSR = 22\ GHz$, which can support signal frequencies with integral numbers of FSR such as 44 GHz. For a 41 GHz signal, given

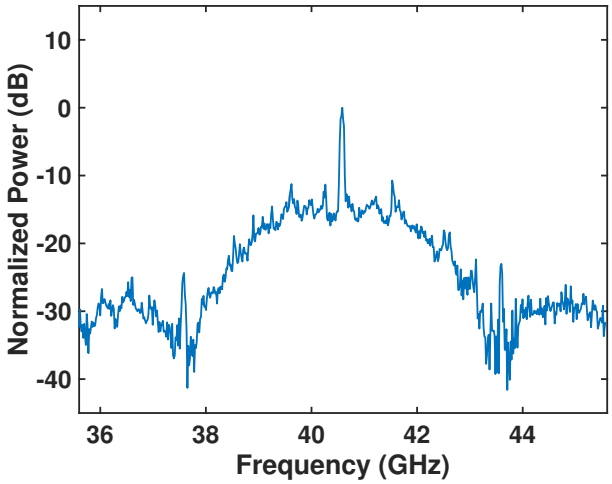

Figure 9.5: Normalized electrical spectrum at the photodiode with 3 *Gbps* OOK NRZ modulation.

that the reference optical tone has a very narrow linewidth and thereby does not require much bandwidth, we can focus on the alignment of data tone to the center of the OBFN TTD response. The reference tone can still lie in the bandwidth of the TTD response.

9.3 W-band mmW Signal Beam Steering

W-band mmW signal experiment was also carried out in this work [63, 150, 151]. In addition to the signal generation, a beam steering experiment of the mmW signal with the integrated OBFN chip was also demonstrated. Similar to the 41 GHz signal generation experiment above, the W-band signal was also generated using a frequency up-conversion heterodyne process. The schematic of the system is depicted in Fig. 9.6(a) and a picture of the experiment setup of the photonic generation stage is given in Fig. 9.6(b). The laser light is modulated by driving a null biased modulator with a local oscillator at half of the mmW frequency $f_{mmW}/2$, which suppresses the laser optical carrier but generates

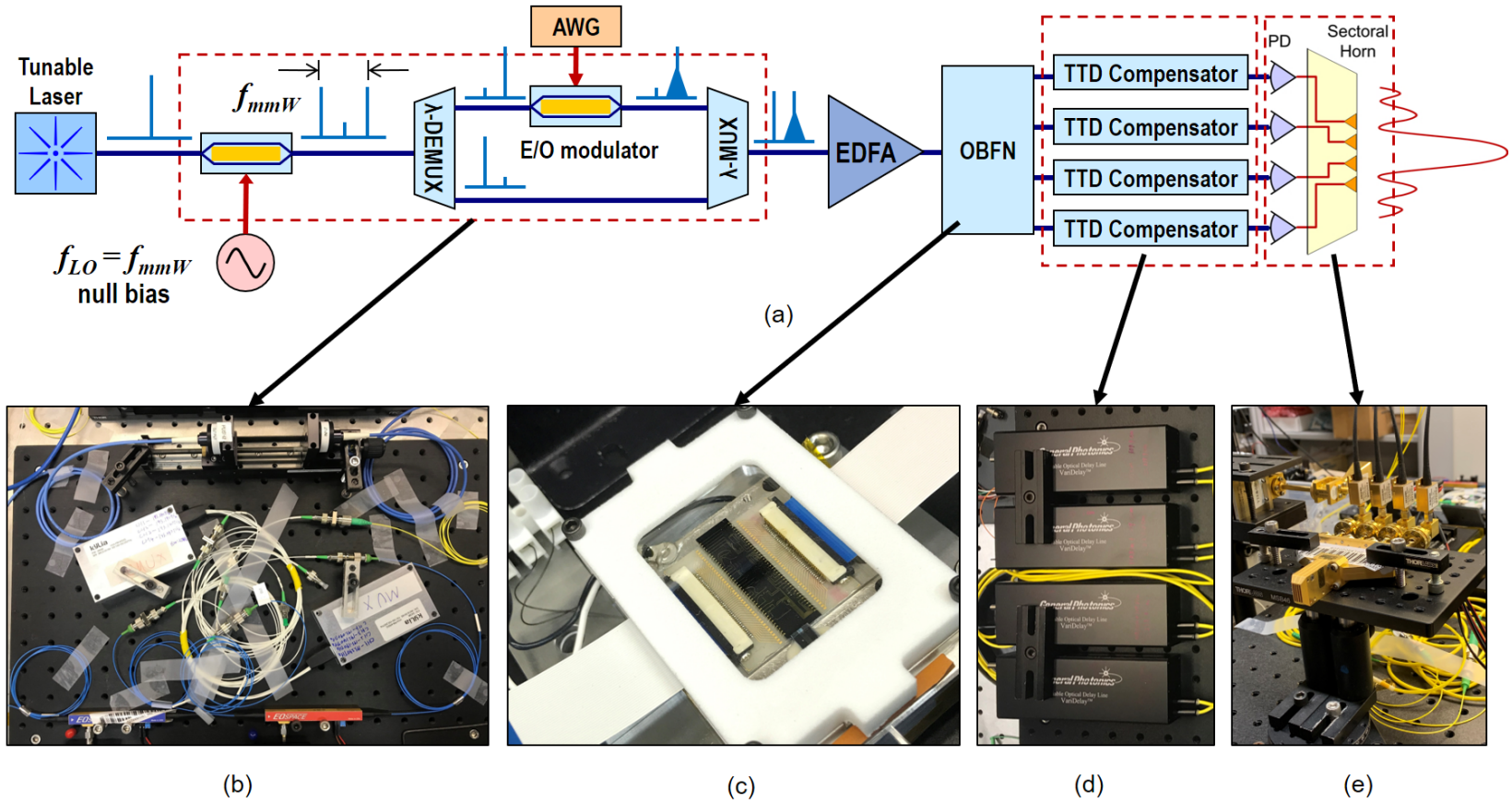

Figure 9.6: (a) Schematic diagram of mmW generation and beam steering experimental setup. (ESA: electrical spectrum analyzer; OSA: optical spectrum analyzer; DE/MUX: de/multiplexer.) (b)-(e) Pictures of the photonic generation and data encoding stage, packaged OBFN, four fiber path length compensator, and four photodiodes and 1×4 antenna array, respectively.

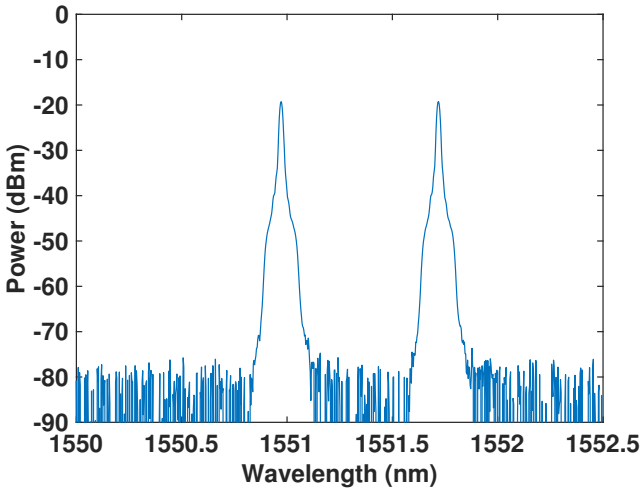

Figure 9.7: Optical spectrum for after the multiplexer in Fig.9.6(a) with 47 GHz of local oscillator.

two dominant 1-st order optical sidebands spaced by the mmW frequency f_{mmW}. Since a chirp free modulation is required for the up-conversion process, an x-cut EOSpace 50 GHz MZM is used in the experiment. A WDM is employed as a demultiplexer to separate the two sidebands. Since the WDM has a 50 GHz channel grid, the narrow linewidth external cavity laser is set to 1551.745 nm to match the second channel of the WDM and the two sidebands will be routed to the 1-st and 3-rd channel, respectively. One sideband serves as the data tone, and is encoded data using a EOSpace 20 *Gbps* modulator, whereas the other sideband serves as the reference tone. The two optical tones are combined by a multiplexer, which is a WDM with the same specifications as the demultiplexing WDM but used reciprocally. The optical path length for the data tone and reference tone should be matched as much as possible between the two WDMs to achieve high correlation and thereby minimized the noise transferred to the RF signal. Figure 9.7 indicates the optical spectrum of the combined two optical signals separated by 94 GHz, in which 47 GHz was used for the local oscillator for driving the MZM.

The signal is amplified by an EDFA and then coupled to the integrated OBFN chip

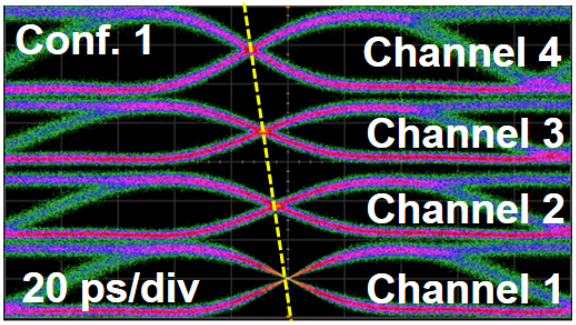

(a)

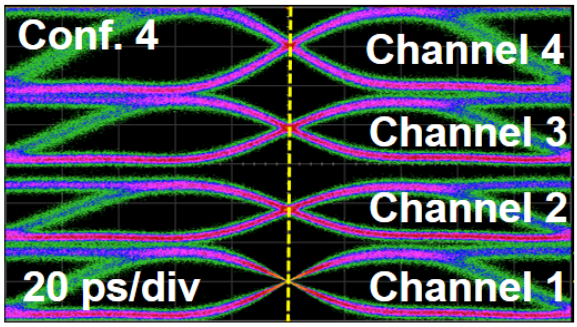

(d)

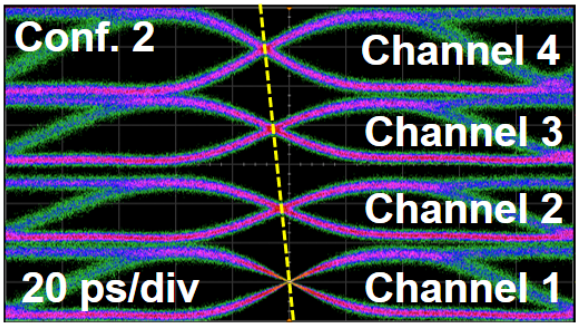

(b)

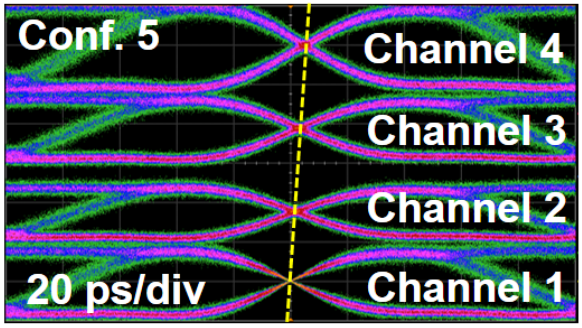

(e)

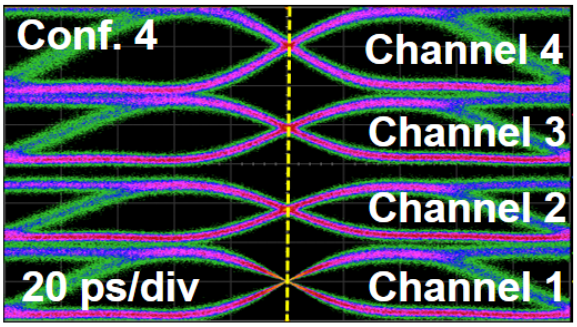

(c)

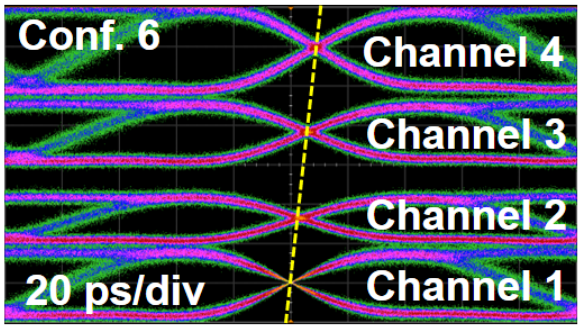

(f)

Figure 9.8: The eyes diagrams for the output each channel of the OBFN system with 10 *Gbps* OOK NRZ data modulation. The offset of the eye representing the delay of the corresponding OBFN system channel.

(Fig. 9.6(c)). The 1×4 SDL-OBFN is chosen as the OBFN for the W-band beam steering experiment as the SDL-OBFN can support much larger TTD bandwidth than the frequency of the W-band signal, which simplifies the tuning of OBFN, comparing to ORR-OBFNs where the optical sidebands, OBFN optimized delay central frequency, RF carrier frequency, and WDM channel grids all should be precisely aligned. Also, due to the large continuous bandwidth of the SDL-OBFN, the mmW carrier frequency is very agile whereas the available mmW carrier frequencies supported by the ORR-OBFN is more or less fixed. Given these reasons, to demonstrate a successful beam steering system with large capacity, the SDL-OBFN is a better option despites that only discrete beam angles are supported.

The OBFN splits the signal into four paths and has 6 delay configurations for 6 beamsteering angles, respectively, as discussed in Chapter 5. The outputs of the OBFN are coupled to 4 optical fibers and sent to four photodiodes for mmW generation. For W-band signals where the wavelength is very short (3 mm in vacuum), it is very difficult to match the length of all the four fibers in sub-mm accuracy. Therefore, a tunable TTD delay line up to 600 ps tuning range is employed for each path, which can compensate up to around 10 cm optical connection mismatches. A picture of the four TTD compensators are shown in Fig. 9.6(d). The tunable delay lines were tuned by connecting the four detectors directly to an oscilloscope. The reference path between the mux/demux is disconnected and data tone is modulated with a 10 $Gbps$ OOK NRZ signal. The reference channel (output 1 in Fig. 5.12) is set as the trigger of the oscilloscope acquisition. Since the horizontal offset of the eye diagrams displayed in the oscilloscope represents the signal delays, if the Conf. 4 is chosen as the 0^o beam angle, the eye diagram of each channel should be aligned. Figure 9.8 (a) - (f) illustrate the alignments of eye diagrams for Conf. 1 to Conf. 6, respectively. As shown, different linear delay configurations are achieved,

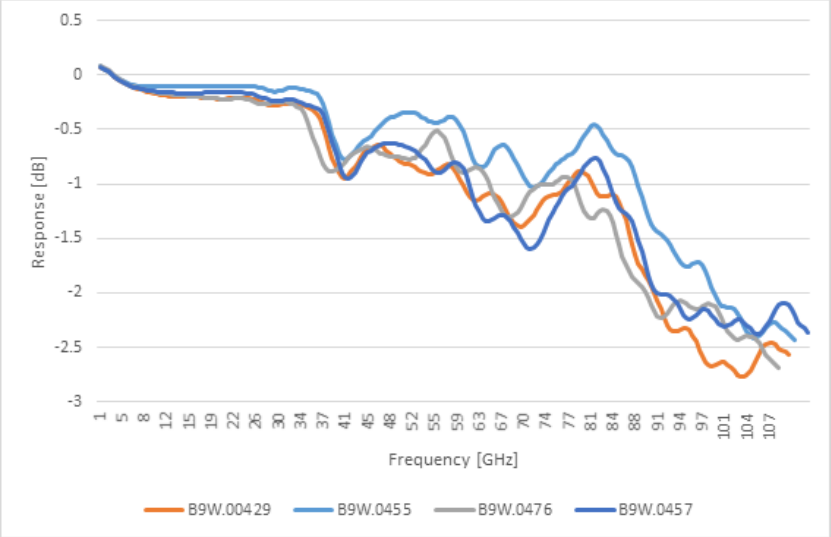

Figure 9.9: The S_{21}response of the four photodiodes.

which represent different beam angles.

Figure 9.6 (d) gives a picture of the emission stage. Four 110 GHz photodiodes (Finisar XPDV4121R-WF-FA) are employed for W-band signal up-conversion. Ideally, for a linear PAA, the emission power of each antenna element should be the same, which requires the same frequency response for all the photodiodes. In this experiment, four photodiodes were picked with matched responses, and the S_{21} responses of the four photodiodes are described in Fig. 9.9. As shown, the frequency response are matched and the 3-dB bandwidth exceeds 107 GHz. The antenna is a 1×4 sectoral horn antenna array with 1.6 mm pitch and 0.9 $mm \times 11.2$ mm unit dimension, which is designed to be a half wavelength pitch for 94 GHz signal. The antenna is also path equalized for 94 GHz signal. Due to waveguide orientation mismatch, the photodiodes connect to the antenna array through a 90° W1 connector to WR10 waveguide adapter and a 90° WR10 waveguide twister. The assembled photodiodes and antenna array are fixed on a motorized rotator to measure the beam pattern, as shown in Fig. 9.6(e).

Figure 9.10 (a) describes the schematic diagram of the receiver. A RF signal f_{LO} is

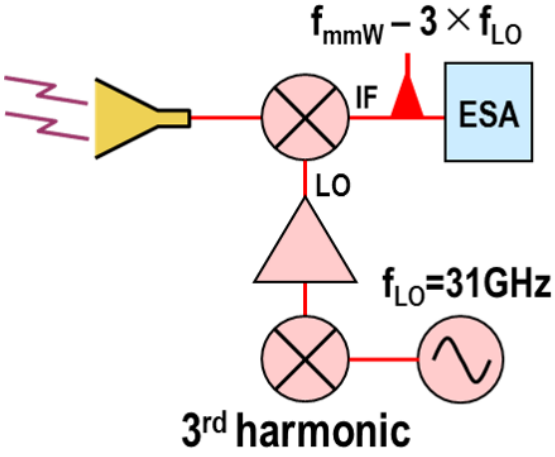

(a)

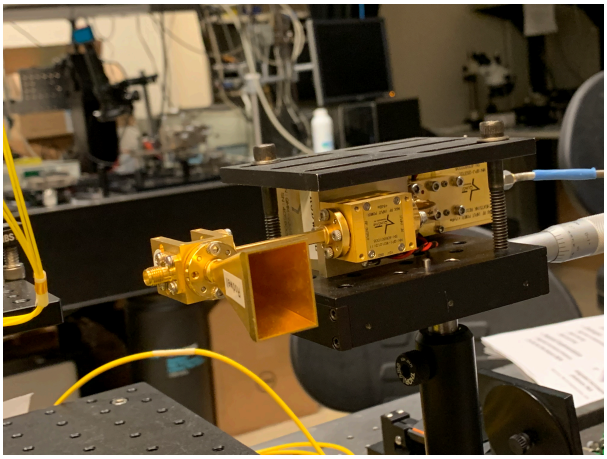

(b)

Figure 9.10: (a) The schematic diagram and (b) a picture of the receiver.

given as the local oscillator of a 3rd harmonic mixer, which triples the RF signal f_{LO}. Then the tripled signal is get amplified as the local oscillator for another mixer. The W-band signal is received by a horn antenna as the input of the second mixer. Therefore, the W-band signal then can be down-converted to an intermediate frequency $f_{mmw} - 3 \times f_{LO}$ and measured by an ESA. In the case of 94 GHz signal, a 31 GHz local oscillator is used and hence the signal is down-converted to an intermediate frequency of 1 GHz. A picture of the W-band signal receiver is given in Fig. 9.10(b).

The radiation pattern of the PAA azimuth plane is measured by rotating the antenna instead of rotating the receiver. As depicted in Fig. 9.6(e), the assembled photodiodes and antenna array are fixed on a breadboard on a motorized rotator where the aperture of the antenna is aligned to the rotating axis of the rotating stage. The receiver is fixed 11 cm from the antenna. This measurement scheme is equivalent to rotating the receiver, and it takes the advantage of the flexibility of photonic-assisted PAA where the antenna head can be remoted and connected with low loss optical fibers. In other words, with photonic-assisted PAAs, complex equipments such as the baseband unit, local oscillators

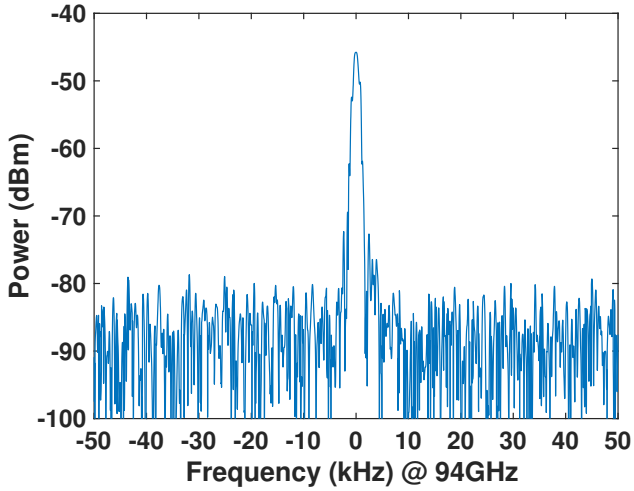

Figure 9.11: Measured W-band signal spectrum at 94 GHz.

and OBFNs that need well-controlled environment can be centralized, and the emitting antenna head could be kilometers apart, which makes the PAA system more flexible and less cost. Figure 9.11 shows the measured signal spectrum at 94 GHz. The 3-dB linewidth of the signal is measured less than 1 kHz and the signal-to-noise ratio (SNR) is 35 dB at 94 GHz. The signal linewidth would be improved if the optical paths between the MUX and DEMUX were balanced shown in Fig. 9.3(a).

Figure 9.12 shows the measured and theoretical radiation patterns of the 94-GHz signal in azimuth plane with multiple OBFN chip configurations for beam angles of -51°, -33°, -16°, -2°, 14° and 31°, respectively. Although it is a sectoral horn antenna array, as discussed in Chapter 3, the beam pattern is mostly determined by the pitch and aperture size of the array rather than the radiation pattern of a single antenna element. Therefore, a uniform rectangular radiation source is assumed for each antenna element, i.e., a one dimensional 1×4 array with 1.6 mm pitch and 0.9 mm single element width is assumed for modeling the antenna array. The red dash curves refer to the theoretical beam pattern whereas the blue solid curves refer to the measured data. The measured data agrees with

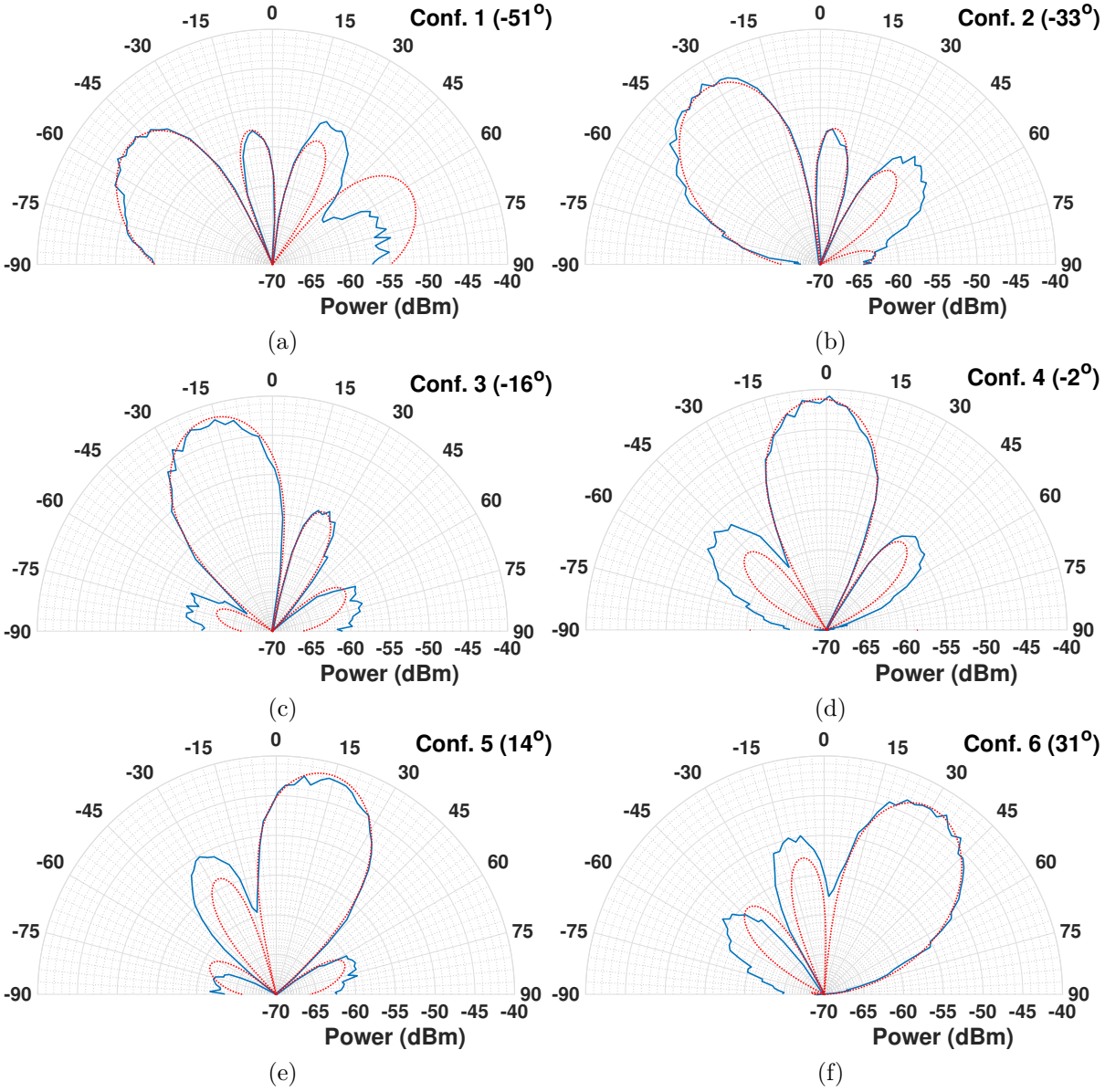

Figure 9.12: 94-GHz azimuth plane beam pattern for beam angle of -51°, -33°, -16°, -2°, 14°, and 31°, respectively. (Blue curves refer to the measured data whereas the red curves refer to the theoretical beam pattern).

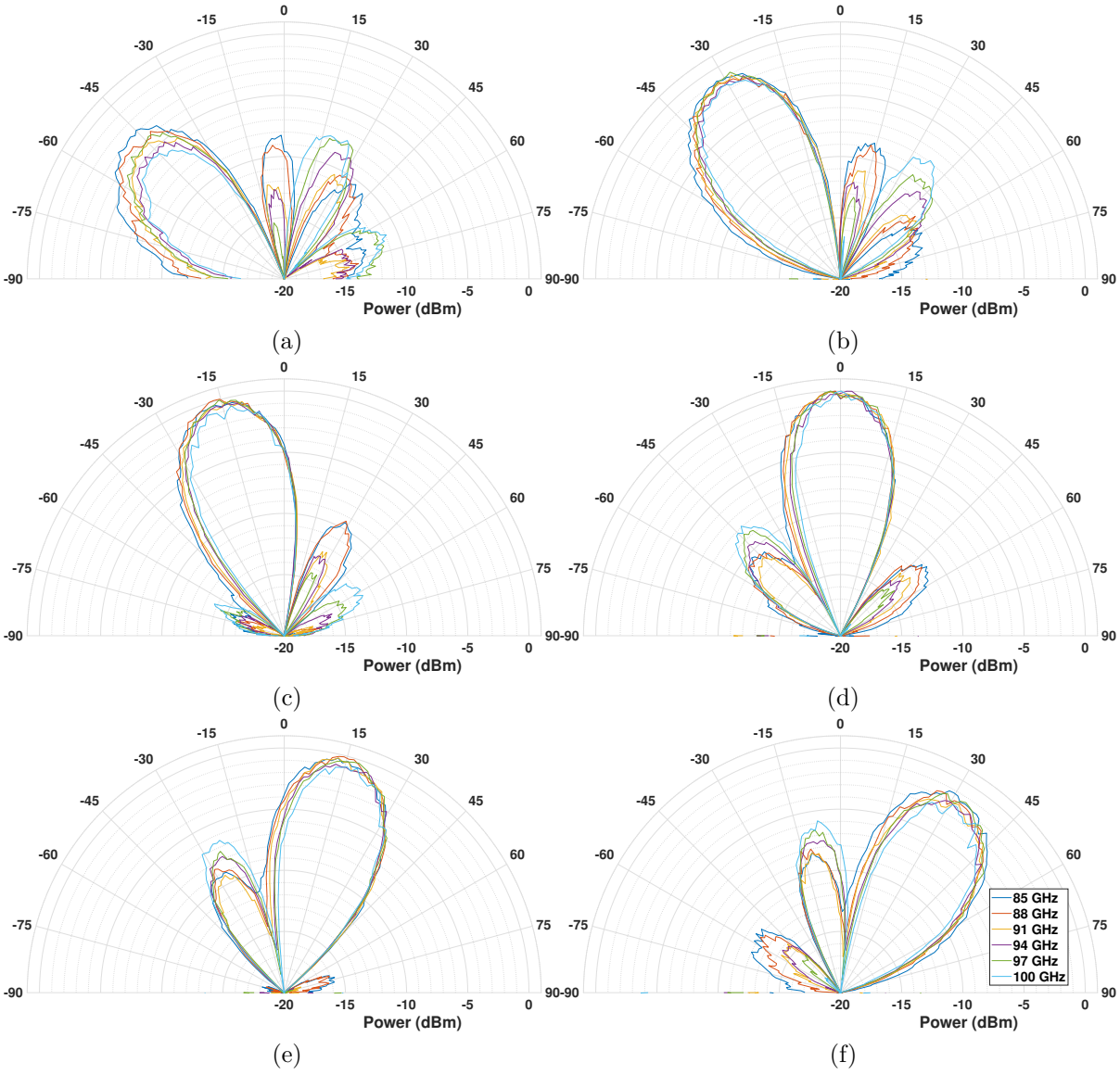

Figure 9.13: Normalized measured azimuth plane beam pattern for W-band signal from 85 GHz to 100 GHz for each beam angle.

Modulation Format	Bits per Symbol	Bit Rate
ASK	1	15 *Gbps*
QPSK	2	30 *Gbps*
16-QAM	4	60 *Gbps*
32-QAM	5	75 *Gbps*
64-QAM	6	90 *Gbps*

Table 9.1: Bit rate supported by 15 GHz bandwidth for different modulation formats.

the theory well, except for some distortions in the side-lobes. This could be due to the slightly mismatched optical length and slight variations in the output intensity of each channel, which could be relieved if the photodiode and antenna array were integrated. The the 3-dB beam width is measured as 28°, and a narrower beam width can be achieved for a larger array size. Only the PAA radiation pattern in the azimuth plane is measured since the 1-D antenna array only affect the radiation pattern in azimuth plane.

By changing the LO frequency, the beam patterns for signal frequency from 85 GHz to 100 GHz were measured, and the normalized result is shown in Fig. 9.13. Excellent beam quality was maintained and no beam squint was observed over 15 GHz, which is as expected for TTD based OBFNs. The beam width and attenuation of the mainlobes at large beam angles, and the sidelobes are varied with the frequency. These variations are expected as well because the wavelength to array dimension ratio changed with frequency. Table 9.1 indicates the bit rate supported by the 15 GHz bandwidth for different modulation format and up to 90 *Gbps* could be supported with 64-QAM advanced modulation. A preliminary 3 *Gbps* data transmission experiment was also performed. The W-band signal encoded with data was down-converted to a intermediate frequency of 5 GHz by the receiver, and an oscilloscope (80 GS/s) was employed to acquire the data. The signal spectrum of the 3 *Gbps* ACK data with 5 GHz is depicted in Fig. 9.14. A

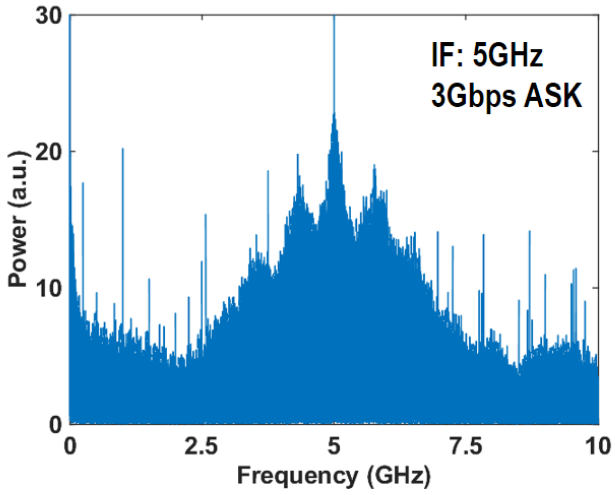

Figure 9.14: Signal spectrum of 3 *Gbps* ASK data with intermediate frequency of 5 GHz.

completed high bit-rate data transmission experiment will be performed in future work.

9.4 Summary

Experiments for mmW signal generation and beamsteering using the integrated OBFN chips were demonstrated in the chapter. The chip was packaged with TEC and optical/electrical I/Os, and the OBFNs were calibrated before the system test. With the ORR-OBFN, a single delay path was employed for generating a 41 GHz mmW signal. The signal was encoded with a 3 *Gbps* ASK modulated data and the signal spectrum was measured. The SDL-OBFN was employed for a W-band signal beam steering experiment. By setting the Conf. 4 of the OBFN for the 0° beam through tuning the TTD compensators, the system experiment demonstrated a beam squint free beam steering for 6 beam angles from -51° to 31° with at least 15 GHz TTD bandwidth from 85 to 100 GHz and a SNR of 35 dB. A 3 *Gbps* ASK data was also encoded on a 94 GHz signal. The received signal was then down-converted to 5 GHz by the receiver and the signal spectrum was measured. Future work will carry out completed high bit rate data transmission experiments through this link.

Chapter 10

Ongoing and Future Works

This thesis has demonstrated two types of integrated TTD based OBFNs for mmW signals – ORR based OBFN and SDL based OBFN. Both of them were realized with ultra-low loss waveguide technology and generated desired delay distributions with large TTD bandwidth. However, these OBFNs may have potential issues for feeding very large scale PAAs. Some of the issues may include:

First, the system scalability should be enhanced. Since the signal delay for each antenna element should be precisely controlled and predicted for a TTD based PAA, for discrete photodiodes and antenna array, TTD compensators are inevitable to compensate the optical path difference, which significantly limits the system scalability.

Second, the delay calibration need to be simplified and the power consumption needs to be optimized. For the previously demonstrated architectures where the signal is split into multiple path and get individually delayed, a large number of tuning elements need to be precisely controlled and the control of these elements are more or less coupled, which makes the calibration of the OBFN very complex, especially for large scale OBFNs. In addition, such large number of tuning elements consumes a large amount of power, and this power is dissipated and cannot be converted to the signal power.

To address the potential issues listed above, some ongoing and future works for OBFNs will be discussed in this chapter, which includes a package-level system inte-

gration of the OBFN, PDs and antenna array where the signal path length is more controllable, and a new OBFN architecture that enhances the scalability and power efficiency, and simplifies the calibration complexity.

10.1 System Integration

As discussed in Chapter 9, all the signal path length of a PAA need to be matched. However, with discrete photodiodes and antenna array, it is very hard to make the fiber connections with length variation less than 1 mm. And this fiber length variation may cause significant phase difference for mmW signal frequencies up to W-band. Therefore, TTD compensators are inevitable to compensate the signal path length difference of the optical fiber connections. However, the use of bulk TTD compensators will significantly increase the footprint, cost, calibration complexity of the system, and thereby limited the system scalability. Moreover, for W-band mmW signals, the antenna aperture is much smaller compared to the footprint of a packaged PD due to should signal wavelength in millimeter scale and the half-wavelength pitch requirement of a linear single-main-lobe antenna array is difficult to achieve. As a result, extra design work is required to taper from a pitch that fit the RF waveguide connectors and packaged PD to the desired aperture with matched waveguide lengths. The design complexity and cost keep increasing as the scaling of the PAA. Therefore, to enhance the system scalability, a straightforward solution is using a package-level, or even chip-level, system integration of the OBFN, PDs and antenna array, where the unpackaged bare device dies have much small footprints and signal path lengths are much shorter and predictable.

Figure 10.1 depicts the design and mask layout of a 1×4 ORR based OBFN using SOI technology. Instead of using SiN ultra-low loss technology, SOI platform can provide active devices such as phase modulators up to 30 GHz, CMOS compatible ger-

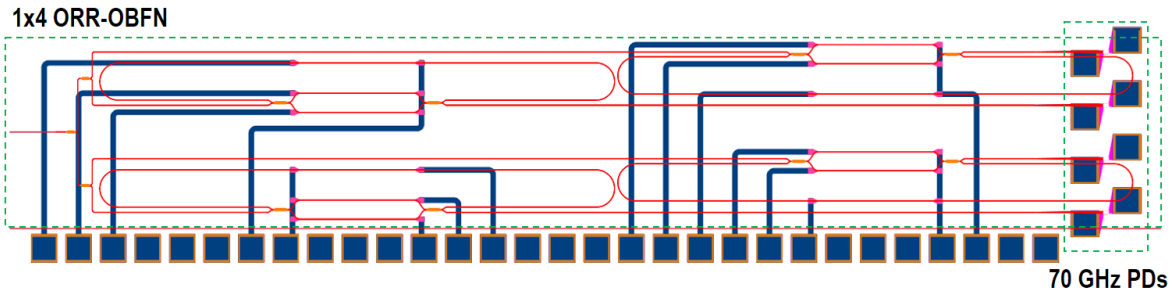

Figure 10.1: Mask layout of the single ORR based OBFN integrated with Si-Ge PDs.

manium (Ge) PDs with bandwidth up to 70 GHz, and very efficient thermo-optical phase shifter as low as 2.5 mW/π. These features are desirable for photonics assisted PAA subsystem integration. As discussed in Chapter 6, despite that multi-ORR delay line can generate large delays, the calibration of a multi-ORR delay line is very complex. The anti-resonance of a single ORR can generate a large TTD bandwidth and continuous delay tuning, however, the delay value is only limited within 0 to the round trip delay τ_r. Therefore, ORRs can be designed to achieve a $\pm 90^{\circ}$beamsteering by increasing the length of feedback loop but at the cost of the TTD bandwidth. For proof of concept demonstration and to simplify the system, the OBFN employs a single ORR as the TTD element for each path of the OBFN and use the delays at the anti-resonance point. Based on (3.19), in order to achieve $\pm 90^{\circ}$beamsteering for a $1 \times N$ OBFN for half-wavelength pitch antenna, the FSR of ORR should satisfy the following condition

$$FSR = \frac{1}{\tau_r} \leq \frac{f}{(N-1)/2} \tag{10.1}$$

where f is the carrier frequency of the RF signal. Also, according to the discussion in Chapter 6, in order to apply the extended bandwidth of the ORR delay lines, the carrier frequency of the RF signal f should be integral number of the ORR FSR. Considered this requirement, the FSR of the ORR can take discrete values f/i where i is an integral

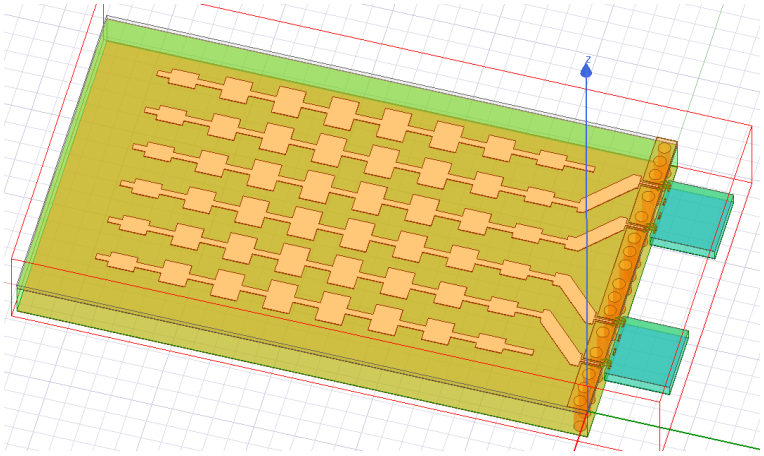

Figure 10.2: Planar 1×4 half-wavelength pitch antenna array.

that greater than $(N-1)/2$. Therefore, for the 1×4 OBFN design in Fig 10.1 where the target RF signal frequency is 60 GHz, which is limited by the 70 GHz PD bandwidth, the FSR was chosen as 30 GHz.

In addition to the integrated OBFN with PDs, planar antenna array should be designed for integration. A 1×4 60 GHz antenna can be designed in the future, as shown in Fig. 10.2. Two dummy antenna elements are added to the edges of the antenna to ensure each antenna has the same boundary condition and thereby the same beam radiation pattern. Because of the high single frequency, high quality substrate such as Ro5880 ($\epsilon_r = 2$) should be employed to realize the antenna array. Also, the impedance of the PD-antenna connection and antenna element should be carefully designed.

Figure 10.3 depicts the package-level integration schemes of the OBFN-PD chip and antenna array. As shown in Fig. 10.3(a), the chip and antenna array are closely mounted on a intermediate carrier, and the PDs and the antenna array are connected using wirebondings. Metal pads the OBFN-PD chip are wirebonded to the metal pads on the carrier as well for external electrical connection. This integration scheme is simply, however, it may not work well for signal frequency higher than 60 GHz such as W-band due to the large inductance of the bonding wire. An alternative solution is using flip-

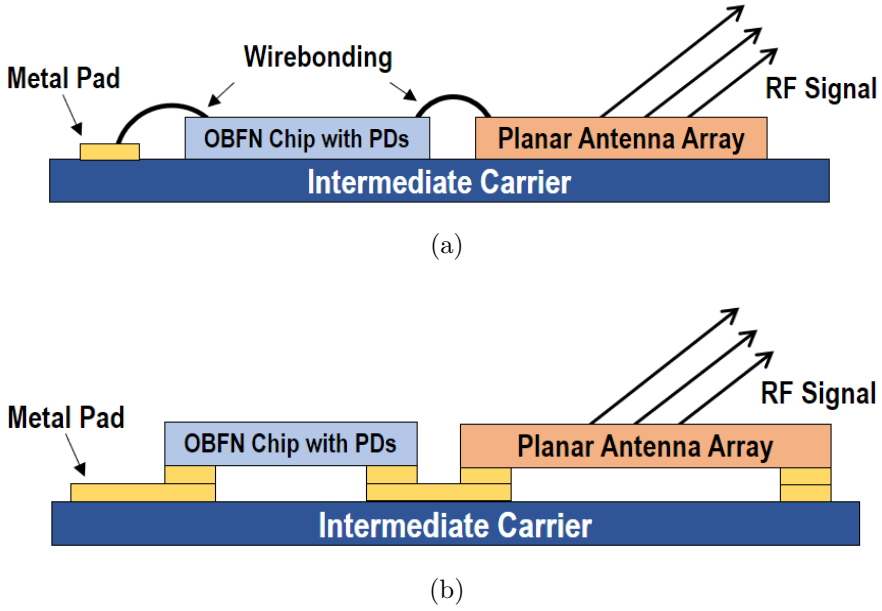

Figure 10.3: Schematic diagram of OBFN-PD-antenna integration with (a) wirebonding and (b) flip-chip bonding.

chip bonding technique, as shown in Fig. 10.3(b), where the inductance of the metal wire on the carrier is smaller and more predictable. Since thermal tuning is employed in the OBFN design, using the flip-chip bonding technique requires a deliberate design for thermal stabilization.

10.2 Recirculating Optical Beamforming Network

Both of the two OBFN architectures demonstrated in previous chapters – SDL-OBFN and ORR-OBFN – employ the same distribution scheme, which splits the signal into multiple paths and delay the signal in each path individually and accordingly. This scheme is simple to realized, but it requires individual tuning of TTD elements in each path. It should work well for a small PAA. As the PAA scale up, however, the required delay tuning range and the number of TTD elements keep increasing significantly, which makes it dramatically difficult to tuning all the TTD elements of the OBFN. Moreover,

the total power budget of the OBFN will increase with TTD element numbers. Particularly, for SiN waveguides where thermo-optical effect is used for tuning TTD elements, a single thermo-optical phase shifter consumes 200 mW for a π phase shift [85]. It will be a very large power consumption for a large scale OBFN. And this power is purely dissipated as heat without any energy contribution to the signal power. For a linear PAA where the delay between two adjacent antenna element is constant, a novel signal delay and distribution scheme is proposed to address both the control complexity and power consumption issues and have very high scalability and flexibility while keeping reasonable footprint, which is the recirculating delay loop (RDL). Similar re-circulating loop has been demonstrated just for high quality optical frequency comb generation [152, 153, 154], but no work for delays or integration ever reported.

10.2.1 Recirculating Delay Loop

Figure 10.4 depicts the schematic diagram of a RDL. The optical is injected to the RDL through a coupler. The input optical signal is split into two parts. One part is transferred to the output of the RDL as the 0 order output signal, and the other part is coupled to the loop. In the loop, the signal is frequency shifted by f_{shift} through a single sideband suppressed carrier (SSB-SC) modulation. Then the optical signal with shifted frequency is amplified and delayed, and injected to the loop coupler. Part of the signal is coupled to the output of the RDL, and the rest of the signal is coupled back to the loop for re-circulating. This process keeps repeating until the filter in the loop terminates the re-circulating process, and an optical signal comb will be generated. Each comb line is a duplication of the previous comb line signal except the optical carrier frequency is shifted and delayed by an additional loop path. Therefore, as illustrated in Fig. 10.4, there is a constant delay between two adjacent comb lines of the output and the delay

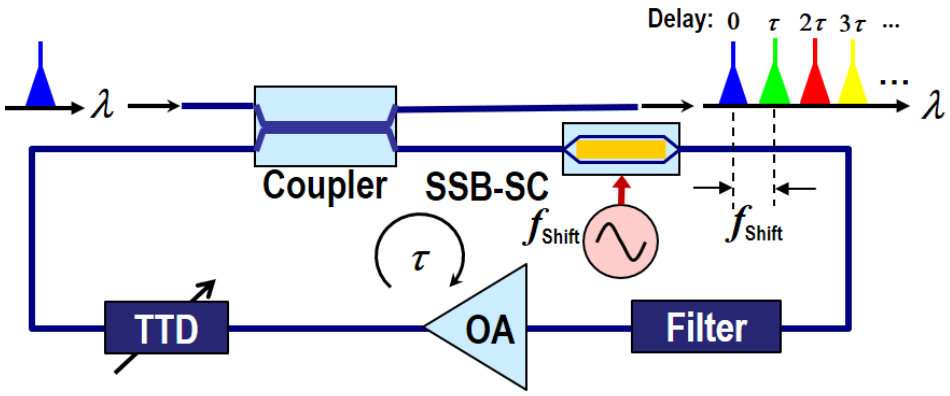

Figure 10.4: Schematic diagram of a RDL. (SSB-SC: single sideband suppressed carrier; OA: optical amplifier.)

can be tuned through the tunable TTD element embedded in the loop. The comb lines are encoded with the same data signal and can be routed to individual paths to feed a PAA. A RDL was simulated using Lumerical INTERCONNECT the simulation results are shown in Fig. 10.5 and 10.6. In the simulation, a single frequency optical signal is injected into the RDL and modulated with a OOK PRBS data pattern. The RDL output then goes through a optical demultiplexer to split the comb lines into individual paths. The blue color in Fig. 10.5 refers to the optical spectrum of the RDL output. As shown, a optical frequency comb with a 40 GHz spacing is generated by the RDL. Other colors other than blue in Fig. 10.5 refer to the output of each channel through the wavelength demultiplexer. Figure 10.6 presents the simulated data pattern from each channel output after the RDL output signal is demultiplexed. The data pattern is shifted for the same amount of time compared to the previous channel, which implies that the signals are distributed and delayed as expected.

InP semiconductor material system is preferred for monolithic integration of a RDL since the high electron mobility and direct bandgap of InP can provide high power semiconductor optical amplifier and high speed modulators [139] that are desired by the RDL. Although lack of optical amplifiers, SOI material system is another option for implement-

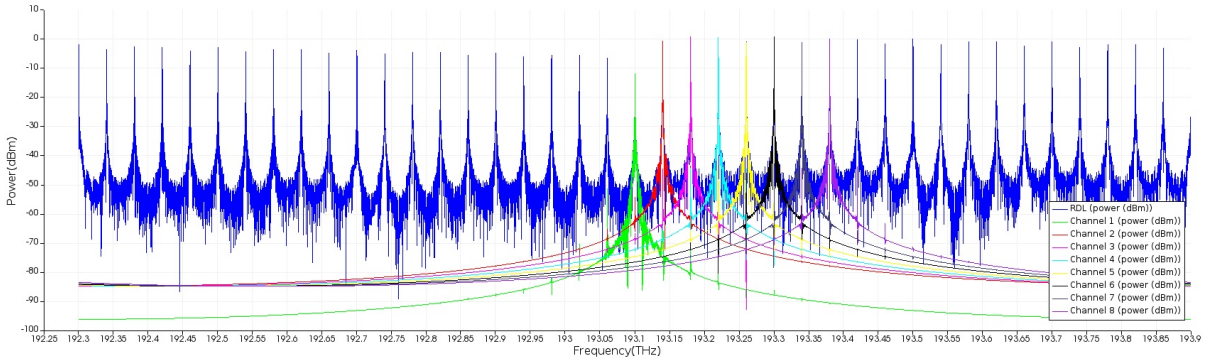

Figure 10.5: Simulated optical spectrum of RDL. The blue color refers to the optical spectrum of the RDL output. Other colors refer to the output of each channel through the wavelength demultiplexer.

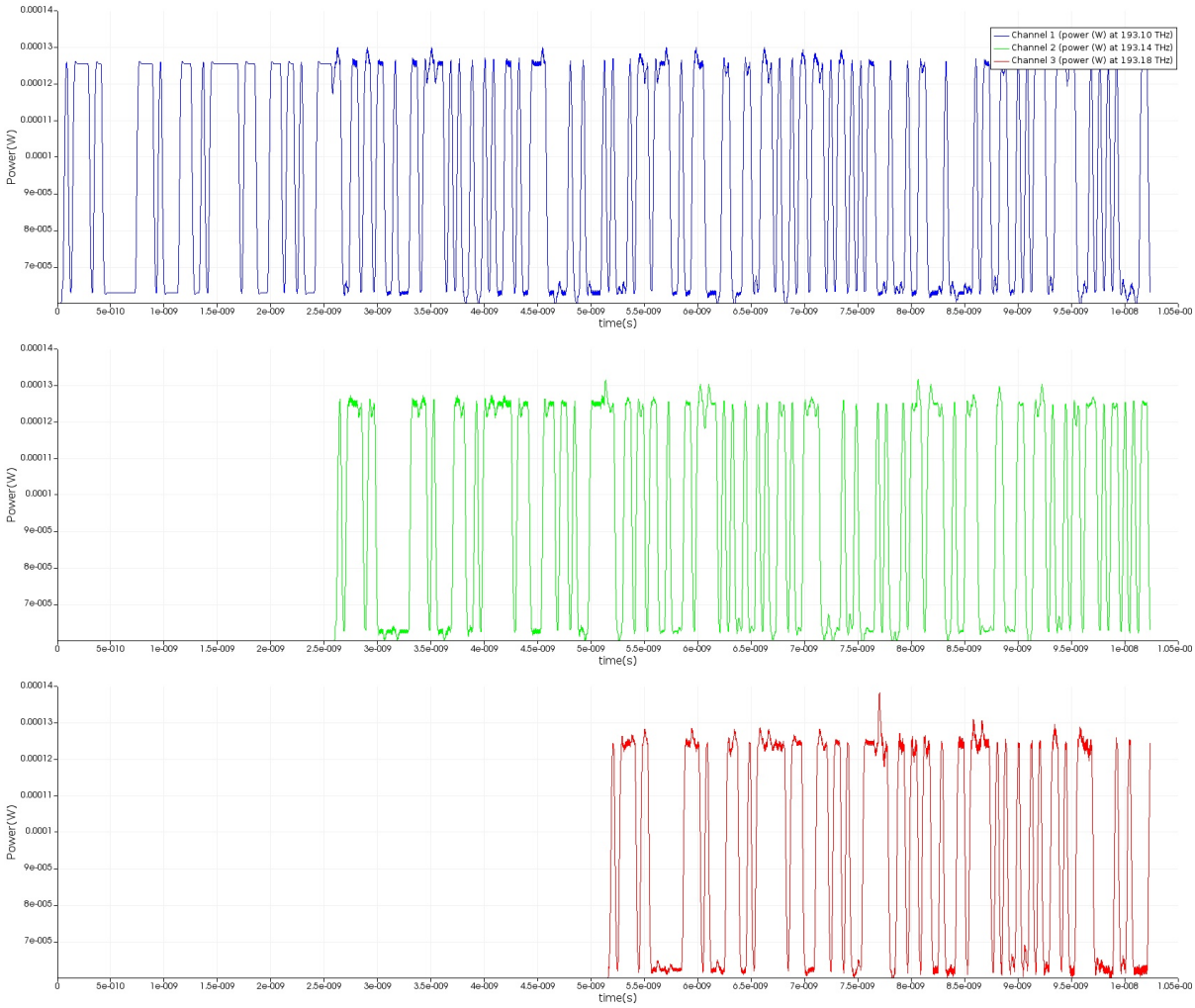

Figure 10.6: Simulation result of the data pattern from each channel output.

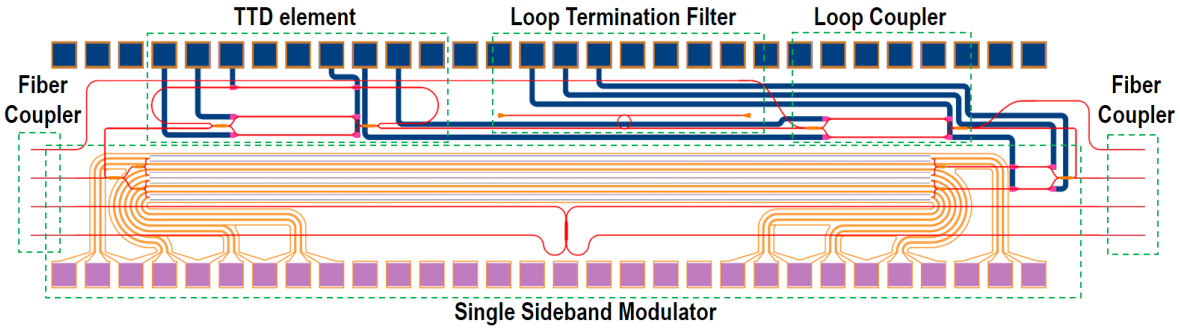

Figure 10.7: Mask layout of the RDL with SOI.

ing RDL because it can also provide high speed modulators, and the fabrication process has been well developed. Also, large number of SOI foundries are available around the world. The optical amplifier can be added to the SOI chip to complete the RDL by integrating InP SOAs using hybrid integration technologies [155, 124, 123, 156, 157, 158, 49, 159]. Figure 10.7 depicts the design and mask layout for of the RDL with SOI. All necessary components are included in the design except for the optical amplifier. A ORR is employed as the tunable TTD element, and another ORR is designed as the loop termination filter to terminate the re-circulating process and limit the number of frequency combs. A tunable symmetric MZI is used as the loop coupler, and fiber couplers are designed for optical signal input/output as well as InP SOA integration. The single sideband modulator is the most important component of the RDL and is also included in the design. The single sideband modulator employs a dual paralleled MZI scheme, and the modulation is achieved by combining a cosinusoidal signal with its Hilbert transformation to generate an analytic signal [160], i.e.,

$$Ae^{j\omega t}\cos(\omega_{shift}t) + jAe^{j\omega t}\sin(\omega_{shift}t) = Ae^{j(\omega+\omega_{shift})t} \tag{10.2}$$

where ω is the angular frequency of the optical signal, and $\omega_{shift} = 2\pi f_{shift}$ is the angular frequency of the driving RF cosinusoidal signal, which is also the frequency that need to

be shifted. Since the the ORR based TTD element has a periodic delay response, to get desired signal delay distribution, the shifting RF frequency the FSR of the ORR should be matched.

10.2.2 Recirculating Optical Beamforming Network Architecture

As described in Chapter 2, a photonic-enabled RF PAA transmitter comprises of three stages – the generation stage, distribution stage and emission stage. Figure 10.8 depicts a complete PAA architecture employing an OBFN based on a RDL. The generation stage generates two highly correlated optical tones in which one tone is encoded with data serving as the data tone, and the other tone is a single frequency tone serving as the beating reference. The two tones are both sent to the RDL for delay and distribution since, as discussed in Chapter 3, the two optical tones for beating should have the same amount of time delay for TTD based PAAs. The RDL then will output two series of frequency combs originating from the data tone and the reference tone. The two series of combs are then re-arranged into corresponding channels to feed each of antenna elements by elaborately designed filters. As discussed above, the signal in each channel is additionally delayed by the round trip delay of the RDL, which can only be positive. And the resulting beam can only be steered in positive angles. Moreover, in addition to the delay by the TTD element, the optical connections in the loop contribute extra delays. Therefore, fixed delay offsets are included for each output channel of the RDL-OBFN to compensate the extra delays induced by the optical connections and to achieve beam steering in both negative and positive angles. The RDL, re-arrangement filters and delay offsets together form the RDL based OBFN.

The parameters of the RDL-OBFN should be carefully designed. Since two optical

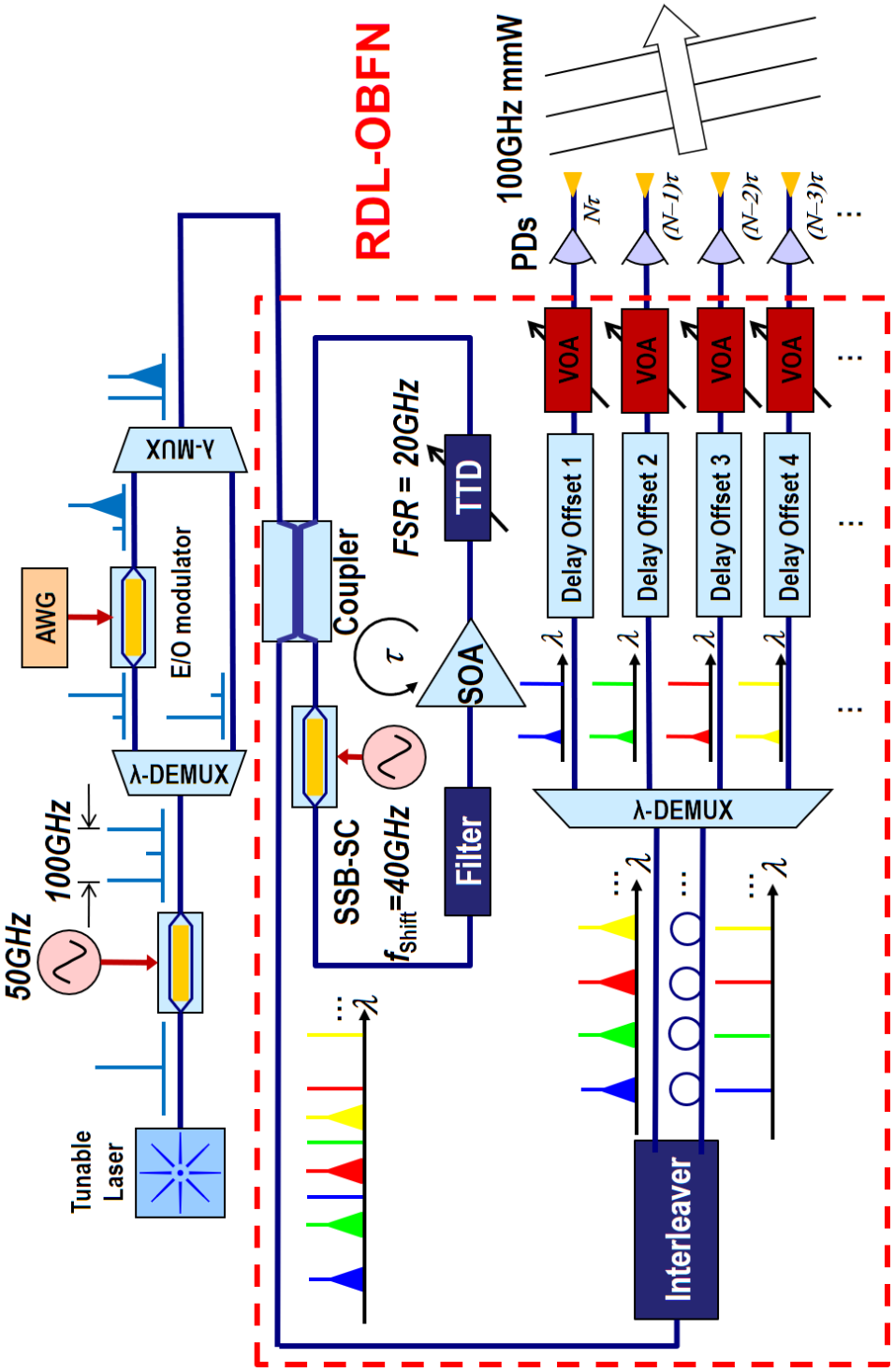

Figure 10.8: Schematic diagram of a recirculating delay loop based PAA architecture.

tones spaced by the RF signal frequency are injected into the RDL, which generates two series of frequency combs with the same comb line spacing, the frequency of the desired RF signal f_{RF} and the shifting frequency f_{shift} should be chosen to avoid frequency aliasing between the two combs. Given the bandwidth requirement of the data tone, the two combs should be aligned to the middles of the comb lines, i.e.,

$$f_{RF} = f_{shift}(M + \frac{1}{2}) \tag{10.3}$$

where M is a non-negative integer. Also, for a linear PAA, the round trip delay of each comb line should be the same and corresponding data comb line and reference comb line should exactly experience the same delay. Therefore, a broadband TTD element should be used such as SDLs. Or a periodic TTD device with the FSR

$$FSR_{TTD} = \frac{f_{shift}}{2} \tag{10.4}$$

The re-arrangement filter can be implemented using a interleaver and a $2 \times N$ arrayed waveguide grating (AWG). As illustrated in Fig. 10.8, the interleaver separates the two combs, which requires the FSR of the interleaver

$$FSR_{IL} = f_{shift} \tag{10.5}$$

After separated, the comb lines are mapped to the corresponding channel accordingly through the AWG. Since the data tone and corresponding reference tone should be mapped into the same channel for beating in the PD, the two inputs of the AWG should be designed to have frequency shift of f_{RF} in the transmission spectra. And the channel spacing of the AWG should match the shifting frequency f_{shift}. The delay offsets in each channel compensate the extra delays of the optical connections in the RDL and also en-

able the negative angle beamsteering. Therefore, the delay offsets should have the delays given by

$$\tau_i = (N - i)(\tau + \frac{1}{2f_{RF}}) \tag{10.6}$$

where N is the number of channels, $i = 1, 2, ..., N$ is the channel number, τ_i is the delay offset of the i-th channel, and τ is the round trip delay of the RDL. Based on the analysis above, Fig. 10.8 actually depicts an example for a 100 GHz signal linear PAA with $M = 2$ in (10.3). Figure 10.9 presents the microscope picture of a fabricated SiN AWG for use in the RDL-OBFN. The AWG is designed to have 3 inputs with 50 GHz spacing, and 24 outputs with 40 GHz channel spacing. Input 1 and input 3 have 100 GHz spacing, which can be used for the RDL-OBFN in Fig. 10.8. The design of AWG beyonds the scope of this thesis and will not be covered. More details can be found in [161, 139]. Figure 10.10 illustrates the measured results of the fabricated AWG. Since the device is partially damaged, only Input 1-2 and Output 1-16 were measured. The results show 39 GHz of output channel spacing and 50 GHz offset of transmission spectra between Input 1 and 2, which is consistent with the design. And it is believed that Input 1 and Input 3 will have 100 GHz offset in the transmission spectra. Future works on RDL based OBFN will be focusing on improving the AWG and realizing a high speed SSB modulator, and realizing other filters of the RDL.

RDL-OBFNs and ORR-/SDL-OBFNs have different distribution and delay strategies. The RDL-OBFN delays the signal first and then distribute the signal, while the ORR-/SDL-OBFN distributes the signal first and delays the signal later. Table 10.1 compares OBFNs with the two different strategies in terms of the control complexity, scalability, power efficiency and fabrication tolerance. First, for ORR-/SDL-OBFNs where the signal is split into multiple paths, the delays of each path are individually controlled and the delay required for TTD element is the absolute delay value, which could be accumulated

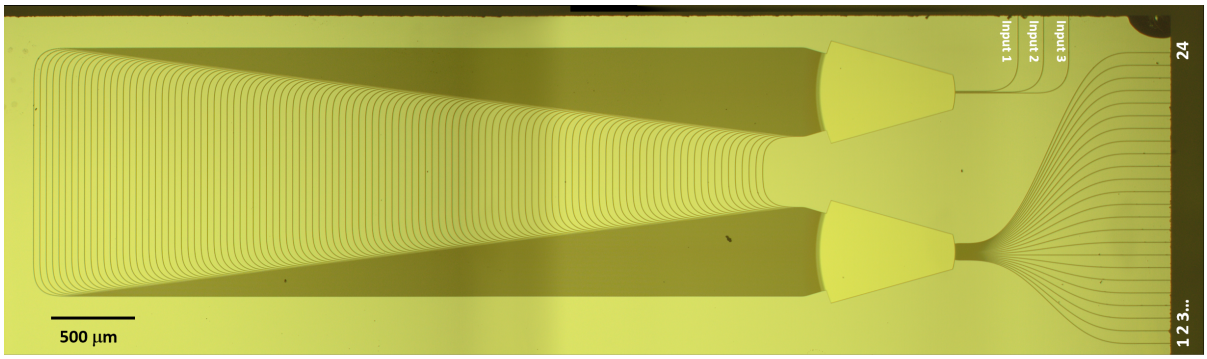

Figure 10.9: Microscope picture of 3×24 AWG for RDL based OBFN.

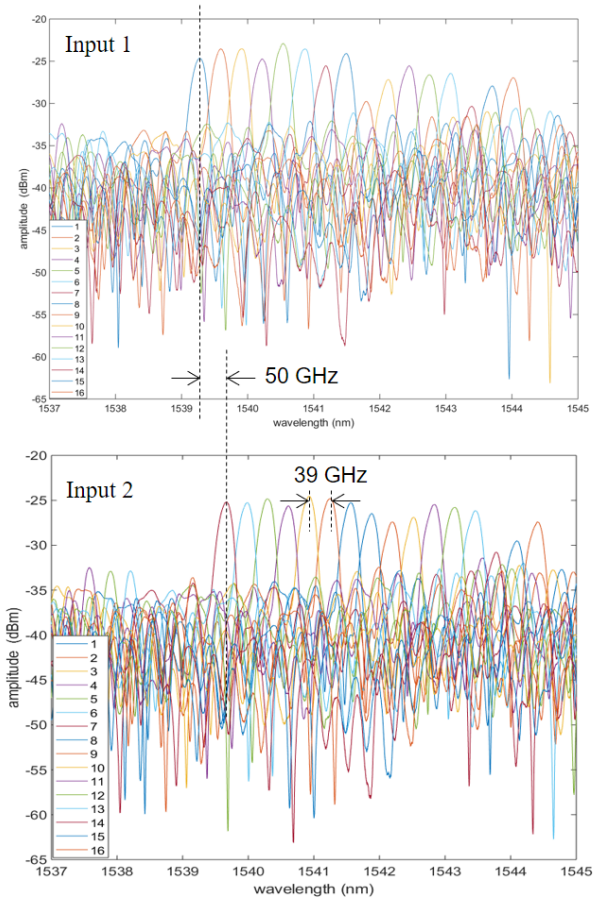

Figure 10.10: Transmission spectra of the first 16 output channels of the AWG with input 1 and input 2, respectively.

	RDL OBFN	ORR/SDL OBFN
Control Complexity	Control only one TTD element for any array scale	At least one TTD element per path, large TTD tuning range required
Scalability	Very cheap to scale up	Increase system footprint and complexity
Power efficiency	Energy converted to signal power	Energy dissipated as heat
Fabrication tolerance	All elements in the loop are reused, more fabrication tolerance	Need identical devices over a large area, high fabrication uniformity requirement

Table 10.1: Comparison of RDL-OBFN with ORR-/SDL-OBFN.

to a very large value and hence the TTD element could be complex. Whereas for a RDL-OBFN, since the optical signal keeps re-circulating and passing through the same TTD element in the RDL, the relative delay between two adjacent channels are determined by the TTD element in the loop, and thus only one TTD element need to be controlled. And the required delay of the TTD element is the relative delay between the channels, which is small and less than $1/2f_{RF}$. Therefore, comparing with ORR-/SDL-OBFN, the RDL-OBFN has less control complexity, especially for large scale PAAs. Second, for ORR-/SDL-OBFNs, the number of TTD elements increases as the OBFN scales up, which increase the system footprint and complexity. However, to scale up a RDL-OBFN, we only need to increase the bandwidth of the termination loop filter and increase the channel number of the wavelength demultiplexer, presuming the SOA can provide sufficient gains. The cost for scalability for a RDL-OBFN is much cheaper than ORR/SDL based OBFNs. Third, when tuning a ORR-/SDL-OBFN, a large number of TTD elements need to be tuned, which consumes a large amount of power. This power is dissipated as heat and have no contribution to the signal power. On contrast, the RDL-OBFN only need to tune one TTD element. Most of the power would be consumed by the SOA where the

energy is converted directly to the signal power, which is more energy efficient compared to ORR-/SDL-OBFNs. Last, since the signal is distributed first and then delayed, a large number of TTD element will be distributed over a large chip area and thereby these TTD elements need delicate fabrication process to ensure all the TTD elements work as designed, which requires a good high fabrication uniformity. Nevertheless, for a RDL-OBFN, all elements in the loop are reused and placed within a small area, which thereby alleviates the requirement for fabrication. Therefore, based on the comparison, RDL based OBFNs are more ideal for large scale linear PAAs compared to the ORR or SDL based OBFN.

10.3 Summary

This chapter discussed the on-going and future works on integrated photonics for photonics enabled PAAs. These works, including the subsystem integration and a new OBFN architecture, focus on addressing the potential issues in scalability, control complexity, power consumption that exists in the SDL-/ORR-OBFNs and PAA systems. For the system integration, an 1×4 OBFN with integrated PDs was tapered out on SOI, and the designing of a 1×4 planar antenna array was planned. These two chips can be mounted on an intermediate carrier and connected with wirebonding to achieve the OBFN-PD-antenna integration. The RDL-OBFN is a novel architecture that delays the signals of all paths by re-circulating the signal in a single loop. Only a single TTD element is employed in the RDL-OBFN, which improves the scalability, power efficiency and controllability, compared to the OBFNs demonstrated in previous chapters. Despite that a SSB modulator is required in a RDL-OBFN, it is very achievable by today's technology [162, 163]. Therefore, RDL-OBFN is promising for achieving compact, highly scalable and low power large scale photonic-enabled TTD based linear PAAs.

Chapter 11

Conclusions

A PAA is a flexible all-solid state approach for directional beamforming to compensate the atmospheric attenuation of mmWs (30-300 GHz). Instead of using phase shifters in PAAs, using TTDs can mitigate the beam squint that limits the usage of the spectrum, and thereby is an ideal solution for wideband communication with PAAs, as discussed in Chapter 3. IMWP technology is fairly suitable for TTD based PAAs as it can precisely control the path delays and realize compact, wide bandwidth and low-loss tunable TTD devices for OBFNs. Among various tunable integrated TTD implementations, SDLs and ORRs are particularly promising for large scale OBFNs. Both the SDLs and ORR based TTD lines were well investigated in this thesis theoretically and experimentally regarding the generation of high quality TTDs.

A modified architecture of SDL to achieve ripple-free operation based on MZI optical switches was developed in Chapter 5. A 1×4 OBFN using 5-stage ripple-free SDLs was realized for linear PAAs using ultra-low loss SiN technology. Six delay configurations with 0, 1.5, 3, 4.5, 6 and 7.5 ps path delay incremental steps and a bandwidth over 8 nm were demonstrated. The ORR based delay line optimization was discussed in Chapter 6. A tradeoff between the ripple level, delay value, bandwidth and the total number of rings were revealed by the optimization. The optimization of a 1×4 3-ORR based OBFN exhibited that the ORR-OBFN architecture, where one ORR is shared

by two adjacent paths, well balanced the ripple level and system complexity. Two 3-ORR based 1×4 OBFNs with the architecture of sharing one and two ORRs were realized on SiN platform. With optimized tuning, a single 3-ORR delay line generated continuous TTD tuning ranges of 209 ps and 172 ps for bandwidth of 6.3 GHz and 8.6 GHz, respectively. The two ORR-OBFNs both generated delay responses for linear PAAs with 4.6 ps between adjacent paths and the OBFN with one ORR shared exhibits much more flattened delay spectrum as expected. Based on the investigation, SDLs shows extremely large TTD bandwidth and simplified controls but only discrete delay tunability, whereas ORRs shows continuous delay tunability, relatively small bandwidth and complex controls. The FSR of an ORR should be specifically designed with the desired mmW frequency to match the desired TTD bandwidth. Both the SDL-OBFN and ORR-OBFN are considered extremely promising for directional beamforming with PAAs.

The integrated OBFN chips were packaged and used in experiments for mmW signal generation and beamsteering. With a single delay path of the ORR-OBFN, a 41 GHz mmW signal was generated and the spectrum of the signal with 3 $Gbps$ ASK modulated data was measured. The SDL-OBFN was employed for a W-band signal beamsteering experiment, and 6 beam angles from -51° to 31° with 15 GHz TTD bandwidth from 85 to 100 GHz and a SNR of 35 dB were demonstrated. Also, a 94 GHz W-band signal with 3 $Gbps$ ASK data was generated and the spectrum was measured. The bandwidth and SNR demonstrates great potential for high-data-rate transmission beyond 100 $Gbps$. To the author's best knowledge, this is the first report of W-band beamsteering and data transmission using an integrated OBFN.

To further improve the scalability and reduce the power consumption and complexity of the current PAA system, the integrated OBFN, PDs and antenna array should be integrated for a large scale TTD based PAA due to its sensitivity to the relative path

lengths and the relative large footprint of the discrete components compared to the signal wavelength. Moreover, the ORR-OBFN and SDL-OBFN involve many tuning elements. The control complexity and power consumption could be a problem for a large-scale OBFN. To address the potential issues above, some of the ongoing work on OBFN-PD-antenna integration was described in Chapter 10. Also, a novel RDL based OBFN architecture was proposed, which re-uses a single TTD element for the signal delays in all channels. Some of the required components for this RDL-OBFN have been realized and demonstrated in Chapter 10.

The work in this thesis serves as an prove of concept of applying IMWP technology to realize TTD based PAAs for EHF high-bit-rate communications. In the author's opinion, despite that only the OBFN of a PAA system is integrated in the work, other components including PDs, antenna array, multiplexer and demultiplexer, modulators and laser are possible to be integrated with today's technology. Therefore, future contributions are needed in full-/sub-system integration and deliberate electrical circuit design for a realistic compact photonic-enabled TTD based PAAs system. Novel OBFN architecture having high scalability, low power consumption and simplified controls such as RDL-OBFN should be considered as well.

Bibliography

[1] *Cisco Visual Networking Index: Forecast and Trends, 2017–2022 - Cisco*, 2017.

[2] A. Ghosh, T. A. Thomas, M. C. Cudak, R. Ratasuk, P. Moorut, F. W. Vook, T. S. Rappaport, G. R. MacCartney, S. Sun, and S. Nie, *Millimeter-Wave Enhanced Local Area Systems: A High-Data-Rate Approach for Future Wireless Networks*, *IEEE J. Sel. Areas Commun.* **32** (jun, 2014) 1152–1163.

[3] *ITU: Guidelines for evaluation of radio interface technologies for IMT-2020*, 2017.

[4] Y. Kim, H.-Y. Y. Lee, P. Hwang, R. K. Patro, J. Lee, W. Roh, and K. Cheun, *Feasibility of Mobile Cellular Communications at Millimeter Wave Frequency*, *IEEE J. Sel. Top. Signal Process.* **10** (apr, 2016) 589–599.

[5] Z. Cao, X. Zhao, F. M. Soares, N. Tessema, and A. M. J. Koonen, *38-GHz Millimeter Wave Beam Steered Fiber Wireless Systems for 5G Indoor Coverage: Architectures, Devices, and Links*, *IEEE J. Quantum Electron.* **53** (feb, 2017) 1–9.

[6] J. A. Nanzer, A. Wichman, J. Klamkin, T. P. McKenna, and T. R. Clark, *Millimeter-Wave Photonics for Communications and Phased Arrays*, *Fiber Integr. Opt.* **34** (jul, 2015) 159–174.

[7] J. Capmany and D. Novak, *Microwave photonics combines two worlds*, *Nat. Photonics* **1** (jun, 2007) 319–330.

[8] M. Agiwal, A. Roy, and N. Saxena, *Next Generation 5G Wireless Networks: A Comprehensive Survey*, *IEEE Commun. Surv. Tutorials* **18** (2016), no. 3 1617–1655.

[9] I. Frigyes and A. J. Seeds, *Optically generated true-time delay in phased-array antennas*, *IEEE Trans. Microw. Theory Tech.* **43** (1995), no. 9 2378–2386.

[10] X. Pang, A. Caballero, A. Dogadaev, V. Arlunno, R. Borkowski, J. S. Pedersen, L. Deng, F. Karinou, F. Roubeau, D. Zibar, X. Yu, and I. T. Monroy, *100 Gbit/s hybrid optical fiber-wireless link in the W-band (75-110 GHz)*, *Opt. Express* **19** (dec, 2011) 24944.

[11] S. Iezekiel, M. Burla, J. Klamkin, D. Marpaung, and J. Capmany, *RF Engineering Meets Optoelectronics: Progress in Integrated Microwave Photonics*, *IEEE Microw. Mag.* **16** (2015), no. 8 28–45.

[12] D. Marpaung, J. Yao, and J. Capmany, *Integrated microwave photonics*, *Nat. Photonics* **13** (feb, 2019) 80–90.

[13] J. Klamkin, Y. Liu, B. Song, F. Sang, and B. Isaac, *Integrated Microwave Photonic Component Technologies*, in *Conf. Lasers Electro-Optics*, (Washington, D.C.), p. JTh3D.5, OSA, may, 2018.

[14] *ITU: Attenuation by atmospheric gases*, 2016.

[15] M. Marcus and B. Pattan, *Millimeter wave propagation: Spectrum management implications*, *IEEE Microw. Mag.* **6** (2005), no. 2 54–62.

[16] J. Wells, *Faster than fiber: The future of multi-G/s wireless*, *IEEE Microw. Mag.* **10** (2009), no. 3 104–112.

[17] J. Esch, *State of the Art in 60-GHz Integrated Circuits and Systems for Wireless Communications*, *Proc. IEEE* **99** (aug, 2011) 1386–1389.

[18] E. J. Violette, R. H. Espeland, and G. R. Hand, *Millimeter-wave urban and suburban propagation measurements using narrow and wide bandwidth channel probes*, *NASA STI/Recon Tech. Rep. N* **86** (1985) 25683.

[19] R. J. Humpleman and P. A. Watson, *Investigation of attenuation by rainfall at 60 GHz*, *Electr. Eng. Proc. Inst.* **125** (1978), no. 2 85–91.

[20] Suiyan Geng, J. Kivinen, Xiongwen Zhao, and P. Vainikainen, *Millimeter-Wave Propagation Channel Characterization for Short-Range Wireless Communications*, *IEEE Trans. Veh. Technol.* **58** (jan, 2009) 3–13.

[21] R. C. Daniels, J. N. Murdock, T. S. Rappaport, and R. W. Heath, *60 GHz Wireless: Up Close and Personal*, *IEEE Microw. Mag.* **11** (dec, 2010) 44–50.

[22] Hao Xu, V. Kukshya, and T. Rappaport, *Spatial and temporal characteristics of 60-GHz indoor channels*, *IEEE J. Sel. Areas Commun.* **20** (apr, 2002) 620–630.

[23] L. Correia and P. Smulders, *Characterisation of propagation in 60 GHz radio channels*, *Electron. Commun. Eng. J.* **9** (apr, 1997) 73–80.

[24] C. Anderson and T. Rappaport, *In-Building Wideband Partition Loss Measurements at 2.5 and 60 GHz*, *IEEE Trans. Wirel. Commun.* **3** (may, 2004) 922–928.

[25] P. Smulders and A. Wagemans, *Wideband indoor radio propagation measurements at 58 GHz*, *Electron. Lett.* **28** (1992), no. 13 1270.

[26] F. Giannetti, M. Luise, and R. Reggiannini, *Mobile and Personal Communications in the 60 GHz Band: A Survey*, *Wirel. Pers. Commun.* **10** (1998), no. 2 207–243.

[27] T. Zwick, T. Beukema, and Haewoon Nam, *Wideband channel sounder with measurements and model for the 60 GHz indoor radio channel*, *IEEE Trans. Veh. Technol.* **54** (jul, 2005) 1266–1277.

[28] Provided by T. Clark, *Johns Hopkins University, Applied Physics Laboratory.*

[29] *ITU: Attenuation due to clouds and fog*, 2017.

[30] Z. Qingling and J. Li, *Rain Attenuation in Millimeter Wave Ranges*, in *2006 7th Int. Symp. Antennas, Propag. EM Theory*, pp. 1–4, IEEE, oct, 2006.

[31] *ITU: Specific attenuation model for rain for use in prediction methods*, 2005.

[32] Y. Niu, Y. Li, D. Jin, L. Su, and A. V. Vasilakos, *A survey of millimeter wave communications (mmWave) for 5G: opportunities and challenges*, *Wirel. Networks* **21** (nov, 2015) 2657–2676.

[33] "E-Band Technology - E-Band Communications http://www.e-band.com/index.php?id=86."

[34] S. Iezekiel, *Microwave photonics : devices and applications.* Wiley, 2009.

[35] R. Maram, S. Kaushal, J. Azaña, L. Chen, R. Maram, S. Kaushal, J. Azaña, and L. R. Chen, *Recent Trends and Advances of Silicon-Based Integrated Microwave Photonics*, *Photonics* **6** (jan, 2019) 13.

[36] T. Fong, D. Sabido, and L. Kazovsky, *Linewidth-insensitive coherent AM analog optical links using semiconductor lasers*, *IEEE Photonics Technol. Lett.* **5** (apr, 1993) 469–471.

[37] A. Seeds, *Microwave opto-electronics*, in *Proc. EDMO '96*, pp. 44–49, IEEE.

[38] B. Cai and A. Seeds, *Optical frequency modulation links: Theory and experiments*, *IEEE Trans. Microw. Theory Tech.* **45** (apr, 1997) 505–511.

[39] Jianping Yao, Fei Zeng, and Qing Wang, *Photonic Generation of Ultrawideband Signals*, *J. Light. Technol.* **25** (2007), no. 11 3219–3235.

[40] T. P. McKenna, J. A. Nanzer, and T. R. Clark, *Photonic Beamsteering of a Millimeter-Wave Array With 10-Gb/s Data Transmission*, *IEEE Photonics Technol. Lett.* **26** (jul, 2014) 1407–1410.

[41] J. A. Nanzer, P. T. Callahan, M. L. Dennis, T. R. Clark, D. Novak, and R. B. Waterhouse, *Millimeter-wave wireless communication using dual-wavelength photonic signal generation and photonic upconversion*, *IEEE Trans. Microw. Theory Tech.* **59** (2011), no. 12 PART 2 3522–3530.

[42] T. P. McKenna, J. A. Nanzer, and T. R. Clark, *Photonic downconverting receiver using optical phase modulation*, *IEEE MTT-S Int. Microw. Symp. Dig.* (2014) 1–3.

[43] T. P. McKenna, J. A. Nanzer, M. L. Dennis, and T. R. Clark, *Fully fiber-remoted 80 GHz wireless communication with multi-subcarrier 16-QAM*, *2012 IEEE Photonics Conf. IPC 2012* **1** (2012) 576–577.

[44] V. R. Supradeepa, C. M. Long, R. Wu, F. Ferdous, E. Hamidi, D. E. Leaird, and A. M. Weiner, *Comb-based radiofrequency photonic filters with rapid tunability and high selectivity*, *Nat. Photonics* **6** (2012), no. 3 186–194, [arXiv:1105.0722].

[45] J. Yao, *A Tutorial on Microwave Photonics*, *IEEE Photonics Soc. Newsl.* **24** (2012), no. April 4–12, [arXiv:1211.4114].

[46] P. Ghelfi, F. Laghezza, F. Scotti, G. Serafino, A. Capria, S. Pinna, D. Onori, C. Porzi, M. Scaffardi, A. Malacarne, V. Vercesi, E. Lazzeri, F. Berizzi, and A. Bogoni, *A fully photonics-based coherent radar system*, *Nature* **507** (mar, 2014) 341–345.

[47] J. Xie, L. Zhou, Z. Zou, J. Wang, X. Li, and J. Chen, *Continuously tunable reflective-type optical delay lines using microring resonators*, *Opt. Express* **22** (jan, 2014) 817.

[48] A. S. P. Khope, M. Saeidi, R. Yu, X. Wu, A. M. Netherton, Y. Liu, Z. Zhang, Y. Xia, G. Fleeman, A. Spott, S. Pinna, C. Schow, R. Helkey, L. Theogarajan, R. C. Alferness, A. A. M. Saleh, and J. E. Bowers, *Multi-wavelength selective crossbar switch*, *Opt. Express* **27** (feb, 2019) 5203.

[49] B. Song, L. Yuning, S. Pinna, Y. Liu, and J. Klamkin, *Dilute Waveguide Reflective Semiconductor Optical Amplifier for 3D Hybrid Silicon Photonics Integration*, in *Compd. Semicond. Week Conf.*, 2019.

[50] F. Gambini, Y. Liu, B. Song, H. Zhao, V. Rosborough, F. Sang, P. Velha, S. Faralli, and J. Klamkin, *Ultra-Compact Bragg-Assisted Silicon Photonics Orbital Angular Momentum Emitter,*, *Adv. Photonics Congr. Integr. Photonics Res. Silicon Nanophotonics* (2019) 5–6.

[51] S. Pinna, Y. Liu, L. A. Coldren, and J. Klamkin, *Integrated star coupler-based multi-beam LiDAR*, in *2017 IEEE Avion. Veh. Fiber-Optics Photonics Conf.*, pp. 41–42, IEEE, nov, 2017.

[52] W. Bogaerts, P. De Heyn, T. Van Vaerenbergh, K. De Vos, S. Kumar Selvaraja, T. Claes, P. Dumon, P. Bienstman, D. Van Thourhout, and R. Baets, *Silicon microring resonators*, *Laser Photon. Rev.* **6** (2012), no. 1 47–73.

[53] F. Morichetti, A. Melloni, C. Ferrari, and M. Martinelli, *Error-free continuously-tunable delay at 10 Gbit/s in a reconfigurable on-chip delay-line*, *Opt. Express* **16** (jun, 2008) 8395.

[54] X. Wang, L. Zhou, R. Li, J. Xie, L. Lu, K. Wu, and J. Chen, *Continuously tunable ultra-thin silicon waveguide optical delay line*, *Optica* **4** (may, 2017) 507.

[55] J. Klamkin, H. Zhao, B. Song, Y. Liu, B. Isaac, S. Pinna, F. Sang, and L. Coldren, *Indium Phosphide Photonic Integrated Circuits: Technology and Applications*, in *2018 IEEE BiCMOS Compd. Semicond. Integr. Circuits Technol. Symp.*, pp. 8–13, IEEE, oct, 2018.

[56] M. Smit, X. Leijtens, H. Ambrosius, E. Bente, J. van der Tol, B. Smalbrugge, T. de Vries, E.-J. Geluk, J. Bolk, R. van Veldhoven, L. Augustin, P. Thijs, D. D'Agostino, H. Rabbani, K. Lawniczuk, S. Stopinski, S. Tahvili, A. Corradi, E. Kleijn, D. Dzibrou, M. Felicetti, E. Bitincka, V. Moskalenko, J. Zhao, R. Santos, G. Gilardi, W. Yao, K. Williams, P. Stabile, P. Kuindersma, J. Pello, S. Bhat, Y. Jiao, D. Heiss, G. Roelkens, M. Wale, P. Firth, F. Soares, N. Grote, M. Schell, H. Debregeas, M. Achouche, J.-L. Gentner, A. Bakker, T. Korthorst, D. Gallagher, A. Dabbs, A. Melloni, F. Morichetti, D. Melati, A. Wonfor, R. Penty, R. Broeke, B. Musk, and D. Robbins, *An introduction to InP-based generic integration technology*, *Semicond. Sci. Technol.* **29** (jun, 2014) 083001.

[57] S. Dwivedi, B. Song, Y. Liu, R. Moreira, L. Johanson, and J. Klamkin, *Demonstration of Compact Silicon Nitride Grating Coupler Arrays for Fan-out of Multicore Fibers*, in *Conf. Lasers Electro-Optics*, (Washington, D.C.), p. ATh3B.4, OSA, may, 2017.

[58] S. Dwivedi, B. Song, Y. Liu, R. Moreira, S. Estrella, L. Johansson, and J. Klamkin, *Integrated Silicon Nitride Fan-in/Fan-out for Multi-Core Fiber Interconnects*, in *Adv. Photonics 2017 (IPR, NOMA, Sensors, Networks, SPPCom, PS)*, (Washington, D.C.), p. IW2A.3, OSA, jul, 2017.

[59] S. Dwivedi, S. Pinna, R. Moreira, Y. Liu, B. Song, S. Estrella, L. Johansson, and J. Klamkin, *Multicore Fiber Link With SiN Integrated Fan-Out and InP Photodiode Array*, *IEEE Photonics Technol. Lett.* **30** (nov, 2018) 1921–1924.

[60] C. G. H. Roeloffzen, L. Zhuang, C. Taddei, A. Leinse, R. G. Heideman, P. W. L. van Dijk, R. M. Oldenbeuving, D. A. I. Marpaung, M. Burla, and K. J. J. Boller, *Silicon nitride microwave photonic circuits*, *Opt. Express* **21** (sep, 2013) 22937.

[61] Y. Liu, B. Isaac, J. Kalkavage, E. Adles, T. Clark, and J. Klamkin, *Beamforming with Photonic Integrated Circuits for Millimeter WaveCommunications and Phased Arrays*, in *Photonics Electromagn. Res. Symp.*, pp. 4–8, 2019.

[62] Y. Liu, B. Isaac, J. Kalkavage, E. Adles, T. Clark, and J. Klamkin, *True Time Delay Millimeter Wave Beam Steering with Integrated Optical Beamforming Network*, in *Conf. Lasers Electro-Optics*, (Washington, D.C.), p. SF3N.6, OSA, may, 2019.

[63] Y. Liu, B. Isaac, J. Kalkavage, E. Adles, T. Clark, and J. Klamkin, *93-GHz Signal Beam Steering with True Time Delayed Integrated Optical Beamforming Network*, in *Opt. Fiber Commun. Conf. 2019*, (Washington, D.C.), p. Th1C.5, OSA, 2019.

[64] E. Yamada, H. Tanobe, H. Yamazaki, J. Ozaki, M. Kohtoku, N. Kikuchi, N. Kashio, S. Kanazawa, T. Fujii, Y. Ogiso, Y. Ohiso, and Y. Ueda, *Over 67 GHz Bandwidth and 1.5 V Vπ InP-Based Optical IQ Modulator With n-i-p-n Heterostructure*, *J. Light. Technol. Vol. 35, Issue 8, pp. 1450-1455* **35** (apr, 2017) 1450–1455.

[65] T. Ishibashi, Y. Muramoto, T. Yoshimatsu, and H. Ito, *Unitraveling-Carrier Photodiodes for Terahertz Applications*, *IEEE J. Sel. Top. Quantum Electron.* **20** (2014), no. 6 79–88.

[66] P. Latzel, F. Pavanello, S. Bretin, M. Billet, E. Peytavit, J. F. Lampin, M. Zaknoune, and G. Ducournau, *High efficiency UTC photodiodes as photonic emitters for 300 GHz high spectral efficiency wireless communications*, *2017 11th Eur. Conf. Antennas Propagation, EUCAP 2017* (2017) 1639–1641.

[67] B. Isaac, S. Pinna, Y. Liu, and J. Klamkin, *Efficiency of Waveguide Uni-Traveling-Carrier Photodiodes for Microwave Signal Generation*, in *Opt. Fiber Commun. Conf. 2019*, (Washington, D.C.), p. Th3B.6, OSA, mar, 2019.

[68] M. Li, L. Wang, X. Li, X. Xiao, and S. Yu, *Silicon intensity Mach-Zehnder modulator for single lane 100 Gb/s applications*, *Photonics Res.* **6** (2018), no. 2 109.

[69] M. Piels and J. E. Bowers, *40 GHz Si/Ge Uni-Traveling Carrier Waveguide Photodiode*, *J. Light. Technol.* **32** (oct, 2014) 3502–3508.

[70] K. Li, X. Xie, Q. Li, Y. Shen, M. E. Woodsen, Z. Yang, A. Beling, and J. C. Campbell, *High-Power Photodiode Integrated With Coplanar Patch Antenna for 60-GHz Applications*, *IEEE Photonics Technol. Lett.* **27** (mar, 2015) 650–653.

[71] G. Carpintero, K. Balakier, Z. Yang, R. C. Guzmán, A. Corradi, A. Jimenez, G. Kervella, M. J. Fice, M. Lamponi, M. Chitoui, F. Van Dijk, C. C. Renaud,

A. Wonfor, E. A. Bente, R. V. Penty, I. H. White, and A. J. Seeds, *Microwave photonic integrated circuits for millimeter-wave wireless communications*, *J. Light. Technol.* **32** (2014), no. 20 3495–3501.

[72] J. E. Bowers, *Integrated microwave photonics*, in *2015 Int. Top. Meet. Microw. Photonics*, pp. 1–4, IEEE, oct, 2015.

[73] T. J. Kippenberg, R. Holzwarth, and S. A. Diddams, *Microresonator-Based Optical Frequency Combs*, .

[74] S. Gundavarapu, G. M. Brodnik, M. Puckett, T. Huffman, D. Bose, R. Behunin, J. Wu, T. Qiu, C. Pinho, N. Chauhan, J. Nohava, P. T. Rakich, K. D. Nelson, M. Salit, and D. J. Blumenthal, *Sub-hertz fundamental linewidth photonic integrated Brillouin laser*, *Nat. Photonics* **13** (jan, 2019) 60–67.

[75] M. L. Cooper, G. Gupta, M. A. Schneider, W. M. J. Green, S. Assefa, F. Xia, D. K. Gifford, and S. Mookherjea, *Waveguide dispersion effects in silicon-on-insulator coupled-resonator optical waveguides*, *Opt. Lett.* **35** (sep, 2010) 3030.

[76] Leimeng Zhuang, C. Roeloffzen, A. Meijerink, M. Burla, D. Marpaung, A. Leinse, M. Hoekman, R. Heideman, and W. van Etten, *Novel Ring Resonator-Based Integrated Photonic Beamformer for Broadband Phased Array Receive Antennas—Part II: Experimental Prototype*, *J. Light. Technol.* **28** (jan, 2010) 19–31.

[77] R. L. Moreira, J. Garcia, W. Li, J. Bauters, J. S. Barton, M. J. R. Heck, J. E. Bowers, and D. J. Blumenthal, *Integrated ultra-low-loss 4-Bit tunable delay for broadband phased array antenna applications*, *IEEE Photonics Technol. Lett.* **25** (jun, 2013) 1165–1168.

[78] Y. Liu, A. Wichman, B. Isaac, J. Kalkavage, E. Adles, T. Clark, and J. Klamkin, *Single Ring Resonator Delays for Integrated Optical Beam Forming Networks*, in *2016 IEEE Int. Top. Meet. Microw. Photonics*, vol. 7, pp. 321–324, 2016.

[79] F. Morichetti, A. Melloni, A. Breda, A. Canciamilla, C. Ferrari, and M. Martinelli, *A reconfigurable architecture for continuously variable optical slow-wave delay lines.*, *Opt. Express* **15** (dec, 2007) 17273–82.

[80] D. Melati, A. Waqas, Z. Mushtaq, and A. Melloni, *Wideband Integrated Optical Delay Line Based on a Continuously Tunable Mach-Zehnder Interferometer*, *IEEE J. Sel. Top. Quantum Electron.* **24** (jan, 2018) 1–8.

[81] C. K. Madsen and G. Lenz, *Optical all-pass filters for phase response design with applications for dispersion compensation*, *IEEE Photonics Technol. Lett.* **10** (1998), no. 7 994–996.

[82] G. Lenz, B. Eggleton, C. Madsen, and R. Slusher, *Optical delay lines based on optical filters*, *IEEE J. Quantum Electron.* **37** (apr, 2001) 525–532.

[83] F. Xia, L. Sekaric, and Y. Vlasov, *Ultracompact optical buffers on a silicon chip*, *Nat. Photonics* **1** (jan, 2007) 65–71.

[84] J. Cardenas, M. A. Foster, N. Sherwood-Droz, C. B. Poitras, H. L. R. Lira, B. Zhang, A. L. Gaeta, J. B. Khurgin, P. Morton, and M. Lipson, *Wide-bandwidth continuously tunable optical delay line using silicon microring resonators.*, *Opt. Express* **18** (dec, 2010) 26525–34.

[85] Y. Liu, A. Wichman, B. Isaac, J. Kalkavage, E. J. Adles, T. R. Clark, and J. Klamkin, *Tuning Optimization of Ring Resonator Delays for Integrated Optical Beam Forming Networks*, *J. Light. Technol.* **35** (nov, 2017) 4954–4960.

[86] A. Melloni, A. Canciamilla, C. Ferrari, F. Morichetti, L. O'Faolain, T. F. Krauss, R. De La Rue, A. Samarelli, and M. Sorel, *Tunable delay lines in silicon photonics: Coupled resonators and photonic crystals, a comparison*, *IEEE Photonics J.* **2** (apr, 2010) 181–194.

[87] J. L. Yang, S. C. Tjin, and N. Q. Ngo, *All chirped fiber grating based true-time delay for phased-array antenna beam forming*, *Appl. Phys. B Lasers Opt.* **80** (2005), no. 6 703–706.

[88] I. Giuntoni, D. Stolarek, D. I. Kroushkov, J. Bruns, L. Zimmermann, B. Tillack, and K. Petermann, *Continuously tunable delay line based on SOI tapered Bragg gratings*, *Opt. Express* **20** (may, 2012) 11241.

[89] S. Khan and S. Fathpour, *Complementary apodized grating waveguides for tunable optical delay lines*, tech. rep., 2012.

[90] W. Shi, V. Veerasubramanian, D. Patel, and D. V. Plant, *Tunable nanophotonic delay lines using linearly chirped contradirectional couplers with uniform Bragg gratings*, *Opt. Lett.* **39** (feb, 2014) 701.

[91] S. Khan and S. Fathpour, *Demonstration of complementary apodized cascaded grating waveguides for tunable optical delay lines*, *Opt. Lett.* **38** (oct, 2013) 3914.

[92] G. Wang, T. Dai, J. Jiang, X. Guo, B. Chen, Y. Wang, H. Yu, X. Jiang, and J. Yang, *Continuously tunable true-time delay lines based on a one-dimensional grating waveguide for beam steering in phased array antennas*, *Appl. Opt.* **57** (jun, 2018) 4998.

[93] V. C. Duarte, M. V. Drummond, and R. N. Nogueira, *Photonic True-Time-Delay Beamformer for a Phased Array Antenna Receiver based on Self-Heterodyne Detection*, *J. Light. Technol.* **34** (dec, 2016) 5566–5575.

[94] D. Melati, A. Waqas, Z. Mushtaq, and A. Melloni, *Wideband Integrated Optical Delay Line Based on a Continuously Tunable Mach-Zehnder Interferometer*, *IEEE J. Sel. Top. Quantum Electron.* **24** (2018), no. 1 1–8.

[95] A. Waqas, D. Melati, and A. Melloni, *Cascaded Mach–Zehnder Architectures for Photonic Integrated Delay Lines*, *IEEE Photonics Technol. Lett.* **30** (nov, 2018) 1830–1833.

[96] N. Ishikura, R. Hosoi, R. Hayakawa, T. Tamanuki, M. Shinkawa, and T. Baba, *Photonic crystal tunable slow light device integrated with multi-heaters*, *Appl. Phys. Lett.* **100** (may, 2012) 221110.

[97] J. Sancho, J. Bourderionnet, J. Lloret, S. Combrié, I. Gasulla, S. Xavier, S. Sales, P. Colman, G. Lehoucq, D. Dolfi, J. Capmany, and A. De Rossi, *Integrable microwave filter based on a photonic crystal delay line*, *Nat. Commun.* **3** (jan, 2012) 1075.

[98] C.-Y. Lin, H. Subbaraman, A. Hosseini, A. X. Wang, L. Zhu, and R. T. Chen, *Silicon nanomembrane based photonic crystal waveguide array for wavelength-tunable true-time-delay lines*, *Appl. Phys. Lett.* **101** (jul, 2012) 051101.

[99] F. M. Soares, F. Karouta, E. Smalbrugge, M. K. Smit, J. j. M. Binsma, J. Lopez, A. Enard, and N. Vodjdani, *An InP-based photonic integrated beamformer for phased-array antennas*, in *Opt. Amplifiers Their Appl. Photonics Res.*, (Washington, D.C.), p. IFB2, OSA, jun, 2004.

[100] Y. Liu, F. Sang, B. Isaac, J. Kalkavage, E. Adles, T. Clark, and J. Klamkin, *Integrated Silicon Nitride Optical Beamforming Networks for Wideband Communications*, in *Adv. Photonics 2018 (BGPP, IPR, NP, NOMA, Sensors, Networks, SPPCom, SOF)*, (Washington, D.C.), p. ITh3B.4, OSA, jul, 2018.

[101] P. Zheng, C. Wang, X. Xu, J. Li, D. Lin, G. Hu, R. Zhang, B. Yun, and Y. Cui, *A Seven Bit Silicon Optical True Time Delay Line for Ka-Band Phased Array Antenna*, *IEEE Photonics J.* **11** (aug, 2019) 1–9.

[102] A. Yeniay and R. Gao, *True Time Delay Photonic Circuit Based on Perfluorpolymer Waveguides*, *IEEE Photonics Technol. Lett.* **22** (nov, 2010) 1565–1567.

[103] Z. Cao, N. Tessema, S. Latkowski, X. Zhao, Z. Chen, V. Moskalenko, K. A. Williams, H. P. A. van der Boom, E. Tangdiongga, and A. M. J. Koonen, *Integrated remotely tunable optical delay line for millimeter-wave beam steering fabricated in an InP generic foundry*, *Opt. Lett.* **40** (sep, 2015) 3930.

[104] J. Wang, R. Ashrafi, R. Adams, I. Glesk, I. Gasulla, J. Capmany, L. R. Chen, P. Cheben, J. Capmany, D. Novak, J. Yao, W. Ng, V. Kaman, X. Zheng, R. J. Helkey, C. Pusarla, J. E. Bowers, J. D. Shin, B. S. Lee, B. G. Kim, J. Sancho, J. Adachi, N. Ishikura, H. Sasaki, T. Baba, A. Melloni, M. Burla, M. S. Rasras, J. Cardenas, P. A. Morton, J. Cardenas, J. B. Khurgin, M. Lipson, J. Xie, M. Spasojevic, L. R. Chen, S. Khan, M. A. Baghban, S. Fathpour, I. Giuntoni, S. Khan, S. Fathpour, M. Burla, W. Shi, V. Veerasubramanian, D. Patel, D. V. Plant, S. Yegnanarayanan, P. Trinh, F. Coppinger, B. Jalali, H. Lee, T. Chen, J. Li, O. Painter, K. J. Vahala, R. L. Moreira, J. Xie, L. Zhou, Z. Li, J. Wang, J. Chen, G. Lenz, B. J. Eggleton, C. K. Madsen, R. E. Slusher, I. Gasulla, J. Capmany, S. Garcia, I. Gasulla, P. J. Bock, R. Halir, M. W. Farn, R. Halir, P. Cheben, Y. Zhou, V. Karagodsky, F. G. Sedgwick, C. J. Chang-Hasnain, Y. Zhou, M. Moewe, J. Kern, M. C. Y. Huang, C. J. Chang-Hasnain, W. Yang, D. Fattal, J. Li, Z. Peng, M. Fiorentino, R. G. Beausoleil, M. C. Y. Huang, Y. Zhou, C. J. Chang-Hasnain, P. J. Bock, J. Wang, I. Glesk, L. R. Chen, V. Donzella, A. Maese-Novo, V. Donzella, Z. Wang, and C. G. H. Roeloffzen, *Subwavelength grating enabled on-chip ultra-compact optical true time delay line*, .

[105] G. Grosskopf, R. Eggemann, H. Ehlers, A. Kortke, B. Kuhlow, G. Przyrembel, D. Rohde, and S. Zinal, *Maximum Directivity Beam-Former at 60 GHz with Optical Feeder*, *IEEE Trans. Antennas Propag.* **51** (2003), no. 11 3040–3046.

[106] X. Wang, L. Zhou, R. Li, J. Xie, L. Lu, and J. Chen, *Nanosecond-range Continuously Tunable Silicon Optical Delay Line Using Ultra-thin Silicon Waveguides*, in *Conf. Lasers Electro-Optics*, (Washington, D.C.), p. STu1G.5, OSA, 2016.

[107] S. Toroghi, C. Fisher, S. Khan, and S. Fathpour, *Performance Comparison of Grating-Assisted Integrated Photonic Delay Lines*, *J. Light. Technol.* **34** (dec, 2016) 5431–5436.

[108] L. Z. Linjie Zhou, X. W. Xinyi Wang, L. L. Liangjun Lu, and J. C. Jianping Chen, *Integrated optical delay lines: a review and perspective [Invited]*, *Chinese Opt. Lett.* **16** (2018), no. 10 101301.

[109] P. Zheng, C. Wang, X. Xu, J. Li, D. Lin, G. Hu, R. Zhang, B. Yun, and Y. Cui, *A Seven Bit Silicon Optical True Time Delay Line for Ka-Band Phased Array Antenna*, *IEEE Photonics J.* **11** (aug, 2019) 1–9.

[110] N. Tessema, Z. Cao, J. V. Zantvoort, A. Dubok, E. Tangdiongga, B. Smolders, and T. Koonen, *Radio Beam-steering via Tunable Si_3N_4 Optical Delays for Multi-Gbps K-band Satellite Communication*, in *Opt. Fiber Commun. Conf.*, (Washington, D.C.), p. W3K.4, OSA, mar, 2016.

[111] C. Roeloffzen, P. van Dijk, D. Marpaung, M. Burla, and L. Zhuang, *Development of a broadband integrated optical beamformer for Kuband phased array antennas*, pp. 3–5, 34th ESA Antenna Workshop, 2012.

[112] A. J. Seeds, C. C. Renaud, H. Shams, and M. J. Fice, *TeraHertz Photonics for Wireless Communications*, *J. Light. Technol. Vol. 33, Issue 3, pp. 579-587* **33** (feb, 2015) 579–587.

[113] H. Ito and T. Ishibashi, *Photonic Terahertz-Wave Generation Using Slot-Antenna-Integrated Uni-Traveling-Carrier Photodiodes*, *IEEE J. Sel. Top. Quantum Electron.* **23** (jul, 2017) 1–7.

[114] P. Latzel, F. Pavanello, S. Bretin, M. Billet, E. Peytavit, J. F. Lampin, M. Zaknoune, and G. Ducournau, *High efficiency UTC photodiodes as photonic emitters for 300 GHz high spectral efficiency wireless communications*, in *2017 11th Eur. Conf. Antennas Propag.*, pp. 1639–1641, IEEE, mar, 2017.

[115] B. Isaac, Y. Liu, S. Pinna, L. Coldren, and J. Klamkin, *Uni-Traveling-Carrier Photodiodes for mmW Signal Generation: Space-Charge Impedance and Efficiency Limitations*, in *Device Res. Conf.*, pp. Th3B–6, 2019.

[116] B. Isaac, Y. Liu, S. Pinna, and J. Klamkin, *Limitations to Power Conversion Efficiency of InP Based Uni-traveling-carrier Photodiodes Due to Space Charge Resistance*, in *Compd. Semicond. Week Conf.*, 2019.

[117] K. Kato, A. Kozen, Y. Muramoto, Y. Itaya, T. Nagatsuma, and M. Yaita, *110-GHz, 50%-efficiency mushroom-mesa waveguide p-i-n photodiode for a 1.55-/spl mu/m wavelength*, *IEEE Photonics Technol. Lett.* **6** (jun, 1994) 719–721.

[118] P. Hill, J. Schlafer, W. Powazinik, M. Urban, E. Eichen, and R. Olshansky, *Measurement of hole velocity in n-type InGaAs*, *Appl. Phys. Lett.* **50** (may, 1987) 1260–1262.

[119] D. K. D. K. Cheng, *Field and wave electromagnetics.* Addison-Wesley, 1989.

[120] C. A. Balanis, *Modern antenna handbook*. Wiley, 2008.

[121] I. D. I. D. Robertson and Institution of Electrical Engineers., *MMIC design.* Institution of Electrical Engineers, 1995.

[122] C. G. H. Roeloffzen, M. Hoekman, E. J. Klein, L. S. Wevers, R. B. Timens, D. Marchenko, D. Geskus, R. Dekker, A. Alippi, R. Grootjans, A. van Rees, R. M. Oldenbeuving, J. P. Epping, R. G. Heideman, K. Worhoff, A. Leinse, D. Geuzebroek, E. Schreuder, P. W. L. van Dijk, I. Visscher, C. Taddei, Y. Fan, C. Taballione, Y. Liu, D. Marpaung, L. Zhuang, M. Benelajla, and K.-J. Boller, *Low-Loss Si3N4 TriPleX Optical Waveguides: Technology and Applications Overview*, *IEEE J. Sel. Top. Quantum Electron.* **24** (jul, 2018) 1–21.

[123] B. Stern, X. Ji, A. Dutt, and M. Lipson, *Compact narrow-linewidth integrated laser based on a low-loss silicon nitride ring resonator*, *Opt. Lett.* **42** (nov, 2017) 4541.

[124] Y. Fan, R. M. Oldenbeuving, M. Hoekman, D. Geskus, R. Dekker, R. G. Heideman, C. G. Roeloffzen, and K.-J. Boller, *290 Hz intrinsic linewidth from an integrated optical chip-based widely tunable InP-Si3N4 hybrid laser*, in *2017 Conf. Lasers Electro-Optics Eur. Eur. Quantum Electron. Conf.*, pp. 1–1, IEEE, jun, 2017.

[125] R. G. Heideman, D. H. Geuzebroek, A. Leinse, A. Melloni, F. Morichetti, C. Roeloffzen, A. Meijerink, L. Zhuang, W. van Etten, E. Klein, and Others, *Low loss, high contrast optical waveguides based on CMOS compatible LPCVD processing*, in *Proc. 13th Eur. Conf. Integr. Opt.*, Citeseer, 2007.

[126] R. Heideman, A. Leinse, W. Hoving, R. Dekker, D. Geuzebroek, E. Klein, R. Stoffer, C. Roeloffzen, L. Zhuang, and A. Meijerink, *Large-scale integrated optics using TriPleX waveguide technology: from UV to IR*, vol. 7221, p. 72210R, International Society for Optics and Photonics, feb, 2009.

[127] D. J. Blumenthal, R. Heideman, D. Geuzebroek, A. Leinse, and C. Roeloffzen, *Silicon Nitride in Silicon Photonics*, *Proc. IEEE* (2018) 1–23.

[128] J. F. Bauters, M. J. R. Heck, D. John, D. Dai, M.-C. Tien, J. S. Barton, A. Leinse, R. G. Heideman, D. J. Blumenthal, and J. E. Bowers, *Ultra-low-loss high-aspect-ratio Si3N4 waveguides.*, *Opt. Express* **19** (2011), no. 4 3163–3174.

[129] K. Wörhoff, R. G. Heideman, A. Leinse, and M. Hoekman, *TriPleX: A versatile dielectric photonic platform*, *Adv. Opt. Technol.* **4** (jan, 2015) 189–207.

[130] J. F. Bauters, M. J. R. Heck, D. D. John, J. S. Barton, C. M. Bruinink, A. Leinse, R. G. Heideman, D. J. Blumenthal, and J. E. Bowers, *Planar waveguides with less than 0.1 dB/m propagation loss fabricated with wafer bonding*, *Opt. Express* **19** (nov, 2011) 24090.

[131] D. Marpaung, C. Roeloffzen, A. Leinse, and M. Hoekman, *A photonic chip based frequency discriminator for a high performance microwave photonic link*, *Opt. Express* **18** (dec, 2010) 27359.

[132] G. Yurtsever, B. Považay, A. Alex, B. Zabihian, W. Drexler, and R. Baets, *Photonic integrated Mach-Zehnder interferometer with an on-chip reference arm for optical coherence tomography*, *Biomed. Opt. Express* **5** (apr, 2014) 1050.

[133] L. Zhuang, D. Marpaung, M. Burla, W. Beeker, A. Leinse, and C. Roeloffzen, *Low-loss, high-index-contrast Si_3N_4/SiO_2 optical waveguides for optical delay lines in microwave photonics signal processing*, *Opt. Express* **19** (nov, 2011) 23162.

[134] M. H. P. Pfeiffer, A. Kordts, V. Brasch, M. Zervas, M. Geiselmann, J. D. Jost, and T. J. Kippenberg, *Photonic Damascene process for integrated high-Q microresonator based nonlinear photonics*, *Optica* **3** (jan, 2016) 20.

[135] P. Del'Haye, A. Schliesser, O. Arcizet, T. Wilken, R. Holzwarth, and T. J. Kippenberg, *Optical frequency comb generation from a monolithic microresonator*, *Nature* **450** (dec, 2007) 1214–1217.

[136] J. P. Epping, M. Hoekman, R. Mateman, A. Leinse, R. G. Heideman, A. van Rees, P. J. van der Slot, C. J. Lee, and K.-J. Boller, *High confinement, high yield Si_3N_4 waveguides for nonlinear optical applications*, *Opt. Express* **23** (jan, 2015) 642.

[137] LioniX, *Platform TriPleX™ MPW run 9: High Contraste*, 2015.

[138] P. Muñoz, G. Micó, L. Bru, D. Pastor, D. Pérez, J. Doménech, J. Fernández, R. Baños, B. Gargallo, R. Alemany, A. Sánchez, J. Cirera, R. Mas, and C. Domínguez, *Silicon Nitride Photonic Integration Platforms for Visible, Near-Infrared and Mid-Infrared Applications*, *Sensors 2017, Vol. 17, Page 2088* **17** (sep, 2017) 2088.

[139] L. A. Coldren, S. W. Corzine, and M. L. Mašanović, *Diode Lasers and Photonic Integrated Circuits*. John Wiley & Sons, Inc., Hoboken, NJ, USA, 2nd ed., mar, 2012.

[140] A. Yariv, *Critical coupling and its control in optical waveguide-ring resonator systems*, *IEEE Photonics Technol. Lett.* **14** (apr, 2002) 483–485.

[141] C. Madsen, *Subband all-pass filter architectures with applications to dispersion and dispersion-slope compensation and continuously variable delay lines*, *J. Light. Technol.* **21** (oct, 2003) 2412–2420.

[142] Y. Liu, A. Wichman, B. Isaac, J. Kalkavage, E. Adles, and J. Klamkin, *Ring Resonator Delay Elements for Integrated Optical Beamforming Networks: Group Delay Ripple Analysis*, *Adv. Photonics 2016 (IPR, NOMA, Sensors, Networks, SPPCom, SOF)* (2016) IW1B.3.

[143] Y. Liu, A. R. Wichman, B. Isaac, J. Kalkavage, E. J. Adles, T. R. Clark, and J. Klamkin, *Ultra-Low-Loss Silicon Nitride Optical Beamforming Network for Wideband Wireless Applications*, *IEEE J. Sel. Top. Quantum Electron.* **24** (jul, 2018) 1–10.

[144] D. H. Sheingold, *Impedance & admittance transformations using operational amplifiers*, *Light. Empiricist* **12** (1964), no. 1 1–8.

[145] "Qt | Cross-platform software development for embedded & desktop."

[146] Y. Liu, A. Wichman, B. Isaac, E. Adles, F. Sang, J. Kalkavage, J. Klamkin, and T. Clark, *Ring Resonator True Time Delay Arrays with Sharing Optimization for Wideband Applications*, *Adv. Photonics 2017 (IPR, NOMA, Sensors, Networks, SPPCom, PS) (2017), Pap. IW2A.2* (jul, 2017) IW2A.2.

[147] Y. Liu, F. Sang, S. Pinna, B. Isaac, J. Kalkavage, E. Adles, T. Clark, and J. Klamkin, *Integrated optical beamforming network for millimeter wave communications*, in *2017 Int. Top. Meet. Microw. Photonics*, pp. 1–4, IEEE, oct, 2017.

[148] Y. Liu, A. Wichman, B. Isaac, J. Kalkavage, E. Adles, T. Clark, and J. Klamkin, *Ring resonator based integrated optical beam forming network with true time delay for mmW communications*, in *2017 IEEE MTT-S Int. Microw. Symp.*, pp. 443–446, IEEE, jun, 2017.

[149] Y. Liu, B. Isaac, J. Kalkavage, E. J. Adles, T. R. Clark, and J. Klamkin, *Low-loss silicon nitride integrated optical beamforming network for wideband communication*, in *Terahertz, RF, Millimeter, Submillimeter-Wave Technol. Appl. XI* (L. P. Sadwick and T. Yang, eds.), vol. 10531, p. 44, SPIE, feb, 2018.

[150] Y. Liu, B. Isaac, J. Kalkavage, E. Adles, T. Clark, and J. Klamkin, *Millimeter Wave Beamsteering with True Time Delayed Integrated Optical Beamforming Network*, in *2019 Eur. Conf. Opt. Commun.*, (Dublin, Ireland), IEEE, sep, 2019.

[151] Y. Liu, B. Isaac, J. Kalkavage, E. Adles, T. Clark, and J. Klamkin, *Programmable Integrated Microwave Photonics Beamforming Networks for Millimeter Wave Communications and Phased Arrays*, in *2019 IEEE Avion. Veh. Fiber-Optics Photonics Conf.*, (Washington, D.C.), p. TuD5, IEEE, 2019.

[152] J. Li, X. Zhang, F. Tian, and L. Xi, *Generation of Stable and High-Quality Multicarrier Source Based on Re-circulating Frequency Shifter for Tb/s Optical Transmission*, in *Opt. Fiber Commun. Conf. Fiber Opt. Eng. Conf. 2011*, vol. 19, (Washington, D.C.), p. OWE4, OSA, jan, 2011.

[153] J. Zhang, J. Yu, N. Chi, Z. Dong, X. Li, and G. K. Chang, *Improved multi-channel multi-carrier generation using gain-independent multi-channel frequency shifting recirculating loop*, *Opt. Express* **20** (dec, 2012) 29599.

[154] X. Wang and S. Mookherjea, *Optimizing Recirculating-Frequency-Shifter performance with Semiconductor Optical Amplifier gain assistance*, in *Conf. Lasers Electro-Optics*, (Washington, D.C.), p. JW2A.63, OSA, may, 2018.

[155] J. Klamkin, L. Wang, B. Shi, S. T. Š. Brunelli, H. Zhao, and B. Song, *Laser Integration Technologies for Silicon Photonics*, in *OSA Adv. Photonics Congr. 2019 (IPR, Networks, NOMA, SPPCom, PVLED)*, p. ITh1A.1, Optical Society of America, 2019.

[156] Y. Zhu, Y. Zhao, and L. Zhu, *Loss induced coherent combining in InP-Si3N4 hybrid platform*, *Sci. Rep.* **8** (2018), no. 1 4–10.

[157] Y. Zhu and L. Zhu, *Narrow-linewidth, tunable external cavity dual-band diode lasers through InP/GaAs-Si 3 N 4 hybrid integration* , *Opt. Express* **27** (2019), no. 3 2354.

[158] B. Song, Y. Liu, S. Ristic, and J. Klamkin, *Tunable 3D Hybrid Integrated Silicon Photonic External Cavity Laser*, in *Conf. Lasers Electro-Optics*, (Washington, D.C.), p. AM4A.3, OSA, may, 2017.

[159] J. Klamkin, *3D hybrid integration for active silicon photonics (Conference Presentation)*, in *Next-Generation Opt. Networks Data Centers Short-Reach Links IV* (A. K. Srivastava, ed.), vol. 10131, p. 1, SPIE, apr, 2017.

[160] J. G. Proakis and M. Salehi, *Communication systems engineering*. Prentice Hall, 1994.

[161] M. Smit and C. Van Dam, *PHASAR-based WDM-devices: Principles, design and applications*, *IEEE J. Sel. Top. Quantum Electron.* **2** (jun, 1996) 236–250.

[162] J. Fujikata, S. Takahashi, T. Mogami, K. Kurata, M. Takenaka, and T. Nakamura, *(Invited) High-Performance Si Optical Modulator and Ge Photodetector and Their Application to Silicon Photonics Integrated Circuit*, *ECS Trans.* **86** (jul, 2018) 17–25.

[163] H. Zhao, S. Pinna, F. Sang, B. Song, S. T. Suran Brunelli, L. A. Coldren, and J. Klamkin, *High-Power Indium Phosphide Photonic Integrated Circuits*, *IEEE J. Sel. Top. Quantum Electron.* **25** (nov, 2019) 1–10.